Experimental and numerical investigation on the LVI response of glass and Kevlar/PU- elastomeric matrix composites

AUTHOR: Regina Mardegan

ADVISOR: Prof. Andrea Manes

CO-ADVISOR: Ing. Alessandro Vescovini

ACADEMIC YEAR: 2022-2023

1. Introduction

A composite material can be defined as a combination of two or more materials that results in better properties than when the individual components are used alone. Because of the wide range of properties which can be attained with composites they have been introduced in almost every industry in some form or fashion. Composites are characterized by high strength and/or stiffness-to-weight ratio, and thus are usually adopted in high performance structural applications. However, when subjected to out-of-plane loads, such as impact events, the structural integrity and performance of the composite are significantly reduced, and sudden failures may occur under critical conditions.

This research project arises from the consolidated collaboration between Politecnico di Milano and Universidade Federal Do Rio Grande do Sul (UFRGS). The work focuses on the investigation, both experimental and numerical, of the impact damage resistance of glass, Kevlar, and inter-ply hybrid glass/Kevlar composites, manufactured with a novel elastomeric polyurethane matrix. The primary objective of the work is to investigate how different composite parameters might influence its response to impact events, in particular the effect of the novel matrix material with respect to standard epoxy resin matrixes.

Firstly, an extensive experimental campaign, including tensile, compressive, and shears tests, was performed for the calibration of the composites mechanical properties and definition of material model in the numerical simulations. Secondly drop weight tests were performed and the resulting damage in the composites were analyzed in detail.

Lastly the impact tests were replicated through finite element numerical analysis and the results compared with the experimental ones.

2. Materials

The composite matrix used in this study is an elastomeric polyurethane—PU (ϱ = 1.05 g/cm^3)

composed of a polyol blend (vegetable oil and poly(propylene oxide), developed by the UFRGS research team [1]. Plain-weave Kevlar29® (440 g/m2, 0.62 mm, 7 threads/cm, $\varrho = 1.45$ g/cm³) fabrics from Dupont, and 8-harness satin S2-glass (302 g/m², 0.24 mm, 22 threads/cm, $\varrho = 2.49$ g/cm³) were used as reinforcements. The composites were manufactured by vacuum infusion process.

For the mechanical characterization, single fiber Kevlar and glass composites were investigated, respectively constituted by five (K5) and eight (G8) fabric layers.

For the low velocity impact tests, the following configurations were considered:

- Sixteen layers glass laminate (G16)
- Eight layers Kevlar laminate (K8)
- Symmetric inter-ply aramid/glass hybrids, twelve layers, with three different configurations (Figure 2-1): (K2G4)S, (G4K2)S, (G2K)2S.
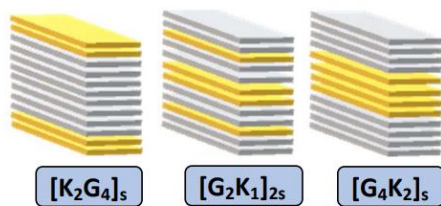

Figure 2-1: illustration of the hybrids configuration.

From now on Kevlar specimens are indicated as KE and glass samples by GL. Number next to the samples designation represent the energy level of the impact test performed.

Stacking sequences and number of layers were chosen to obtain similar final thickness for all configurations, approximately 4.5 mm. Hybrids were selected with same number of layers for each fiber type, and all with a symmetric configuration, to focus the investigation specifically on the influence of varying stacking sequence.

For impact tests some specimens with an epoxy resin matrix and equal configuration of the above-mentioned composites were also tested [2]. The obtained results were compared with the ones from the polyurethane matrix composites to further investigate the role of the matrix material in impact events.

3. Experimental analysis

Tests were performed mainly at the Mechanical Department labs, following the ASTM standards for PMC materials. The derived properties were later used in the performed impact numerical simulations.

3.1. Characterization tests

For the calibration of the composites mechanical properties tensile, compressive, and shear tests were performed.

Tensile tests were performed following the D3039/D3039M – 17 standards [3]. The following relevant properties were calculated in the specimens transverse and longitudinal direction: tensile Young's modulus ($E_{1,2+}$), Poisson ratio (ν_{12+}), maximum stress at failure ($\sigma_{1,2+}$), and maximum strain at failure ($\varepsilon_{1,2+}$).

Compressive tests were performed following the D3410/D3410M – 16 standards [4]. Maximum stress at failure was derived from the test, while elastic modulus ($E_{1,2-}$,) and Poisson ratio (ν_{12-}) values to be used in the finite element analysis (FEA) were taken as equal to the tensile tests one.

Shear tests were performed following the D3518/D3518M – 13 standards [5]. From shears tests Shear modulus (G_{12}), maximum shear stress (τ_{max}) and maximum shear strain (γ_{max}) at failure were calculated. In addition, cyclic shear tests were also performed for derivation of damage initiation and propagation parameters necessary for the definition of the material model in the (FEA).

3.2. Low velocity impact tests

Drop weight tests were performed following the D7136/D7136M – 15 standards [6].

Specimens were tested at three different energy levels: 50J, 90J, and 120J. When the number of specimens was enough an extra energy test at 20J or 30J was also performed.

Maximum impact force, maximum displacement, and absorbed energy were measured and calculated from the tests. The impacted panels were then also subjected to non-destructive analysis (NDA) to further investigate the extent of damage inside the structure.

In general, relevant differences in the materials response emerged only at the highest energy,

while for instance at 50J and 90J, results showed negligible divergences.

In terms of stiffness, single fiber glass composite showed in general the best performance for all energy levels.

Considering the absorbed energy, single fiber Kevlar laminate exhibited the highest results both at 50J and 90J, while the remaining specimens all showed similar but lower values. A different scenario was observed at 120J. The highest and the lowest recorded values were given by two hybrids. Maximum absorbed energy was observed for the (G4K2)S configuration while the minimum by the (K2G4)S specimen. In that case the inversion of internal and external plies type in the composites stacking sequence corresponds to an opposite behavior in terms of energy absorption from the impacts. The configuration having higher stiffness material on the outside and high absorbance material placed internally in the structure lead to an enhanced absorption capability in the composite.

Anyhow, all composites exhibited a high value of absorbed energy. In Figure 3-1 the proximity of the registered values to the equal energy line is an evidence of this aspect.
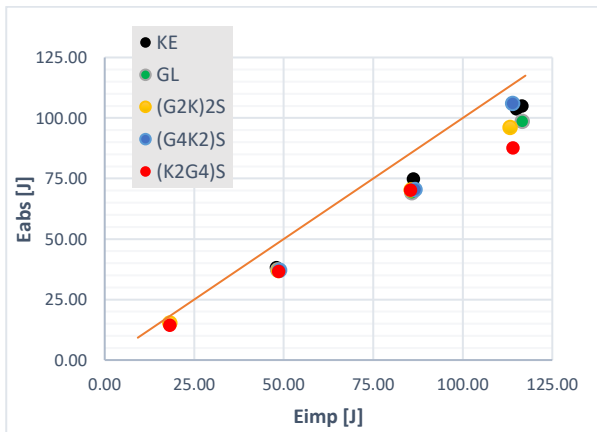

Figure 3-1 : E_{abs} - E_{imp} curve.

This characteristic emerged even more when the PU matrix composites were compared to same configuration epoxy resin matrix composites. Available samples for confrontation were glass, Kevlar, and (K2G4)S hybrid. Few samples were available for confrontation thus not all energy tests could be repeated. The analysis showed, in all cases, an evident increase in the capability of the PU matrix composite to absorb the energy imparted by the impact. In Figure 3-2 the values of the percentage absorbed energy respect to the

impact one for the tested specimens at different energy levels are shown. The blue columns represent the epoxy composites and the orange columns the PU composites. This confrontation of results is useful to readily visualize the divergence arising between the two types of materials. For the PU resin matrix, the absorbed energy is never lower than 75% of the overall impact energy.
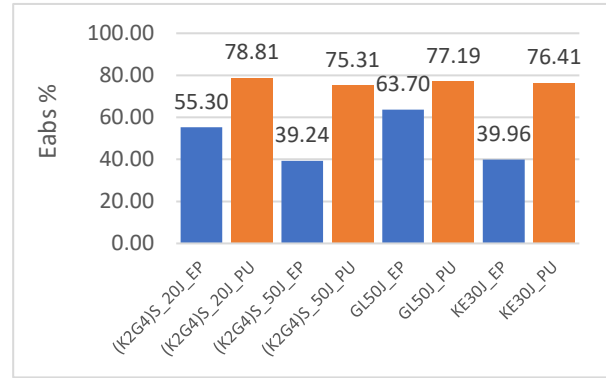

Figure 3-2: comparison between specimens E_{abs} in percentage values at different energy levels.

In particular, for specimens KE30J and (K2G4)S_50J the recorded absolute absorbed energy for the PU matrix composites reached a value up to 90% higher respect the one registered by the epoxy matrix composite samples. The curves in Figure 3-3, which represent the energy-time history for specimens KE30, PU and EPOXY, visually and numerically highlight this difference. The absorbed energy is given by the energy measured when the curve reaches the final plateau.
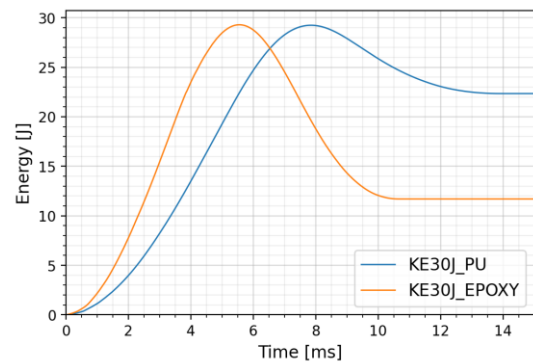

Figure 3-3: Energy-Time curves for KE30 specimens.

In accordance with this behavior, when considering the maximum impact force values, the epoxy resin composites always showed higher values with respect to the PU composites. When

comparing the maximum displacement, instead, epoxy matrix composites always exhibited lower results. This is evidence of the higher stiffness characterizing the epoxy resin composites.

Moreover, PU matrix laminates resisted higher impact energies before a critical visible damage could be observed on the specimens surface, while for the epoxy laminates, already at 50J, an initial perforation of the specimens could be usually noticed. In Figure 3-4 the impacted glass specimen at 120J can be observed. On the impact site some cracks and splits can be noticed, while on the back side of the specimen no damage is observed at all. It was common for the investigated composites to show negligible external damage after the impacts. Also, from the NDA, extension of internal damage was not easily detected. It can indicate either the difficulty in the adopted method to inspect this kind of material or a small propagation of internal damage and delamination.
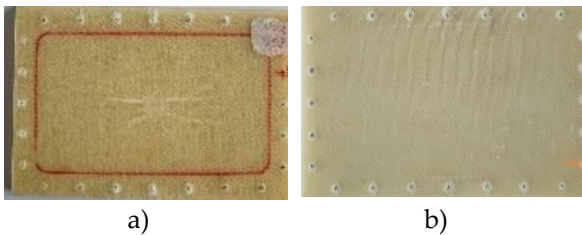

a)   b)

Figure 3-4: glass specimen tested at 120J (a)impact side and (b) back side.

From those experiments it has emerged then how the different matrix material in the composite really has an important role in determining the response of the material to impact loads. Softer matrices seem to infer to the composite a much-enhanced capability in absorbing the energy imparted by the impact and increase the overall composite damage resistance. It can be affirmed that the investigated polyurethane composites show an increased toughness with respect to the epoxy ones.

4.   Numerical analysis

The numerical investigation was performed with Abaqus/CAE software. The material model adopted is defined through a user subroutine (VUMAT) incorporated in Abaqus/Explicit and specifically designed for the characterization of woven composites [7]. For computational costs

saving the model represents one fourth of the real test dimensions, which is possible due to the symmetry of the problem. The built model is shown in the Figure below.
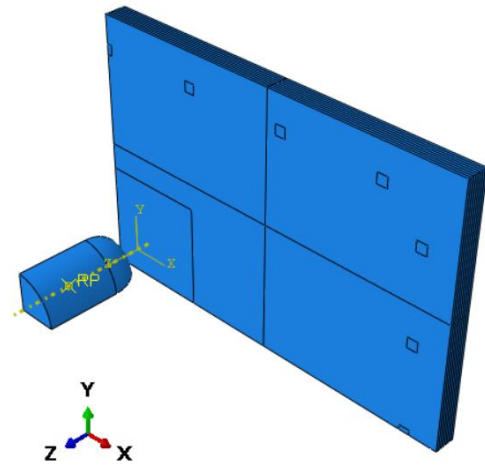

Figure 4-1: impact test numerical model.

From initial trial simulations performed with the created model some important issues regarding the hourglass modes of the elements have emerged.

Continuum shell elements were used for the definition of the panel part in the model and rigid body elements for the impactor. Hourglass modes are common in continuum shell elements under bending loads but changing element type was not a possibility as only few elements are allowed to be used in the above mentioned VUMAT. The hourglass phenomena was solved through the performance of sensitivity tests on the model, from which the most appropriate hourglass control and mesh settings were derived.

From the numerical analysis at 50J the best results were obtained for the KE composite, which showed good agreement with the experimental test. For the remaining samples the divergence between simulated and experimental results increased going from the hybrid (K2G4)S configuration, with Kevlar layers on the external surface, to the single fiber GL composite, which exhibited the most significant mismatch. The results from the simulations showed the typical behavior of materials with a higher stiffness with respect to the ones investigated here, with higher impact forces and lower displacements.

Figure 4-2 visually highlights the above considerations, in which the comparison between experimental and numerical impact-time curve is shown for GL and KE. Anyhow, for all composites,

including KE which showed the best match in results, the registered absorbed energy was always pretty distant from the effective measured value, as illustrated for instance in Figure 4-3 Figure 4 for the pure composites.
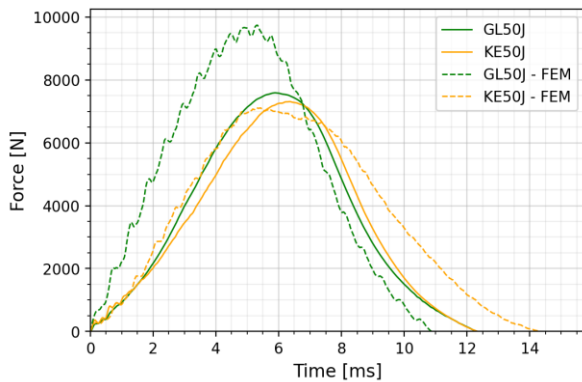

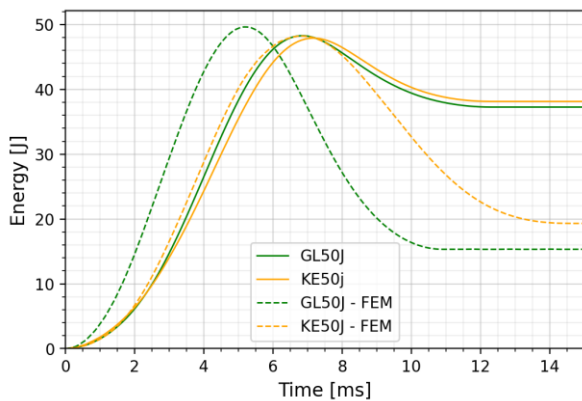Figure 4-2: force-time experimental and simulated curves for GL and KE specimens at 50J.

Figure 4-3 : energy-time experimental and simulated curves for GL and KE specimens at 50J.

At 90J critical impact damage started to be prematurely observed in the simulations.
For the glass specimen the performance of the material in terms of measured properties was degraded, but not reaching yet a critical level. For the tested hybrids instead, the simulated curves illustrate the typical trend of structures in which perforation has been already reached. This can be visualized in Figure 4-4 representing (G2K)2S and (K2G4)S configurations.
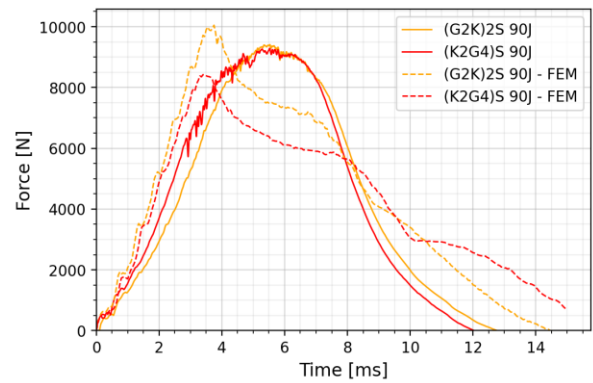

Figure 4-4: force-time experimental and simulated curves for (G2K)2S and (K2G4)S specimens at 90J.

Given the observed results from the performed simulations, the same material model probably would have given much better results if utilized to define a standard epoxy matrix composite characterized by relatively high stiffness.

5.   Conclusions

From the impact experimental tests an interesting behavior from the composites manufactured with the elastomeric polyurethane matrix has emerged. The composites showed promising behavior in terms of impact resistance. First, an enhanced capability in absorbing the energy imparted by the impact was observed, with increase in absorption values up to 90%. A higher deformation was also measured on the specimens but visually it seems like a great part of this deformation is recovered by the specimen after the test, exhibiting the elastomeric character of the matrix. Also, at the same energy level at which the epoxy resin composites started to reach perforation, in the PU composites the visible damage on their surface could still be considered as negligible and propagation of damage then less extended.

For what concern the numerical simulations it has emerged the poor capability of the material model adopted to replicate the peculiar behavior of the studied composites. The behavior observed for the PU matrix laminates is not easy to simulate in first place because the material models currently used for the description of composites were mainly developed thinking about more brittle and less deformable materials. For instance, the specimens subjected to the impacts exhibited high displacements during the tests, but once concluded

they would recover almost completely this deformation, in accordance with the elastomeric character of the matrix. This kind of behavior instead is not typically observed for resin matrixes composites, in which, given the brittleness of the resin, perforation is instead reached at lower energies.

In addition, problems characterized by large deformations are intrinsically difficult to simulate and often lead to computational errors during the analysis. Erosion of critically damaged elements can be useful when dealing with those kinds of problems, because usually they are the elements from which numerical problems mainly arise. For the PU matrix composites this possibility was not considered because experimentally no perforation or critical damage was observed for the simulated energies.

Moreover, considering for instance the enhanced toughness observed in the studied PU composites, damage initiation and propagation modes might be dictated by slightly different mechanisms, which are not accounted for by the commonly material models adopted in composites numerical simulations, as it is in the current case.

6.   Future developments

The current project could represent the starting point for further research about the influence of similar matrix materials on composites impact resistance. The confrontation between standard matrix composites, for instance epoxy resin, and elastomeric matrix composites, such as the one here investigated, is a fundamental aspect of the research. Tests should be organized considering the lower energies at which standard composites are critically damaged during impacts. More tests should be performed systematically on different specimens with varying but less severe energy levels to avoid the panels to reach perforation, which would not allow to correctly investigate the damage response. From a similar experimental campaign more specific considerations could be derived concerning the impact resistance of those kinds of materials. Moreover, following this path, not only the impact resistance but also the composites residual strength after the impact could be considered in future investigations.

Concerning the finite element analysis, a first step to obtain improvements in the numerical simulations would be to develop or use a more appropriate material model, able to consider the influence of softer matrixes and higher toughness compared.

The currently available models were mainly developed for stiff composites constituted by brittle matrixes. In those terms a first part of the work would be related to the characterization of the composite mechanical behavior with the aid of experimental tests, not only concerning impacts. Being then able to analytically describe the material with good fitting equations the best way to proceed would be then to incorporate those equations in a user subroutine to be adopted as the material model in the numerical analysis.

7.   Bibliography

[1] J. A. Cruz, S. C. Amico and O. Bianchi, "Effect of the aramid pulp on the physicochemical, viscoelastic properties and rheokinetics of polyurethanes," Journal of Polymer Research, vol. 30, 2022.

[2] J. A. Cruz, E. F. Kerche, O. Bianchi, A. Manes and S. C. Amico, "Castor Oil-Based Polyurethane/S2-Glass/Aramid Hybrid Composites Manufactured by Vacuum Infusion,"Polymers, vol. 14, 2022.

[3] ASTM D3039/D3039M-17 Standard Test Method for Tensile Properties of Polymer Matrix Composite Matreials.

[4] D3410/D3410M – 16 Standard Test Method for Compressive Properties of Polymer Matrix Composite Materials.

[5] D3518/D3518M – 13 In-Plane Shear Response of Polymer Matrix Composite Materials by Tensile Test of a 45 laminate.

[6] D7136/D7136M – 15 Measuring the Damage Resistance of a Fiber-Reinforced Polymer Matrix Composite to a Drop-Weight Impact Event.

[7] S. S. Corp., VUMAT for Fabric Reinforced Composites, Providence, RI, USA, 2008.

POLITECNICO

MILANO 1863

SCUOLA DI INGEGNERIA INDUSTRIALE
E DELL'INFORMAZIONE

Experimental and numerical investigation on the LVI response of glass and Kevlar/PU- elastomeric matrix composites

TESI DI LAUREA MAGISTRALE IN
MATERIALS ENGINEERING AND NANOTECHNOLOGY
INGEGNERIA DEI MATERIALI E DELLE NANOTECNOLOGIE

Author: **Regina Mardegan**

Student ID: 10596758
Advisor: Andrea Manes
Co-advisor: Alessandro Vescovini
Academic Year: 2022-23

Abstract

This thesis work is focused on studying the impact response of woven aramid, glass, and aramid/glass reinforced polymers with varying structural configurations and which were constituted by a novel elastomeric polyurethane matrix. The composites impact resistance was investigated by performing drop weight impact tests. FEM models were also developed for replicating and investigating the structural response of the composite panels and damaging. The project stems from the consolidated collaboration established between Politecnico di Milano and Universidade Federal do Rio Grande do Sul, which mainly concerns composites related research. First, a vast experimental campaign was performed for the calibration of the composites mechanical properties and the definition of the material model in the numerical analysis. Secondly impact tests were carried out, from which the impact resistance of the investigated materials was analyzed and discussed in detail. Some peculiar behavior has emerged from the experimental tests for the material's mechanical properties calibration. Moreover, from impact test investigation, it was shown in first analysis a promising behavior for what concern the materials capability to resist impact events, with respect to same laminates constituted by a standard epoxy resin matrix. In particular, an enhanced capability in absorbing energy from the impact has emerged from the results. This behavior in the composites was assigned to the use of the novel polyurethane matrix. The presented work could represent a good starting point for the further investigation of the damage resistance in composites constituted by a matrix material with similar properties of the one here adopted. Concerning instead the numerical investigation, from the analysis of the obtained results, it was concluded that for a better reproducibility of the tests a more sophisticated material model should be developed/used for the description of the investigated composites, taking into account the influence of the matrix material in the model.

Key-words: glass fibre reinforced composite, Kevlar fibre reinforced composite, hybrid composites, ABAQUS, impact resistance, impact damage.

Abstract in italiano

Questo lavoro di tesi è incentrato sullo studio della risposta all'urto di compositi rinforzati con fibre aramidiche, vetro e aramide/vetro con diverse configurazioni e costituiti da una nuova matrice poliuretanica elastomerica. La resistenza all'impatto dei compositi è stata studiata eseguendo prove di impatto. Sono stati inoltre sviluppati modelli FEM per replicare e studiare la risposta strutturale dei pannelli compositi e il loro danneggiamento. Il progetto nasce dalla consolidata collaborazione instaurata tra il Politecnico di Milano e l'Universidade Federal do Rio Grande do Sul, che riguarda principalmente ricerca legata a materiali compositi. In primo luogo, è stata eseguita una vasta campagna sperimentale per la calibrazione delle proprietà meccaniche dei compositi e la definizione del modello di materiale utilizzato nell'analisi numerica. In secondo luogo, sono state eseguite le prove di impatto, dai cui risultati è stata analizzata e discussa in dettaglio la resistenza all'impatto dei materiali. Alcuni comportamenti peculiari sono emersi dalle prove sperimentali già durante la calibrazione delle proprietà meccaniche. Inoltre, dall'indagine sugli impatti, è stato mostrato in prima analisi un comportamento promettente per quanto riguarda la capacità dei materiali di resistere ad essi, rispetto agli stessi laminati costituiti da una matrice di resina epossidica standard. In particolare, dai risultati è emersa una migliorata capacità di assorbire energia dall'impatto. Questo comportamento nei compositi è stato attribuito all'uso della nuova matrice poliuretanica. Il lavoro presentato potrebbe rappresentare un buon punto di partenza per ulteriori indagini sulla resistenza al danneggiamento in compositi costituiti da matrici con proprietà simili a quella qui adottata. Per quanto riguarda invece le simulazioni numeriche, si è giunti alla conclusione che, per ottenere una migliore riproducibilità dei risultati delle prove, un modello di materiale più sofisticato dovrebbe essere adottato o sviluppato per descrivere il comportamento dei compositi qui investigati, prendendo maggiormente in considerazione l'influenza della matrice.

Parole chiave: compositi in fibre di vetro, compositi in fibre aramidiche, compositi ibridi, ABAQUS, resistenza all'impatto, danneggiamento da impatto.

Contents

Introduction

Composite materials are given by the macroscopic combination of two or more distinct materials, usually indicated as matrix and reinforcement, which maintain a discrete and recognizable interface separating them. Composites are naturally present in nature, most common example being wood. Composites of interest in this discussion are the synthetic ones, being materials characterized by high strength and/or stiffness relative to weight and thus commonly adopted in high performance structural applications. Composite's primary engineering properties are mainly given by the reinforcement. The matrix supports the fibers under compressive loads, provides shear capabilities in two-dimensional fiber lay-ups, and transfer loads internally inside the composite. Moreover, in two dimensional composites the matrix provides the basic resistance to impact damage and delamination [1].

One of the weaknesses of composite materials is their susceptibility to out-of-plane loads, which are critical under low velocity impacts. When subjected to impacts, the structural integrity, stiffness, and toughness of the material are significantly reduced, resulting in catastrophic failure of the structure in extreme scenarios.

The damage resistance of composite materials under impact events have been widely investigated, as demonstrated by the consistent number of studies which can be retrieved in the literature. In multiple cases the research is focused on how the variation of specific parameters can affect the response of the material to the impact. For instance, they can be specifically related to the composite structure (thickness, lamina type, reinforcement material and mechanical properties, density, stacking sequence, hybridization effect, boundary conditions…) or also external conditions related to the impact itself (impactor shape, size, mass, velocity, impact energy …). In comparison, however, the influence of the matrix material has been considered much less respect to other composite features.

The current thesis work is part of a collaborative project between Politecnico di Milano (Department of Mechanical Engineering) and Universidade Federal do Rio Grande do Sul (UFRGS), in which a novel polyurethane matrix material has been adopted for the manufacturing of the composites under investigation. The two institutions have been already working together in composites related projects for the last few years. For instance, some of the most recent works includes: influence of pre-existing impact damage on low velocity impact response of CFRP [2], perforation resistance of alumina/aramid fiber composite material to ballistic impact [3], and the effect of fiber bundle uncertainty on the mechanical behavior of plain-woven composites [4]. Of high

interest for this thesis are the very last performed research about hybrid composites, in which inter-ply woven aramid/s2-glass epoxy laminates were investigated under different conditions. The effect of hybridization and stacking sequence was studied for what concern the composite ballistic response [5], in terms of resulting dynamic-mechanical properties [6], and also the different behavior under repeated impacts [7].

The composites hereby considered have same structural properties of the ones in the above-mentioned studies, except for the matrix material. As mentioned, it is constituted by an elastomeric polyurethane resin, which was developed by the UFRGS research team (PU (CO/PE)®) [8] and a first evaluation of resulting properties arising from the use of such material has been already performed in [9]. PU/ Aramid, PU/s2-Glass, and Hybrids with varying configurations were manufactured by vacuum infusion process at UFRGS and then sent to Politecnico di Milano for mechanical characterization and the investigation of the impact response. Primary objective of this project is the evaluation of how the composites structural parameters and matrix affect its damage resistance, by subjecting the laminates to drop weight impact tests. The influence of the elastomeric matrix material is evaluated also by confronting the obtained results with the ones from the epoxy composites investigated in the previous mentioned researches.

A Finite Element Model (FEM) was then also developed in this thesis to replicate the impact response of the composites. For the derivation of the mechanical properties to be inserted in the model a consistent initial experimental campaign was performed. Compared with experiments, numerical analysis is an effective and less expensive method to predict the response of laminated composites under impact loading and in recent years numerous sophisticated FE models have been developed. The aim here was to evaluate the replicability of the impact tests by the numerical simulations performed adopting a material model, already incorporated in ABAQUS/Explicit, specifically designed for woven composites. If the FEM was to be validated, it could be considered as a valid starting point to evaluate the influence of different configurations prior to experimental tests, with time and cost saving benefits.

In Chapter 1 the state of the art is presented. Composite materials are first generally introduced and described in terms of mechanical properties, manufacturing, damage initiation and propagation, and failure modes criteria. The discussion is then extended also to woven composites, which present some peculiarities respect to unidirectional ones. Impact tests are then described, with emphasis on the investigation of the damage resistance of composites under such kind of loads.

In Chapter 2 numerical simulation theoretical basis, necessary for the description of the FEM created for the impact simulations, are depicted. For the finite element modelling Abaqus/CAE software is exploited. Here the fundamentals of the analysis procedure adopted and elements used are reported. The material model used is then described in detail.

In Chapter 3 the experimental test campaign is illustrated. First part concerns the experiments performed for the material mechanical characterization, fundamental for the definition of the material model in the impact simulations. Second part regards the low velocity impact tests. Results for this part are discussed in detail, with emphasis on the influence of the composites configuration and matrix material on its damage resistance.

In Chapter 4 the finite element model developed for the impact test numerical simulations is described. The results obtained are then compared with the experimental ones.

In Chapter 5 conclusions and future developments are depicted.

1   State of the art

An introduction to composite materials is first reported for what concern their general characteristics such as structure, constituting materials, configuration, and production methods. The elastic behaviour of unidirectional laminae is then briefly presented, after which, the mechanical behaviour of a more complex laminate structure is considered through the Classical Lamination Theory. Following, possible damage modes in composites are illustrated, and the general concepts described till that point are extended to the case of textile fabric composites. Last, a brief consideration about impact events and their consequences on composites is reported.

1.1.   Introduction to composite materials

A composite material is defined as a material constituted by at least two distinct materials with physical and/or chemical properties significantly different from each other, and which, combined together, can generate a new material with novel and usually enhanced properties aimed to be used in a very specific application, for example structural applications or electric and thermal isolation [10], [11]. Main components are then:

- the matrix, or continuum phase, weaker from a mechanical point of view, which fundamentally gives the shape and the geometry to the material;
- the reinforcement, or dispersed phase, which function is to sustain the mechanical solicitations the material is subjected to.

For engineering applications, of main interest are the so-called *reinforced composites,* in which the mechanical properties of the dispersed phase are considerably superior with respect to the matrix properties. As a general rule, for a composite to be considered as a reinforced one, the elastic modulus of the dispersed phase must be five times higher respect the modulus of the continuum phase: if not the composite is considered as a *modified composite.* Reinforced composites are mainly used for structural applications.

Matrix material can be of different nature: metallic, ceramic and polymeric. As well, also the dispersed phase can be of different kind, and in that case multiple characteristics must be considered:

- the geometry, for what concern shape, dimensions and distribution;

- the orientation of the phase with respect to the symmetry axis of the material (relevant in case of fibers);
- concentration.

The composites under investigation in this thesis work fall into the FRP (Fiber Reinforced Plastics) group: combination of a homogeneous polymeric matrix reinforced with synthetic fibers.

Many combinations of matrix/fiber materials, ratio between them, processing techniques and configurations are possible, leading to unique properties in the final structure.

Adhesion between the phases is also a fundamental aspect to consider: the bonding strength between fiber and polymer matrix in the composite is one of the major factors to obtain superior fiber-reinforcement-polymer composite properties. Commonly, to enhance the adhesion, fibers are also treated superficially with some chemical agents, creating a sort of interphase between matrix and reinforcement [10], [12].

In a composite, a mono layer of fibers constitutes a *lamina*. In the lamina, fibers can be oriented in the same direction (unidirectional lamina, 1D) or they can be arranged in such a way to form a textile fabric (bidirectional lamina, 2D). Multiple laminas form a *laminate*. The final properties of the laminate are in first place modulated by the nature of the reinforcement (and resin) which constitute the laminas, by the type of laminas (uni- or bidirectional), the total number of layers and the relative orientation of each lamina with respect to the others (mono- and multiaxial laminates). Combining layers of different materials, a hybrid laminate composite is obtained.

1.1.1. Matrix

Among the polymer matrix composites, thermoset matrixes are predominant with respect to thermoplastic ones. Thermosets in fact, often provide easy wetting of reinforcing fiber and easy forming to final part geometries. It means that in general it is easier to process them with respect to the counterpart. Thermosets are classified into polyester resins, epoxy resins, vinyl ester resins, phenolic, polyurethane, and other high-temperature resins such as cyanate esters [13].

Thermoplastics, on the other hand, tend to be less brittle than thermosets and in addition they can also show better chemical resistance and are more easily molded and repaired. Also, as they are capable of being repeatedly softened by the application of heat and hardened by cooling, they have the potential to be more easily recycled, which has seen them most favored in recent commercial uptake. Usual thermoplastic materials are acrylic, polyolefin, ABS, etc.

For its benefits, the use of thermoplastics has increased consistently in the FRP industry in the last years, even though better realization of the fiber properties is generally achieved using thermosets.

Table 1 schematically shows some of the key aspects about the two macro-sets of matrixes.

	Thermoset	Thermoplastic
Processing	Contain monomers that cross-link together during the curing process to form an irreversible chemical bond. Thermosets are ideal for high-heat applications, such as electronics and appliances.	Pellets soften when heated and become more fluid as additional heat is applied. This allows thermoplastics to be remolded and recycled.
Features	• good mechanical properties • cannot be recycled • cannot be remolded or reshaped • easy to wet the reinforcing fibres and fillers * • more resistant to high temperatures than thermoplastics • high levels of dimensional stability • cost effective	• commonly offer high strength, shrink-resistance, and easy bendability; • highly recyclable • can melt if heated and reshaped • more difficult to wet the reinforcing fibres and fillers • high impact resistance • chemical resistance • generally, more expensive than thermosets

Table 1: thermoset and thermoplastic matrixes features.

1.1.2. Reinforcement

Fibers can be continuous or discontinuous. From now on only continuous fibers are going be considered. Most common fibers used are carbon fibers (AS4, IM7, etc.), glass fibers (E-glass, S-glass, etc.) and aramid fibers (Kevlar® and Twaron®) [13].

Carbon fiber is a unique reinforcement material because its properties can cover a huge range of thermal and physical characteristics which can be modulated in function of the final application. It shows the highest specific stiffness and tensile strength, low weight, high chemical and temperature resistance. Moreover, it infers an excellent fatigue resistance to the structural composite materials. On the other hand, toughness is relatively low and it is much more expensive than other fibers.

Considering the glass fibers, a variety of glass compositions for reinforcement are available. Representatives are grade E, which is electrical insulation grade, and is the most common reinforcement grade for composites; grade S is high strength grade glass, a common variant is S2-glass. This last fiber has higher Young's modulus and temperature resistance than E-glass but it is also significantly more expensive. In general glass fibers are fragile but they show good stiffness and resistance.

Aramid fibers are polymeric, and they are commonly called as Kevlar fibers, commercial name from DuPont who invented, and, are still nowadays the main supplier of this kind of material. Kevlar fibers do not show extremely high strength and stiffness but they are characterized by good toughness. Kevlar is commonly used for personal protection devices such as ballistics helmets and jackets. Under impact solicitations, in fact, they are able to absorb a high amount of energy.

1.1.3. Production methods

Due to its peculiarity, specific manufacturing techniques have been developed to produce composites. FRP manufacturing processes can be divided into five main categories [14] [10]:

- Open mould processes. It includes hand lay-up and automated tape-laying. The starting materials (resin, fibers, fabrics …) are applied to the mould in layers, building up the desired thickness. This is followed by curing and part removal.
- Closed mould processes. Inside this fabrication method a distinction can be made between vacuum bag moulding and press moulding. During vacuum bagging operation the composite layers are compacted down, and a higher quality laminate can be obtained. The second method is performed in moulds consisting of two sections that open and close each moulding cycle. Those kinds of processes are much more expensive with respect to open mould ones, due to the more complex equipment. Advantages are good finish on all part surfaces, higher production rates, closer control over tolerances, more complex three-dimensional shapes.
- Filament winding, in which resin-impregnated continuous fibers are wrapped around a rotating mandrel that has the internal shape of the desired FRP product. The resin is then cured, and the mandrel removed.
- Pultrusion processes, similar to extrusion only adapted to include continuous fiber reinforcement.
- Others.

For the manufacturing of the composites under investigation in this thesis work, vacuum infusion process (VIP) was adopted, which is one of the many variants of closed mould techniques. It is a very advanced and cost-effective manufacturing technology and plays an important role in the production of composites with complex structure and high-dimensional accuracy [15]. This technique uses vacuum pressure

to drive resin into a laminate. Dry materials are laid into the mould and the vacuum is applied before resin is introduced. Once a complete vacuum is achieved, resin is literally sucked into the laminate via a carefully placed tubing. Some of the advantages of VIP with respect to traditionally vacuum bagged parts are: better fiber-to-resin ratio; less wasted resin; unlimited set-up time; cleaner process. The main difference is that in this case the resin is infused using vacuum pressure, while vacuum bagging starts with an excess of resin which is eventually drawn out. Also, as reinforcements are initially dry, no time constraints are introduced until it is decided to infuse the resin inside the vacuum bag. It means changes in the set up can be made multiple times before actually starting the impregnation process.

1. Resin pump
2. Vacuum bag
3. Mould tool
4. Resin drawn across and through reinforcement by vacuum
5. Reinforcement stack
6. Peel ply and or Resin distribution fabric
7. Vacuum pump
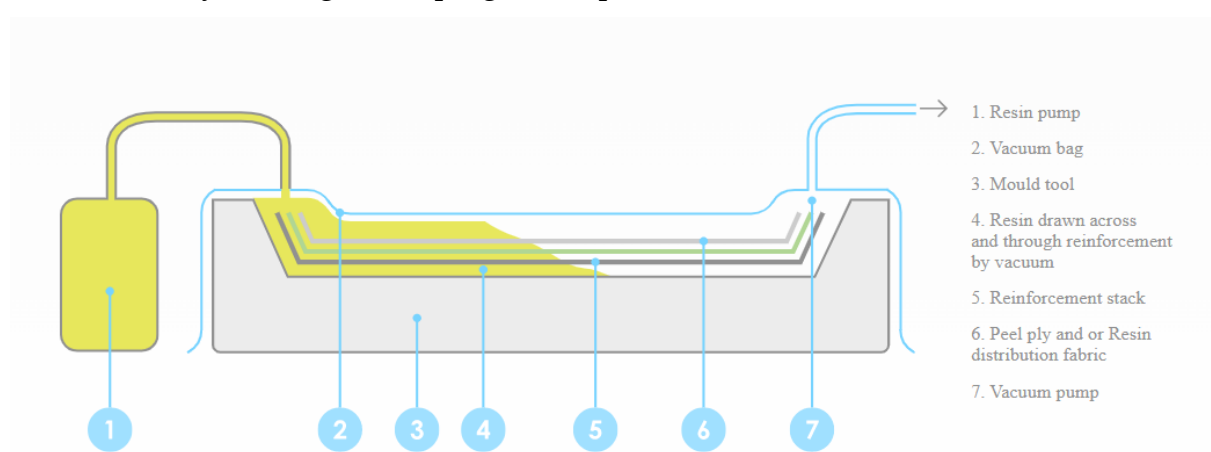
Figure 1-1: schematic representation of VIP set up [16].

1.2. Composite materials mechanical properties

1.2.1. Elastic behavior of a composite lamina

A generic material elastic behavior can be described according to the Hooke's law.

$$\sigma_{ij} = C_{ijkl}\varepsilon_{kl}$$

(1)

Stresses acting on the material depend on the stiffness tensor and on the strains applied. The stiffness tensor C_{ijkl}, in its most general form, is fourth order tensor. For *anisotropic materials* all the 81 elastic constants characterizing the mechanical behavior of the material can be different than zero and are dependent on the direction considered. As stress σ_{ij} and strain ε_{kl} tensors are symmetric, a first simplification is obtained, and the number of constants required to describe the material response become 36 instead of 81. Moreover, the stiffness tensor maintains, as for isotropic materials, the symmetry properties respect to its principal diagonal. Considering the individual elements of the matrix it can be expressed by this relation [10]:

$$C_{ij} = C_{ji}$$

<div align="right">(2)</div>

where $i \neq j$.

So, from 36 components the number of independent constants become 21. This kind of material show yet no symmetry plane for its properties. In case of symmetry of the material respect to a single plane the number of elastic constants further decrease, from 21 to 13.

Higher degree of symmetry is present in *orthotropic materials*. This kind of material possess three mutually orthogonal planes of symmetry: it means that rotations of 180° with planes keep the material's microstructure unchanged. Unidirectional laminas for instance are orthotropic.
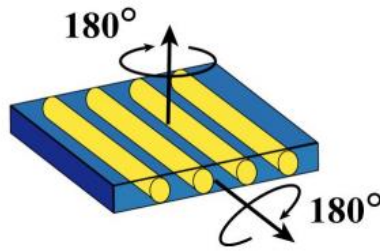
Figure 1-2: unidirectional lamina subjected to 180° rotation [12].

Independent elastic constants are then further reduced from 13 to 9, and the constitutive relations assume a similar shape to that of isotropic materials. Considering here the inverted relationship between stresses and strains trough the compliance matrix [S] we have the following constitutive equations:

$$
\begin{bmatrix} \varepsilon_1 \\ \varepsilon_2 \\ \varepsilon_3 \\ \gamma_{23} \\ \gamma_{31} \\ \gamma_{12} \end{bmatrix} =
\begin{bmatrix}
\dfrac{1}{E_1} & \dfrac{-\nu_{21}}{E_2} & \dfrac{-\nu_{31}}{E_3} & 0 & 0 & 0 \\
\dfrac{-\nu_{12}}{E_1} & \dfrac{1}{E_2} & \dfrac{-\nu_{32}}{E_3} & 0 & 0 & 0 \\
\dfrac{-\nu_{13}}{E_1} & \dfrac{-\nu_{23}}{E_2} & \dfrac{1}{E_3} & 0 & 0 & 0 \\
0 & 0 & 0 & \dfrac{1}{G_{23}} & 0 & 0 \\
0 & 0 & 0 & 0 & \dfrac{1}{G_{31}} & 0 \\
0 & 0 & 0 & 0 & 0 & \dfrac{1}{G_{12}}
\end{bmatrix}
\begin{bmatrix} \sigma_1 \\ \sigma_2 \\ \sigma_3 \\ \tau_{23} \\ \tau_{31} \\ \tau_{12} \end{bmatrix}
$$

<div align="right">(3)</div>

For the usual tensor symmetry property:

$$\frac{\nu_{21}}{E_2} = \frac{\nu_{12}}{E_1}$$

$$\frac{v_{31}}{E_3} = \frac{v_{13}}{E_1}$$

$$\frac{v_{32}}{E_3} = \frac{v_{23}}{E_2}$$

(4)

Then substituting in the previous constitutive equations, the following relationships are obtained:

$$\begin{bmatrix} \varepsilon_1 \\ \varepsilon_2 \\ \varepsilon_3 \\ \gamma_{23} \\ \gamma_{31} \\ \gamma_{12} \end{bmatrix} = \begin{bmatrix} \frac{1}{E_1} & \frac{-v_{12}}{E_1} & \frac{-v_{13}}{E_1} & 0 & 0 & 0 \\ \frac{-v_{12}}{E_1} & \frac{1}{E_2} & \frac{-v_{23}}{E_2} & 0 & 0 & 0 \\ \frac{-v_{13}}{E_1} & \frac{-v_{23}}{E_2} & \frac{1}{E_3} & 0 & 0 & 0 \\ 0 & 0 & 0 & \frac{1}{G_{23}} & 0 & 0 \\ 0 & 0 & 0 & 0 & \frac{1}{G_{31}} & 0 \\ 0 & 0 & 0 & 0 & 0 & \frac{1}{G_{12}} \end{bmatrix} \begin{bmatrix} \sigma_1 \\ \sigma_2 \\ \sigma_3 \\ \tau_{23} \\ \tau_{31} \\ \tau_{12} \end{bmatrix}$$

(5)

It can be observed that:

- there is no coupling between longitudinal deformations and tangential stresses nor between tangential deformations and normal stresses;

- the engineering properties required to calculate the elastic constants of the material are 9 in total: three young modulus (E_1, E_2, E_3); three Poisson coefficients (v_{12}, v_{13}, v_{23}); three tangential moduli (G_1, G_2, G_3).

Further considerations can be done by considering an even higher degree of symmetry in the material. If there is a symmetry plane, for which, the elastic constants remain unchanged for every rotation angle around the normal to that plane, the material is considered as a *transversally isotropic*. Material properties on that plane do not depend on the direction considered. This kind of symmetry characterizes, again, for example unidirectional laminas, in which it can be assumed as a first approximation that fibers are homogeneously distributed in the lamina volume. In that case, assuming as normal to the isotropy plane the direction of the fibers, the following properties are obtained:

$$E_3 = E_2$$

$$v_{13} = v_{12}$$

$$G_{13} = G_{12}$$

(6)

For a transversally isotropic material the constitutive equations are:

$$
\begin{bmatrix} \varepsilon_1 \\ \varepsilon_2 \\ \varepsilon_3 \\ \gamma_{23} \\ \gamma_{31} \\ \gamma_{12} \end{bmatrix} =
\begin{bmatrix}
\dfrac{1}{E_1} & \dfrac{-v_{12}}{E_1} & \dfrac{-v_{12}}{E_1} & 0 & 0 & 0 \\
\dfrac{-v_{12}}{E_1} & \dfrac{1}{E_2} & \dfrac{-v_{23}}{E_2} & 0 & 0 & 0 \\
\dfrac{-v_{12}}{E_1} & \dfrac{-v_{23}}{E_2} & \dfrac{1}{E_2} & 0 & 0 & 0 \\
0 & 0 & 0 & \dfrac{1+v_{23}}{2E_2} & 0 & 0 \\
0 & 0 & 0 & 0 & \dfrac{1}{G_{12}} & 0 \\
0 & 0 & 0 & 0 & 0 & \dfrac{1}{G_{12}}
\end{bmatrix}
\begin{bmatrix} \sigma_1 \\ \sigma_2 \\ \sigma_3 \\ \tau_{23} \\ \tau_{31} \\ \tau_{12} \end{bmatrix}
$$

(7)

The engineering properties required to completely define the compliance, and reversely the stiffness tensor of the material, are 5 instead of 9: two young moduli (E_1, E_2), two Poisson coefficients (v_{12}, v_{23}), one tangential modulus (G_{12}).

Consider now the thickness of a single lamina with respect to its dimensions on the plane. It is reasonable then to assume as negligible the tensions present in the plane's orthogonal direction, respect to the entity of tensions acting on the lamina's plane. This condition is referred to as *plane state of stress,* expressed by:

$$\sigma_3 = \tau_{23} = \tau_{31} = 0$$

(8)

from which the following three constitutive equations are obtained:

$$
\begin{bmatrix} \varepsilon_1 \\ \varepsilon_2 \\ \gamma_{12} \end{bmatrix} =
\begin{bmatrix}
\dfrac{1}{E_1} & \dfrac{-v_{12}}{E_1} & 0 \\
\dfrac{-v_{12}}{E_1} & \dfrac{1}{E_2} & 0 \\
0 & 0 & \dfrac{1}{G_{12}}
\end{bmatrix}
\begin{bmatrix} \sigma_1 \\ \sigma_2 \\ \tau_{12} \end{bmatrix}
$$

(9)

Material constants to completely characterize a monodirectional lamina with continuous fibers in a plane state of stress are in that case only four: E_1, E_2, G_{12}, v_{12}.

1.2.2. Classical lamination theory

The use of unidirectional laminas as transversal reinforcements may be inconvenient in many engineering applications, because of low strength and stiffness in transversal direction. To overcome those kinds of design problems laminated composites are used, in which several laminae are stacked together with different orientation [10] [12]. Depending on stacking sequence laminates may be:

- symmetric: sequence of layers is symmetric respect to the reference mid-plane;

- antisymmetric: sequence of layers is antisymmetric to the reference mid-plane;

- balanced: same total thickness of layers with fibers at ± θ;

- quasi-isotropic: symmetric laminates made with N (N>3) layers (of same thickness) with a certain sequence of angles.
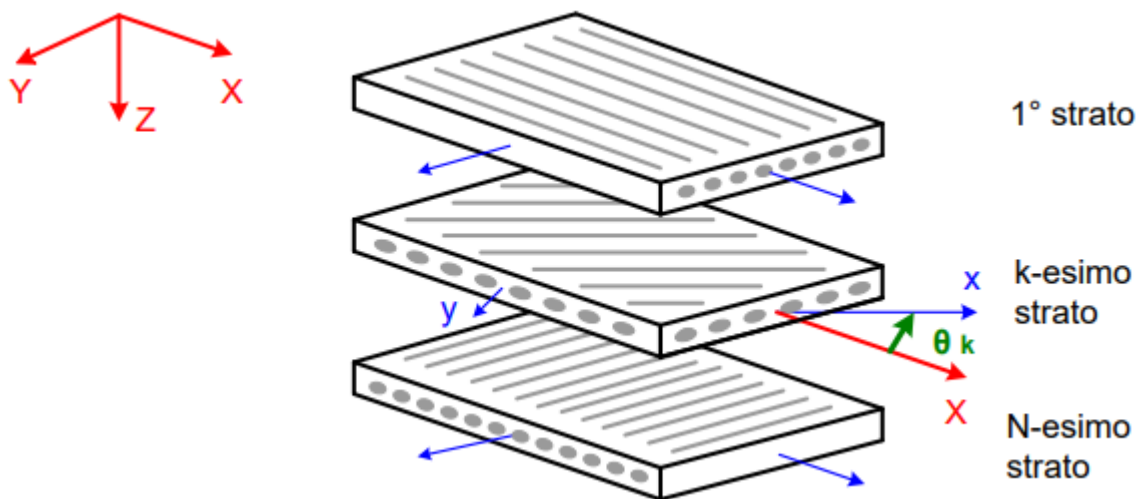
Figure 1-3: laminate stacking-sequence representation [12].

The classical lamination theory (CLT) allows to predict and derive the relations ruling the mechanical behavior of the entire composite depending on the stacking sequence of the laminae.

The CLT approach assumes that the complete laminate acts as a single layer where there is perfect bonding between the laminas enabling continuous displacement between the laminas, so that no lamina can slip relative to the other. Such an equivalent single layer is assumed to be thin and to obey to kinematics hypotheses of a classical Kirchhoff-Love plate. For the kinematics assumptions: a segment that is originally straight and perpendicular to the middle surface of the laminate before deformation is assumed to remain straight, with the same length, and perpendicular to the middle surface when the laminate is deformed [17] [18].
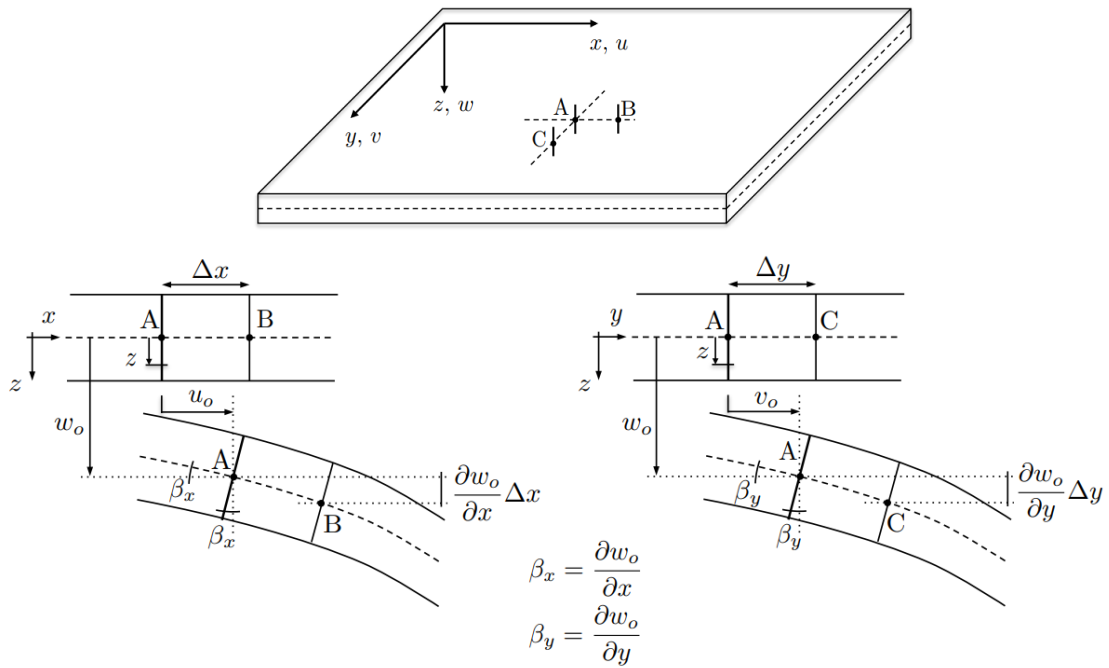
Figure 1-4: laminate section before and after deformation [19].

Kinematics assumptions:

$$\varepsilon_z = \frac{\partial w}{\partial z} = 0$$

$$\gamma_{xz} = \frac{\partial u}{\partial z} + \frac{\partial w}{\partial x} = 0$$

$$\gamma_{yz} = \frac{\partial v}{\partial z} + \frac{\partial w}{\partial y} = 0$$

(10)

u, v and w represent the displacement along the x, y and z axis respectively:

$$u(x, y, z) = u_0(x, y) - z \frac{\partial w_0}{\partial x}$$

$$v(x, y, z) = v_0(x, y) - z \frac{\partial w_0}{\partial y}$$

$$w(x, y) = w_0(x, y)$$

(11)

u₀(x, y), v₀(x, y) and w₀(x, y) are the displacement components for the mid-surface at z = 0.

The deformation of the plate for small displacement is given by the following equations:

$$\begin{bmatrix} \varepsilon_x \\ \varepsilon_y \\ \gamma_{xy} \end{bmatrix} = \begin{bmatrix} \dfrac{\partial u_0}{\partial x} \\ \dfrac{\partial v_0}{\partial y} \\ \dfrac{\partial u_0}{\partial y} + \dfrac{\partial v_0}{\partial x} \end{bmatrix} + z \begin{bmatrix} -\dfrac{\partial^2 w_0}{\partial x^2} \\ -\dfrac{\partial^2 w_0}{\partial y^2} \\ -2\dfrac{\partial^2 w_0}{\partial x \partial y} \end{bmatrix} = \begin{bmatrix} \varepsilon_x^0 \\ \varepsilon_y^0 \\ \gamma_{xy}^0 \end{bmatrix} + z \begin{bmatrix} \kappa_x^0 \\ \kappa_y^0 \\ \kappa_{xy}^0 \end{bmatrix}$$

$$(12)$$

Where the matrix $\varepsilon_x^0, \varepsilon_y^0, \gamma_{xy}^0$ represents the middle-surface strains and the matrix $\kappa_x^0, \kappa_y^0, \kappa_{xy}^0$ represents the middle-surface curvatures.

The stresses for the kth layer are expressed in terms of the laminate middle-surface strains and curvatures as:

$$\begin{bmatrix} \sigma_x \\ \sigma_y \\ \sigma_{xy} \end{bmatrix}^k = \begin{bmatrix} \bar{Q}_{11} & \bar{Q}_{12} & \bar{Q}_{16} \\ \bar{Q}_{21} & \bar{Q}_{22} & \bar{Q}_{26} \\ \bar{Q}_{16} & \bar{Q}_{26} & \bar{Q}_{66} \end{bmatrix}^k \left(\begin{bmatrix} \varepsilon_x^0 \\ \varepsilon_y^0 \\ \gamma_{xy}^0 \end{bmatrix} + z \begin{bmatrix} \kappa_x^0 \\ \kappa_y^0 \\ \kappa_{xy}^0 \end{bmatrix} \right)$$

$$(13)$$

The component of the transformed stiffness matrix $\bar{Q}$ can be different for each layer of the laminate. This implies that the stresses at the interface are not continuous even though the strain variation is linear through the lamina interface. While the stress variation is discontinuous at the interface it does vary linearly within each of the laminas [19].
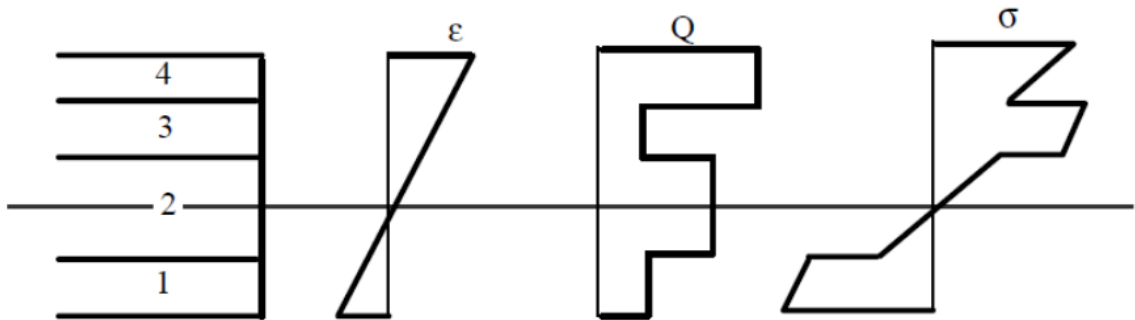
Figure 1-5: representation of the linear strain and the discontinuous stress variation though the laminas [19].

Resultant forces and moments

Forces and moments per unit length of the laminate are obtained through the integration of the stresses in each layer through the laminate thickness:

$$N_i^k = \int_{-t/2}^{t/2} \sigma_i dz$$

(14)

$$M_i^k = \int_{-t/2}^{t/2} \sigma_i z dz$$

(15)

Where:

- N_i is the normal force per unit length;
- M_i is the bending moment per unit length.
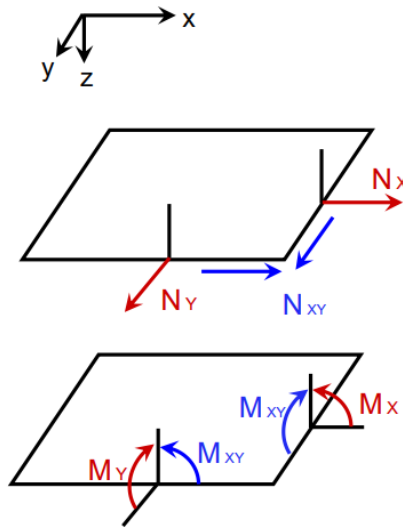
Figure 1-6: forces and moments acting on a lamina [12].

The resultant total force and moment of the entire laminate can then be obtained simply by summing the contributions given by all the layers.

$$N_i = \sum_{k=1}^{n} \int_{z_{k-1}}^{z_k} \sigma_i dz$$

(16)

$$M_i = \sum_{k=1}^{n} \int_{z_{k-1}}^{z_k} \sigma_i z dz$$

(17)

Where z_k and z_{k-1} are the coordinates of each ply.
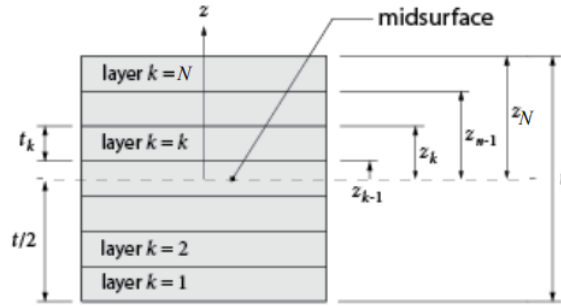
Figure 1-7: laminate with multidirectional laminas and coordinates of the plies [12].

By substituting the stress-strain relationships in the above equations we obtain the following generalized constitutive laws, which relates forces and moments to strains and curvatures ad the middle surface of the composite. In its more generalized-compact form:

$$\begin{bmatrix} N \\ M \end{bmatrix} = \begin{bmatrix} A & B \\ B & C \end{bmatrix} \begin{bmatrix} \varepsilon^0 \\ \kappa \end{bmatrix}$$

(18)

Where A, B and D are 3x3 submatrices depending on the lamina elastic properties. Specifically:

- A is related to the extensional laminate stiffness, relating in plane stresses and strains;

- B is the membrane-bending coupling laminate stiffness, relating in plane load to curvature and moments to in plane strains;

- D is the bending laminate stiffness submatrix, relating moments and curvatures.

For symmetric laminates, for which angle and thickness of the layers are the same above and below the mid-plane, Bij=0, which indicates that there is no coupling between bending and membrane effects. In other words, in planes stresses do not produce any out of plane strains. If the laminated is also balanced further simplifications are possible and the following equations becomes valid:

$$\begin{bmatrix} N_x \\ N_y \\ N_{xy} \\ M_x \\ M_y \\ M_{xy} \end{bmatrix} = \begin{bmatrix} A_{11} & A_{12} & 0 & 0 & 0 & 0 \\ A_{12} & A_{22} & 0 & 0 & 0 & 0 \\ 0 & 0 & A_{66} & 0 & 0 & 0 \\ 0 & 0 & 0 & D_{11} & D_{12} & 0 \\ 0 & 0 & 0 & D_{12} & D_{22} & 0 \\ 0 & 0 & 0 & 0 & 0 & D_{66} \end{bmatrix} \begin{bmatrix} \varepsilon_x \\ \varepsilon_y \\ \gamma_{xy} \\ \kappa_x \\ \kappa_y \\ \kappa_{xy} \end{bmatrix}$$

(19)

1.3. Damage and failure of composites

1.3.1. Damage modes

Analyzing the failure mechanism of a composite is much more complex with respect to traditional materials: different kinds of failure modes can take place, not only individually, but in general interfering with each other. Damage can start locally at the fibers, inside the matrix, at the interface between them and at the interface between two different laminas. In this last case the damage is referred to as *delamination* and it is an *inter-lamina* kind of damage. The other cases instead are grouped under the category of *intra-laminar* damage or *trans-laminar* damage. Intralaminar failure (often denoted as ply splits) consists in the formation of in-plane cracks, parallel to the reinforcement direction. Translaminar cracks are those associated with the tensile or compressive failure of the reinforcement fibers [20]. A representative illustration of the above-mentioned damage modes is shown in Figure 1-8.

If the laminate has a brittle behavior, failure can be coincident directly with the fracture of the composite. When the laminate show also some ductility, it can be associated to the point from which the material no more responds as linear elastic to the solicitations. The principal failure mechanisms of fiber reinforced composites are here very briefly described. Summarizing, failure can happen for: breakage of the fibers, debonding, microcracking of the matrix or delamination [10] [21]. In Figure 1-9 some of the failure modes of composites are captured.
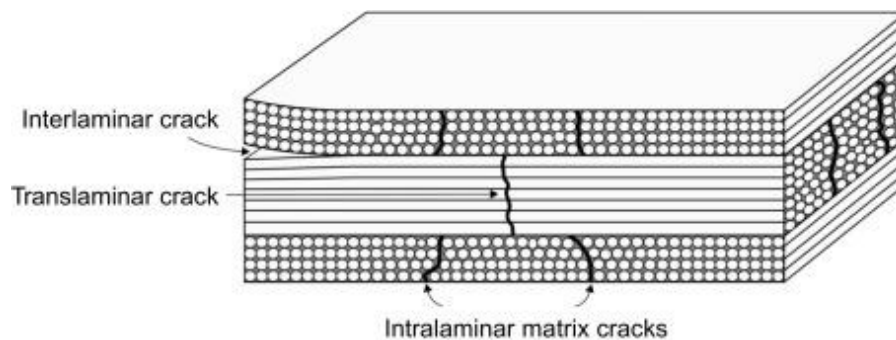
Figure 1-8: different fracture mechanisms illustration [20].
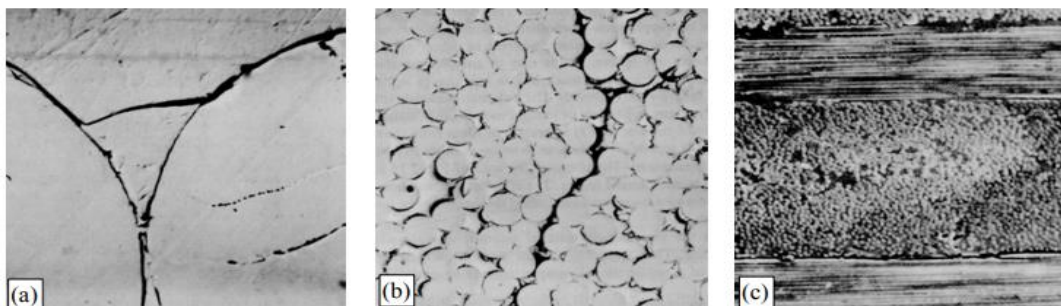
Figure 1-9: failure modes of laminates. (a) debonding; (b) matrix fracture; (c) delamination [21].

Debonding

Debonding takes place when the reinforcement is no longer adherent to the matrix. This kind of damage is common under in plane shear stresses. As a consequence of the damage, the matrix is not able anymore to transmit correctly the stresses to the reinforcement. Progressive debonding is dangerous for the integrity and the performance of the composite, as matrix alone is not able to sustain the external loads. For instance cracking of the matrix may take place also at relatively low stresses, which can induce other premature damage phenomena. Good adhesion between fibers and matrix is a very important aspect to consider and, during production, usually fibers are treated chemically in order to increase the bond to the resin.

Delamination

Delamination is a major failure mode in laminated composites. It is the process in which the different layers of the composite laminate separates from each other [22]. This kind of damage mainly concern the inter-laminar areas, in which there is abundancy of resin material. Thus, even in case the reinforcement phase has not been damaged, the overall composite strength can be reduced consistently. This mode of failure is especially insidious because it may easily escape detection since the delamination is frequently embedded within the composite structure. Their effect on the structure may also include a dramatic loss of compressive residual strength. Delamination can be induced by mismatching of mechanical properties between the different layers, presence of pre-existing defects (such as matrix micro-cracks and discontinuities) and also by poor processing during production, besides of external solicitations during service [23]. After the initiation of damage, crack propagation can proceed according to three different modes: MODE I, in which tensile forces are normal to the plane of propagation; MODE II, in which shear forces are acting in the direction of propagation; MODE III, in which shear forces are parallel to the propagation debonding front. The dominating mode depends on the overall state of stress acting on the structure and all modes can be active contemporary.
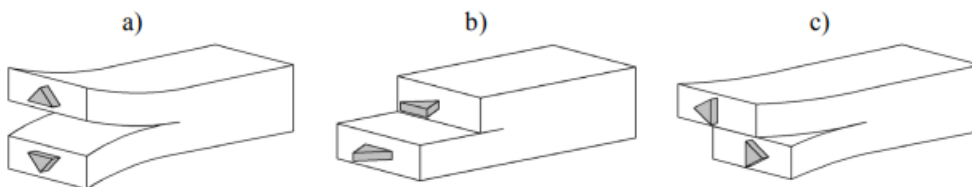
Figure 1-10: fracture mode a) I, b) II , and c) III [24].
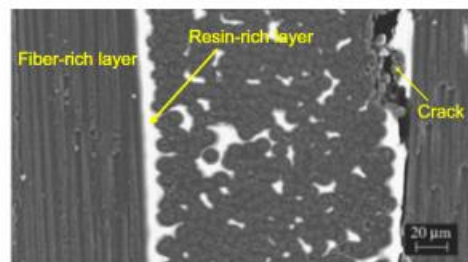
Figure 1-11: Photomicrograph of a composite where resin-rich zones and delamination are shown [25].

Tensile fibre failure

This mechanism of failure is usually catastrophic and releases a huge amount of elastic energy. It happens when the structure is subjected to tensile stresses higher than the ones supported by the fibers. When the material is not able to redistribute homogeneously the stresses after fiber rupture it can lead to sudden break of the entire structure (brittle failure).

Compressive fibre failure

Takes place when the material is subjected to compressive stresses. How the matrix behaves under shear stresses, the presence of imperfections in the structure, or, pre-defects in the constituent materials themselves, are all determining factors in this kind of damage. Usually what is observed is firstly the manifestation of a micro-instability at the local level of the fibers (micro-buckling), followed by a shear rupture of the matrix and, finally, the total failure of the entire fiber bundle [21].

Matrix cracking

As for homogeneous materials it can happen in the orthogonal direction respect to the applied normal tension, or by effect of shear tensions. Fibers can act in that case both as stress concentrators, reducing the value of the required load to break the resin as it is, or as barriers for the growth of the generated crack.

Failure of the overall composite under compression

This kind of failure is controlled by a complex interaction between the damage modes described previously, which can start inside a single lamina, for example, failure of matrix under shear stresses or instability of the fibers under the compression loads, and/or delamination. It is highly dependent on fibers orientation in each ply of the laminate [10].

1.3.2. Damage initiation

In general, structures built using composite materials, can accumulate a huge amount of damage before failure and often it leads to a highly conservative approach when dealing with failure criteria for composites [10].

Failure analysis of composites is based on two steps:

- Identification of the failure criteria of a single lamina: which load state will produce the failure of each specific lamina inside the laminate sequence.

- Effect of the lamina failure on the laminate: models to predict the effect of the progressive failure of the laminas on the overall laminate.

The accuracy of the failure criteria of the single lamina is the most crucial aspect to consider. For what concern the second point usually the design approach used is that of the *ply discount*: when a lamina inside the laminate structure fails its elastic properties are multiplied by a reducing factor, based on the damage entity. The simplest case considers a factor equal to zero, so that the lamina will not be considered anymore as part of the laminate sequence and not able to support any load.

The damage analysis for a single lamina will be considered first. This step consists in the identification of the failure mode inside a monodirectional composite under a complex state of stress. Failure criteria are mainly phenomenological (micromechanics). Moreover, they are based on a linear elastic analysis, as plasticization phenomena are limited to the matrix and are in general very localized phenomena, and so, do not influence consistently the laminate behavior [26].

Failure modes can be grouped under three principal categories: failure of fibers; matrix cracking under tension and matrix cracking under shear. Numerous failure theories have been proposed and they can be classified into three macro-groups:

- Limit or non interactive theories (maximum stress, maximum strain);

- Interactive theories (Tsai-Hill, Tsai-Wu)

- Partially interactive or failure mode-based theories (Hashin-Rotem, Hashin, Puck).

In the equations presented in the following the bellow notation will be adopted:

- X_t: tensile strength in fiber direction

- X_c: compressive strength in fiber direction

- Y_t: tensile strength in transverse direction

- Y_c:compressive strength in transverse direction

- S_l: in plane shear strength

- S_t: out of plane shear strength.

1.3.2.1. Tsai - Hill and Tsai-Wu interactive theories

The Tsai-Hill criterion is a phenomenological-based failure theory, considered as an extension of the Von Mises failure criterion for anisotropic materials [27]. Failure strengths in the principal material directions are assumed to be known. The simplest, plane stress form, of the Tsai-Hill failure theory is the following (Tsai, 1965):

$$\frac{\sigma_1^2}{X} - \frac{\sigma_1 \sigma_2}{X^2} + \frac{\sigma_2^2}{Y} + \frac{\tau_{12}^2}{S} = 1$$

(20)

Tsai-Hill criterion describes a smooth elliptical failure envelope. The maximum stress value X and Y must be chosen according to the state of stress, whether it is tensile or compressive. Tsai-Hill is a mode independent criterion: does not account for the difference between the possible material failure modes.

To include stress and strength interactions in the fiber and matrix directions, Tsai-Hill criterion has been generalized into the Tsai Wu criterion. The Tsai-Wu criterion is, as well, a mode independent failure criterion. However, it is a more advanced polynomial criterion, which also considers the specificities of the materials behavior in tension and compression (Tsai and Wu 1971).

1.3.2.2. Hashin failure-mode based criterion

Hashin failure criteria distinguish among the various different failure modes of the unidirectional lamina: tensile and compressive fiber failures and tensile and compressive matrix failure. Hashin criterion for instance has a stronger physical basis with respect to the mode independent criteria previously considered. For each of the different failure modes the conditions are expressed as follows [28].

- Tensile Fiber mode

$$\left(\frac{\sigma_1}{X_t}\right)^2 + \frac{\tau_{12}^2 + \tau_{13}^2}{S_l^2} = 1$$

(21)

- Compressive fiber mode

$$\left(\frac{\sigma_1}{X_c}\right)^2 = 1$$

(22)

- Tensile matrix mode

$$\left(\frac{\sigma_2}{Y_t}\right)^2 + \frac{\tau_{23}^2 - \sigma_2 \sigma_3}{S_t^2} + \frac{\tau_{12}^2 - \tau_{13}^2}{S_{12}^2} = 1$$

(23)

- Compressive matrix mode

$$\left[\left(\frac{Y_c}{2S_t}\right)^2 - 1\right]\frac{\sigma_2 + \sigma_3}{Y_c} + \left(\frac{\sigma_2 + \sigma_3}{2S_t}\right)^2 + \left(\frac{\tau_{12} + \tau_{13}}{S_l}\right)^2 + \frac{\tau_{23}^2 + \sigma_2\sigma_3}{S_t^2} = 1$$

(24)

Hashin failure criteria assume that two distinct fiber and matrix failure modes occur in two different fracture planes and only relevant stress components on the associated fracture plane of each mode will contribute to the failure criteria for that failure mode.

As a consequence, the failure envelope described by Hashin failure criteria is only piecewise smooth, with each smooth branch modeling a distinct failure mode.

1.3.3. Damage propagation

The damage initiation at the lamina level do not correspond (in most general cases) to the final failure of the composite structure. When a single layer fails inside a laminate, the remaining plies are still able to sustain the imposed loads. In this optics it is possible to define a first (FPF) and an ultimate ply failure (UPF). Composite failure takes place when the last lamina fails.

After a layer has experienced damage/failure, the material properties of the damaged layer are multiplied by a factor according to the degradation rules. The simplest degradation rule uses knockdown factors close to zero. This means that the damaged layers will not carry any transverse or shear loads after failure and the loads will be transferred to the remaining undamaged plies. This degradation rule is known, as previously mentioned, as the *ply discount model* (when the knockdown factors are equal to zero). Another post-failure degradation rule is the *constant stress model*, which assumes that the damaged layer will carry its failure load, but no additional loads are supported. The ply behavior can be considered as something in between these two models, in which gradual unloading takes place [29]. The damage propagation inside the overall composite reflects this behavior, with a more gradual degradation model with respect to the ply discount model alone.
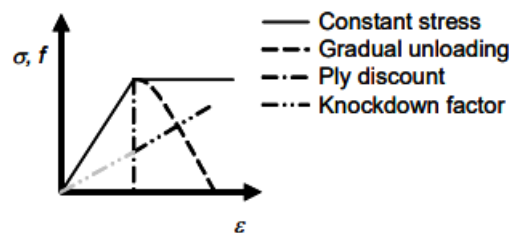
Figure 1-12: Ply behaviour according to different degradation rules [29].

1.4. Textile composites

The description given till now about composites properties, damage modes, failure criteria and so on, is mainly related to theories which were developed in the first place to define laminates constituted by unidirectional laminas. Here some of those concepts

and theories will be again briefly considered and extended to also describe the behavior of bidirectional laminas and their laminates [30].

Specifically, the laminates under investigation in this thesis work are textile composites: fiber-reinforced composite materials in which the reinforcement is in the form of a textile fabric (woven, knitted, braided, etc.). In a textile, fibers are assembled into yarns or fibrous plies, then arranged in such a way to form the textile fabric. Textiles are hierarchical and structured materials, with three different levels of hierarchy: fibers (micro) -yarns / plies (meso) – fabrics (macro).

Use of textile fabric reinforcements can bring advantages, for example, in:

- production, in which the use of textile reinforcements brings benefits in handability of the fabrics and in easier applicability of closed-mold processes (higher automatization);

- performance, due to interlacing of yarns, the interlaminar/through-the-thickness/impact properties of composite are improved: matrix cracks, inside the yarns, do not propagate though the material but are stopped when the yarn changes direction. This leads for instance to higher energy absorption capabilities in crash resistant applications.

1.4.1. Woven fabrics

Interlacing two orthogonal systems of yarns the so-called woven fabric is obtained. The two orthogonal system of yarns are indicated respectively, for lenghtway and widthway of the fabric, as warp and weft yarns.
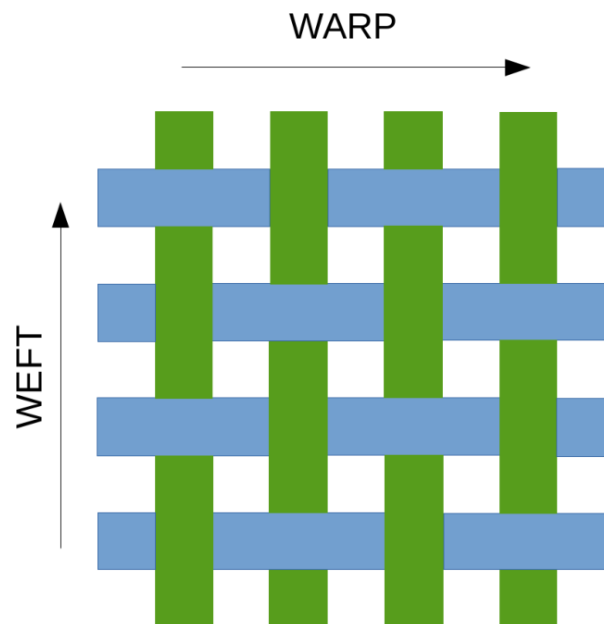
Figure 1-13: fabric warp and weft yarns interlacing illustration [30].

Principal kind of woven fabrics used as reinforcement in composite materials are:

- Plain weave: each warp yarn has an intersection with each weft yarn;

- Satin: the crossings of warp and weft yarns are shifted at the neighboring yarns by a constant number of positions, which is called step s. Most used in composite reinforcements are the five-harness (5H) and eight-harness(8H);

- Twill: a weave that produces diagonal lines on the face of the fabric. Depending on the *float* of the warp/weft yarns a twill is designated as twill f_{wa}/f_{we}. The most used are twill 1/2, 1/3, and 2/2.
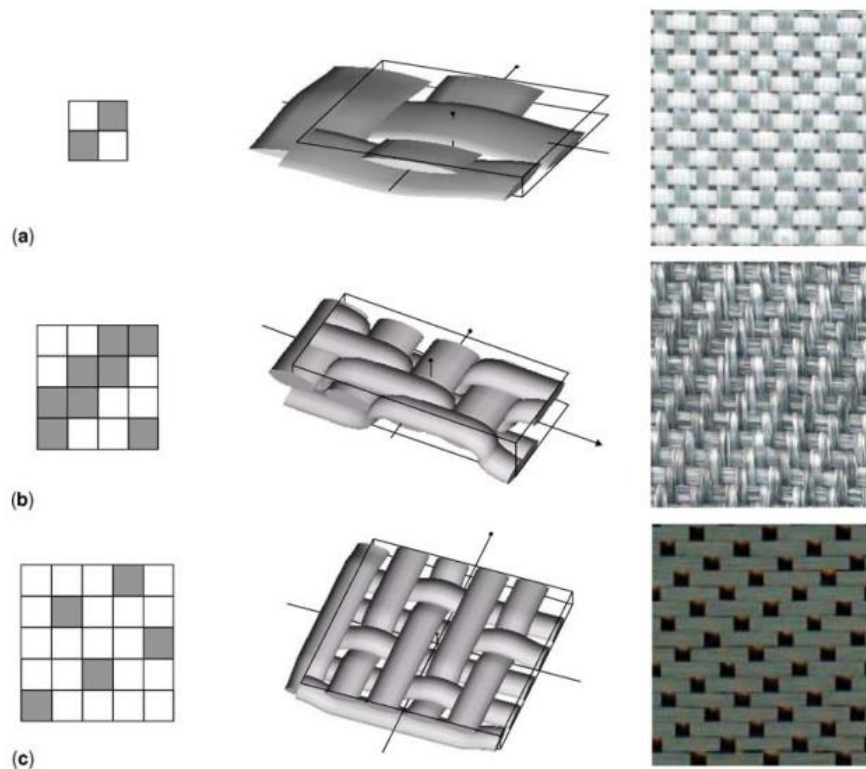
Figure 1-14: Weaves, 3D representations of the fabric repeat, and examples of composite reinforcements. (a) Plain weave, glass; (b) twill 2/2 weave, carbon; (c) 5H satin weave, carbon [30].

The performance of the final composite structure is determined by the internal structure of the fabric. The stress response to a local deformation depends on the local orientation of fibers, which in turn is a function of the reinforcement architecture. The location for damage initiation and its following propagation, or not, is controlled by this parameter.

1.4.2. Stiffness

Textile fabrics are characterized by a high degree of symmetry and so, for most types of the textile reinforcements, textile composites plates are considered as orthotropic materials. Their stiffness is defined by the usual engineering constants already considered previously for orthotropic materials: Young modulus, Shear Modulus,

Poisson coefficients. Moreover, an important aspect is that the stiffness of those kind of textile composites, in which yarns are straight in plane, can be in a first approximation derived by the Classical Laminate Theory (CLT). The textile composite is considered as equivalent to a cross-ply laminate, in which the ply directions in the latter corresponds to the principal yarns directions in the textile composite.

1.4.3. Damage development

When a textile material is subjected to a unidirectional tensile load it fails as a result of a long and complex series of damage events. The damage processes take place on all the hierarchical levels of the composite structure: fibers in the impregnated yarns (micro), yarns and matrix pockets in the unit cell of the textile reinforcement (meso), composite plies forming a plate (macro). On the different structural levels, as usual, heterogeneities of the material can behave as stress-strain concentrations [26].

Consider as representative of the series of events which can take place the following study case: a woven composite loaded in the warp direction. The first cracks observed are positioned parallel to the weft direction. Increasing the load cracks become longer and start to multiply rapidly. A well-developed system of long, multiple cracks, oriented perpendicular to the loading direction is formed: they split the weft yarns and generate large, delaminated regions between the layers of plain weave fabric. Transverse cracks in matrix pockets are also observed. Lastly, fibers break, and the material fails.
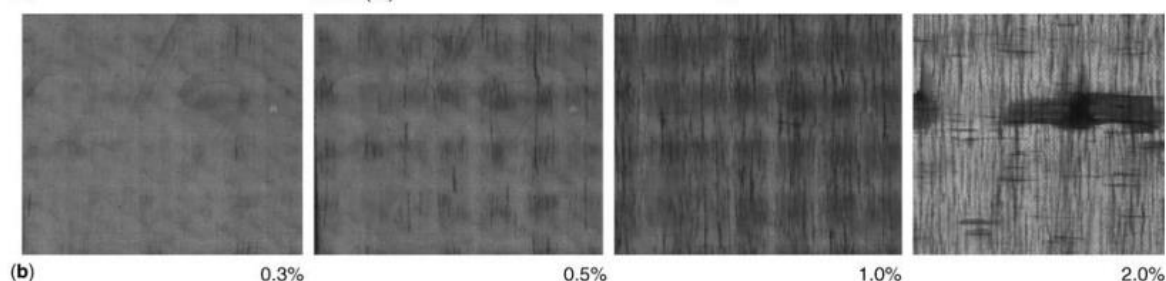
Figure 1-15: Damage evolution under tensile loading of a plain weave glass/epoxy composite, loading in horizontal direction. The applied strain is indicated [30].

In compression, bending, and other types of out-of-plane loading, the behavior of textile composites is controlled by the same phenomena as for UD laminates: delamination, fiber kinking, matrix shear failure. Depending on the architecture, the fabric can:

- deviate the crack from a flat trajectory and increase the apparent energy needed for crack propagation;

- in crash, lead to multiple cracking, increasing the effectiveness of energy consumption;

- in transverse impact, can limit delamination area and increase energy absorption.

Naturally these changes with respect to UD laminates depend very much on the reinforcement type and its geometric features.

1.4.4. Failure criteria and damage propagation

Failure can be predicted using different criteria, one of which is the Hashin criterion for woven fabrics. It defines the conditions for the damage initiation inside the composite. Six failure indices are considered. Four for fiber damage: warp and weft directions in tension and compression.

$$F_{1t}^f = \left(\frac{\sigma_1}{X_t}\right)^2 + \left(\frac{\sigma_{12}}{S_{12}}\right)^2 + \left(\frac{\sigma_{13}}{S_{13}}\right)^2, \sigma_1 > 0$$

$$F_{1c}^f = \left(\frac{\sigma_1}{X_c}\right)^2 + \left(\frac{\sigma_{12}}{S_{12}}\right)^2 + \left(\frac{\sigma_{13}}{S_{13}}\right)^2, \sigma_1 < 0$$

$$F_{2t}^f = \left(\frac{\sigma_2}{Y_t}\right)^2 + \left(\frac{\sigma_{12}}{S_{12}}\right)^2 + \left(\frac{\sigma_{23}}{S_{12}}\right)^2, \sigma_2 > 0$$

$$F_{2c}^f = \left(\frac{\sigma_3}{Y_c}\right)^2 + \left(\frac{\sigma_{12}}{S_{12}}\right)^2 + \left(\frac{\sigma_{23}}{S_{23}}\right)^2, \sigma_2 < 0$$

$$(25)$$

and two for matrix failure, onset of cracking in the impregnated yarns under through-the-thickness and shear stresses:

$$F_t^m = \left(\frac{\sigma_3}{Z_t}\right)^2 + \left(\frac{\sigma_{12}}{S_{12}}\right)^2 + \left(\frac{\sigma_{13}}{S_{13}}\right)^2 + \left(\frac{\sigma_{23}}{S_{12}}\right)^2, \sigma_3 > 0$$

$$F_c^m = \left(\frac{\sigma_3}{Z_c}\right)^2 + \left(\frac{\sigma_{12}}{S_{12}}\right)^2 + \left(\frac{\sigma_{13}}{S_{13}}\right)^2 + \left(\frac{\sigma_{23}}{S_{12}}\right)^2, \sigma_3 < 0$$

$$(26)$$

where:

- σ_{ij} , i = 1, 2, 3, are average stresses in the woven composite
- Xt, Xc, Yt, Yc are strength values for the composite in the warp (X) and weft (Y) directions, respectively;
- Zt, Zc are transversal UD strength values in tension and compression;
- S_{ij} , i = 1, 2, 3, are shear strength values for the composite.

The simplicity of the quadratic failure criterion reflects its phenomenological nature.

For what concern instead the progression of damage the most developed model used for textile composite laminates is based on the works of Ladeveze, in which damage variables are introduced in the criteria [31]. Damage is considered as a weakening of

the material due to all kinds of mechanisms acting prior to the actual failure of the structure (matrix cracking, fiber-matrix debonding, fiber failure). The stiffness of the material is progressively degraded as damage increases (and the damage variables d change during this process). The stress-strain relation for a damaged material is expressed as follow:

$$\begin{bmatrix} \varepsilon_{11} \\ \varepsilon_{22} \\ \varepsilon_{12}^{el} \end{bmatrix} = \begin{bmatrix} \dfrac{1}{(1-d_1)E_1} & \dfrac{-v_{12}}{E_1} & 0 \\ \dfrac{-v_{21}}{E_2} & \dfrac{1}{(1-d_2)E_2} & 0 \\ 0 & 0 & \dfrac{1}{(1-d_{12})2G_{12}} \end{bmatrix} \begin{bmatrix} \sigma_{11} \\ \sigma_{22} \\ \sigma_{12} \end{bmatrix}$$

$$(27)$$

where the compliance matrix shows degradation of Young moduli E1, E2 and shear modulus G12 with the damage parameters d1, d2, and d12. The dependence of the damage parameters on the applied load should be identified with a set of well-defined experiments, which adapt the set of identification experiments for UD laminates (Ladeveze and Le ` Dantec, 1992) to the particular case of textile composite under consideration. For woven laminates, for example, these include tension and compression in warp and weft direction and quasi-static cyclic tests in 45° directions.

1.5. Impact

Generally, impacts are categorized into either low or high velocity. Low velocity impacts (LVI) are usually considered as events which can be treated as quasi-static, the upper limit of which can vary from one to tens of m/s depending on the target stiffness. High-velocity impact response is dominated by stress wave propagation though the material, in which the structure does not have time to respond, leading to very localized damage [32].

One of the throwbacks of laminated composites is that, usually, they show poor resistance to impact loading, accompanied by the risk of failure from the consequent produced damage. The damage resistance and tolerance of a polymer base composite is usually investigated by performing low velocity drop weight tests. *Impact damage resistance* addresses the resistance to damage formation at a given impact, while the *impact damage tolerance* addresses the ability of the structure to perform with a given damage [33]. Many experiments have demonstrated that the impact response of the laminate depends first of all on the composite structural parameters (thickness, lamina type, elastic and fracture properties, density, stacking sequence, boundary conditions...) and the impactor parameters (shape, size, mass, velocity, impact energy...) [34]. For that reason damage resistance is considered as a structural rather than a material property. Low velocity impact events can be considered one of the most dangerous loads on composites, as, unlike higher energy impacts where

significant amounts of damage are readily visible on the impacted surface, low speed impact damage shows (almost) no evidence of damage on the surface (barely visible impact damage BVID). Inside the laminate, however, below the impact site, significant damage may be present, as illustrated in Figure 1-16 and Figure 1-17. Typically, matrix cracking is the first damage to occur at early stages of the impact load. Matrix cracking can induce delamination, which grows as the load increase. Perceptible fiber breakage might then occur depending on the level of impact energy [35].
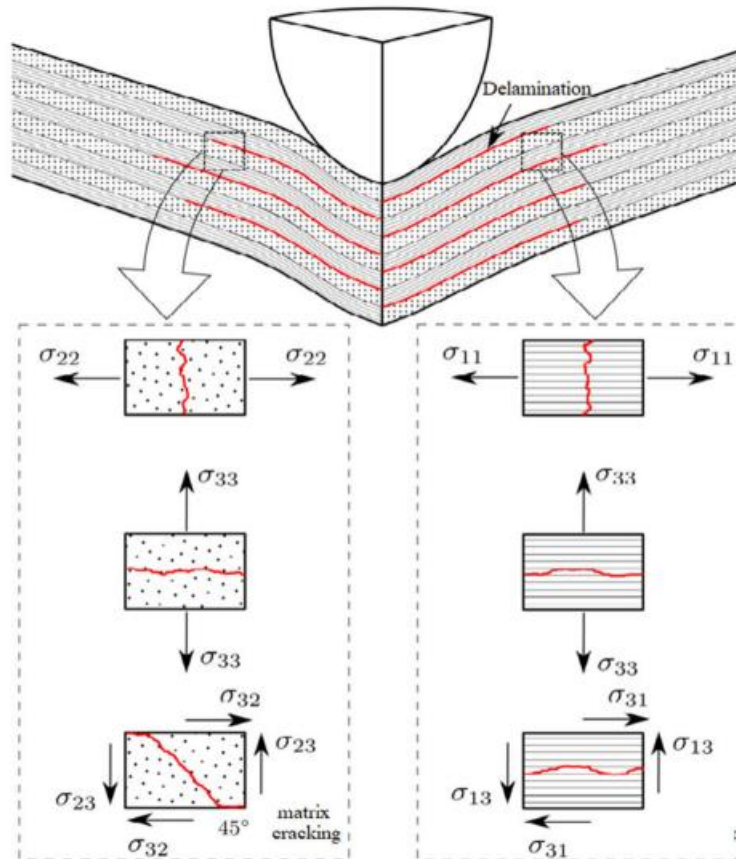
Figure 1-16: failure modes of laminates subjected to LVI [36].
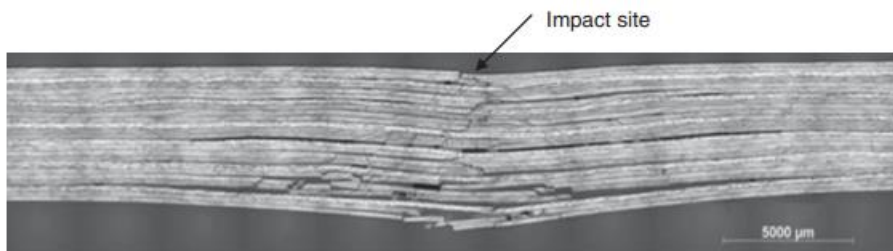
Figure 1-17: section cut showing the damage created in a laminate after impact test [35].

A low velocity impact test does not produce perforation, or at least it is not intended to. Mostly, as mentioned, it creates internal damage and delamination. The latter is considered as the major damage mechanism in case of impact events, as it reduces considerably also the compressive, the tensile, and the shear strength of the overall

material, leading to further damage and risk of failure [37]. Poor post impact compressive strength is the greatest weakness of composite laminates in terms of residual properties. This is mainly due to local instability resulting from the delamination. Delamination divides the laminate into sub-laminates which have a lower bending stiffness and thus are less resistant to bucking loads [38]. It is important, however, to recognize, that the extent and type of damage formed (linked to the materials damage resistance) is not uniquely related to the residual strength of the structure after impact (related to the damage tolerance issue). As an example of the multiple possible situations where larger damage extent does not imply lower compression after impact, the case illustrated in Figure 1-17 will be considered. In (a) multiple small delaminations are created after impact, and if a compression load is applied, most of the sub-laminates would buckle early because of their lower bending stiffness, and final failure would soon take place. Differently, in (b), even if delamination is larger, the resulting sub-laminates are thicker and have a higher bending stiffness compared to the previous case. Consequently, they would buckle at a much higher load [35].
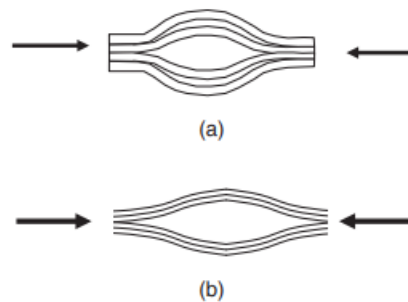
Figure 1-18: Special cases of damage extent caused by impact. (a) Multiple small delaminations and (b) single larger delamination [35].

Good damage resistance then does not always imply good damage tolerance. However, in the absence of other means to quantify damage tolerance, coming up with a design that has good damage resistance is a good starting point in also reaching a good damage tolerance in the material.

As mentioned at the beginning of this Section, composites damage resistance characterization is usually done by performing LVI tests. In this optics the most important information are derived through the analysis of force-time, force-displacement and energy-time curves. Maximum contact force, maximum displacement, and absorbed energy from impact shall always be calculated from the tests. In Figure 1-19 a typical energy-time curve is shown, illustrating the properties which might be derived from it and considered in the evaluation of the composite damage response.
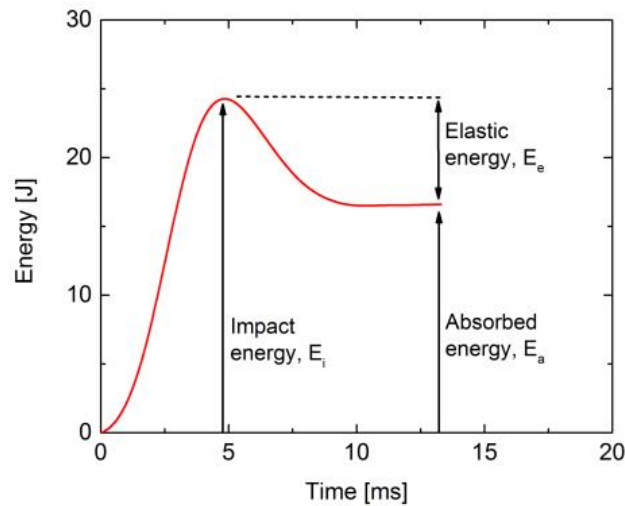
Figure 1-19: schematic of typical energy-time curve obtained from LVI test [39].

Considering a generic force-time history curve (Figure 1-20), four characteristic quantities can be identified: three force values and the contact time. Pcr, the critical force, represents the force for which the first relevant drop occurs. This drop is caused by a reduction of the transverse stiffness of the laminate, which can be associated to a rapid propagation of delaminations. The force decreases up to a rest load, Pr, after which a reloading phase can take place if the impactor retains enough energy, reaching the maximum measured force, Pmax. This quantity depends on the residual stiffness after initial damage, which takes place when load exceeds Pcr [40].
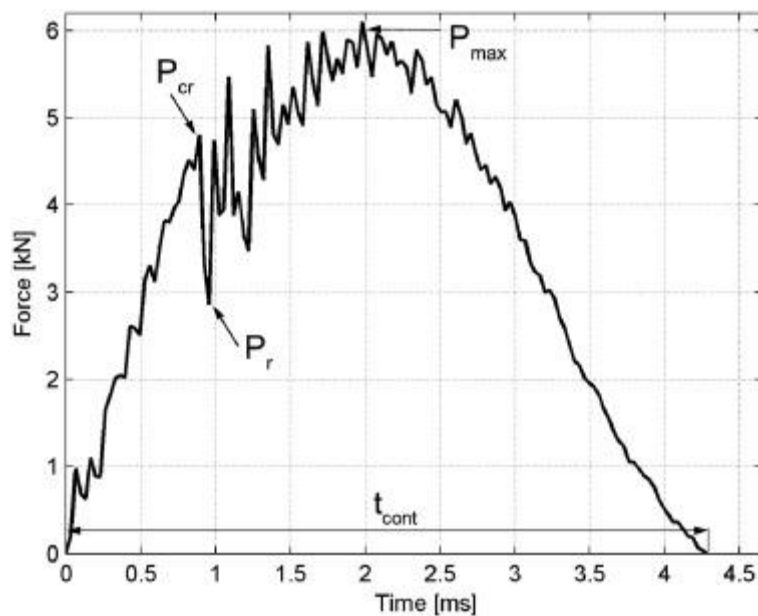
Figure 1-20: typical force-time curve obtained from LVI test [40].

The so-called Delamination Threshold Load (DTL) is normally identified by locating Pcr. This drop is especially observed for unidirectional composites but not as often for other fibers architecture, such as woven composites [41]. Moreover, this value of force is actually not unanimously considered to represent physically the initiation of

delamination, or damage in general, as sub-critical matrix cracks and small delaminations may initiate at lower force. Pcr rather represent the initial value of force at which change in the stiffness characteristics of the specimen can be detected. It must be also noticed that force versus time histories typically contain many oscillations, which may be introduced by two primary sources. The first source is the natural frequency of the impactor, typically referred to as "impactor ringing". The second source of force oscillations is the flexural vibration of the impacted specimen. The ringing oscillations generally occur at higher frequencies than the oscillations generated by the specimen and do not typically represent an actual force transmitted to the specimen. Significant resonance can make the determination of Pcr quite difficult [42]. The assessment of the damage after impact in the composite can also be performed using the slope of the force displacement curve, which again assumes that the presence of damage has the direct effect of changing the stiffness, thus the slope of the curve [43].

For woven composites it has been observed however, that, although damage after low velocity impact tests might be visible through NDI methods, force time and force displacement curves often do not reveal, as for unidirectional laminates, any evident trend changes, such as load drop or slope change, that can be associated with the incipient of (critical) damage initiation [44] [41]. Those considerations might be interesting for the impact tests analysis performed in Chapter 3, as the composites under investigation are constituted by woven fabrics. In the above-mentioned studies this kind of behavior was rationalized by considering the differences in the mechanism involved in the initiation and propagation of the delamination of the woven composite under low velocity impact.

It is possible to act on the response of a composite to impact loads by modifying different parameters, most of all related to the matrix and the reinforcement, and by consequence the interphase between them. The properties of each of these constituents affect the threshold energies required to initiate the different failure modes induced by impact. For instance, impact resistance of a laminate can be improved by changing the matrix material, fiber architecture, and through hybridization, which is a promising method when enhanced combined properties are to be obtained [45]. In particular it represents one of the effective ways to increase penetration resistance and energy absorption capability using high strength fibers but at the same time also decrease costs using more economic fibers like glass. In multiple studies about hybridization of carbon fiber composites with glass fibers, it was concluded that the positive hybrid effect has resulted when glass layers were placed on the outer surfaces [46] [47].

Considering the matrix material, it is known that the majority of structural applications employ epoxy resins as they better meet the hot/strength requirements in final applications. However, epoxy is brittle and has poor resistance to crack growth (i.e. delamination). Attempts to reduce matrix damage and improve the interlaminar

fracture toughness of thermoset resins has involved incorporating plasticizing modifiers or adding rubber or thermoplastic particles to the resin. The inclusion of a thin discrete layer of very tough, high shear strain resin can also be employed to minimize delamination. The use of thermoplastic resins also have exhibit an increase in fracture toughness over thermoset composites [48].

2 Numerical modelling

In this thesis work dynamic-impact numerical simulations were performed, and the obtained results were compared with the impact experimental tests of the composite materials. The numerical analyses have been performed with the Abaqus FEA software. Abaqus is a software suite for finite element analysis and computer-aided engineering. The Abaqus product suite consists of five core software products. In particular, the software engaged in this work, was the Abaqus/CAE, or "Complete Abaqus Environment". It allows both the modelling and analysis of mechanical components and assemblies and the visualization of the FEA results. Abaqus is especially used in the automotive, aerospace, military, and for characterization of industrial products.

In the current chapter some important general theoretical concepts regarding the performed simulations are considered. First, a brief explanation about the possible analysis procedures is done, followed by the general description of the types of elements that can be used in a numerical analysis. The elements used in the current work simulations were then considered in more detail. Hourglass mode is also briefly described, as it is specifically issue related to the kind of analysis which were performed. Last, a detailed explanation about the material model adopted in the numerical simulations is reported.

2.1. Dynamic analysis procedures

Abaqus offers several methods for performing dynamic analysis. Direct integration of the system must be used when nonlinear dynamic response is being studied. Implicit direct integration is provided in ABAQUS/Standard; explicit direct integration is provided in ABAQUS/Explicit. In the following table the key differences between the two products, Standard and Explicit, are briefly summarized [49].

	ABAQUS/Standard	ABAQUS/Explicit
Element library	Extensive element library	Extensive element library well suited for explicit analyses. The elements available are a subset of those in Abaqus/Standard

Analysis procedures	General and linear perturbation procedures	General procedures
Material models	Wide range of material models	Similar to Abaqus/Standard. Failure material models are allowed
Contact formulation	Robust capability for solving contact problems	Robust contact functionality that readily solves even the most complex contact simulations
Solution technique	Stiffness-based solution technique that is unconditionally stable	Uses explicit integration solution technique that is conditionally stable
Disk space and memory	Due to large numbers of iterations possible in an increment, disk space and memory usage can be large	Disk space and memory usage is typically smaller

Table 2: key differences between ABAQUS/Standard and ABAQUS/Explicit products [49].

The direct-integration dynamic procedure provided in ABAQUS/Standard uses the implicit Hilber-Hughes-Taylor operator for integration of the equations of motion, while ABAQUS/Explicit uses the central-difference operator. In an implicit dynamic analysis, the integration operator matrix must be inverted, and a set of nonlinear equilibrium equations must be solved at each time increment. Because displacements and velocities in an explicit dynamic analysis are calculated in terms of quantities that are known at the beginning of an increment, the global mass and stiffness matrices need not be formed and inverted, which means that at each increment is relatively inexpensive compared to the increments in an implicit integration scheme.

ABAQUS/Explicit offers fewer element types than ABAQUS/Standard. For example, only first order, displacement method elements and modified second-order elements are used.

Some important advantages of the method provided in ABAQUS/Explicit are:

- The analysis cost rises only linearly with problem size, whereas the cost of solving the nonlinear equations associated with implicit integration rises more rapidly. Therefore, ABAQUS/Explicit is attractive for very large problems.
- The explicit integration method is more efficient than the implicit integration method for solving extremely discontinuous events or processes.
- It is possible to solve complicated, very-general, three-dimensional contact problems with deformable bodies in ABAQUS/Explicit.

- Problems involving stress wave propagation can be far more efficient computationally in ABAQUS/Explicit.

For the numerical simulations carried out in this thesis the Explicit method was adopted.

2.1.1. Explicit dynamic analysis

An explicit dynamic analysis is computationally efficient for the analysis of large models with relatively short dynamic response times and for the analysis of extremely discontinuous events or processes. Moreover, it uses a consistent, large-deformation theory: models can undergo large rotations and large deformations. By default, it uses automatic time incrementation with the global time estimator.

The explicit dynamics analysis procedure is based upon the implementation of an explicit integration rule together with the use of diagonal ("lumped") element mass matrices. The equations of motion for the body are integrated using the explicit central-difference integration rule:

$$\dot{u}^N_{(i+\frac{1}{2})} = \dot{u}^N_{(i+\frac{1}{2})} + \frac{\Delta t_{(i+1)} + \Delta t_{(i)}}{2} \ddot{u}^N_{(i)}$$

$$u^N_{(i+1)} = u^N_{(i)} + \Delta t_{(i+1)} \dot{u}^N_{(i+\frac{1}{2})}$$

(28)

Where u^N is a degree of freedom (a displacement or rotation component) and the subscript i refers to the increment number in an explicit dynamics step. The central-difference integration operator is explicit in the sense that the kinematic state is advanced using known values of $\dot{u}^N_{(i+\frac{1}{2})}$ and $\ddot{u}^N_{(i)}$ from the previous increment.

The explicit integration rule is quite simple but itself does not provide the computational efficiency associated with the explicit dynamics procedure. The key to the computational efficiency of the explicit procedure is the use of diagonal element mass matrices because accelerations at the beginning of the increment are computed by

$$\ddot{u}^N_{(i)} = (M^{NJ})^{-1}(P^J_{(i)} - I^J_{(i)})$$

(29)

where M^{NJ} is the mass matrix, P^J is the applied load vector, and I^J is the internal force vector. A lumped mass matrix is used because its inverse is simple to compute and because the vector multiplication of the mass inverse by the inertial force requires only n operations, where n is the number of degrees of freedom in the model. The explicit procedure requires no iterations and no tangent stiffness matrix. The internal force vector, I^J, is assembled from contributions from the individual elements such that a global stiffness matrix need not be formed.

Stability and time incrementation

The explicit procedure integrates through time by using many small time increments. The central-difference operator is conditionally stable, and the stability limit for the operator is given in terms of the highest frequency of the systems as

$$\Delta t \leq \frac{2}{\omega_{max}}$$

(30)

The actual highest frequency in the system is based on a complex set of interacting factors, and it is not computationally feasible to calculate its exact value. Instead of considering the global model, a more efficient and conservative approach is adopted: the highest frequency value is estimated in each individual element. It can be shown that the highest element frequency determined on an element-by-element basis is always greater than or equal to the highest frequency in the assembled element model. The default time incrementation scheme in Abaqus/Explicit is fully automatic and requires no user intervention. An analysis always starts by using the element-by-element estimation method for the calculation of the stability limit and may switch to the global estimation method under certain circumstances. A fixed incrementation scheme is also available in Abaqus/Explicit. It may be useful when a more accurate representation of the higher mode response of a problem is required.

Advantages

The use of small increments (dictated by the stability limit) is advantageous because it allows the solution to proceed without iteration and without requiring tangent stiffness matrices to be formed. It also simplifies the treatment of contact. The explicit dynamics procedure is ideally suited for analyzing high-speed dynamic events.

The results in an explicit dynamics analysis are not automatically checked for accuracy as they are in Abaqus/Standard (half step-residual). In most cases this is not of concern because the stability condition imposes a small time increment such that the solution changes only slightly in any one time increment, which simplifies the incremental calculations. While the analysis may take an extremely large number of increments, each increment is relatively inexpensive, often resulting in an economical solution. It is not uncommon for Abaqus/Explicit to take over 10^5 increments for an analysis. The method is, therefore, computationally attractive for problems where the total dynamic response time that must be modeled is only a few orders of magnitude longer than the stability limit; for example, wave propagation studies or some "event and response" applications.

2.2. Element type

Abaqus has an extensive element library to provide a powerful set of tools for solving many different problems. As mentioned previously the elements available in Abaqus/Explicit are a subset of those in Abaqus/Standard. Five aspects of an element characterize its behaviour:

- Family : indicates the type of element considered, for example continuum solid, truss, shell, rigid, membrane, etc.
- Degrees of freedom (directly related to the element family): for stress/displacement simulation the degrees of freedom are the translations, and, for shell, pipe, and beam elements, the rotations at each node.
- Number of nodes: displacements and other DOF are calculated at the nodes of the element. At any other point in the element, the displacements are obtained by interpolating from nodal displacements.
- Formulation: refers to the mathematical theory used to define the element's behaviour. In the Lagragian, or material, description of behaviour the element deforms with the material. In the alternate Eulerian, or spatial, description elements are fixed as the material flows through them.
- Integration: Abaqus evaluates the material response at each integration point in each element.

In this subsection the two types of elements used for the numerical analysis, continuum shell and rigid element types, are described with more detail [50].

2.2.1. Continuum shell elements

As a very general rule shell elements are used to model structures in which one dimension, the thickness, is significantly smaller than the other dimensions. Abaqus shell element library is divided into three categories consisting of general purpose, thin, and thick shell elements. Thin shell elements provide solutions to shell problems that are adequately described by classical (Kirchhoff) shell theory [51], thick shell elements yield solutions for structures that are best modelled by shear flexible (Mindlin) shell theory [52], and general-purpose shell elements can provide solutions to both thin and thick shell problems. All shell elements use bending strain measures that are approximations to those of Koiter-Sanders shell theory [53].

Abaqus/Explicit provides only general-purpose shell elements. The general-purpose shell elements are distinguished between axisymmetric elements and three-dimensional elements, the second including conventional and continuum shell elements. Conventional stress/displacement shell elements use this condition to discretize a body by defining the geometry at a reference surface. In contrast, the stress/displacement continuum shell elements discretize an entire three-dimensional body and so can be used in three-dimensional analysis. Conventional and continuum shell elements are compared in Figure 2-1.

Continuum shells have displacement degrees of freedom only (three degrees of freedom), use linear interpolation, and allow mechanical and/or thermal (uncoupled) loading for static and dynamic procedures. The continuum shell elements are general-purpose shells that allow finite membrane deformation and large rotations and, thus, are suitable for non-linear geometric analysis. These elements include the effects of transverse shear deformation and thickness change.
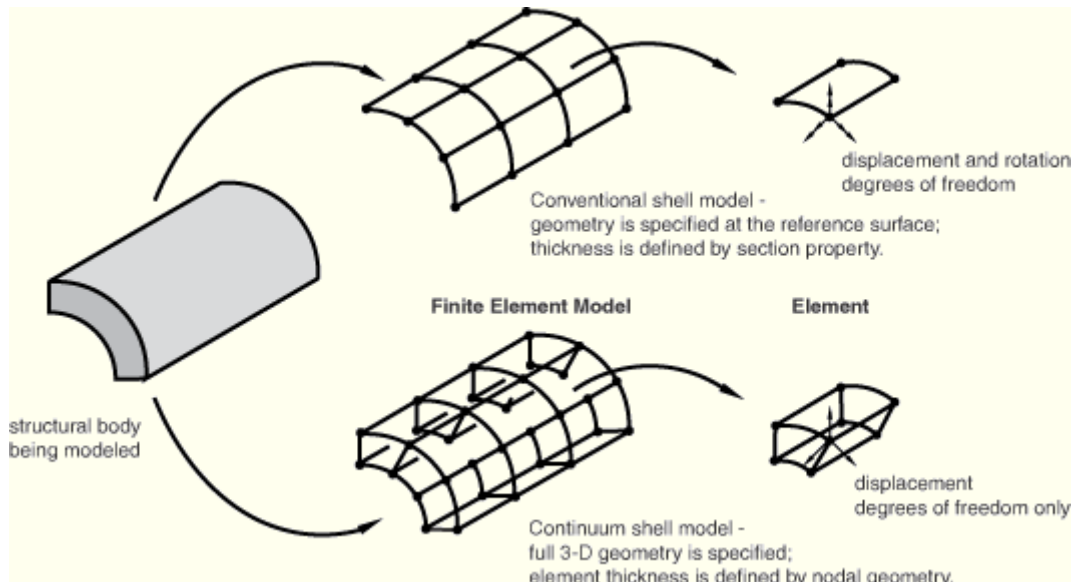
Figure 2-1: comparison between conventional and continuum shell elements [54].

From a modelling point of view continuum shell elements look like three-dimensional continuum solids, but their kinematic and constitutive behaviour is similar to conventional shell elements [54].

Stress/displacement continuum shell elements available are (Figure 2-2) the SC6R (6-node triangular in-plane continuum shell wedge, general-purpose, finite membrane strains) and the SC8R (8-node hexahedron, general-purpose, finite membrane strains).
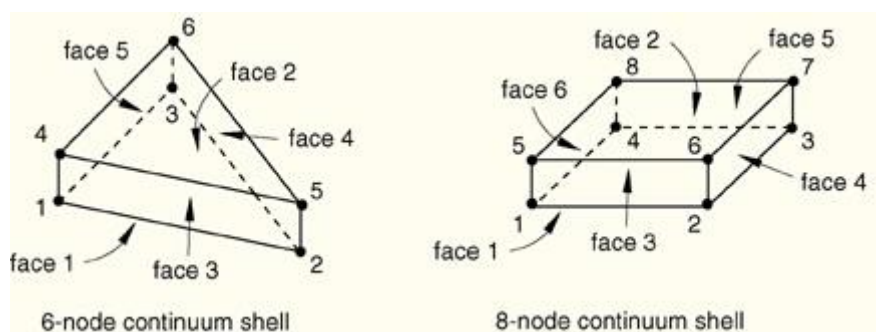
Figure 2-2: nodes position in continuum shell elements [54].

Continuum shell elements use a reduce-integration scheme. Reduced-integration, linear elements have just a single integration point located at the element's centroid, as shown in Figure 2-3.
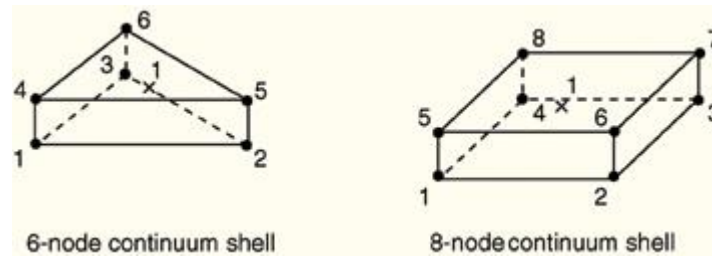
Figure 2-3: integration point for continuum shell elements with reduced integration scheme [54].

Those kinds of elements tend to be too flexible because they suffer from their own numerical problem called *hourglassing* (see section 2.3).

2.2.2. Rigid elements

Rigid elements can be used for multiple purposes, in particular it is mandatory when it is needed to define rigid bodies for multibody dynamic solutions. A rigid body is a collection of nodes, elements, and/or surfaces whose motion is governed by the motion of a single node, called the rigid body reference node. The relative positions of the nodes and elements that are part of the rigid body remain constant throughout a simulation. Therefore, the rigid body elements do not deform but can undergo large rigid body motions.

In multibody dynamic simulations rigid bodies are useful for many reasons. Although the motion of the rigid body is governed by the six degrees of freedom at the reference node, rigid bodies allow accurate representation of the geometry, mass, and rotary inertia of the rigid body. Furthermore, rigid bodies provide accurate visualization and postprocessing of the model.

The principal advantage to representing portions of a model with rigid bodies rather than deformable finite elements is computational efficiency. Element-level calculations are not performed for elements that are part of a rigid body. Although some computational effort is required to update the motion of the nodes of the rigid body and to assemble concentrated and distributed loads, the motion of the rigid body is determined completely by a maximum of six degrees of freedom at the reference node.

Rigid bodies are particularly effective for modeling relatively stiff parts of a model in Abaqus/Explicit for which tracking waves and stress distributions are not important. Element stable time increment estimates in the stiff region can result in a very small global time increment. Since rigid bodies and elements that are part of a rigid body do not affect the global time increment, using a rigid body instead of a deformable finite element representation in a stiff region can result in a much larger global time increment, without significantly affecting the overall accuracy of the solution [54].

Bi-dimensional, three-dimensional and axisymmetric rigid elements are available.

2.3. Hourglass mode

Hourglass modes are nonphysical, zero-energy modes of deformation that produce zero strain and no stress. The hourglass phenomenon in the model is noticed as apparent deformation of the finite element mesh, which looks like a collection of hourglass-like shapes. In finite element analysis the element stiffness matrix is determined through the full-integration method or though the reduced integration method. The main advantage of the reduced scheme is the shorter calculation time but it can lead to some pathological solutions, such as hourglass effect [50].

Consider a single reduced-integration element modelling a small piece of material subjected to pure bending, as represented in Figure 2-4.
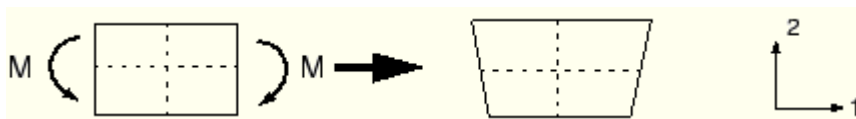
Figure 2-4: deformation of a linear element with reduced integration subjected to bending moment M [54].

Neither of the dotted visualization lines has changed in length, and the angle between them is also unchanged, which means that all components of stress at the element's single integration point are zero. This bending mode of deformation is thus a zero-energy mode because no strain energy is generated by this element distortion. The element is unable to resist this type of deformation since it has no stiffness in this mode. In coarse meshes this zero-energy mode can propagate though the mesh, producing meaningless results. In Abaqus a small amount of artificial "hourglass stiffness" is introduced in reduced integration elements to limit the propagation of hourglass modes. This stiffness is more effective at limiting the hourglass modes when more elements are used in the model, which means that linear-reduced integration elements can give acceptable results as long as a reasonably fine mesh is use.

2.3.1. Hourglass control

When refinement of mesh is not enough to contrast hourglassing of the elements during analysis, the following methods are Available in Abaqus/Explicit for suppressing the hourglass modes (and available for continuum shell elements) [54].

Integral viscoelastic approach – Relax Stiffness

The integral viscoelastic approach generates more resistance to hourglass forces early in the analysis step where sudden dynamic loading is more probable.

Let q be an hourglass mode magnitude and Q be the force (or moment) conjugate to q. The integral viscoelastic approach is defined as

$$Q = \int_0^t sK(t - t') \frac{dq}{dt} dt'$$

$$(31)$$

where K is the hourglass stiffness selected by Abaqus/Explicit, and s is one of up to three scaling factors s^s, s^r and s^ω that you can define (by default all equal to 1). The scale factors are dimensionless and relate to specific displacement degrees of freedom. It is the most computationally intensive hourglass control method.

Kelvin viscoelastic approach – Stiffness

The kelvin-type viscoelastic approach is defined as

$$Q = s[(1-\propto)Kq + \propto C\frac{dq}{dt}]$$

$$(32)$$

Where K is the linear stiffness and C is the linear viscous coefficient. This general form has pure stiffness and pure viscous hourglass control as limiting cases.

Enhanced hourglass approach

The enhanced hourglass control approach represents a refinement of the pure stiffness method in which the stiffness coefficients are based on the enhanced assumed strain method; no scale factor is required. This method gives more accurate displacement solutions for coarse meshes with linear elastic materials as compared to other hourglass control methods. It also provides increased resistance to hourglassing for nonlinear materials. Although generally beneficial, this may give overly stiff response in problems displaying plastic yielding under bending.

2.4. Material model

In this thesis work a constitutive model for fabric reinforced composites, which was introduced in Abaqus/Explicit 6.8, was adopted [55]. The model has been implemented as a built-in VUMAT user subroutine, defined in Abaqus as "ABQ_PLY_FABRIC".

This model is currently supported for plane-stress elements, which includes shell (S4R and S3R), continuum shell (SC6R and SC8R), plane stress (CPS family) and membrane (M3D) elements.

The constitutive stress-strain relations are formulated in a local Cartesian coordinate system with base vectors aligned with the fiber directions.
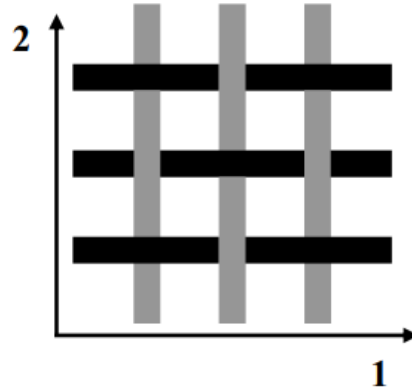
Figure 2-5 : Schematic representation of woven fabric.
Fibers are aligned with directions 1 and 2 of a local coordinate system [55].

The fabric-reinforced ply is modeled as a homogeneous orthotropic elastic material with the potential to sustain progressive stiffness degradation due to fiber/matrix cracking, and plastic deformation under shear loading.

2.4.1. Elastic stress- strain relations

It is assumed that the elastic stress-strain relations are given by orthotropic damaged elasticity. The elastic relations are the following:

$$
\begin{bmatrix} \varepsilon_{11} \\ \varepsilon_{22} \\ \varepsilon_{12}^{el} \end{bmatrix} = \begin{bmatrix} \dfrac{1}{(1-d_1)E_1} & \dfrac{-v_{12}}{E_1} & 0 \\ \dfrac{-v_{21}}{E_2} & \dfrac{1}{(1-d_2)E_2} & 0 \\ 0 & 0 & \dfrac{1}{(1-d_{12})2G_{12}} \end{bmatrix} \begin{bmatrix} \sigma_{11} \\ \sigma_{22} \\ \sigma_{12} \end{bmatrix}
$$

(33)

The damage variables d_1 and d_2 are associated with fiber fracture along the 1 and 2 directions respectively, whereas d_{12} is related to matrix micro-cracking due to shear deformation. The model differentiates between tensile and compressive fiber failure modes by activating the corresponding damage variable depending on the stress state in the fiber directions:

$$
d_1 = d_{1+} \frac{\langle \sigma_{11} \rangle}{|\sigma_{11}|} + d_{1-} \frac{\langle -\sigma_{11} \rangle}{|\sigma_{11}|}
$$

(34)

$$
d_2 = d_{2+} \frac{\langle \sigma_{22} \rangle}{|\sigma_{22}|} + d_{2-} \frac{\langle -\sigma_{22} \rangle}{|\sigma_{22}|}
$$

(35)

In order to incorporate different initial (undamaged) stiffness in tension and compression, the values of the elastic constants E_1, E_2 and v_{12} are assumed to take their tensile or compressive values depending on the sign of $tr(\varepsilon) = \varepsilon_{11} + \varepsilon_{22}$.

2.4.2. Fiber response

The material response along the fiber directions is characterized with damaged elasticity. It is assumed that the fiber damage variables are a function of the corresponding effective stress, which are defined as:

$$\tilde{\sigma}_{1+} = \frac{\langle \sigma_{11} \rangle}{(1 - d_{1+})}$$

(36)

$$\tilde{\sigma}_{2+} = \frac{\langle \sigma_{22} \rangle}{(1 - d_{2+})}$$

(37)

$$\tilde{\sigma}_{1-} = \frac{\langle -\sigma_{11} \rangle}{(1 - d_{1-})}$$

(38)

$$\tilde{\sigma}_{2-} = \frac{\langle -\sigma_{22} \rangle}{(1 - d_{2-})}$$

(39)

Considering $\alpha = 1(+/-)$, $2(+/-)$ depending on the sign of the corresponding stresses, the four equations for the damage mentioned above are then expressed as the following:

$$d_\alpha = d_\alpha(\tilde{\sigma}_\alpha)$$

(40)

The effective stresses $\tilde{\sigma}_\alpha$ are directly related to the thermodynamic forces, Y_α, that are work conjugate to the damage variables, through the relationship $\tilde{\sigma}_\alpha = \sqrt{2E_\alpha Y_\alpha}$ This equation states that the fiber damage variables depend only on the corresponding thermodynamic force. At any given time, the elastic domain is defined in terms of the damage activation functions, F_α, as

$$F_\alpha = \Phi_\alpha - r_\alpha \leq 0$$

(41)

The functions Φ_α provide a criterion for fiber failure and are assumed to take the form:

$$\Phi_\alpha = \frac{\tilde{\sigma}_\alpha}{X_\alpha}$$

(42)

where X_α are the tensile/compressive strengths for uniaxial loading along the fiber directions.

The damage thresholds, $r\alpha$, are initially set to one. After damage activation ($\Phi_\alpha = 1$) they increase with increasing damage according to:

$$r_\alpha(t) = \max_{\tau \leq t} \Phi_\alpha(\tau)$$

(43)

The definition ensures that the damage thresholds are non-decreasing quantities. The damage thresholds are assumed to obey the Kuhn-Tucker complementary conditions:

$$F_\alpha \leq 0 ; \ \dot{r}_\alpha \geq 0 ; \ \dot{r}_\alpha F_\alpha = 0$$

(44)

The evolution of the damage variables are a function of the damage thresholds and the fracture energy per unit area under uniaxial tensile/compressive loading, G_f^α.

The evolution of the damage variables is given by the equation:

$$d_\alpha = 1 - \frac{1}{r_\alpha} \exp\left(-A_\alpha(r_\alpha - 1)\right)$$

(45)

where

$$A_\alpha = \frac{2 g_0^\alpha L_c}{G_f^\alpha - g_0^\alpha L_c}$$

(46)

Here, Lc is the characteristic length of the element and g0 is the elastic energy density at the point of damage initiation:

$$g_0^\alpha = \frac{X_\alpha^2}{2 E_\alpha}$$

(47)

The formulation of the damage evolution law ensures that the damage variables are monotonically increasing quantities. It also ensures that the correct amount of energy is dissipated when the lamina is subjected to uniaxial loading conditions along the fiber directions. For instance, under uniaxial tensile loading in fiber direction 1, the dissipated energy per unit area in equal to the fracture energy G_{f1+}.

This holds true provided that:

$$G_f^\alpha - g_0^\alpha L_c > 0 \ \leftrightarrow \ L_c < L_{max} = \frac{G_f^\alpha}{g_0^\alpha}$$

(48)

The formulation therefore imposes a restriction on the maximum element size that can be used to accurately capture the right amount of energy dissipation during fracture. If the characteristic element size of the FE mesh is greater than L_{max}, the analysis will over-predict the energy dissipation.

2.4.3. Shear response

Shear response is dominated by the non-linear behavior of the matrix, which includes both plasticity and stiffness degradation due to matrix microcracking.

2.4.3.1. Elasticity

The elastic relations give the effective (undamaged) stress in terms of elastic strain:

$$\tilde{\sigma}_{12} = \frac{\sigma_{12}}{1 - d_{12}} = 2G_{12}\varepsilon_{12}^{el} = 2G_{12}(\varepsilon_{12} - \varepsilon_{12}^{pl})$$

(49)

2.4.3.2. Plasticity

- Yield function:

$$F = |\tilde{\sigma}_{12}| - \tilde{\sigma}_0(\bar{\varepsilon}^{pl}) \leq 0$$

(50)

  The hardening function is assumed to be of the form :
$$\tilde{\sigma}_0(\bar{\varepsilon}^{pl}) = \tilde{\sigma}_{y0} + C(\bar{\varepsilon}^{pl})^p$$

(51)

- Flow rule: assuming associated flow, then:

$$\dot{\varepsilon}_{12}^{pl} = \dot{\bar{\varepsilon}}^{pl}\frac{\partial F}{\partial \tilde{\sigma}_{12}} = \dot{\bar{\varepsilon}}^{pl} sign(\tilde{\sigma}_{12})$$

(52)

  The evolution of the plastic work during yielding is given as
$$\dot{U}^{pl} = 2\sigma_{12}\dot{\varepsilon}_{12}^{pl} = 2(1 - d_{12})\tilde{\sigma}_{12}\dot{\varepsilon}_{12}^{pl} = 2(1 - d_{12})\tilde{\sigma}_0\dot{\bar{\varepsilon}}^{pl}$$

(53)

2.4.3.3. Damage

The elastic domain is defined in terms of the damage activation function, F12, as

$$F_{12} = \phi_{12} - r_{12} \leq 0$$

(54)

The function phi12 provides the criterion for initiation of shear damage of the matrix, which is assumed to be of the form

$$\phi_{12} = \frac{\tilde{\sigma}_{12}}{S}$$

$$(55)$$

Here $\tilde{\sigma}_{12}$ is the effective shear stress, and S is the shear stress for initiation of matrix damage. The damage threshold is initially set to one and increases after damage activation according to

$$r_{12}(t) = \max_{\tau \leq t} \phi_{12}(\tau)$$

$$(56)$$

Finally, based on [56] it is assumed that the shear damage variable increases with the logarithm of r123 until a maximum value d12max is reached. Thus:

$$d_{12} = \min(\alpha_{12} \ln(r_{12}), d_{12}^{max})$$

$$(57)$$

Where $\alpha_{12} > 0$, and $d_{12}^{max} \leq 1$ are material properties.

2.4.4. Calibration procedure

The elastic constants and the fiber tension/compression strengths, X_{α}, are easily measured from standard coupon tests under uniaxial tension/compression loading of the malinates.

The shear response is usually calibrated with a cyclic tensile test on a ±45 laminate, where the strains along the fiber directions can be neglected. Figure 2-6 shows the typical shear response of a fabric reinforced composite. It is noted that the unloading/reloading paths in this figure correspond to an idealization of the actual response, which usually exhibits hysteretic behavior. The figure will serve as the starting point for the discussion of a general calibration procedure for the parameters that enter the damage and plasticity equations.
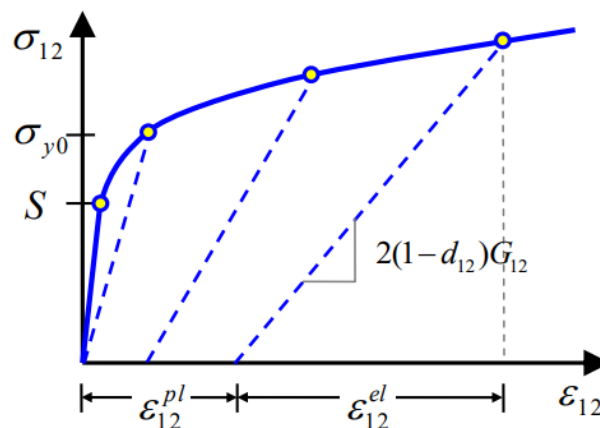
Figure 2-6: schematic representation of typical shear response of fabric reinforced composite [55].

The level of damage can be measured from the ratio of the unloading stiffness to the initial (undamaged) elastic stiffness. This allows us to compute pairs of stress-damage

values, (σ_{12}, d_{12}), for each unloading curve. This data can be represented in the space of d_{12} versus $\ln(\tilde{\sigma}_{12)}$ where $\tilde{\sigma}_{12)} = \sigma_{12}/(1 - d_{12})$. A linear fit of the data provides the values of α12 (slope of the line) and S (intersection with the horizontal axis) as shown in Figure 2-7. Sometimes the damage data shows indication of a saturation value, which would be used to determine $d_{12}^{max} \leq 1$. Otherwise a value of $d_{12}^{max} = 1$ should be used.
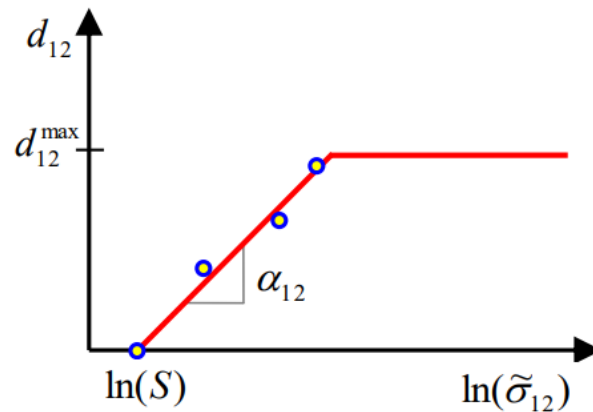
Figure 2-7: calibration of the shear damage parameters [55].

For each unloading curve in Figure 2-6, the plastic strain ε_{12}^{pl} at the onset of unloading is determined from the value of residual deformation in the unloading state. The values of ($\tilde{\sigma}_{12}, \varepsilon_{12}^{pl}$) at the onset of unloading are then used to fit the parameters of the hardening curve.
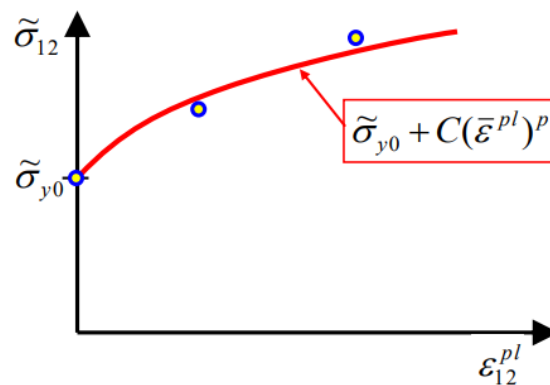
Figure 2-8: calibration of the hardening curve [55].

2.4.5. Output

In addition to the standard (material-independent) output variables in Abaqus/Explicit for stress-displacement elements, the following output variables have a special meaning for the user material. Notice that SDV in Table 3 states for "solution-

dependent state variable" and represents in fact an additional output that a user can generate with a user subroutine, such as in this case.

Output variable	symbol	description
SDV1	d_{1+}	Tensile damage along fiber direction 1
SDV2	d_{1-}	Compressive damage along fiber direction 1
SDV3	d_{2+}	Tensile damage along fiber direction 2
SDV4	d_{2-}	Compressive damage along fiber direction 2
SDV5	d_{12}	Shear damage
SDV6	r_{1+}	Tensile damage threshold along fiber direction 1
SDV7	r_{1-}	Compressive damage threshold along fiber direction 1
SDV8	r_{2+}	Tensile damage threshold along fiber direction 2
SDV9	r_{2-}	Compressive damage threshold along fiber direction 2
SDV10	r_{12}	Shear damage treshold
SDV11	$\bar{\varepsilon}^{pl}$	Equivalent plastic strain
SDV12	ε_{11}^{el}	Elastic strain component 11
SDV13	ε_{11}^{el}	Elastic strain component 22
SDV14		Not used
SDV15	ε_{12}^{el}	Elastic strain component 12
SDV16	MpStatus	Material point status: 1 if active, 0 if failed

Table 3: output variables for ply reinforced composites VUMAT [55].

3 Experimental tests

In this Chapter the experimental campaign performed in this thesis work is depicted. The composite materials under investigation are briefly described, followed by the standards adopted for the tests. The first part of the experimental campaign regards the calibration of the composite's mechanical properties. Tensile, compressive, and shear tests were performed. Second part of the experimental work consisted in the performance of drop weight tests, which are characterized in detail. The comparison between the currently examined PU matrix composites and same configuration epoxy matrix composites is also performed.

3.1. Materials

Pure glass, pure aramid and hybrid composites were produced with different stacking sequences and configurations by the UFRGS (Universidade Federal do Rio Grande do Sul) by vacuum infusion process. The laminates were then sent to Politecnico of Milano to be mechanically characterized and, from impact tests, obtain information about their damage resistance.

The composites are constituted by a novel elastomeric polyurethane resin (PU (CO/PE)®), which was developed by the UFRGS research team [8]. The resin was characterized by ASTM D412 tensile testing by the UFRGS. The modulus of elasticity, tensile stress at break and strain at break of the resin were recorded at different speeds. Stress-strain curves are reported in Figure 3-1 and results are shown in Table 4.

a)   b)

c)
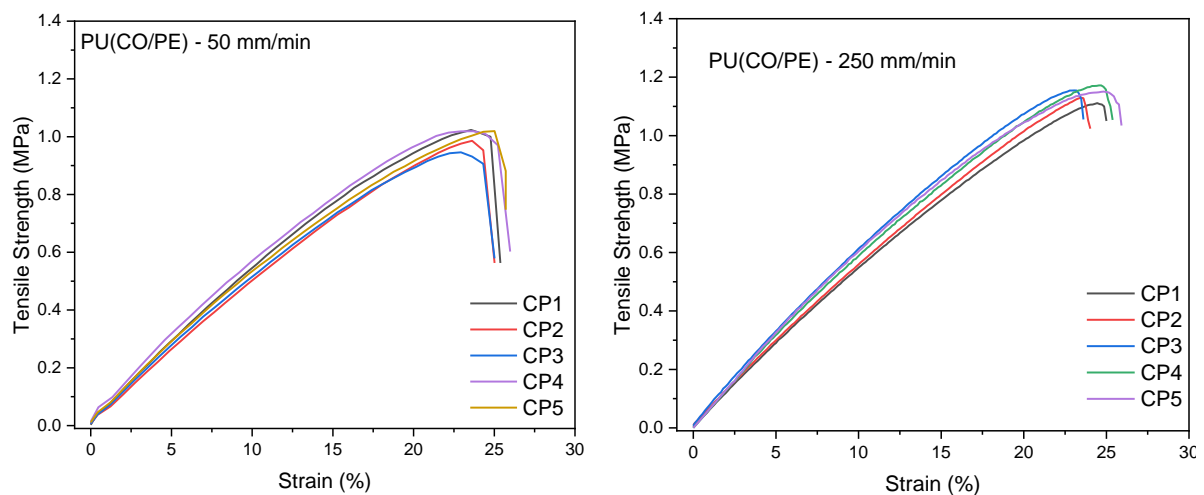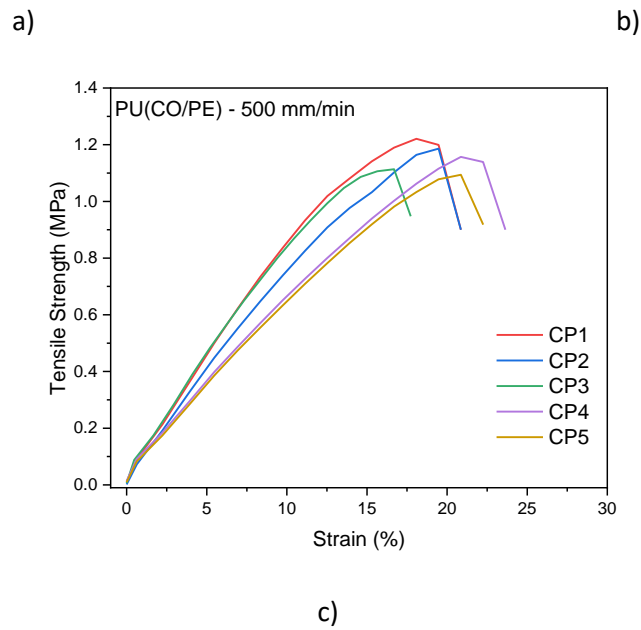
Figure 3-1: stress-strain curves of PU(CO/PE) registered at (a) 50mm/min, (b) 250 mm/min, and (c) 500 mm/min rate.

POLYURETHANE (PU(CO/PE)	Velocity [mm/min]		
	50	250	500
Modulus at 10% [MPa]	5.4	5.8	6.0
Tensile stress at break [MPa]	1.04	1.18	1.39
Strain at break [%]	24.78	25.10	29.17

Table 4: mechanical properties measured from PU resin tensile tests.

For the aramid laminas Kevlar®29 plain- weave fabric with a superficial density of 440 g/m² (DUPONT) was used and for the glass laminas a s2-glass 8-harness satin fabric with a superficial density of 300 g/m² (HEXCEL) was adopted. The fabrics can be visualized in Figure 3-2.

<center>a)   b)</center>
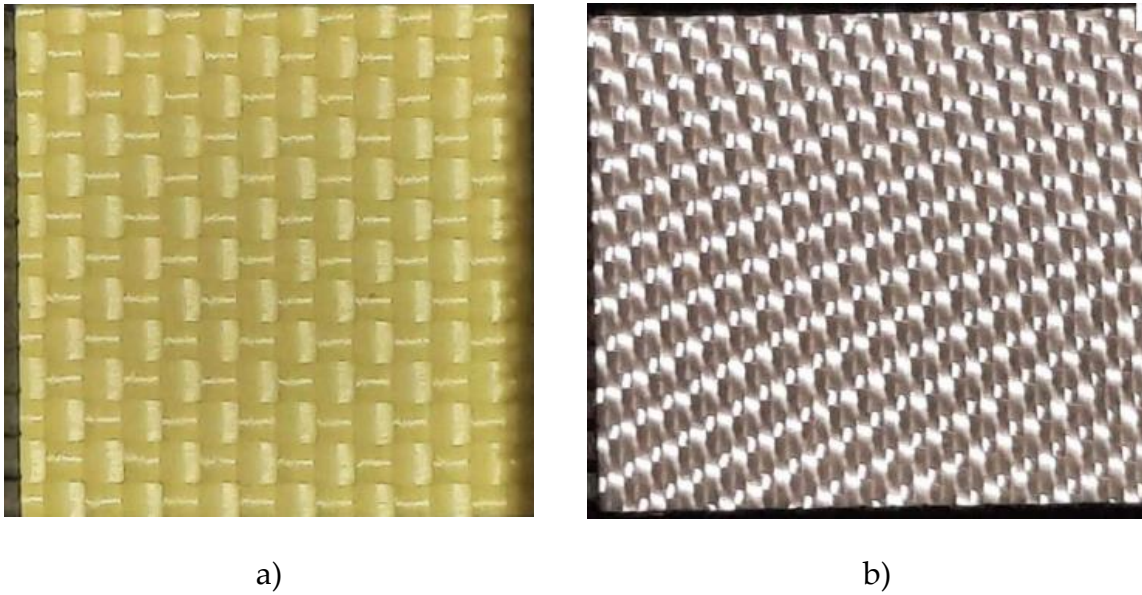
Figure 3-2: (a) plain weave Kevlar fabric and (b) 8-harness satin s2-glass fabric.

Among the pure composites, five different kinds of Kevlar laminates were available with increasing number of layers: 5, 8, 10, 13 and 18. For the calibration of mechanical properties of the composite the K5 laminate was used. For the pure glass instead six different laminates were available, in that case with 5, 8, 10, 15, 16 and 20 layers. For calibration of mechanical properties, the G8 composite was used. For impact tests K8 and G16 pure composites panels were investigated in this thesis work. In Table 5 and Table 6 the laminates properties in terms of thickness, density, volume, and weight fraction of reinforcement can be visualized, while a representative illustration of the composites is shown in Figure 3-3.

PU/aramid	K5	K8
t [mm]	2.75	4.20
t/layer [mm]	0.53	0.52
ϱ[g/cm³]	1.32	1.32
Wf[%]	67.2±1.0	67.9±2.2
Vf[%]	59.7±1.2	60.5±1.0

<center>Table 5: Kevlar composites features.</center>

PU/S2-glass	G8	G16
t [mm]	2.30	4.95

t/layer [mm]	0.29	0.31
$\varrho[g/cm^3]$	2.05	2.06
Wf[%]	69.85±0.3	69.91±0.5
Vf[%]	49.00±0.7	50.21±1.1

Table 6: Glass composites features.
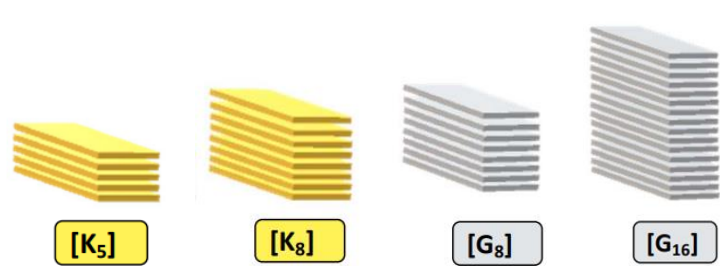
Figure 3-3: representation of the composite laminates with corresponding number of plies.

Once the mechanical characterization of the pure laminates was done it was possible to start also investigating the hybrid composites. In that case only impact tests were performed. In total ten different configurations of hybrids were produced and were then available for testing. Besides the study of the matrix influence on the tests, one of the main goals of this collaboration project between Politecnico of Milano and UDRGS is to investigate the effect of different composite parameters, such as thicknesses, different aramid/glass ratios, different stacking sequences, effect of symmetry and asymmetry, and the effect of block/alternate layers layup on the damage response of the composite itself. Hybrid composites selected for impact tests were: [K2G4]S, [G2K]2S, [G4K2]S. An illustration of the composites lay-up is shown in Figure 3-4. As it can be observed in Table 7, those panels have same number of aramid and glass layers, same density, almost equal total thickness, volume, and weight fraction of reinforcement. Also, compared to the pure panels which were subjected to the impact tests (K8 and G16), they have comparable overall thickness. Moreover, all of them have the common characteristic to be symmetric composites. For the above considerations, maintaining as similar as possible all the other properties, those panels were chosen to investigate the influence of the stacking sequence of the laminas in the composite.

Hybrids	$[K_2G_4]_S$	$[G_2K]_{2S}$	$[G_4K_2]_S$
t[mm]	4.37	4.44	4.48
K layers	4	4	4

G layers	8	8	8
t/layer [mm]	0.36	0.37	0.37
ϱ[g/cm^3]	1.75	1.75	1.75
Wf[%]	70.21	70.15	70.08
Vf[%]	56.41	56.44	56.33

Table 7: Hybrid composites features.

$[K_2G_4]_s$ $[G_2K_1]_{2s}$ $[G_4K_2]_s$
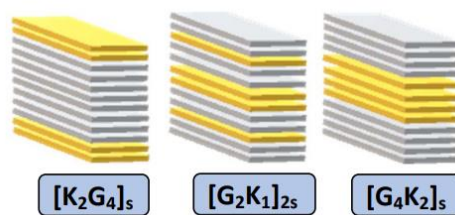
Figure 3-4: representation of the selected hybrid laminates for impact testing.

3.2. Instrumentation

Tensile and shear tests

All tensile and shear tests performed in this thesis work have been done with the MTS Alliance RT100 testing machine, shown in Figure 3-5. The grips used were the ones provided by the testing machine and grips pressure was kept constant in all tests: 5MPa. Crosshead speed imposed changed according to test type, tensile or shear, and material tested, glass and Kevlar composites. This value is reported in the following Sections for each testing case.

In order to record the deformation, extensometer MTS 634.25F-54 was placed in the middle of the samples. The extensometer gage was 50 mm and data acquisition rate was set to 25 Hz. In Figure 3-6 grips and extensometer adopted are shown.

Figure 3-5: testing machine MTS Alliance RT100

a)

b)

Figure 3-6: a) grips and b) extensometer

On a limited number of samples strain gages have been applied in order to obtain also information about the materials transverse strain during elongation: one sample for each kind of material have been tested, both for the tensile and the shear test (four samples in total). The strain gages used were HBM 1-XY98-6/120 with 2,15 ± 1% gage

factor. The strain gage is a X rosette, specifically designed for polymeric materials: the number 8 in the serial number is the tempearture matching code specific for polymeric material. Strain gage scheme is shown in Figure 3-7 and its characteristics in Table 8.
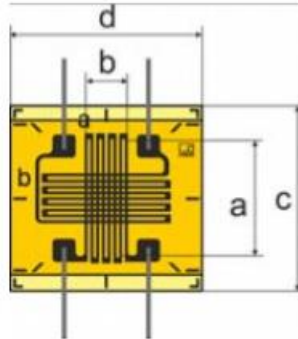
Figure 3-7: strain gage scheme.

Ordering number	Nominal resistance [Ω]	Dimensions [mm]					Vmax[V]
		Measuring grid [mm]			Carrier [mm]		
		a	b1	b2	c	d	
1-XY98-6/120	120	6	1.9	2.2	10	9.6	3.5

Table 8: strain gage characteristics.

The HBM MGCplus machine (Figure 3-8) have been adopted to record data synchronized with the acquisition machine.
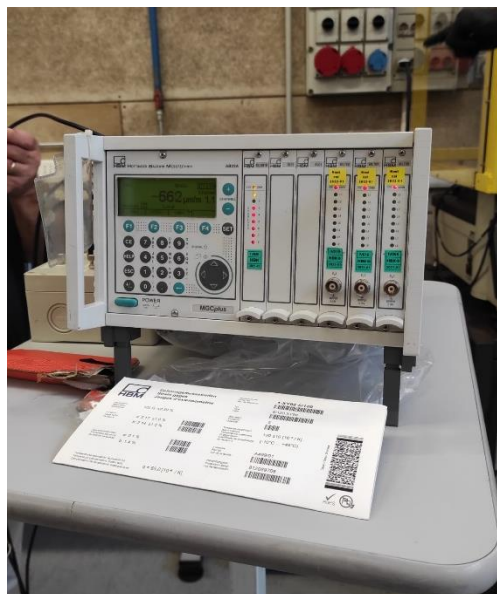
Figure 3-8: HBM MGCplus machine.

Figure 3-9: picture of a specimen tested with both strain gage (front) and extensometer (back)

Impact tests

The impact tests were performed using the Step-Lab Drop Weight Tester machine, shown in Figure 3-10, with a hemispherical impactor with a diameter of 16 mmm (Figure 3-11). The total weight loaded on the machine for all the impacts was 9.44 Kg. According to the impact energy imposed, which ranged from 20J to 120J, and setting the value of the dropping weight, drop height is automatically defined. The acquisition rate (load signal) of the data was of 3MHz. Speed measurement is performed right before the impactor strikes the sample, via an optical measuring system. Before tests the anti-rebound system of the impactor was activated. The debounce system holds up the drop weight, preventing further secondary impacts which might affect the physical state of the sample and the final results. Output data recorded, versus time, by the machine are the impact force, the impact velocity, energy, and displacement.
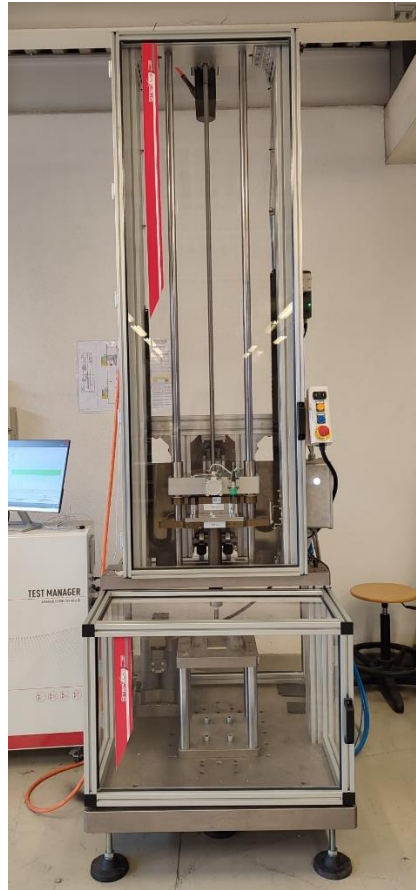
Figure 3-10: Drop Weight Tester machine.
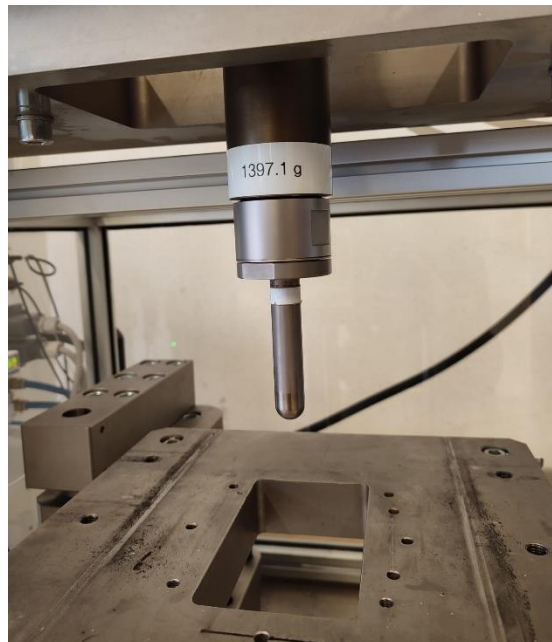
Figure 3-11: hemispherical impactor adopted for the drop weight tests.

3.3. Test standards

3.3.1. D3039/D3039M – 17

This test method [57] determines the in-plane tensile properties of polymer matrix composite materials reinforced by high-modulus fibers. Properties, in the test direction, which may be obtained from this test method include ultimate tensile strength, ultimate tensile strain, tensile chord modulus of elasticity, Poisson ratio. Significant recommendations from the standard are here briefly described.

The suggested dimension for balanced and symmetric coupon specimens are:

Width [mm]	Length [mm]	Thickness [mm]
25	250	2.5

Table 9: dimensions for the specimens indicated in the standard.

The thickness and width of the specimen should be measured in the gage section for the calculation of the cross-section area. The speed of testing shall be set in order to have a nearly constant strain rate in the gage section. Although a precise value is not specified, strain rate should be selected to produce failure within 1 to 10 minutes. The suggested standard head displacement rate for constant head-speed tests is of 2 mm/min, but it can be increased at occurrence. In case the strain response is to be determined the strain-indication transducer must be attached to the specimen, symmetrically about the mid-span, mid-width location. Force versus crosshead displacement (and force versus strain if extensometers are utilized) is recorded. For this test method, a sampling rate of 2 to 3 data recordings per second, and a target minimum of 100 data points per test are recommended. Mode and location of failure of the specimen must be recorded and if possible, by using the standard description of the three-part failure mode code, as indicated in Figure 3-12.

First Character		Second Character		Third Character	
Failure Type	Code	Failure Area	Code	Failure Location	Code
Angled	A	Inside grip/tab	I	Bottom	B
edge Delamination	D	At grip/tab	A	Top	T
Grip/tab	G	<1W from grip/tab	W	Left	L
Lateral	L	Gage	G	Right	R
Multi-mode	M(xyz)	Multiple areas	M	Middle	M
long. Splitting	S	Various	V	Various	V
eXplosive	X	Unknown	U	Unknown	U
Other	O				
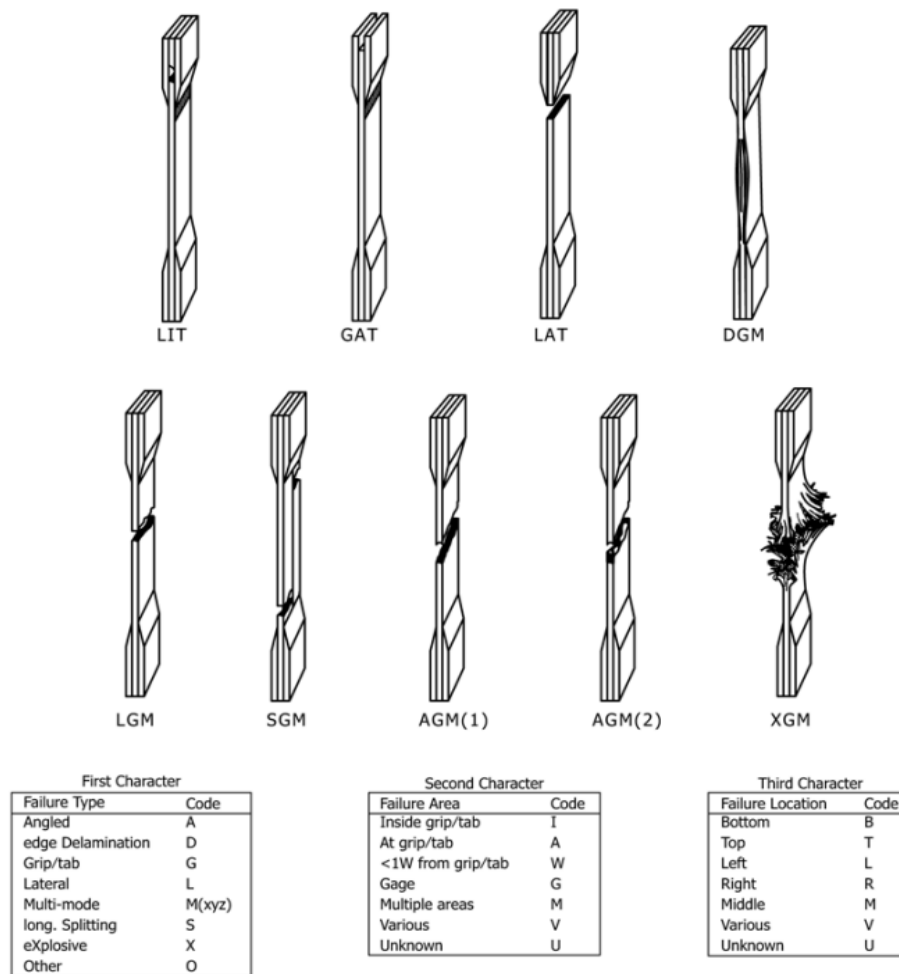
Figure 3-12: tensile test specimen three-part failure identification codes.

Equations to be used for the calculation of the mechanical properties are listed below:

- Tensile stress/tensile strength:

$$\sigma_i = \frac{P_i}{A}$$

(58)

Where:

σ_i = tensile stress at i-th point, [MPa];

P_i= tensile force at i-th point, [N];

A= average cross section, [mm²].

The tensile strength is calculated by choosing as Pi the maximum force, Pmax, before failure of the specimen.

- Tensile strain/ultimate tensile strain

$$\varepsilon_i = \frac{\delta_i}{L_g}$$

(59)

Where:

ε_i = tensile strain at ith data point;

δ_i = extensometer displacement at ith data point, [mm];

L_g = extensometer gage length, [mm].

- Tensile chord modulus of elasticity

$$E^{chord} = \frac{\Delta\sigma}{\Delta\varepsilon}$$

(60)

Where:

E^{chord} = tensile chord modulus of elasticity, [GPa];

$\Delta\sigma$ = difference in applied tensile stress between the two strain points chosen;

$\Delta\varepsilon$ = difference between the two strain points (nominally 0.002).

- Poisson ratio

$$v = \frac{\Delta\varepsilon_t}{\Delta\varepsilon_l}$$

(61)

Where:

v = Poisson's ratio;

$\Delta\varepsilon_t$ = difference in lateral strain between the two longitudinal strain points;

$\Delta\varepsilon_l$ = difference between the two longitudinal strain points (nominally either 0.001, 0.002 or 0.005).

- Statistics

For each series of tests the average value ($\bar{x}$), the standard deviation (S_{n-1}) and the coefficient of variation (CV) for each property determined are to be calculated.

$$\bar{x} = \frac{\sum_{i=1}^{n} x_i}{n}$$

$$62$$

$$S_{n-1} = \sqrt{\frac{\left(\sum_{i=1}^{n} x_i^2 - n\bar{x}^2\right)}{n-1}}$$

$$63$$

$$CV = \frac{100 * S_{n-1}}{\bar{x}}$$

$$(64)$$

Where:

$\bar{x}$ = sample mean;

S_{n-1} = sample standard deviation;

CV = sample coefficient of variation, in percent;

n = number of specimens;

x_i = measured or derived property.

3.3.2. D3410/D3410M – 16

This test method [58] determines the in-plane compressive properties of polymer matrix composite materials reinforced by high modulus fibers. Properties, in the test direction, that may be obtained from this test method include ultimate compressive strength, ultimate compressive strain, compressive modulus of elasticity, Poisson ratio in compression.

Geometry recommendations for the compression specimen are the following:

Width [mm]	Gage length [mm]	Tab length [mm]	Overall length [mm]	Tab thickness [mm]
25	10-25	65	140-155	1.5

Table 10: indicated dimensions for the compressive test specimen and tabs.

64

Before the testing the specimen cross section area must be determined. Strain gages (or extensometers) should be applied to both faces of the specimen. As for the tensile test, a constant strain rate in the gage section is desired and it should be imposed to produce failure within 1 to 10 minutes from the beginning of force application. The standard crosshead displacement is of 1.5 mm/min. If the specimen fails the maximum force, the failure force and the displacement should be measured at a point as near as possible to the moment of failure. Mode, area, and location of failure for each specimen shall be indicated following a failure identification code based on the three-part code, as indicated in Figure 3-13.

First Character

Failure Mode	Code
Angled	A
Brooming	B
end-Crushing	C
Delamination	D
Euler buckling	E
tHrough-thickness	H
Kink bands	K
Lateral	L
Multi-mode	M(xyz)
long.-Splitting	S
Transverse shear	T
eXplosive	X
Other	O

Second Character

Failure Area	Code
Inside grip/tab	I
At grip/tab	A
Gage	G
Multiple Areas	M
Tab adhesive	T
Various	V
Unknown	U

Third Character

Failure Location	Code
Bottom	B
Top	T
Left	L
Right	R
Middle	M
Various	V
Unknown	U

Figure 3-13: compression test specimen three-part failure identification codes.

Calculation of properties:

- Compressive stress/Ultimate compressive stress

$$\sigma_i^c = \frac{P_i}{A}$$

(65)

Where:

σ_i^c = compressive stress at ith data point, [MPa];

P_i = force at ith data point, [N];

A = cross sectional area, [mm²].

For the ultimate compressive stress P^max, maximum force before failure, is used.

- Compressive chord modulus of elasticity

$$E^{chord} = \frac{\Delta\sigma}{\Delta\varepsilon}$$

(66)

Where:

E^{chord} = chord modulus of elasticity, [MPa];

$\Delta\sigma$ = difference in applied compressive stress between the two strain points chosen, [MPa]

$\Delta\varepsilon$ = difference in the average compressive strain between the two strain points.

- Statistics are the same indicated for D3039/D3039M

3.3.3. D3518/D3518M – 13

This test method [59] determines the in-plane shear response of polymer matrix composite materials reinforced by high modulus fibers. The composite material form is limited to a continuous-fiber-reinforced composite ±45° laminate capable of being tested in the laminate x direction (. Properties that may be derived from this test method include in-plane shear stress versus shear strain response; in-plane shear chord modulus of elasticity; maximum in-plane shear stress for a ±45° laminate; maximum in-plane engineering shear strain for a ±45° laminate.

x and y represent the Specimen or Reference Axes, while
1 and 2 represent the Material or Local Axes
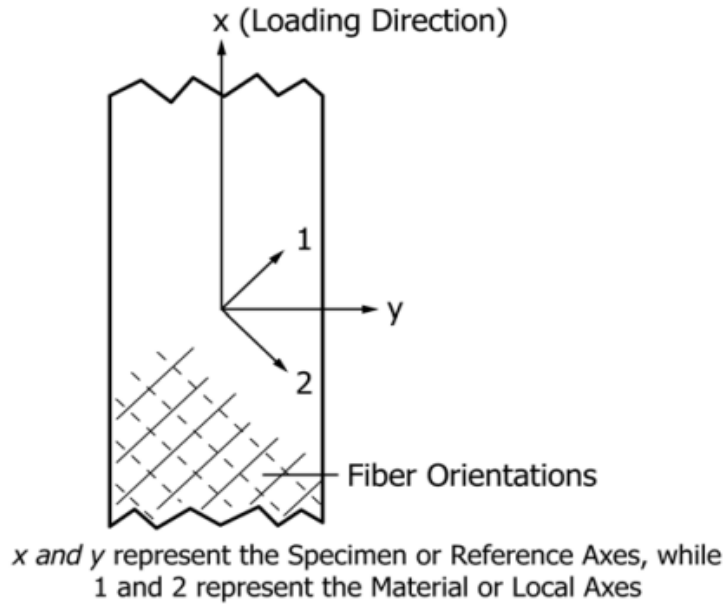
Figure 3-14: definition of specimen and material axes.

The recommended coupon width is 25 mm, and the recommended coupon length range is from 200 to 300 mm. Tabs are not required.

Many aspects of the test such as specimen preparation, geometry, calibration, and conditioning are in accordance with test method D3039/D3039M.

The procedure can be schematized as follow: a tension test is performed on the laminate coupon in accordance with test method D3039/D3039M, with, if possible, normal strain instrumentation in both longitudinal and transverse directions while a nearly continuous force-normal strain is recorded. If the ultimate failure does not occur within 5% engineering shear strain, the data shall be truncated to that value. Then for following calculations this 5% engineering shear strain point shall be considered as the maximum shear stress.

Calculation:

- Shear stress/ maximum shear stress

$$\tau_{21i} = \frac{P_i}{2A}$$

67

Where:

τ_{21i} = shear stress at ith data point, [MPa];

P_i = force at ith data point, [N];

A = cross-sectional area, [mm²].

For the calculation of maximum in-plane shear stress, maximum force Pmax at or below 5% engineering shear strain, is to be used.

- Shear strain/ maximum shear strain

$$\gamma_{12i} = \varepsilon_{xi} - \varepsilon_{yi}$$

68

$$\gamma_{12}^m = \min \begin{cases} 5\% \\ \gamma_{12i \ at \ maximum \ shear \ stress} \end{cases}$$

69

Where:

γ_{12i} = engineering shear strain at ith data point;

ε_{xi} = longitudinal normal strain at ith data point;

ε_{yi} = lateral normal strain at ith data point;

γ_{12}^m = maximum engineering shear strain.

- Shear chord modulus

The chord shear modulus is to be calculated taking a 4000±200 $\mu\varepsilon$ engineering shear strain range, starting with the lower strain point in the range of 1500 to 2500 $\mu\varepsilon$.

$$G^{chord} = \frac{\Delta\tau_{12}}{\Delta\gamma_{12}}$$

(70)

Where:

G^{chord} = shear chord modulus of elasticity, [GPa];

$\Delta\tau_{12}$ = difference in applied engineering shear stress between the two shear strain points, [MPa]

$\Delta\gamma_{12}$ = difference between the two engineering shear strain points (nominally 0.004).

- Statistics refer to D3039/D3039M.

3.3.4. D7136/D7136M – 15

This test method [42] determines the damage resistance of multidirectional polymer matrix composite laminated plates subjected to a drop-weight impact event. It is important to notice that the damage resistance properties generated by this test method are highly dependent upon several factors, which include specimen geometry, layup, impactor geometry, impactor mass, impact force, impact energy, and boundary conditions. For this reason, the results are generally not scalable to other

configurations, and are particular to the combination of geometric and physical conditions tested.

The properties obtained using this test method can provide guidance regarding anticipated damage resistance capability of composite structures of similar material, thickness, stacking sequence and so on.

For woven fabric composites the laminate overall thickness should be as near as possible to 5 mm. The specimen dimensions are 100x150 mm and impact location is at the center of the panel.

Before testing, if possible, inspect specimens by NDI in order to detect flaws of defects which may exist prior to impact testing. More important, NDI should be performed also after tests to better understand the damage response of the materials.

Damage modes and extend of damage for each specimen, and surface(s) and location(s) at which the damage modes are observed, must be recorded. More than one damage mode may be present contemporary. In the figures below indications about measuring extent of damage and commonly observed damage modes are illustrated.
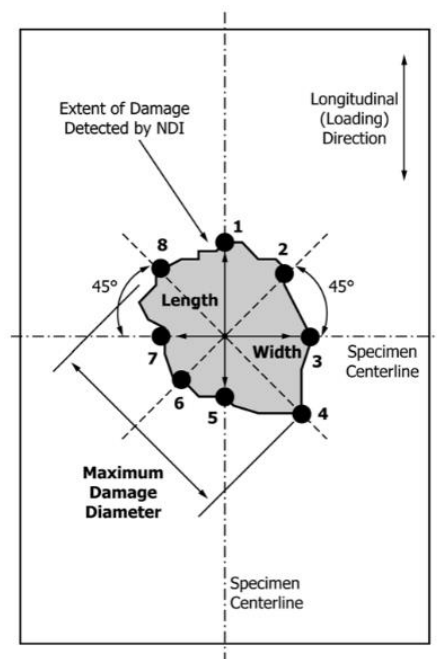
Figure 3-15: measurement of extent of damage.
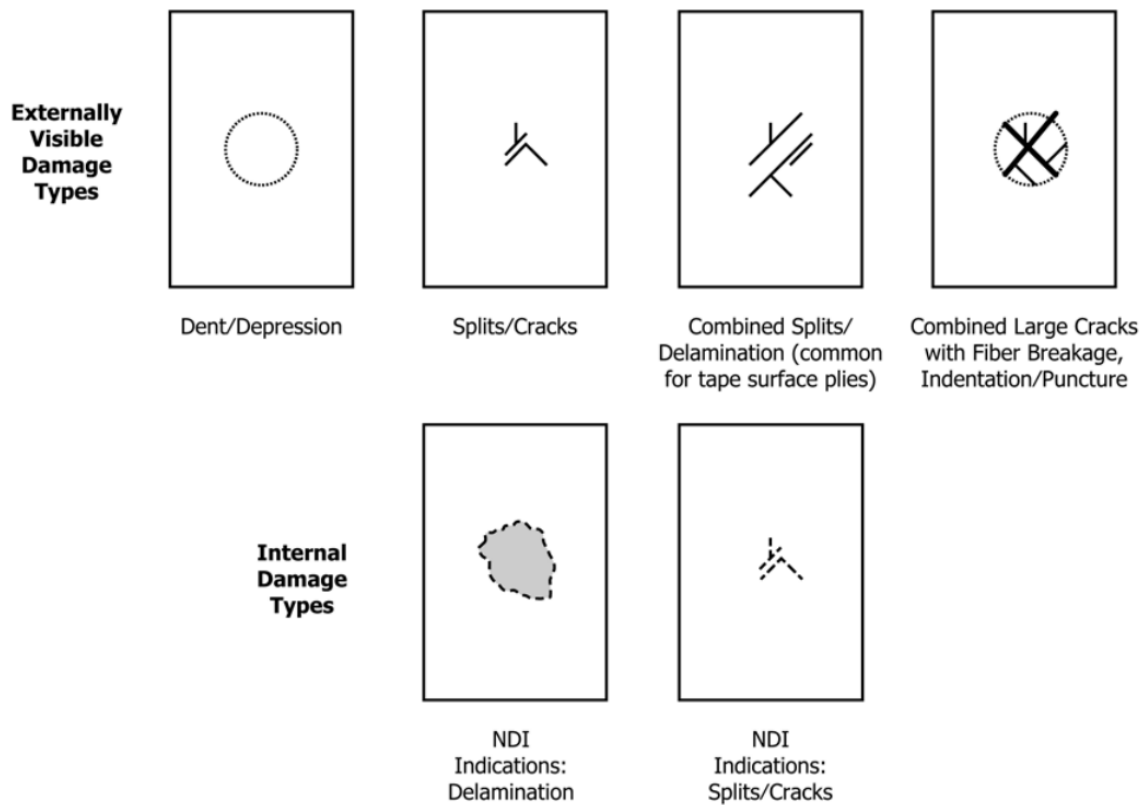
Figure 3-16: damage modes from out-of-plane drop-wight impact.

Following values are automatically calculated by the machine:

- Impact velocity

- Impact energy

- Impact force

Statistics should be calculated as well using same equations showed in the previous test standards.

3.4. Characterization tests results

For the material characterization, for both glass (G8) and Kevlar (K5) laminates, the number of specimens per test available were (Figure 3-16):

- 5 tensile specimens in the transverse direction;

- 4 tensile specimens in the longitudinal direction;

- 6 compressive specimens (3 for each direction);

- 4 shear specimens.
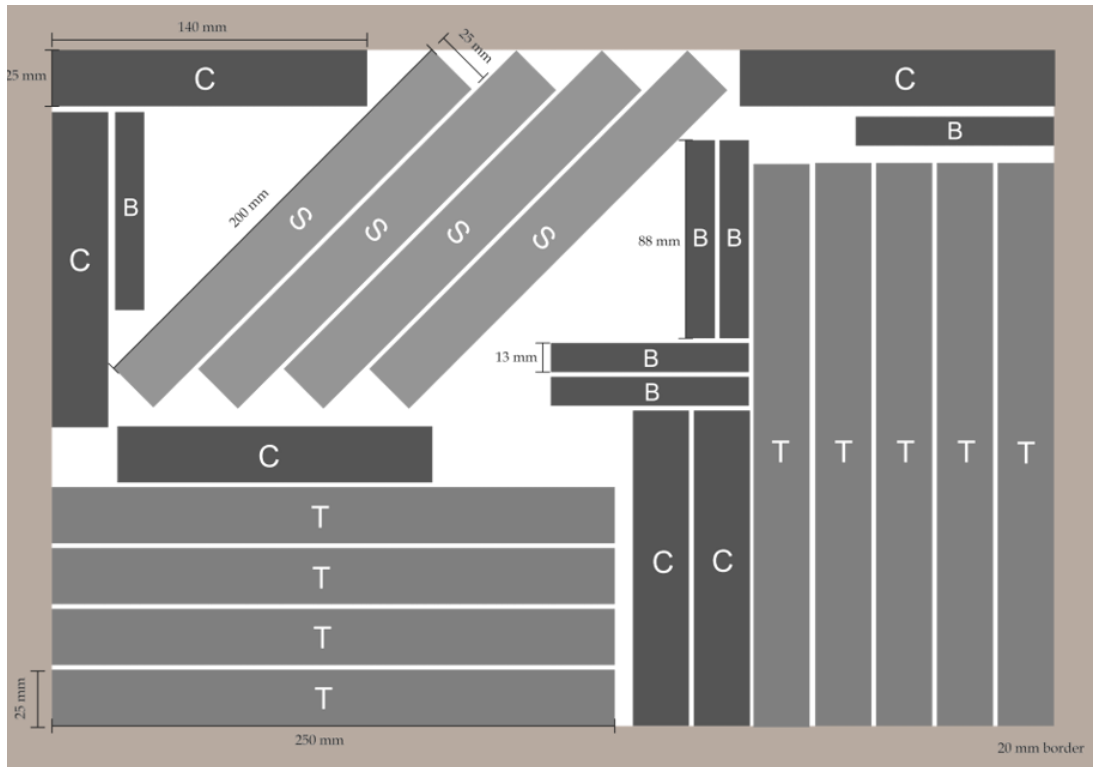
Figure 3-17: scheme for the cutting of the samples for testing.

3.4.1. Tensile tests

Tests were performed following the ASTM D3039/D3039M standard. Previous to the tensile tests, the cross section area at gage section of each sample was calculated. As tabs are not specifically required by the standards for this kind of laminate, in the first trial of tests all the available specimens were to be tested without their addition. Failure of the specimens during the tests was observed all at the clamping site. Tests were interrupted and it was decided to add tabs to the remaining samples before proceeding. The objective of the addition of tabs was to move the failure location closer to the gage section, to obtain more reliable and appropriate results. In total 3 glass and 4 Kevlar samples were tested without tabs, which can be observed after testing in Figure 3-18.

a)   b)

Figure 3-18: failure location of (a) glass and (b) Kevlar samples at clamping cite.

Aluminum tabs were prepared according to standards with dimensions of 25x50 mm and then adhesively attached to the remaining samples (Figure 3-19).

a)

b)
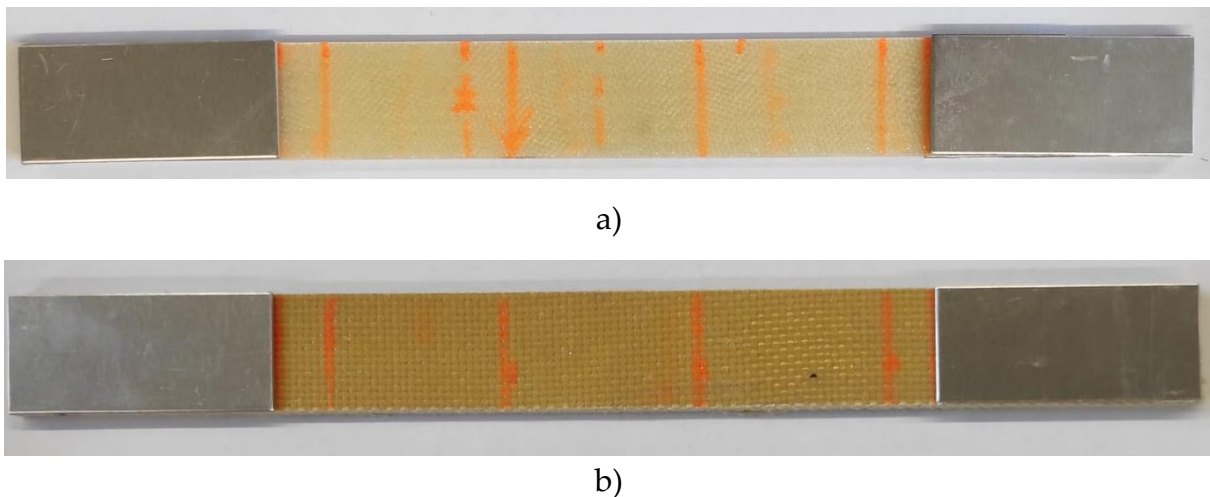
Figure 3-19: samples after addition of tabs. (a) Glass; (b) Kevlar.

After adding tabs to the specimens, the tensile tests were completed. It was observed an improvement on the failure mode of the specimens and its location for most of the glass samples (Figure 3-20), while for Kevlar ones almost no difference was perceived before and after. On the other side, for what concern the measured properties of the composite specimens from the tests, results did not show significant differences in the two different configurations, even for the glass specimens. For that reason, the results obtained after the addition of tabs were analyzed together with results obtained from the first trial of tests. Results were then distinguished only according to the directions of the samples considered (longitudinal and transversal). In Figure 3-20 failure location on the tested glass samples with tabs addition is shown.
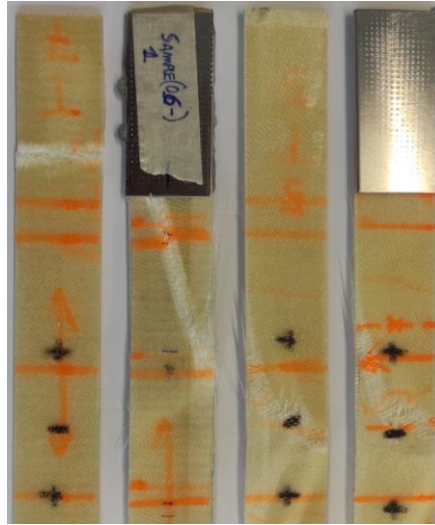
Figure 3-20: picture of glass specimens with tabs showing variation of the failure location.

Among the nine tensile specimens per type, one each was tested with the addition of strain gages to also measure the transverse strain during the deformation of the specimen, necessary to calculate the Poisson ratio of the laminate. In that case statistic calculation was not possible as only one sample each material was tested with strain gages.

3.4.1.1. Glass composites

The testing speed was set initially to 5mm/min. The first specimen tested, G1(T), failed almost immediately and in correspondence to the clamping cite. It was decided to decrease the load speed to the suggested value from the standard, and the remaining glass samples were all tested with a constant displacement rate of 2mm/min. Grip pressure was set to 5 MPa. Cross section area at gage section of samples is shown in Table 11.

Sample	Thickness [mm]	Width [mm]	A [mm²]
G1(T)	2.08	25.01	52.02
G2(L)	2.11	25.15	53.07
G3(T)	2.05	25.12	51.5
G4(L)	2.10	25.8	54.18
G5(T)	2.01	25.4	51.05
G6(L)	2.00	25.2	50.4
G7(T)	2.00	25.3	50.6

G8(L)	2.00	25.12	50.24
G9(T)	2.04	25.28	51.57

Table 11: glass samples cross section dimensions and area.

In the following, graphical and numerical results are shown for specimens first in longitudinal (Table 12) and then in the transversal (Table 13) direction. The stress-strain curves, represented in Figure 3-21, show a brittle-like behavior of the glass composite samples: the material shows an elastic trend till it reaches its maximum stress value before sudden collapse of the specimen.

Longitudinal direction samples	E [MPa]	Maximum stress [MPa]	Maximum strain [mm/mm]
G2(L)	18988.74	338.04	0.0182
G4(L)	17759.00	414.17	0.0242
G6(L)	18260.00	286.02	0.0161
G8(L)	18188.42	432.55	0.0242

Table 12: elastic modulus, maximum stress and strain at rupture of longitudinal glass samples.

Transversal direction samples	E [MPa]	Maximum stress [MPa]	Maximum strain [mm/mm]
G1(T)	13591.80	264.32	0.0198
G3(T)	17272.05	303.03	0.0178
G5(T)	16892.50	349.94	0.0229
G7(T)	17097.50	360.62	0.0213
G9(T)	18161.47	286.02	0.0161

Table 13: glass samples in longitudinal direction elastic modulus, maximum stress and strain at failure.
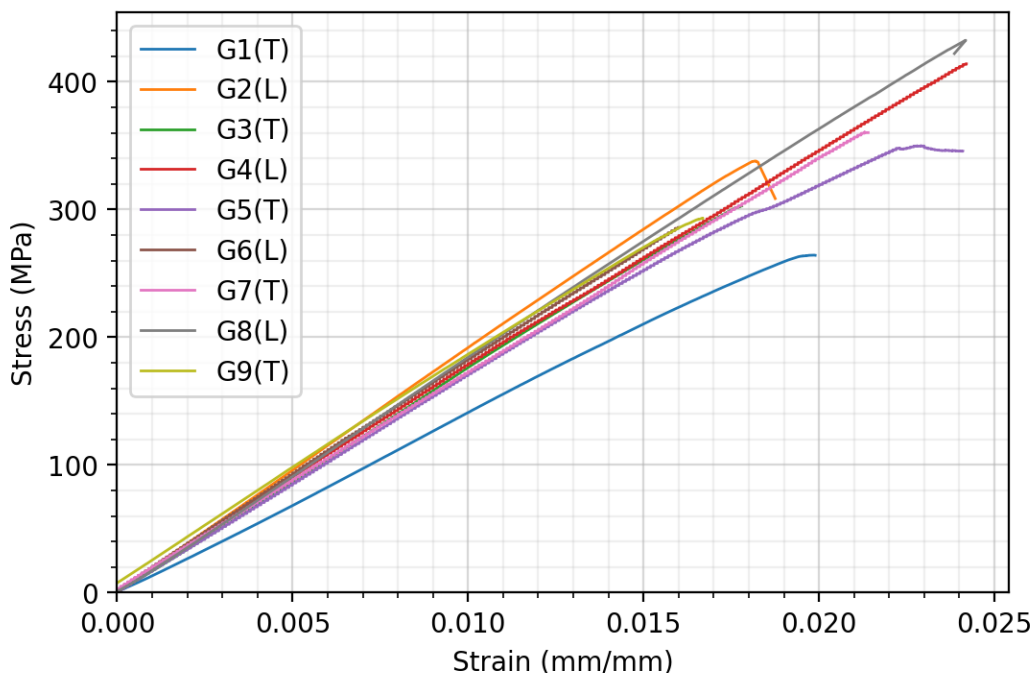
Figure 3-21: stress-strain curves of all tested glass samples.

Statistic results for Young's modulus, maximum stress and maximum strain at failure are shown respectively in Tables 13, 14 and 15. Comparing results for average elastic modulus and maximum stress at failure obtained in the two orthogonal directions, both values are higher in the longitudinal direction. However, the difference between the calculated average values is not so consistent and more samples should be tested to confirm if this kind of behavior is systematic or might depend only on experimental variabilities.

Specimen G1(T) was not considered in the statistic calculations because of the different displacement rate adopted for the test (5mm/min instead of 2mm/min). In fact, observing the curves altogether, its behavior is clearly divergent from the other samples, which instead show pretty much the same trend. This alike behavior is also confirmed from the low coefficient of variation value calculated for the material Young's modulus (Table 14).

Elastic modulus [MPa]	All samples	Longitudinal direction	Transverse direction
Average	17827.46	18299.04	17355.88
SD	706.87	510.26	559.01
CV	3.97	2.79	3.22

Table 14: statistic results for glass samples elastic modulus.

Maximum stress [MPa]	All samples	Longitudinal direction	Transverse direction
Average	347.21	367.70	326.72
SD	54.30	68.11	33.49
CV	15.64	18.52	10.25

Table 15: statistic results for glass samples maximum stress at failure.

Maximum strain [mm/mm]	All samples	Longitudinal direction	Transverse direction
Average	0.0179	0.0207	0.0157
SD	0.0033	0.0042	0.0029
CV	18.77	20.12	18.48

Table 16: statistic results for glass samples maximum strain at failure.

Specimen G8(L), shown in Figure 3-22, was tested with the application of strain gages and transverse strain was detected during test. Poisson ratio was then calculated from the obtained data. Absolute transverse strain versus longitudinal strain curve is shown in Figure 3-23. An absolute longitudinal strain interval of 0.002 was used for the calculation, as suggested by the standard, precisely from 0.001 longitudinal strain to 0.003. The calculated Poisson ratio value is 0.0056.

Figure 3-22: G8(L) tensile specimen with applied strain gages.
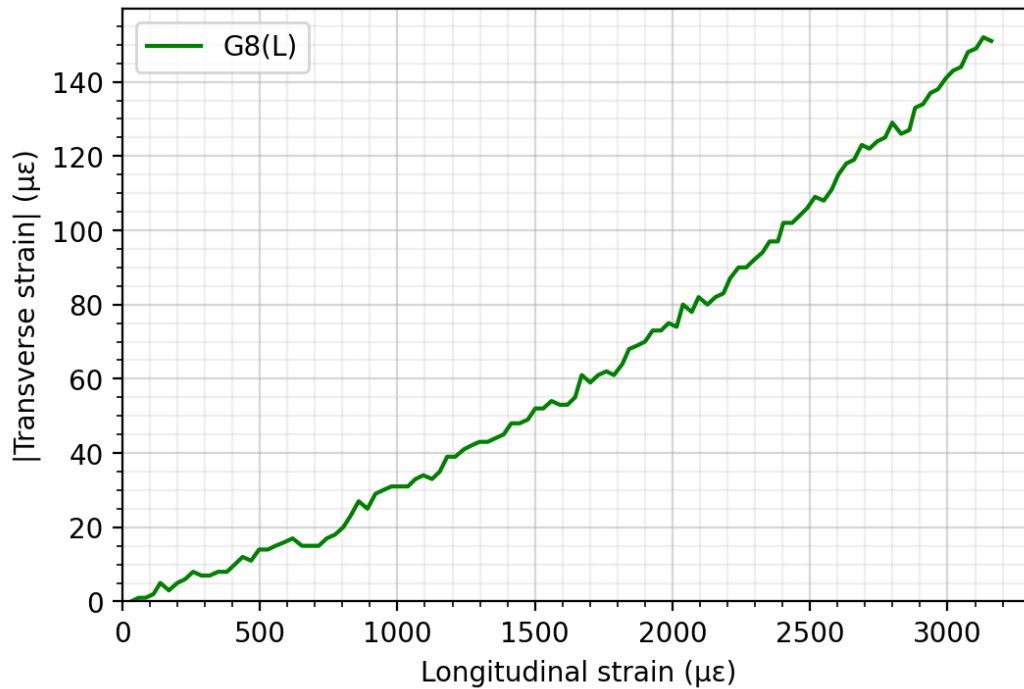
Figure 3-23: absolute transverse strain-longitudinal strain curve of G8(L) tensile specimen.

Respect to data found in literature about glass/epoxy composites the calculated value for the sample is relatively low, which is an indication of the different resin influence on the overall composite behavior. However, no comparison is possible with composites with the same matrix type used in our experimental campaign, as no data was found in the available literature. Also, not even an internal confrontation between same specimens can be done, as this is the only performed test from which this specific property can be calculated. In Figure 3-24 the pictures of the failed specimens is shown. Specimens G1, G2, G3, and G9 failed at the clamping site. Specimens G6 and G8 failure is located inside tabs. In specimens G4, G5, and G7, failure location moved to the gage area showing a long splitting though the specimen length.

G4(L)

G5(T)

G6(L)

G7(T)

G8(L)

G9(T)
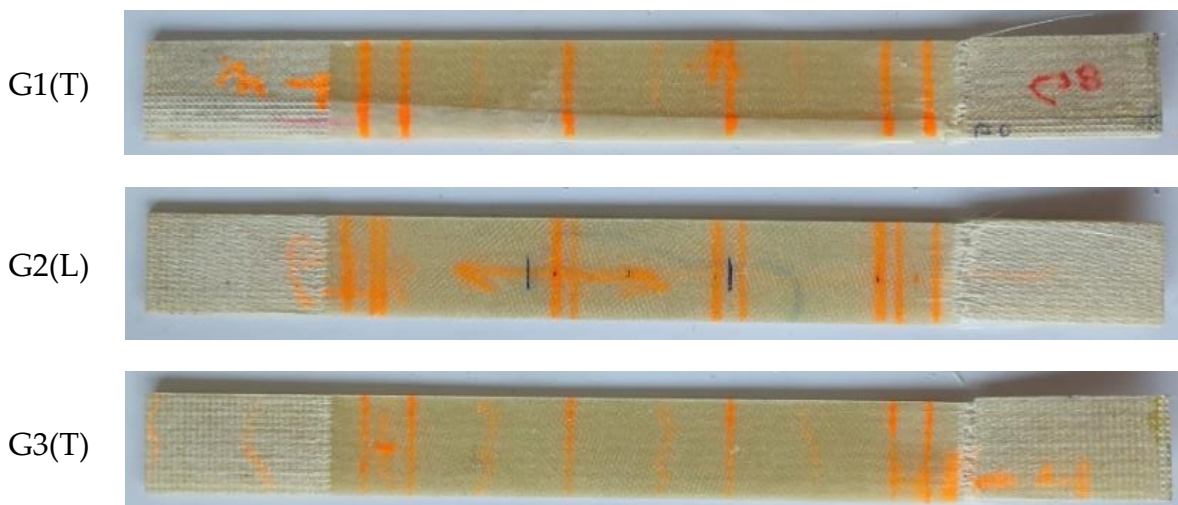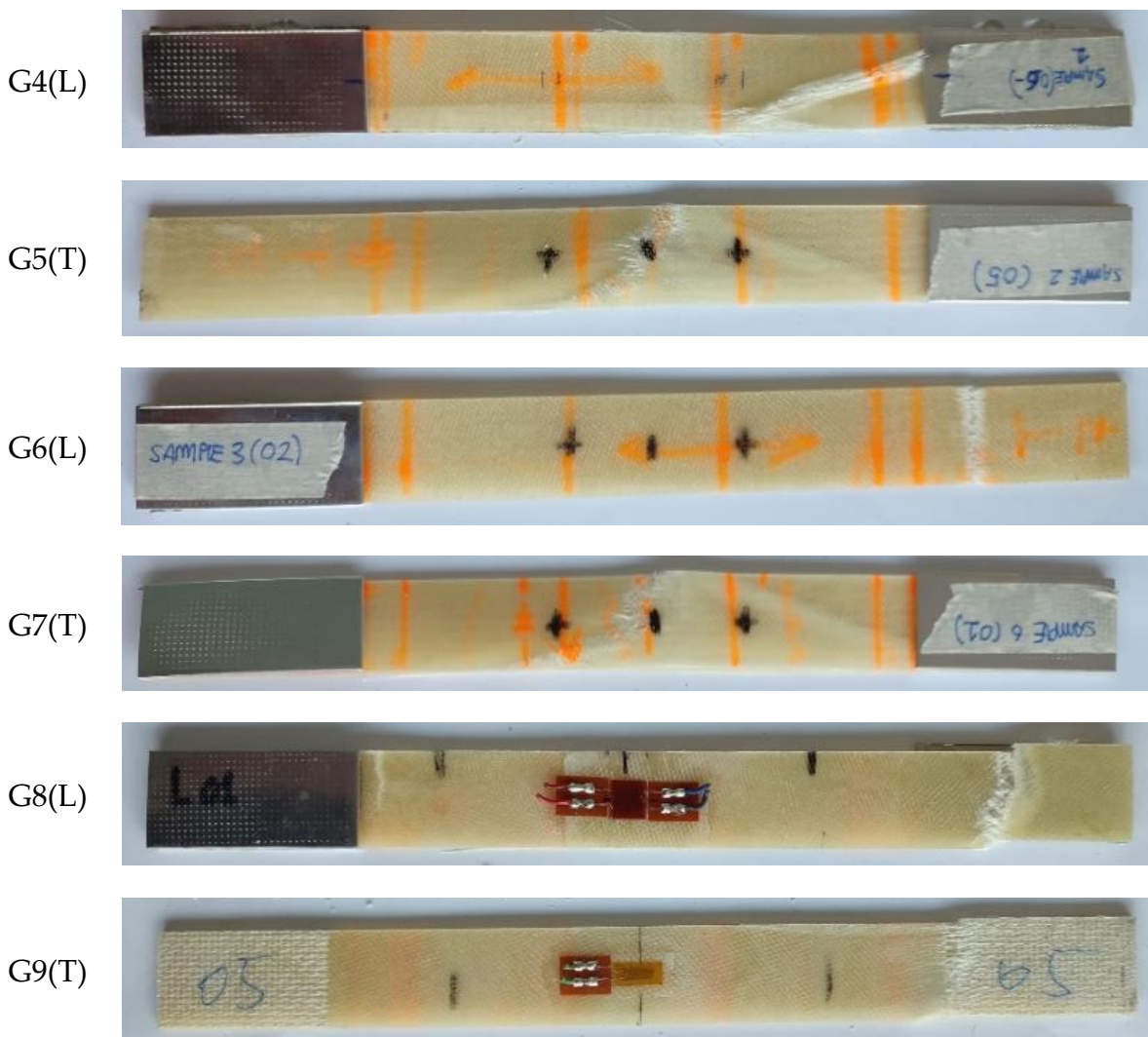
Figure 3-24: failed glass tensile test specimens.

3.4.1.2. Kevlar composites

Kevlar samples were tested at a constant test speed of 4mm/min, slightly higher with respect to the glass samples. The reason was that Kevlar took more time to reach failure and there was the risk it wouldn't break inside the interval time of 10 min given by the standards. Grip pressure was set to 5MPa. The cross-section area at the gage section for each sample is shown in Table 17.

Sample	Thickness [mm]	Width [mm]	A [mm]
K1(L)	2.96	25.11	74.33
K2(L)	2.93	25.24	73.95
K3(T)	2.98	25.16	74.98

K4(L)	2.91	25.46	74.09
K5(T)	3.00	25.00	75.00
K6(T)	2.94	25.50	74.97
K7(T)	2.90	25.50	73.95
K8(L)	2.90	25.65	74.39
K9(T)	2.87	25.49	73.16

Table 17: Kevlar samples cross section dimensions and area.

Elastic modulus, maximum stress and strain are indicated for each sample in Tables 17 and 18, respectively for samples tested in longitudinal and transversal direction. Kevlar samples show a different behavior compared to the glass ones. Stress-strain curves in Figure 3-25 shows an initial modulus with progressively decreasing slope and, a transition area, after which a higher modulus with increasing slope is observed. Following the standards, the interval for calculation of elastic modulus corresponds to the initial part of the curve, from 0.001 to 0.003 strain (0.002 absolute strain interval). These results are indicated as E_{std} in all the following Tables present in this section. However, for the numerical simulation, under the hypothesis of a better representation of the material's behavior during the analysis, a single modulus was calculated, taking the slope of the straight line connecting initial point of curve and point of failure. Those values are also listed in the following as E_{tan}.

Longitudinal direction samples	E_{std} [MPa]	E_{tan} [MPa]	Maximum failure stress [MPa]	Maximum strain [mm/mm]
K1(L)	2677.19	5006.49	277.86	0.0555
K2(L)	2357.95	5117.54	283.08	0.0553
K4(L)	2498.75	5322.81	291.69	0.0548
K8(L)	3068.90	5776.67	319.45	0.0553

Table 18: Kevlar samples in longitudinal direction elastic modulus, maximum stress and strain at failure.

Transversal direction samples	E_{std}[[MPa]	E_{tan} [MPa]	Maximum failure stress [MPa]	Maximum strain [mm/mm]

K3(T)	4046.55	7688.11	297.53	0.0387
K5(T)	3365.0	6527.70	278.08	0.0426
K6(T)	3114.0	8853.65	351.49	0.0397
K7(T)	3849.0	9623.16	353.17	0.0367
K9(T)	4400.0	8409.91	364.99	0.0434

Table 19: Kevlar samples in transverse direction elastic modulus, stress and strain at failure.

Considering the results altogether, it can be observed how Kevlar shows, already from the beginning, a higher elastic modulus when tensioned in the transverse direction. This behavior becomes pretty evident graphically (Figure 3-25) for higher strains, where the two sets of curves for samples tested in material's longitudinal and transverse directions are clearly disposed in two separate groups. Maximum stress at failure also is on average higher in the transverse direction but the difference in that case is negligible.
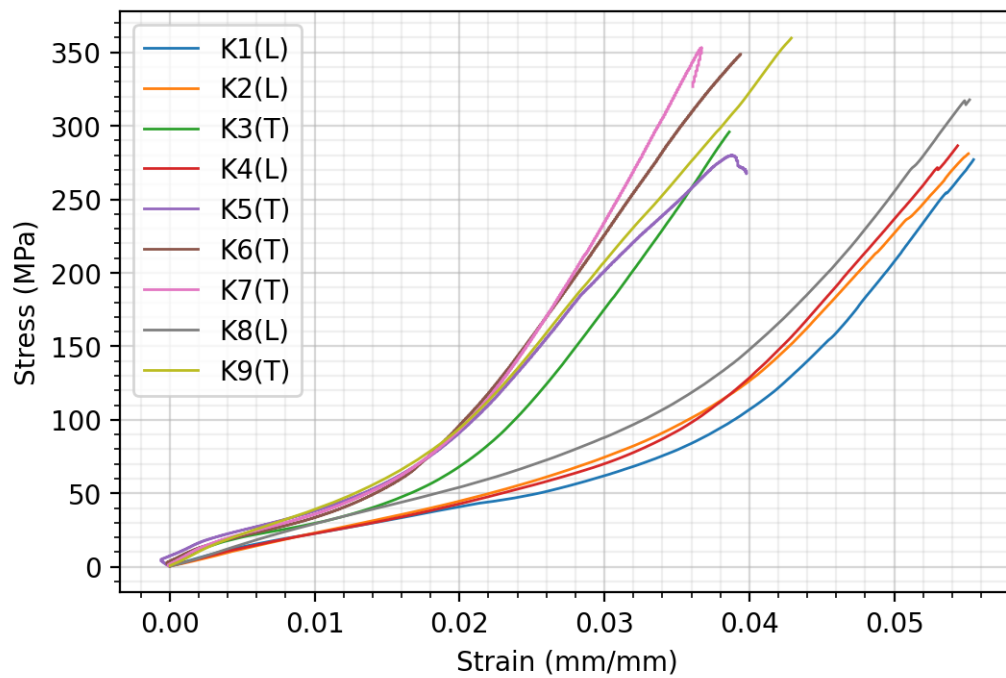
Figure 3-25: stress-strain curves of all tested Kevlar samples.

Statistic results about elastic modulus, maximum stress and strain are shown respectively in Tables 19-20,21, and 22. The deviation in the elastic modulus for the two orthogonal directions is highlighted even more when considering the second method for its calculation (higher values of SD and CV), which takes into consideration also the second part of the curves, where the slope is much increased.

E_{std}[MPa]	All samples	Longitudinal direction	Transverse direction
Average	3264.15	2650.70	3754.91
SD	712.98	307.89	517.89
CV	21.84	11.61	13.79

Table 20: statistic results for Kevlar samples E_{std} elastic modulus.

E_{tan} [MPa]	All samples	Longitudinal direction	Transverse direction
Average	6925.12	5305.88	8220.51
SD	1759.91	340.12	1178.26
CV	26.41	6.41	14.33

Table 21: statistic results for Kevlar samples E_{tan} elastic modulus.

Maximum stress [MPa]	All samples	Longitudinal direction	Transverse direction
Average	313.03	293.00	329.05
SD	35.16	4.63	7.73
CV	11.23	1.58	2.35

Table 22: statistic results for Kevlar samples maximum stress.

Maximum strain [mm/mm]	All samples	Longitudinal direction	Transverse direction
Average	0.0469	0.0552	0.0402
SD	0.0081	0.0003	0.0028
CV	17.38	0.54	6.89

Table 23: statistic results for Kevlar samples maximum strain.

Among the samples, specimen K8(L), which is shown in Figure 3-26, was tested with strain gages and transverse strain was detected. Poisson ratio was calculated as for the

G8(L) specimen, using same longitudinal strain interval. The corresponding Poisson ratio value is 0.36.
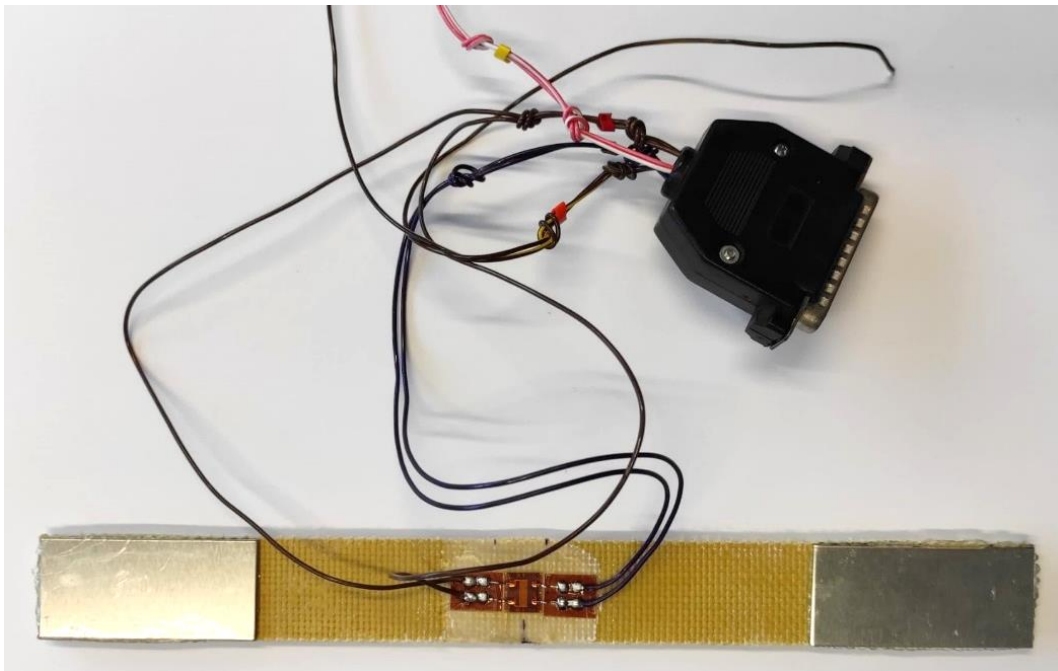
Figure 3-26: K8(L) tensile specimen with applied strain gages.
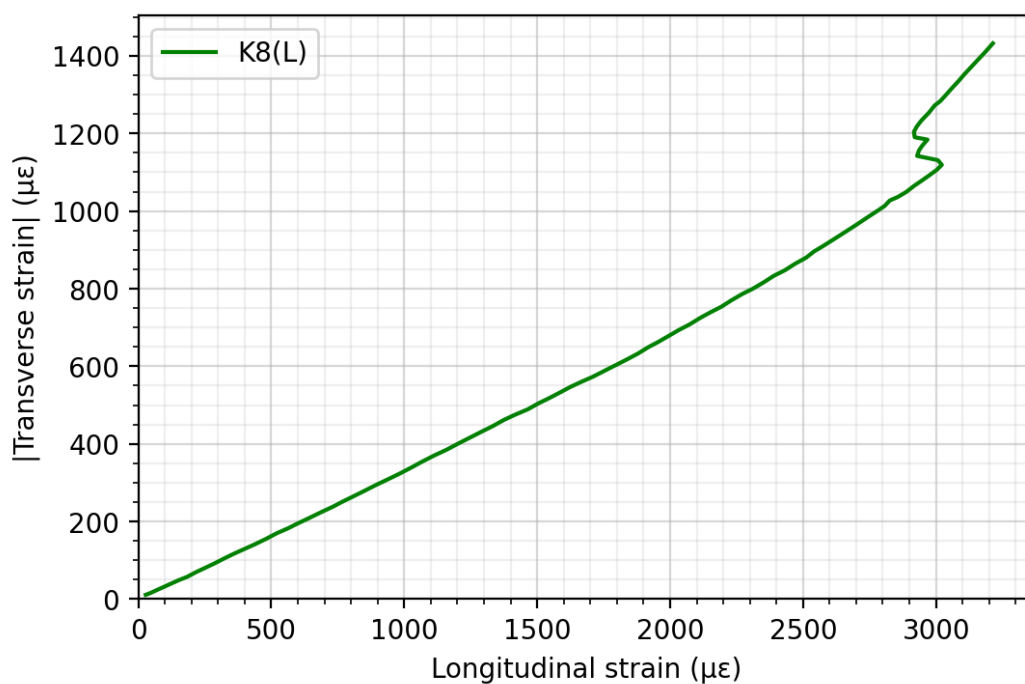
Figure 3-27: absolute transverse strain-longitudinal strain curve of K8(L) tensile specimen.

Contrary to G8(L) Poisson ratio result, in this case the calculated value is consistent with values found in literature for Kevlar/epoxy composites. This difference between glass and Kevlar results could be due to the fact that Kevlar intrinsically tends to absorb much more the resin material with respect to glass fibers. As consequence, it

might be assumed that its final behavior during the test is less affected by the specific resin material, as it could have happened instead for the tested glass specimen. In Figure 3-28 pictures of the failed specimens are shown. Specimens K1,K2,K3,K4 failed at the clamping site. For the remaining specimens location of failure is not readily identified as mixed modes of failure are observed. In all specimens delamination also took place, as evidenced in Figure 3-29.

K8(L)

K9(T)
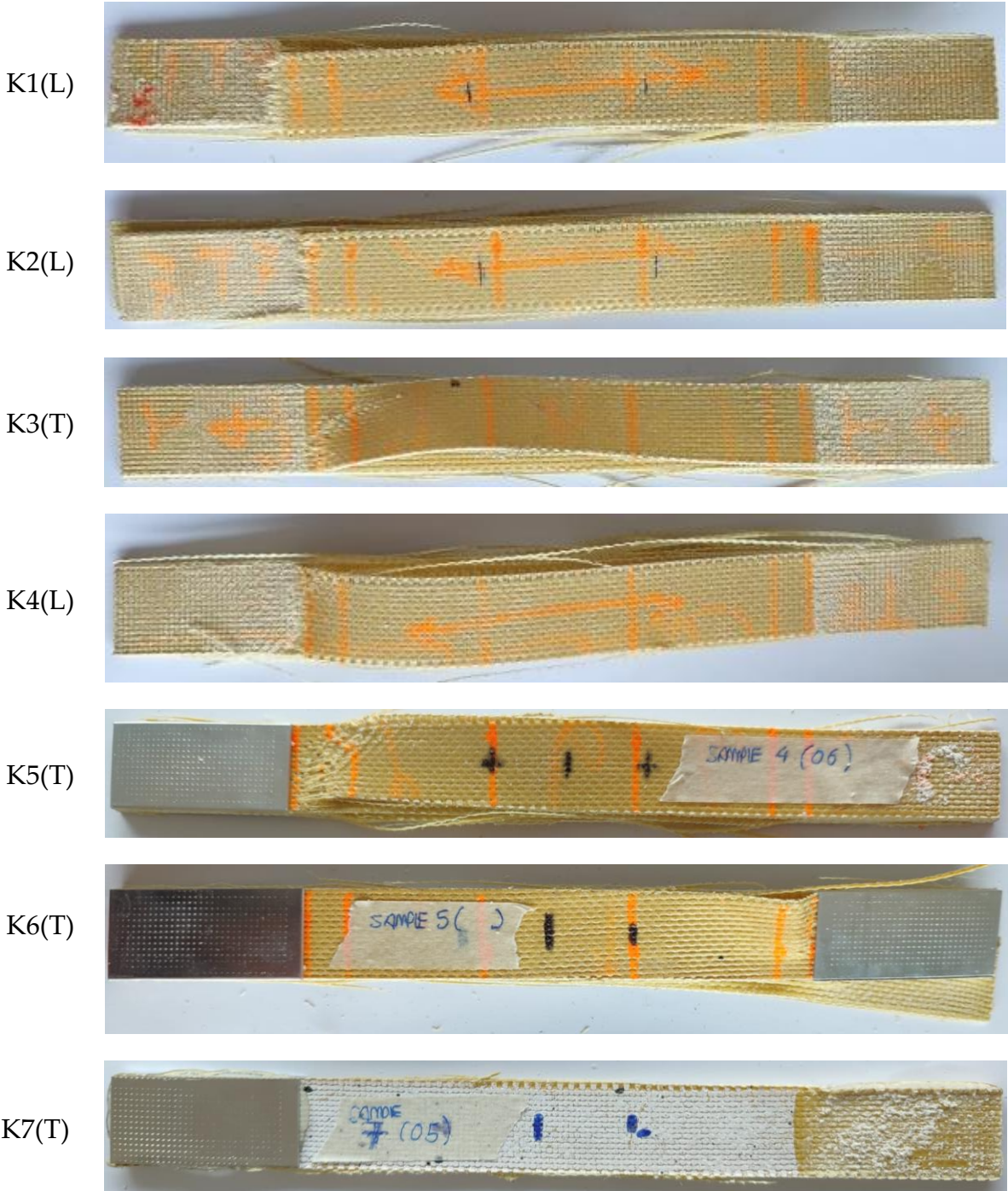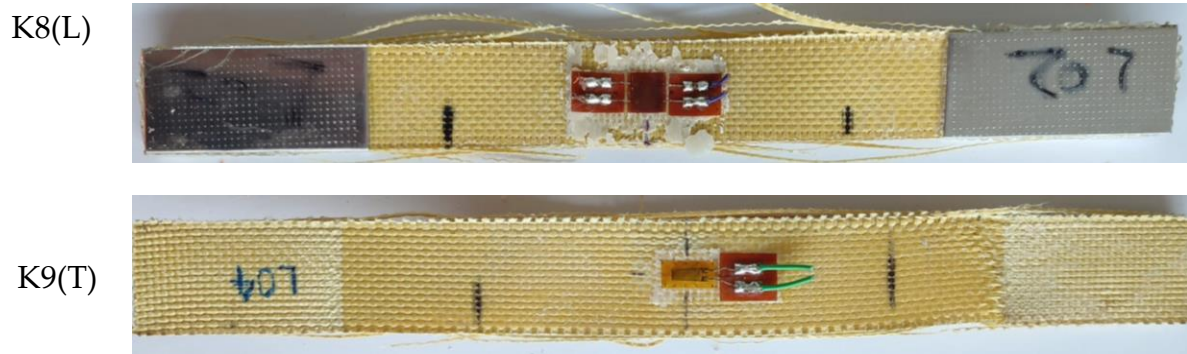
Figure 3-28: failed Kevlar tensile test specimens.

Figure 3-29: side picture of a failed specimen showing delamination.

3.4.2. Compressive tests

Tests were performed following the D3410/D3410M ASTM standard. The minimum selected gage section of the samples of 10 mm length did not allow the compressive tests to be performed using neither strain gages or extensometers. The length of the gage section was determined considering the intrinsic mechanical behavior of the material: for longer gage sections, the risk of instabilities such as buckling to occur, would be increased. Aluminum tabs with standard dimensions of 65x25mm were applied to the samples to be tested, as can be observed in Figure 3-30. For some of the glass specimens, for dimensional related issues after addition of tabs, it was not possible to correctly insert them inside the machine test (two out of six) and so, not all the samples were tested.
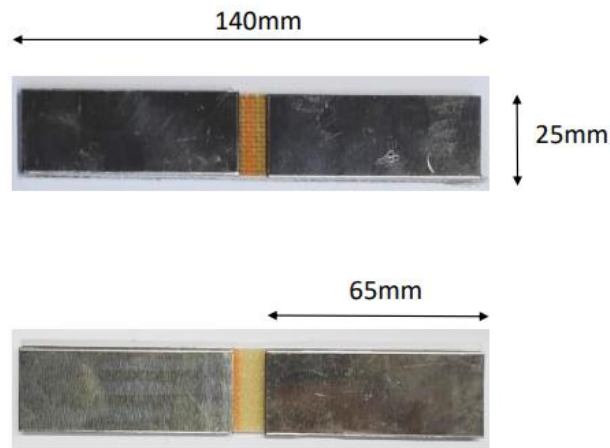
Figure 3-30: Kevlar and glass compressive samples with relative dimensions.

Without extensometers the displacement at the gage section was not measured during the testing. A rough approximation was done initially by considering the elongation of the sample equal to the crosshead displacement. Therefore, results for elastic modulus obtained from the tests were not to be considered reliable. With the available data reported, the only value which was possible to calculate with a certain reliability, was the maximum stress at failure in compression. As an approximation, in the numerical analysis, it was decided thus to use as elastic modulus in compression the same we found from the tensile tests.

Before testing the cross section area was measured at the gage section. Crosshead speed was set to the standard value of 1.5 mm/min both for glass and Kevlar composites.

3.4.2.1. Glass composites

Four glass composite samples were tested in compression: two in the transversal direction and two in the longitudinal direction. In Figure 3-31 a picture of the specimens before test is shown. It is possible to notice from the picture how small the gage section length was respect to the clamping region dimensions. In Table 24 cross section dimensions are reported. Only the value of the maximum stress is here presented for the compressive test, along with the statistics calculation related (Table 25).

Figure 3-31: glass compressive samples previous to testing.

Sample	Thickness [mm]	Width [mm]	A [mm²]	Maximum stress [MPa]
G1(T-c)	2.02	25.25	51.01	35.40
G2(T-c)	2.04	25.24	51.50	40.60
G3(L-c)	2.03	25.30	51.36	38.27
G4(L-c)	2.02	25.27	51.05	36.28

Table 24: glass samples cross-section area and measured maximum stress in compression.

Maximum stress [MPa]	All samples	Longitudinal direction	Transverse direction
AVERAGE	37.64	37.28	38
SD	2.31	1.41	3.68
CV	6.14	3.78	9.68

Table 25: statistic results for glass samples maximum stress in compression.

The measured values of stress at rupture in compression are relatively low respect to values reported in the literature for glass/epoxy composites. Again, as commented for the tensile tests, no direct confrontation is really possible, as the matrix material here is completely different to epoxy matrix materials commonly used. Positive aspects are the low value of coefficient of variation in the results and the mode of failure of the samples. In Figure 3-32 fracture mode of the specimens can be observed. Analyzing

the specimens fracture mode according to the adopted standard for the test, all four samples have broken according to an "acceptable mode of failure and area": though the thickness failure, at tab or in the middle of the gage section. Most important aspect for the fracture to not be considered as an "unacceptable mode of failure" is for the sample not to fail inside the clamping area.
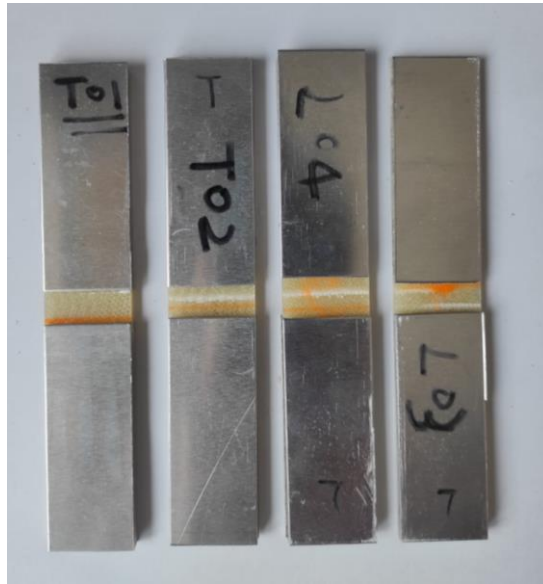
Figure 3-32: glass compressive samples after testing.

3.4.2.2. Kevlar composites

Six Kevlar specimens were subjected to testing: three in the transversal direction and three in the longitudinal direction. In Figure 3-33 a picture of the specimens before test is shown. Tables in the following contain values of the cross section dimensions, maximum stress (Table 26) and the relative statistic calculation (Table 27).
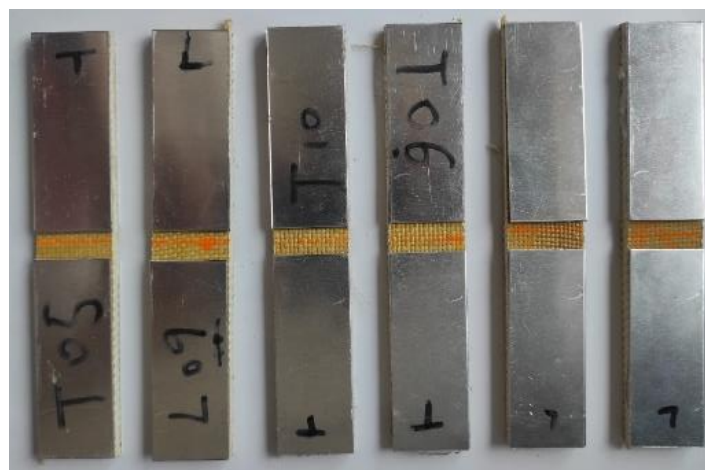
Figure 3-33: Kevlar compressive samples previous to testing.

Sample	Thickness [mm]	Width [mm]	A [mm2]	Maximum stress [MPa]

K1(T-c)	3.01	25.24	75.97	17.23
K2(T-c)	3.06	25.41	77.75	10.82
K3(L-c)	2.94	25.39	74.65	10.01
K4(L-c)	3.39	25.32	85.83	6.82
K5(L-c)	3.40	25.34	86.16	7.22
K6(T-c)	3.11	25.35	78.84	11.42

Table 26: Kevlar samples cross-section area and measured maximum stress in compression.

Maximum stress [MPa]	All samples	Longitudinal direction	Transverse direction
AVERAGE	10.58	8.01	13.15
SD	3.76	1.74	3.54
CV	35.55	21.69	26.93

Table 27: statistic results for Kevlar samples maximum stress in compression.

Values of maximum stress at failure in compression are relatively low for the Kevlar specimens respect to literature values for Kevlar/epoxy composites, as was also observed for the glass samples. Moreover, the coefficient of variation is pretty high, which might be an indication of the experimental variability of the performed tests. Related to this point, in fact, it must be noticed how Kevlar specimens showed some instabilities during the testing, as can be seen for example in Figure 3-34. Even though this behavior, which may have influenced the results, the measured values are reasonably consistent among them and are then used in the numerical simulations. A picture of the specimens after failure is not reported because the fracture mode and location is not clearly visible on the specimens.
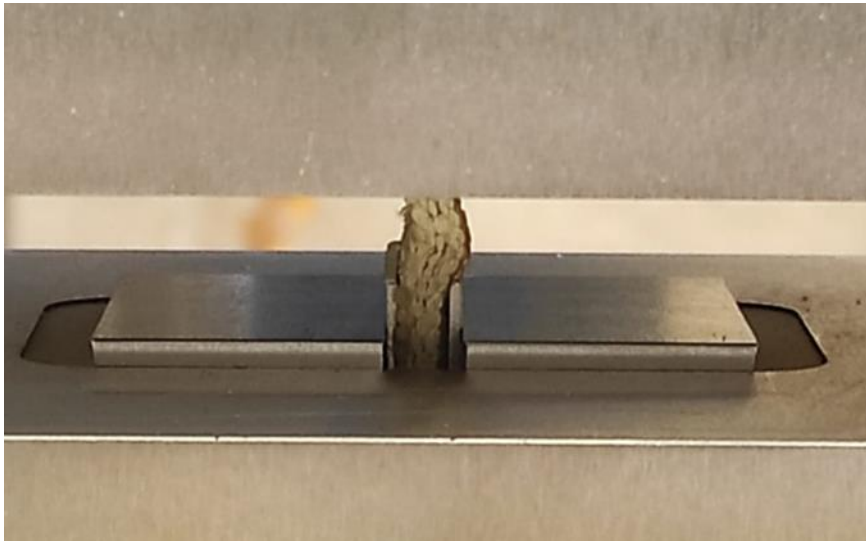
Figure 3-34: buckling of a Kevlar specimen during compressive testing.

3.4.3. Shear tests

Tests were performed following the D3518/D3518M – 13 standard. The machine used for the tests is the same adopted for the tensile ones. For shear tests tabs were not required. For the two different laminates, three out of the four available samples were tested applying a continuous head displacement rate. Among those, only one specimen per material was tested with application of strain gages. The remaining one sample per material was subjected to a cyclic shear test, specifically necessary for derivation of properties required in the numerical simulations, as described in detail in Section 2.2.

3.4.3.1. Glass composites

The three curves in Figure 3-35 represent the data collected for the samples tested with the extensometer. Specimen G4(S) was tested also with strain gages, but for comparison with the other specimens, also results concerning the longitudinal stress-strain are reported. The crosshead speed for all glass specimens was set to 6mm/min. Longitudinal strain was measured but not the transversal one, so it was not possible to derive shear stress nor shear strain from this data. In Table 27 the measures of the cross section area of all samples are reported.

Sample	Thickness [mm]	Width [mm]	A [mm2]
G1(S)	2.04	25.31	51.63
G2(S)	2.07	25.29	52.35

| G3(S) | 2.00 | 25.20 | 50.40 |
| G4(S) | 2.01 | 25.41 | 51.07 |

Table 28: shear glass samples cross section dimensions and area.
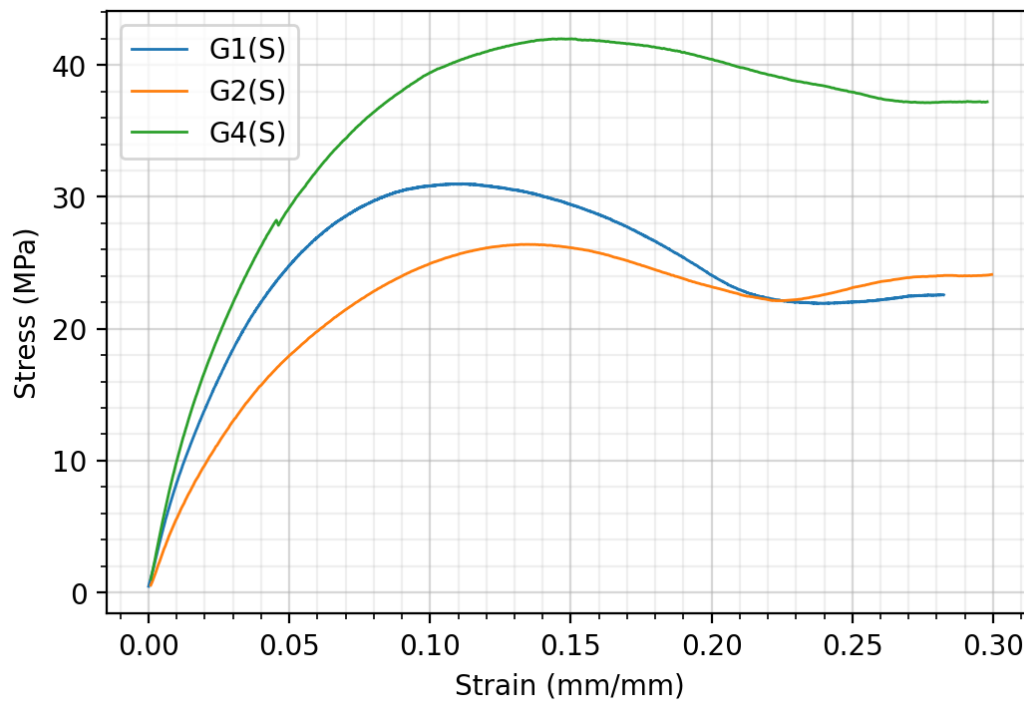
Figure 3-35: stress-strain curves of shear tested glass samples.

From the specimen G3(S), tested with the application of the strain gage (Figure 3-36), it was possible to derive the shear stress and the shear strain points for the building of the shear stress-strain curve, shown in Figure 3-37. From that, the shear modulus of the specimen was calculated, besides maximum shear stress and maximum shear strain at failure. For the calculation of the shear modulus, as indicated in the standard, an absolute strain interval of 0.002 was considered, from 0.001 to 0.003 shear strain. The resulting shear modulus for the glass composite is equal to 523.4 MPa, the maximum stress 11.99 MPa, and the shear strain 0.0379.

a)   b)
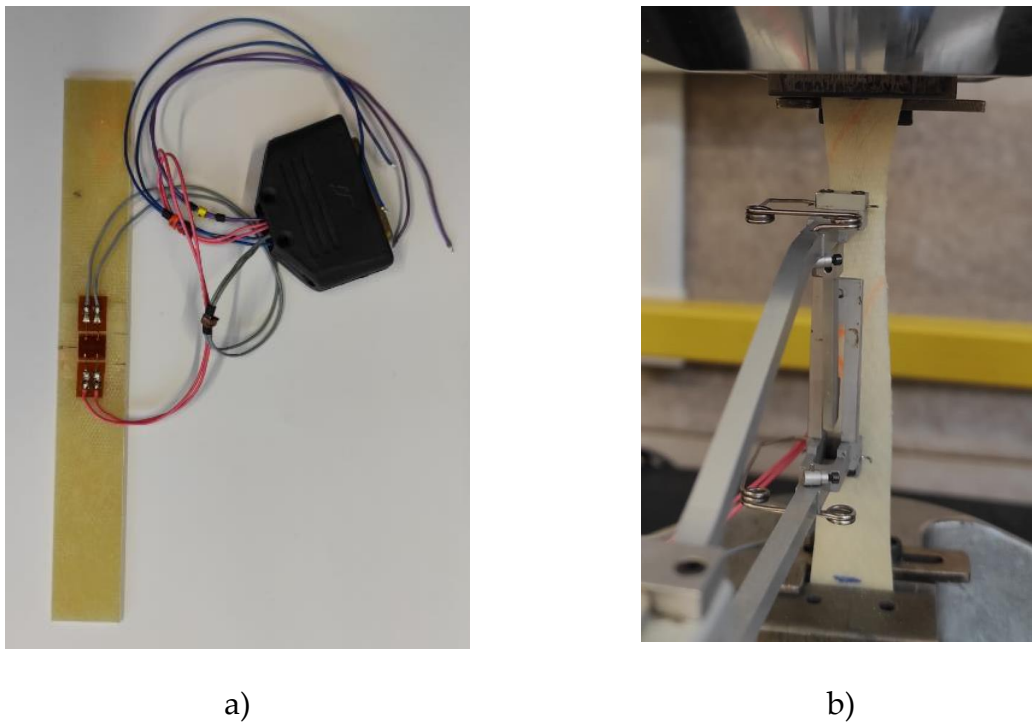
Figure 3-36: G4(S) shear specimen (a) previous to test and (b) after testing.
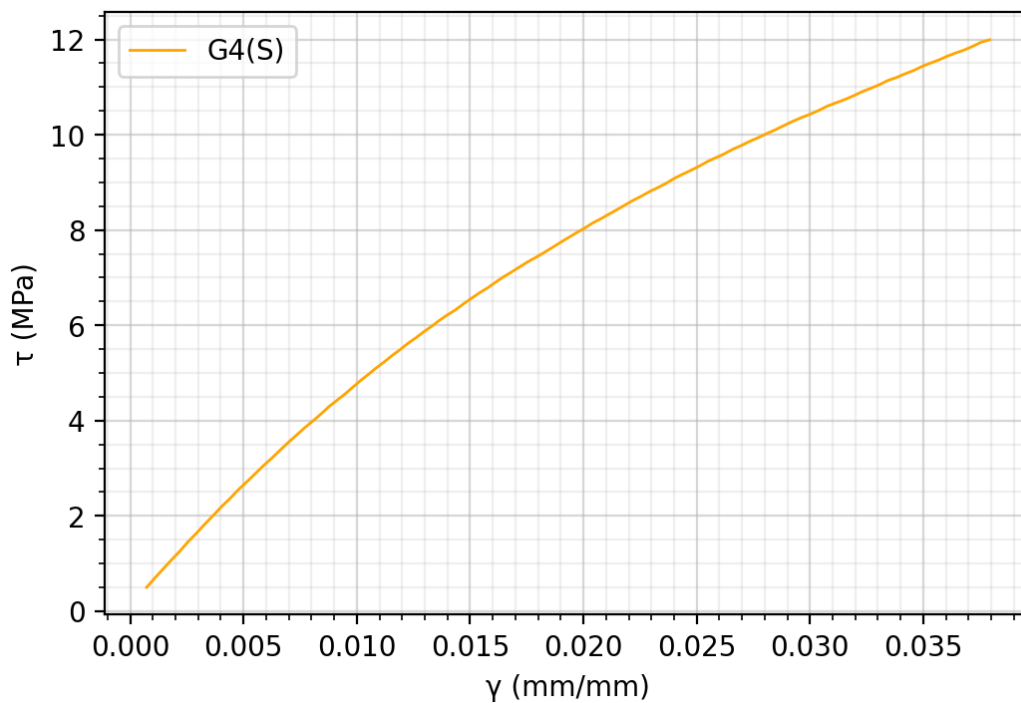
Figure 3-37: shear stress-shear strain curve for G4(S) glass specimen.

From the cyclic shear test performed on specimen G3(S) properties necessary for the material definition in the numerical analysis were derived: shear damage parameters

and shear plasticity coefficients, as described in Section 2.2. In total six loading-unloading cycles were performed, with loading cycles proceeding by intervals of 0.005 strain. Results of this calculation are shown in subsection 3.4.4, where all material properties calculated from the experimental tests are listed.
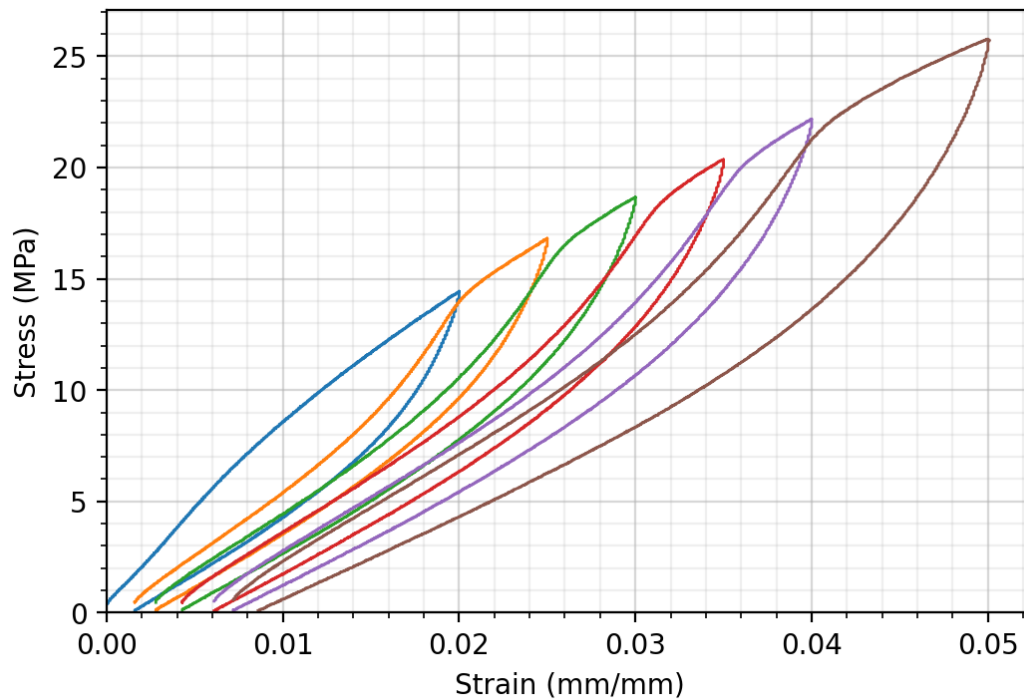
Figure 3-38: cyclic shear test of G3(S) specimen.

In Figure 3-39 specimens after the shear test are shown, and an additional side picture of specimen G1 is reported in Figure 3-40, which shows the flexibility of the specimens after the test.
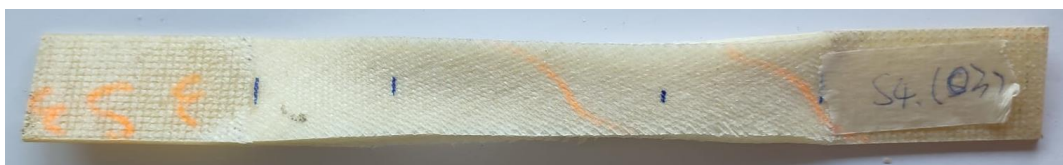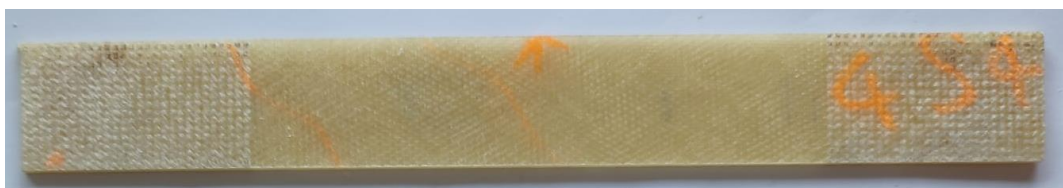
G4(S)
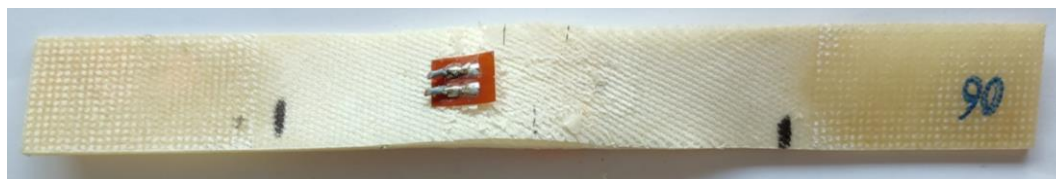
Figure 3-39: glass shear samples after testing.

Figure 3-40: side picture of sample G1(S).

3.4.3.2. Kevlar composites

Same considerations done for the glass shear specimens can be extended for the Kevlar specimens. Table 28 reports the cross-section dimensions of the shear specimens, and in Figure 3-41 the stress-strain curves obtained from the tests are represented.

Sample	Thickness [mm]	Width [mm]	A [mm2]
K1(S)	2.97	25.12	74.61
K2(S)	3.14	25.08	78.75
K3(S)	3.00	25.20	75.60
K4(S)	3.25	25.27	82.13

Table 29: shear Kevlar samples cross section dimensions and area.
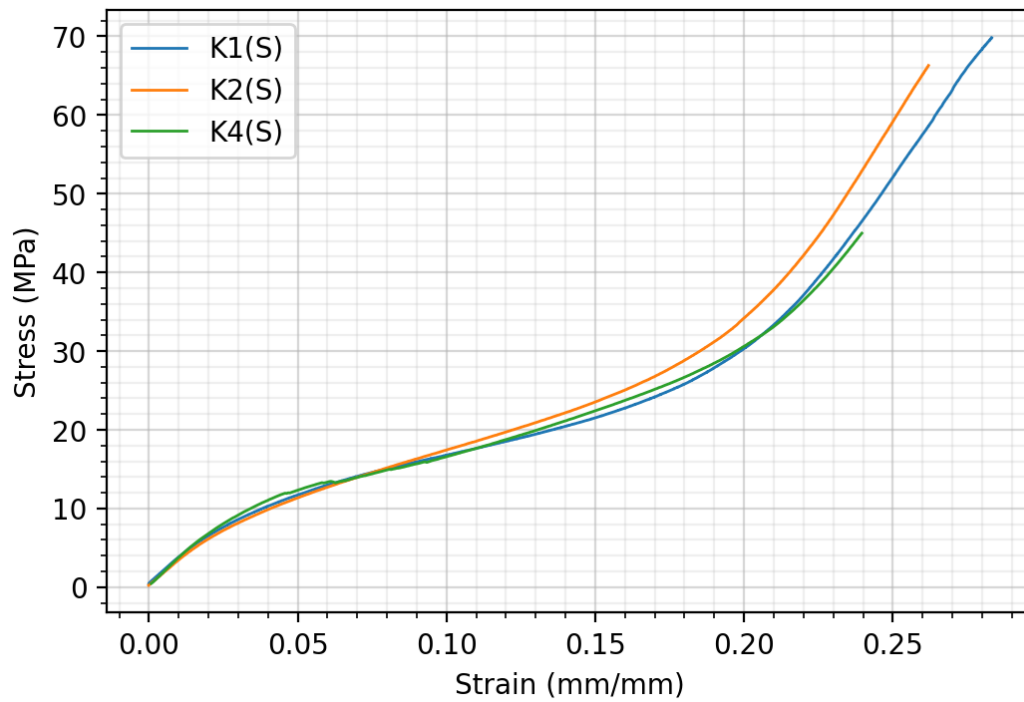
Figure 3-41: stress-strain curves of shear tested Kevlar samples.

Specimen K4(S), shown in Figure 3-42, was tested with application of strain gages and from the obtained data shear stresses and shear strain were calculated. From the resulting shear stress-shear strain curve (Figure 3-43) a shear modulus value equal to 357.107 MPa was found, maximum shear stress equal to 5.97 MPa, and corresponding shear strain of 0.0293. Interval adopted for calculation of shear modulus is the same reported previously for the glass shear specimen.

94

a)   b)
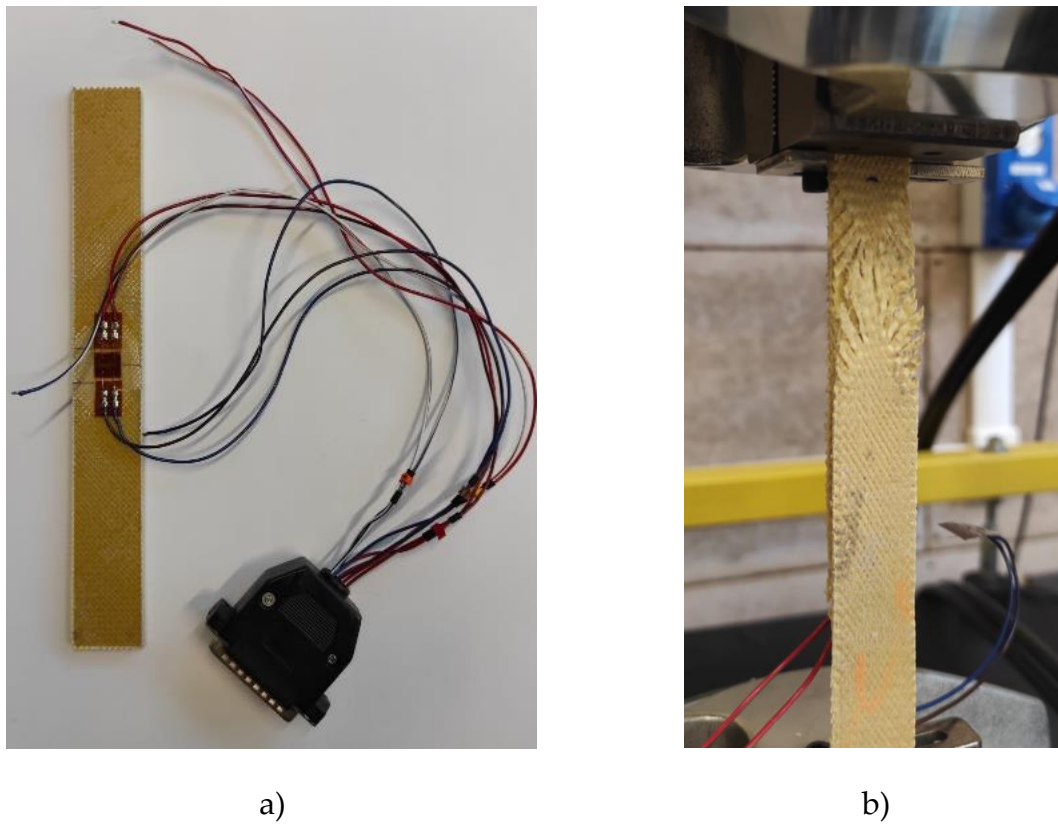
Figure 3-42: K4(S) shear specimen (a) previous to test and (b) after testing.
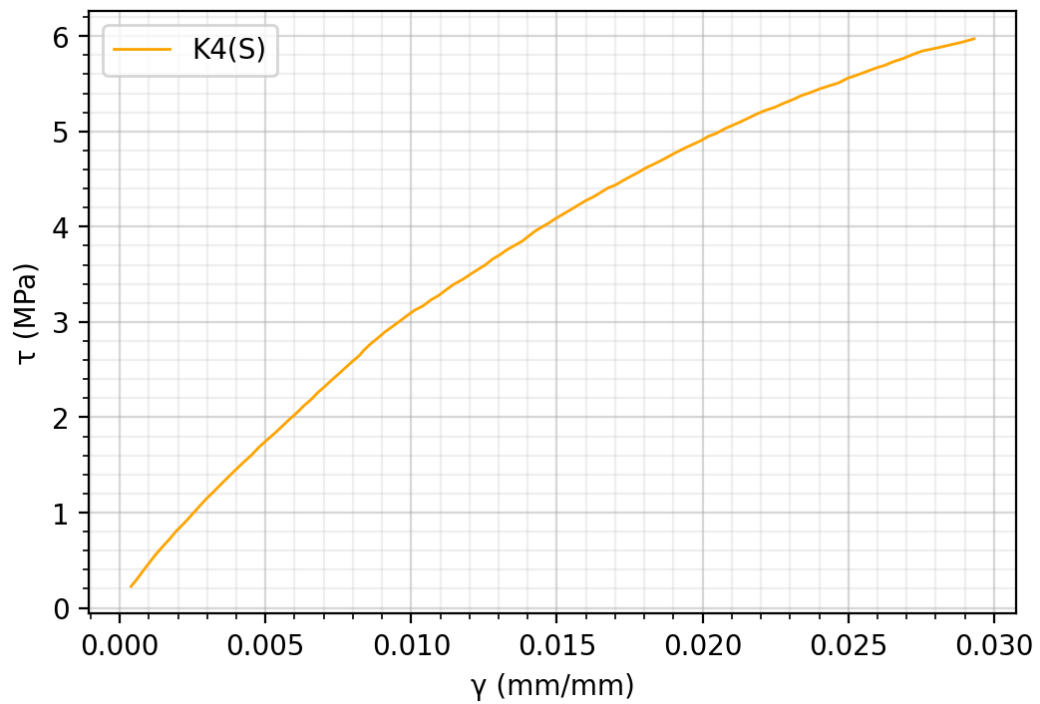
Figure 3-43: shear stress-shear strain curve for K4(S) kevlar specimen.

In Figure 3-44 the cyclic shear test curve of specimen K3(S) is shown. As described for the glass composite samples, shear damage coefficients and shear plasticity coefficients were derived from the test. The resulting parameters are shown in the following subsection.
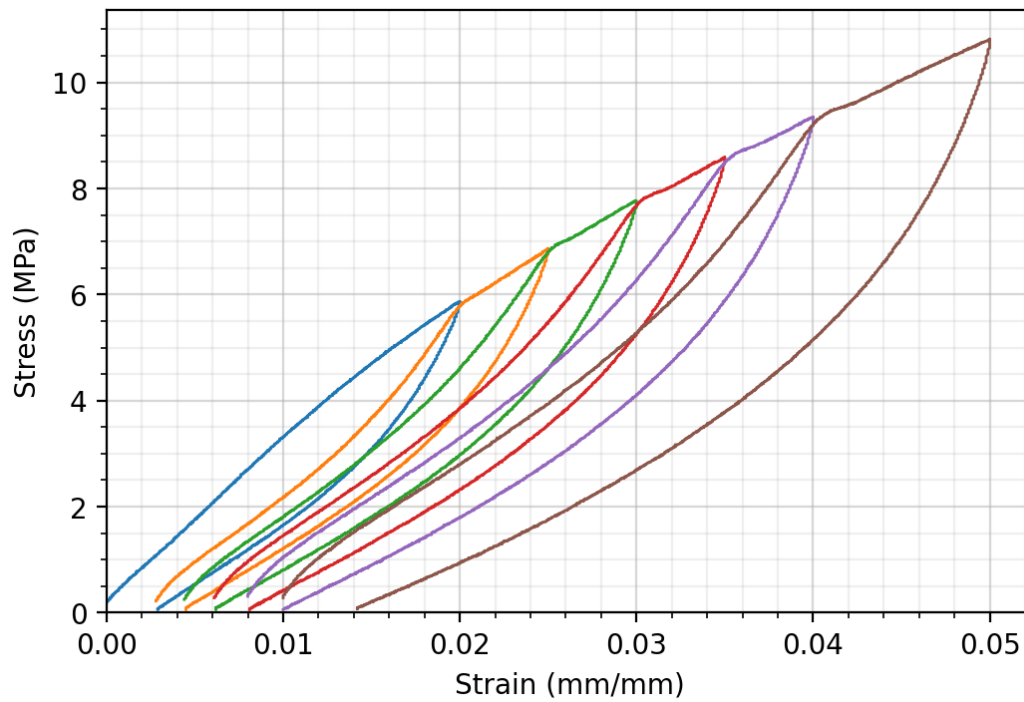
Figure 3-44: cyclic shear test of K3(S) specimen.

In Figure 3-45 the pictures of the tested samples are reported.
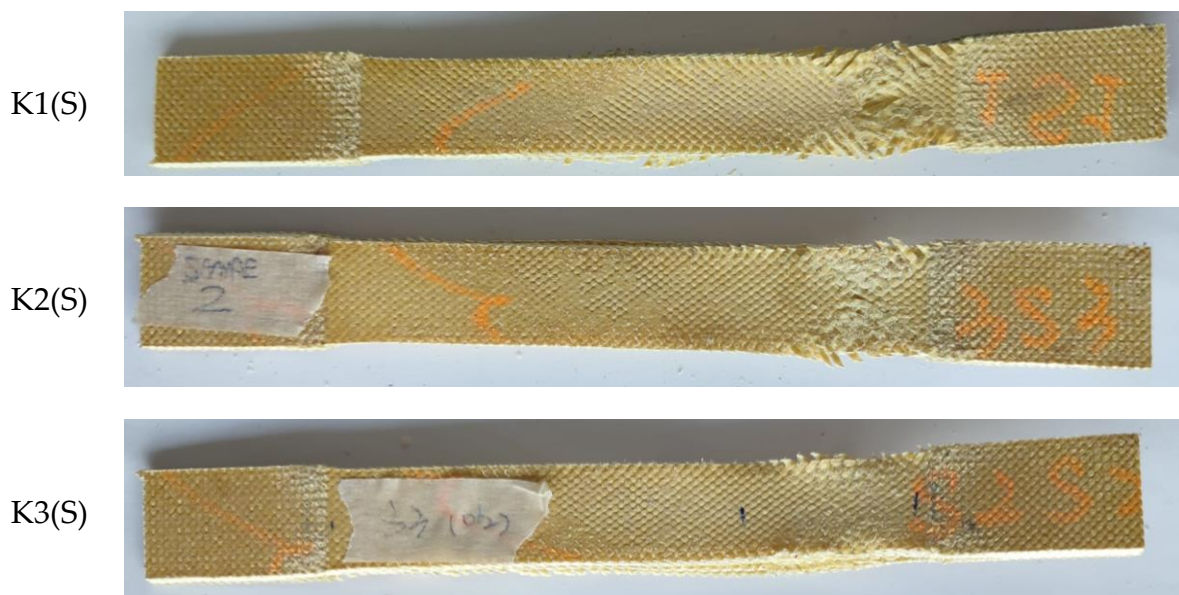
K4(S)

Figure 3-45: Kevlar shear samples after testing.

3.5. Impact tests

Impact tests were performed according to the D7136/D7136M – 15 standard. The laminates selected for the low velocity impact tests were:

- G16
- K8
- [G2K]2S
- [G4K2]S
- [K2G4]S

For each configuration 9 specimens were available (Figure 3-46). Specimens have surface dimensions of 100x150mm and varying thickness according to the different configuration, as shown in Table 30.

specimen	G16	K8	[G2K]2S	[G4K2]S	[K2G4]S
Thickness [mm]	4.95	4.20	4.44	4.48	4.37

Table 30: impact test specimens thicknesses.
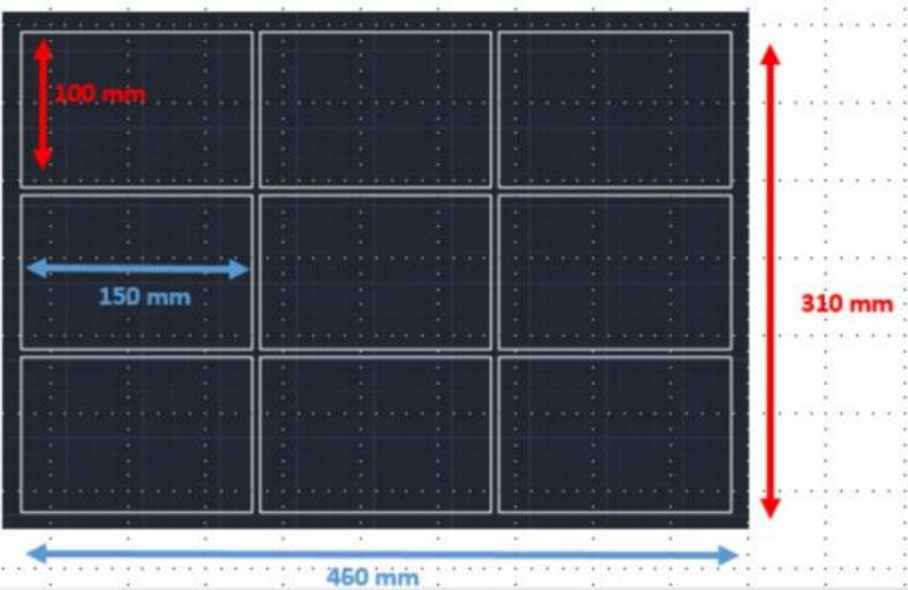
Figure 3-46: initial composite panel from which impact specimens were cut and relative dimensions.

During the first trial of impact tests some issues regarding the fixture took place. After the impact there was the slippage of the panel from the rubber fixture, as it can be observed in Figure 3-47: impacted panel after the test.

Figure 3-47: impacted panel after the test.

This event occurred especially for higher energies, such as 90J and 120J impact energy. Anyway, even for lower energies, a slight slippering of the panels was also present. The reason for this behavior is to be associated to the novel matrix material used to produce those composites. The last set of panels, tested in the previous collaboration project together with UFRGS, had same characteristics of the ones investigated here: reinforcement material, fabric architecture, and stacking sequence. Also, test set-up (impactor mass and shape, boundary conditions, impact energies) was kept the same, for comparison of the laminates. The only main difference is the constituting matrix material. As illustrated in Section 3.1, in the present case, an elastomeric PU soft material is adopted, while for the precedent set of laminates a classic epoxy resin was used. No slippage at all was never observed for the epoxy matrix composite. Here, instead, a huge deformation of the composites took place due to the slippage, but once removed from the fixture, the panels were able to return almost completely to their original shape. Tests were then interrupted, and a new set-up was designed and built, changing the boundary conditions of the test. New fixture design and dimensions is shown in Figure 3-48.
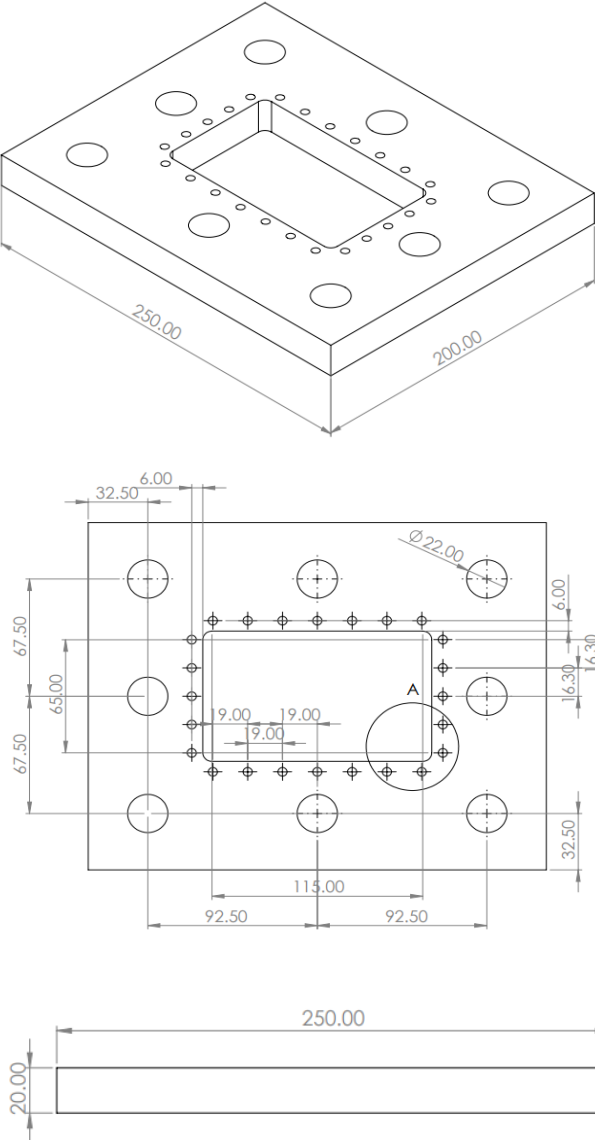
Figure 3-48: geometric features of the frame adopted for the drop weight tests.
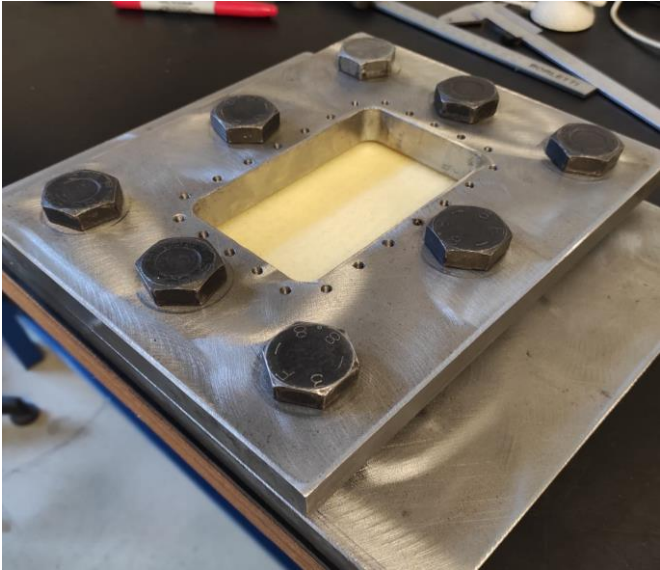
Figure 3-49: picture of the frame.

The results of the tests performed using the initial fixture will not be considered in the following, as, first of all, the movement of the panels during impact leads to results which are not reliable, and also, it would not be accurate to confront results taken considering two completely different kinds of boundary conditions for the impacts. Because of that, the initial objective of performing twice tests with the same energy level, for confrontation of results, was not possible, as some of the panels were consumed during the initial impacts.

In the following sub-sections, the relevant experimental results and the graphical representation obtained from the tests will be first presented for each composite configuration, with initial comments just related to the external visible damages on the impacted specimens. Then, the analysis of the exposed results will be commented for specimens altogether, followed by the comparison with impact results from the above-mentioned epoxy resin matrix composites.

3.5.1. Glass composites

In total three G16 panels were tested with impact energies of 50J, 90J and 120J. The effective impact energy (E_{eff}) is also indicated, as during the drop of the impactor energy dissipation occurs. Absorbed energy from the panel (E_{abs}), elastic energy (E_{el}), maximum force (Fmax) and maximum displacement were calculated and are shown in Table 31 for each test energy. The graphical representation of force-time, force-displacement, and energy-time histories for all testing energies is also shown in Figure 3-50.

a)

b)
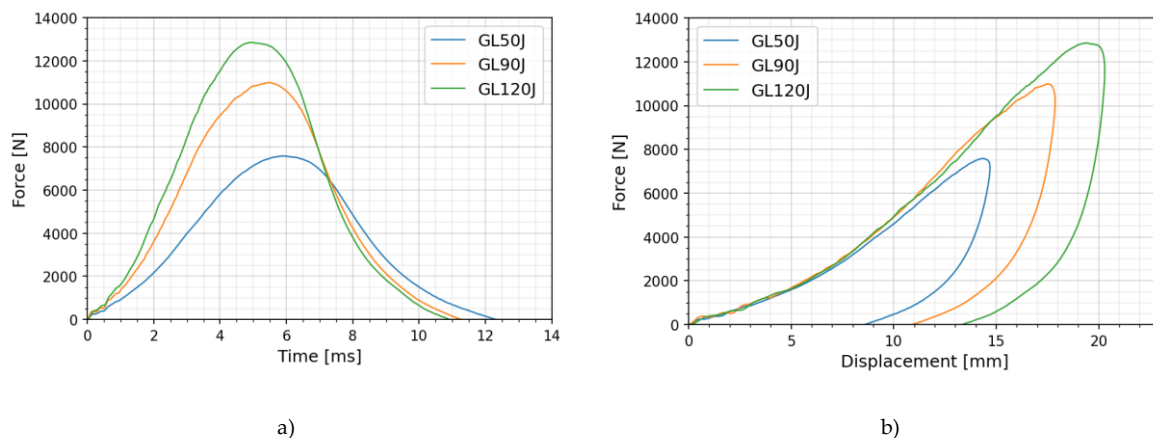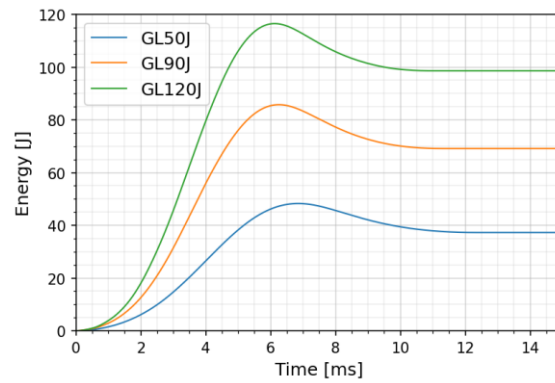
c)

Figure 3-50: G16 (a) Force-time curves , (b)Force- displacement curves, (c) Energy-time curves for the tested energies.

Specimen	E_{eff}[J]	E_{abs} [J]	E_{el} [J]	F_{max} [N]	Max displacement [mm]
GL50	48.28	37.27	11.01	7587.79	14.69
GL90	85.76	69.12	16.64	10991.42	17.87
GL120	116.52	98.64	17.88	12855.47	20.29

Table 31: properties derived from G16 composite impact tests at different energies.

Below, in Figure 3-51, the pictures of the glass samples after the impact test are shown for each energy. On the impact side splits and cracks are visible on the surface, while on the back side damage is almost imperceptible.

a)

b)

c)
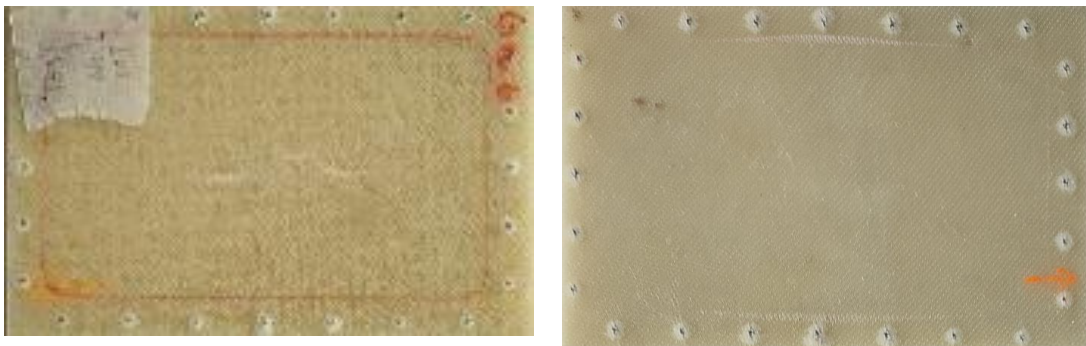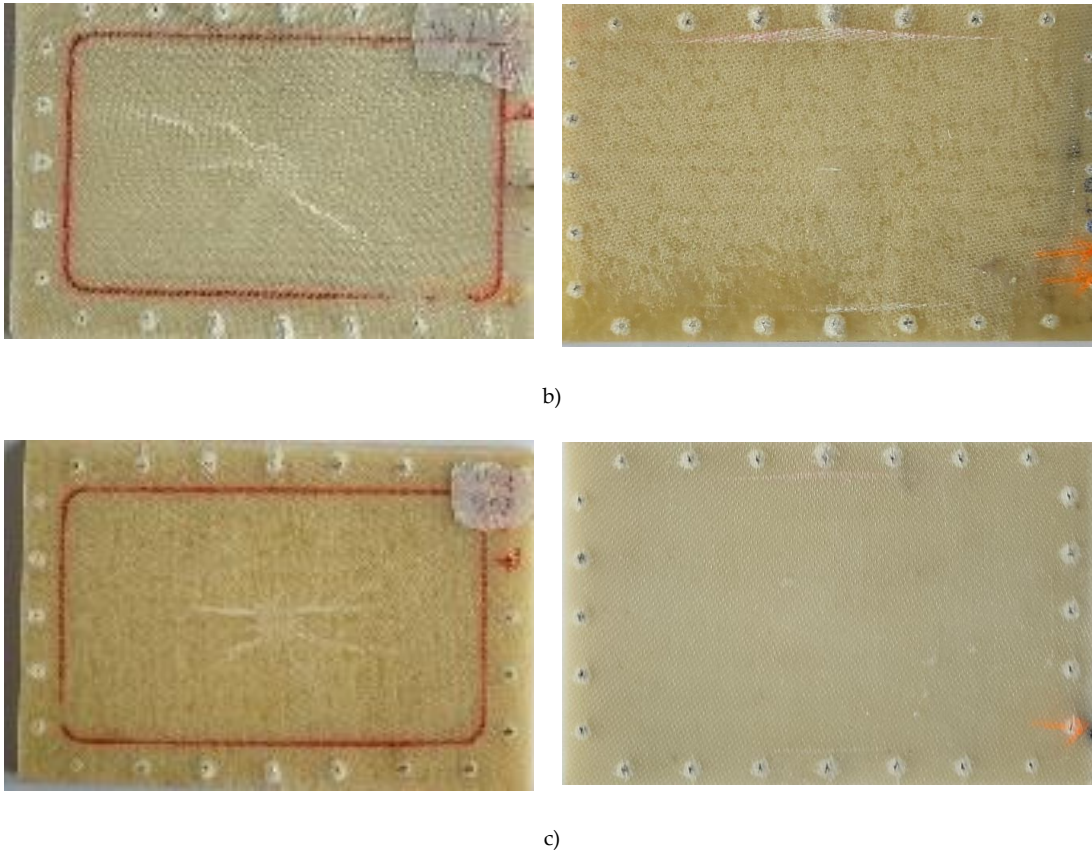
Figure 3-51: glass specimens pictures of impact front (left) and back front (right) at a) 50J, b) 90J, and c) 120J.

3.5.2. Kevlar composites

Five K8 panels were available. As for glass samples, the panels were tested at 50J, 90J and 120J, but having two more specimens available in that case, it was possible to test the material also at the lower energy of 30J and perform an extra test at 120J. Results are shown in Table 32. Graphical representation of the recorded data is reported as well in Figure 3-52.
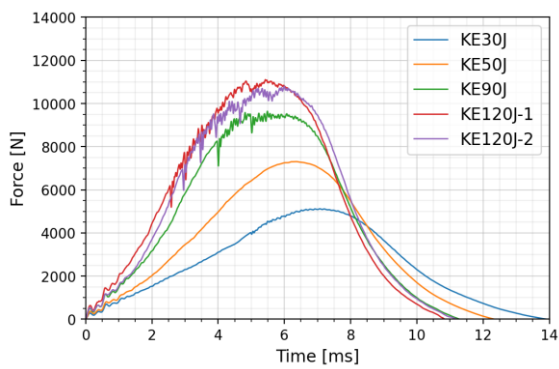
a)
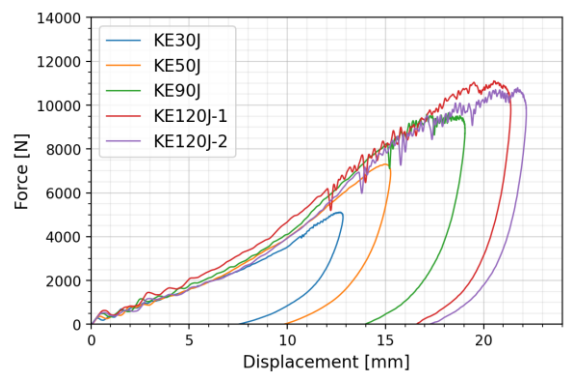
b)
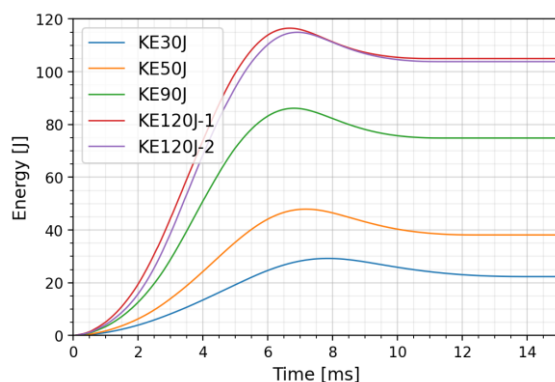
c)

Figure 3-52: K8 (a) Force-time curves , (b)Force- displacement curves, (c) Energy-time curves for the tested energies.

Specimen	E_{eff}[J]	E_{abs} [J]	E_{el} [J]	F_{max} [N]	Max displacement [mm]
KE30	29.24	22.34	6.892	5118.88	12.84
KE50	47.91	38.14	9.78	7307.38	15.26
KE90	86.15	74.86	11.28	9639.68	19.05
KE120-1	116.49	104.99	11.50	11106.28	21.38
KE120-2	114.95	103.83	11.12	10795.35	22.17

Table 32: properties derived from K8 composite impact tests at different energies.

In Figure 3-53 the specimens after the impact are shown. Respect to the glass specimens, even at the lower energies of 30J and 50J, some visible effects of the impacts are observed also on the back side of the panels. On the impact side splits and cracks can be noticed. At 90J and 120J a depression is formed on the impact side and on the back the indentation becomes evident, with visible fiber breakage at 120J.
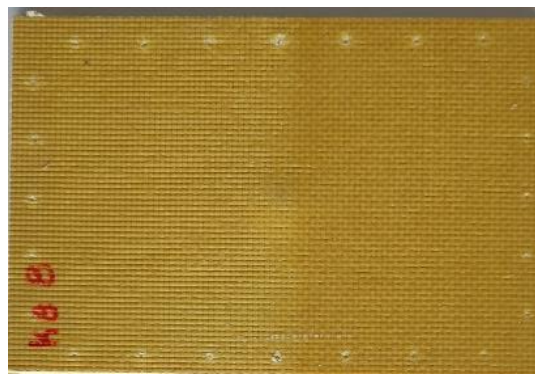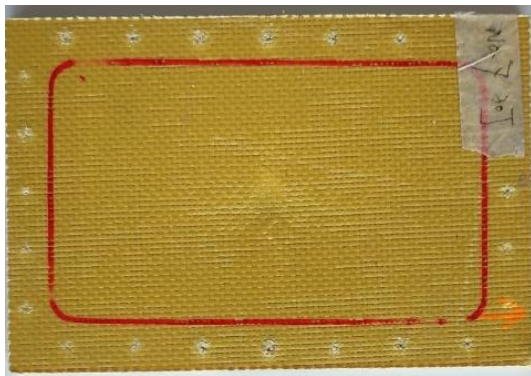
a)

b)
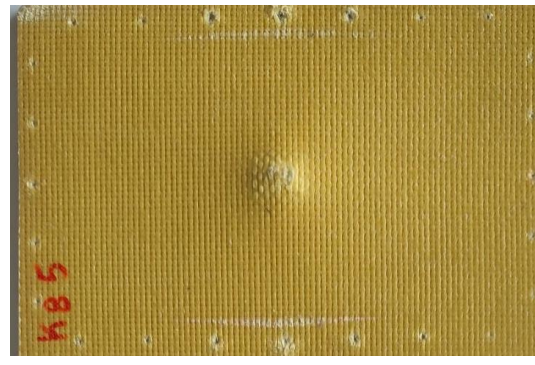
c)
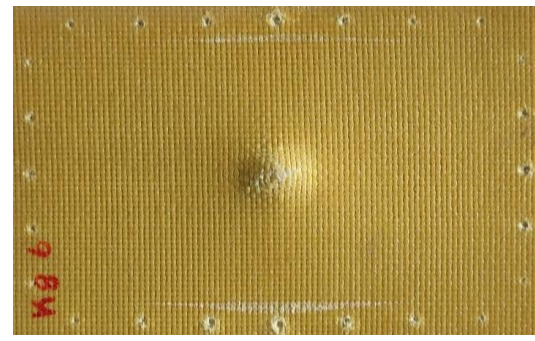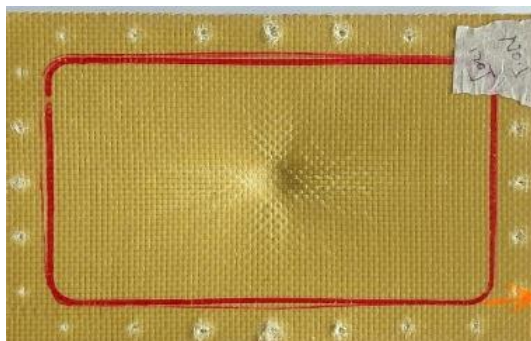
d)
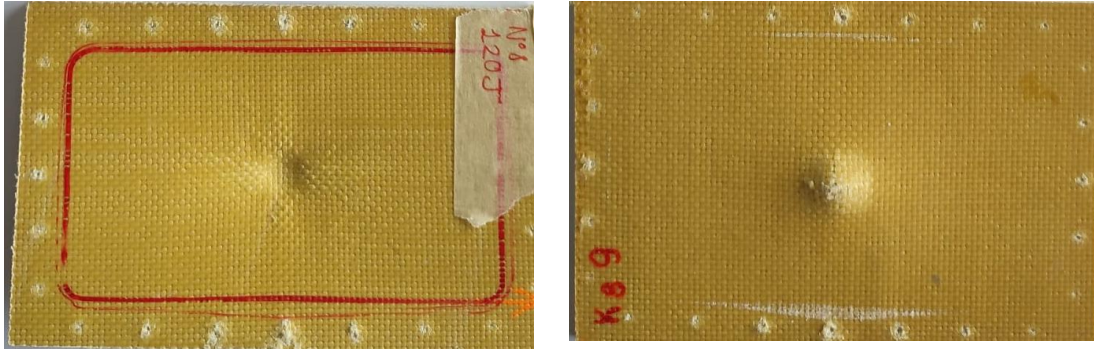
e)

Figure 3-53: Kevlar specimens pictures of impact front (left) and back front (right) at a) 30J, b) 50J, c) 90J, and d)-e) 120J.

3.5.3. Hybrid composites

(G2K)2S, (G4K2)S, (K2G4)S hybrid configurations were tested at 50, 90 and 120J, as for the pure composite samples, and at the lower extra energy of 20J. Results are exposed respectively in TablesTable 33Table 34Table 35 and history curves in Figure 3-54,Figure 3-56,Figure 3-58.

- (G2K)2S
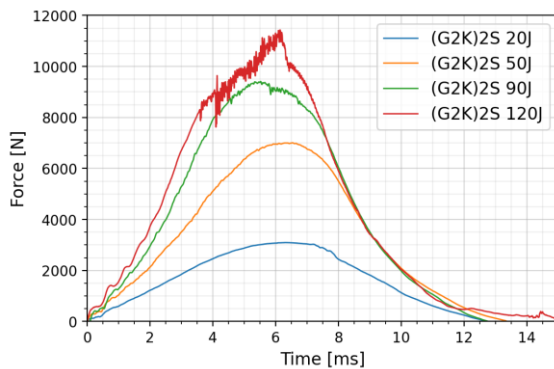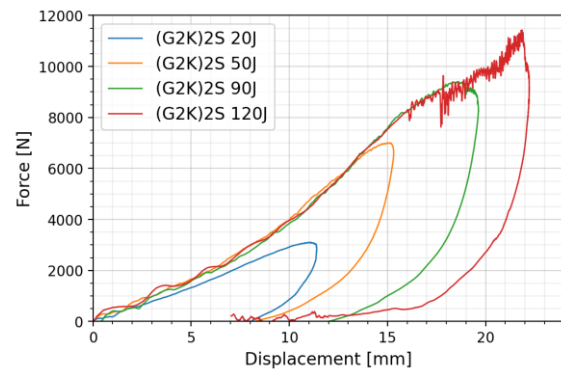
a)   b)
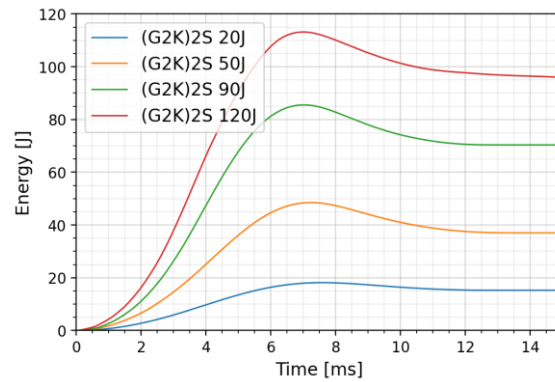
c)

Figure 3-54: (G2K)2S (a) Force-time curves , (b)Force- displacement curves, (c) Energy-time curves for the tested energies.

Specimen	E_{eff}[J]	E_{abs} [J]	E_{el} [J]	F_{max} [N]	Max displacement [mm]
(G2K)2S_20	18.16	15.27	2.89	3095.51	11.39
(G2K)2S_50	48.51	37.03	11.49	7006.83	15.32
(G2K)2S_90	85.52	70.37	15.15	9409.95	19.63
(G2K)2S_120	113.15	96.03	17.12	11432.40	22.22

Table 33: properties derived from (G2K)2S composite impact tests at different energies.

In the figure below the pictures of the impacted specimens are shown. For 20J and 50J no damage is detected at the specimens back side and some surface cracks are observed on the impact surface. For 90J and 120J surface splits and cracks are more evident and diffused on the impact cite and on the back of the panel also fiber breakage is noticed.

a)

b)

c)

d)
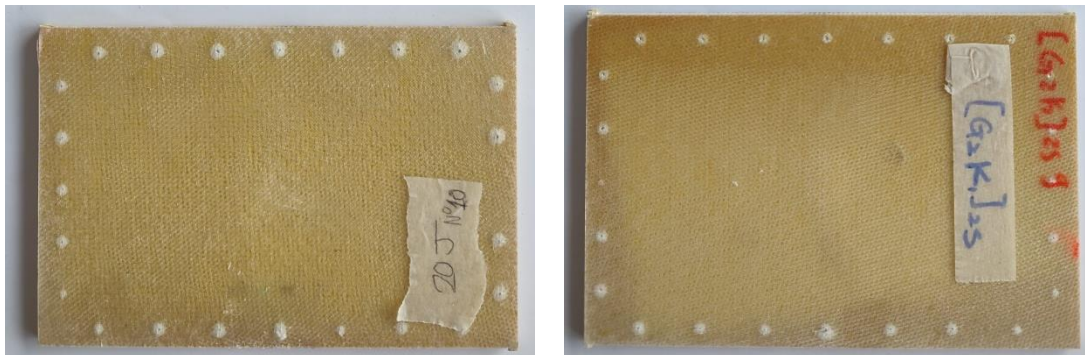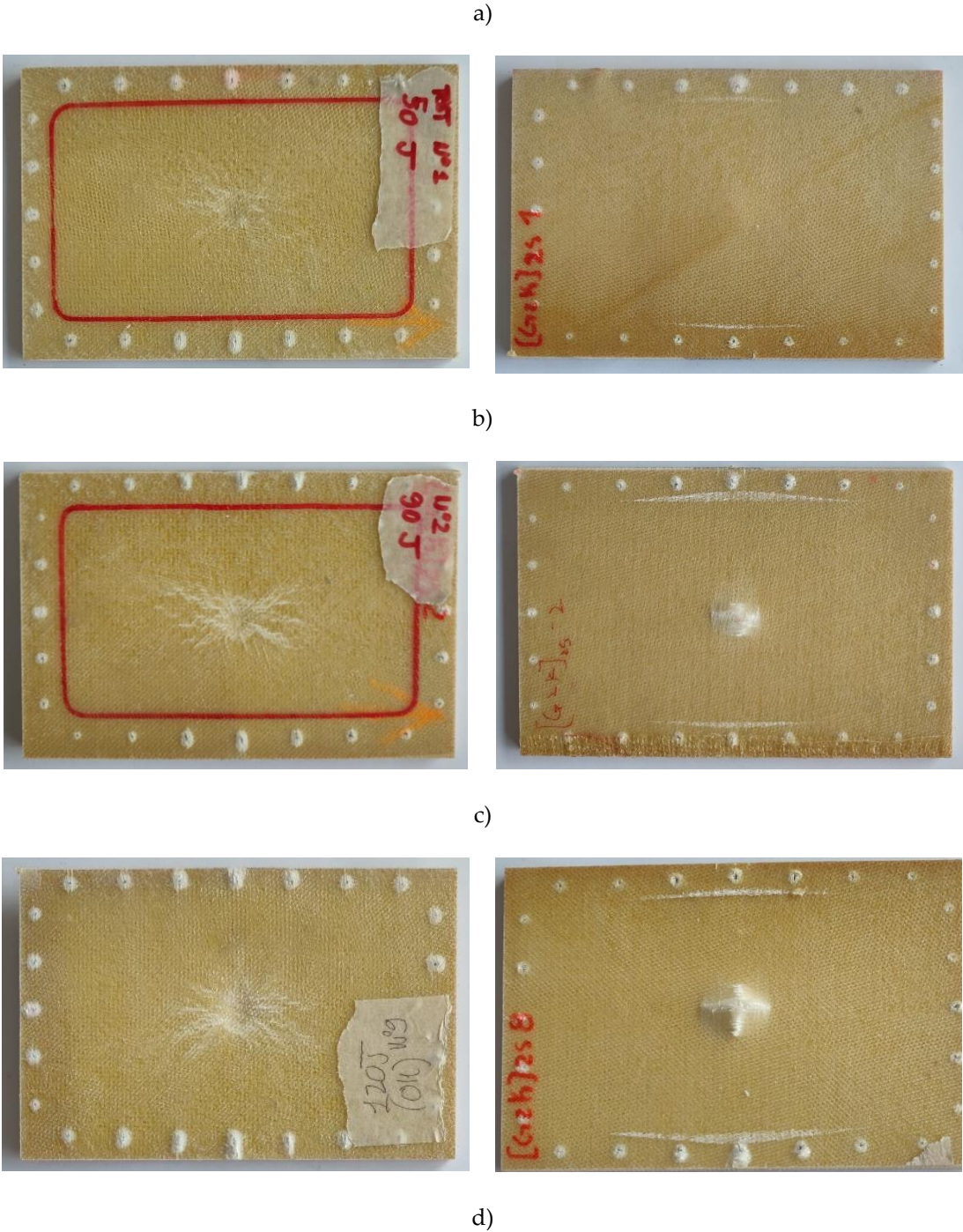
Figure 3-55: (G2K)2S specimens pictures of impact front (left) and back front (right) at a) 20J, b) 50J, c) 90J, and d) 120J.

- (G4K2)S

a)

b)

c)
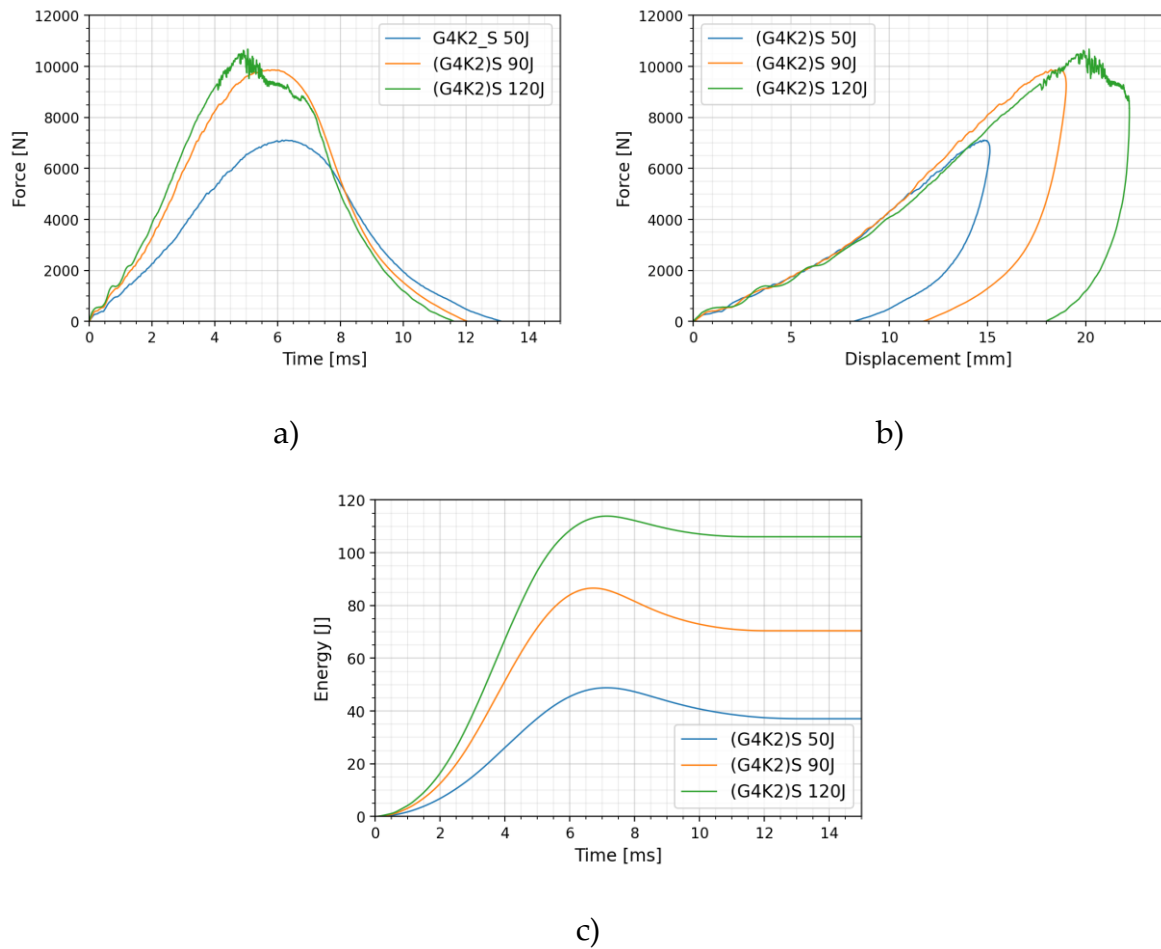
Figure 3-56: G4K2)S (a) Force-time curves , (b)Force- displacement curves, (c) Energy-time curves for the tested energies.

Specimen	E_{eff}[J]	E_{abs} [J]	E_{el} [J]	F_{max} [N]	Max displacement [mm]
(G4K2)S_50	48.81	37.07	11.74	7107.08	15.12
(G4K2)S_90	86.58	70.43	16.14	9870.32	19.01
(G4K2)S_120	113.87	106.05	7.82	10681.48	22.23

Table 34: properties derived from (G4K2)S composite impact tests at different energies.

In Figure 3-57 it can be observed how the impact damage in this hybrid configuration is less pronounced than in the last case. At 90J, for instance, on the back side of the panel no evident damage is detected, contrary to the previous considered hybrid. Even

108

if not clearly evident from the picture, also at 120J the generated indentation is less profound and damage less extended.
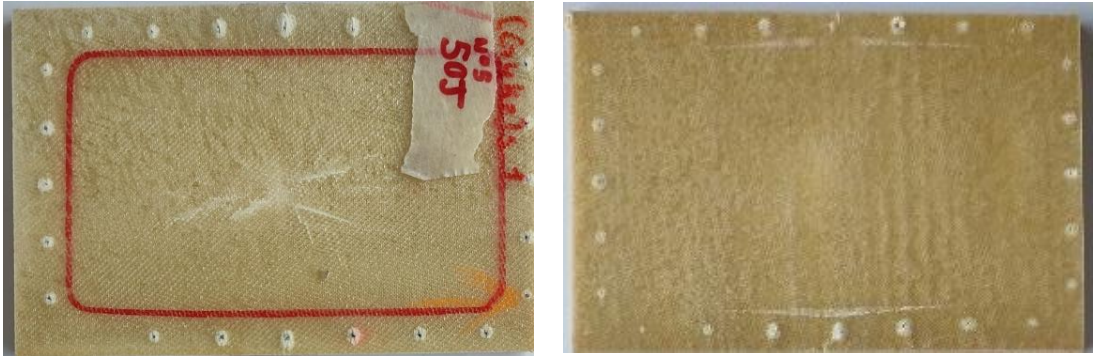
a)
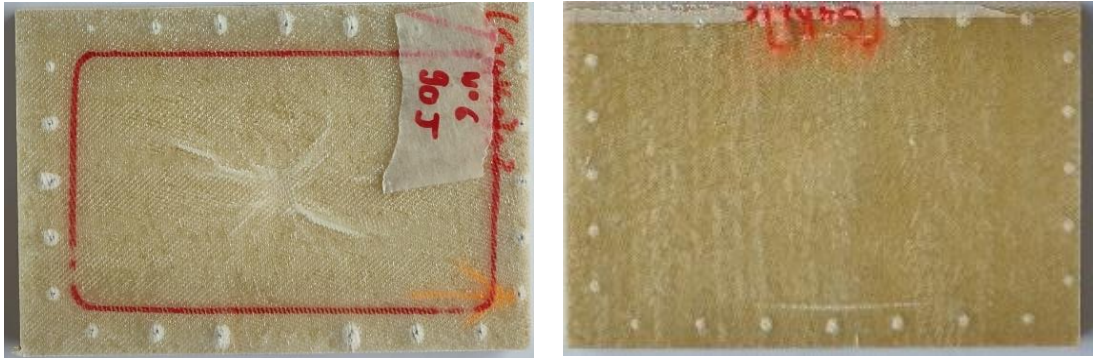
b)
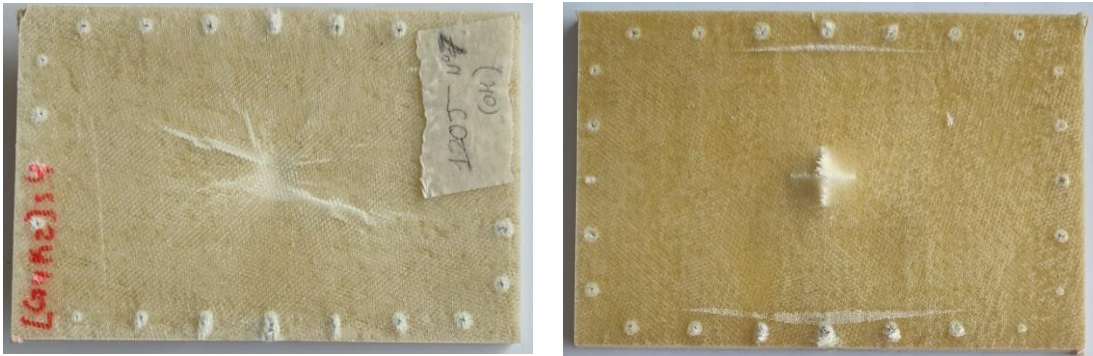
c)

Figure 3-57: (G4K2)S specimens pictures of impact front (left) and back front (right) at a) 50J, b) 90J, and c) 120J.

- (K2G4)S

a)

b)

c)
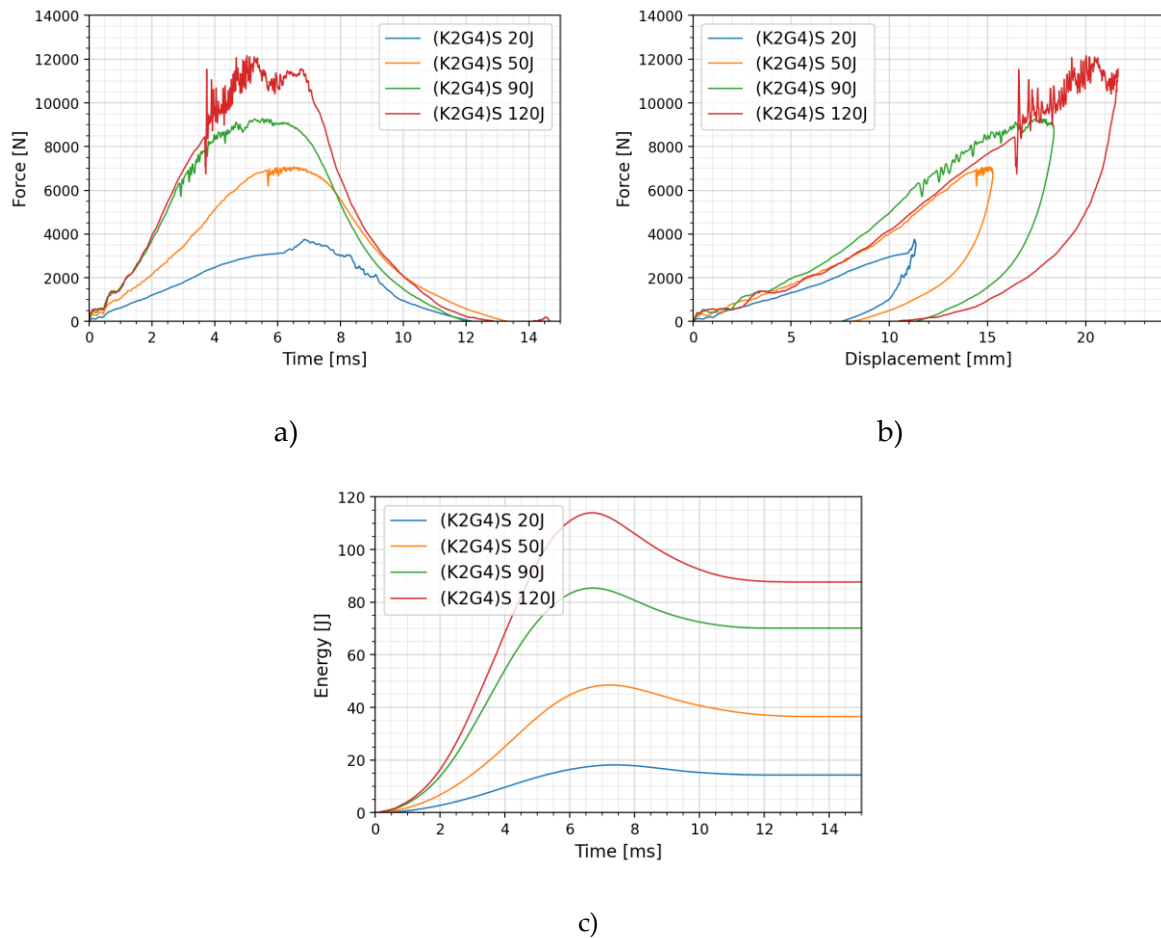
Figure 3-58: (K2G4)S (a) Force-time curves , (b)Force- displacement curves, (c) Energy-time curves for the tested energies.

Specimen	E_{eff} [J]	E_{abs} [J]	E_{el} [J]	F_{max} [N]	Max displacement [mm]
(K2G4)S_20	18.16	14.31	3.85	3749.44	11.35
(K2G4)S_50	48.52	36.54	11.98	7071.26	15.28
(K2G4)S_90	85.37	70.16	15.21	9285.33	18.38
(K2G4)S_120	113.96	87.65	26.31	12162.46	21.65

Table 35: properties derived from (K2G4)S composite impact tests at different energies.

In Figure 3-59 it can be noticed on the back side how damage has propagated differently respect to the other two hybrids, not surprisingly as here external layers are made ok Kevlar instead of glass. While before the propagation from the impact

location took place in both the longitudinal and transversal direction (forming a sort of cross) here the extension of the damage follows only the longitudinal direction of the sample. Initial perceptible fiber breakage is observed already at 90J.
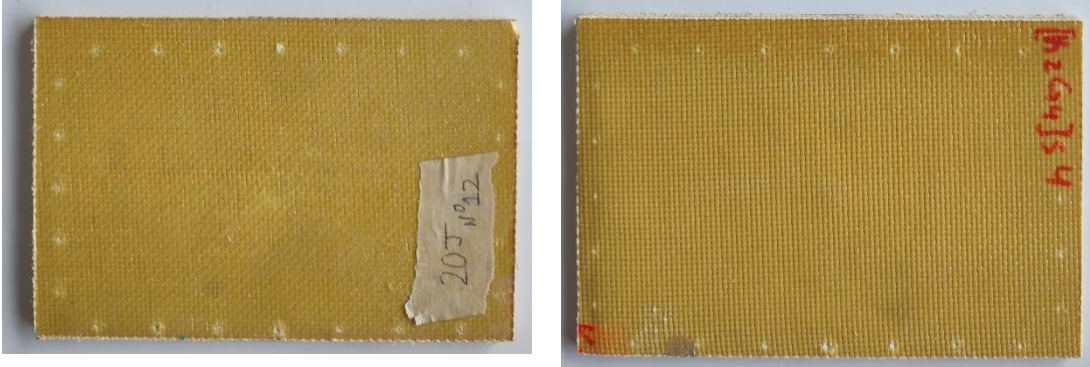
a)
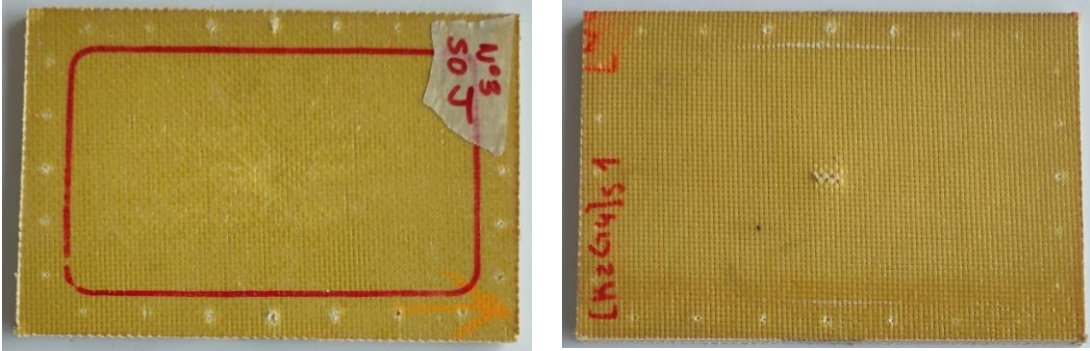
b)
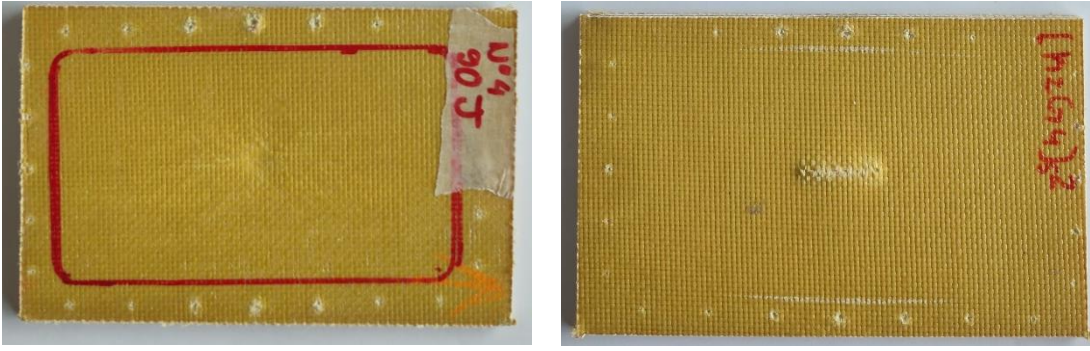
c)

d)

Figure 3-59: (K2G4)S specimens pictures of impact front (left) and back front (right) at a) 20J, b) 50J, c) 90J, and d)120J.

3.5.4. Test results analysis

In accordance with what discussed in Section 1.5, from the results shown in the previous subsections it is not always feasible to individuate sudden drops from the force-time history curves which could represent an approximate threshold load value for damage initiation. Also, for the aim of the current work analysis this was not considered as a crucial parameter necessary to evaluate the impact response of the composites under investigation. For these reasons, in the following discussion this aspect will not be considered.

In this subsection, the results previously reported separately for each of the specimens will be commented, grouping the composites together under same impact energies. This subdivision allows for a better visualization of possible differences which may arise from the different composites' configuration in terms of damage resistance properties.

Energy absorption

As can be observed in Figure 3-60 and Figure 3-61 (a, b), the absorbed energy from the composite specimens during the impact has its highest value in the Kevlar one, both at 50J and 90J impact energies, which is not surprising considering general intrinsic properties of aramid fibers composite materials. In the above-mentioned Figures, it can also be noticed how the measured values for absorbed energy for those two energies, in hybrid composites, do not show consistent differences to permit any kind of consideration yet about possible divergences in their behavior. It must be recalled, as exposed more in detail in Section 3.1, that the tested hybrids have almost equal properties with only exception of the stacking sequence. It is normal then to expect for the composites to behave similarly when impacted at the same energy level. However, with the increase in the impact energy to 120J, more marked variations are observed

in the materials response. Distance between curves becomes more evident in Figure 3-60 (c), and this divergence is again highlighted also by the histogram in Figure 3-61 (c). In particular, the highest absorbed energy is not registered anymore by the Kevlar sample, although maintaining a high value. In the current case, maximum energy absorption comes from the (G4K2)S hybrid and the lowest by the (K2G4)S hybrid.
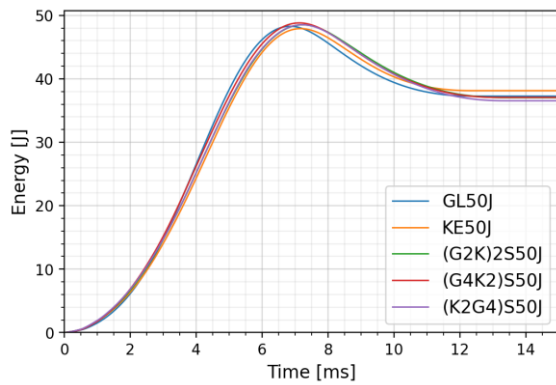
a)
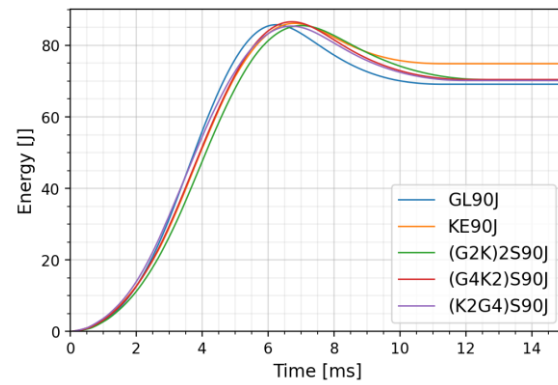
b)
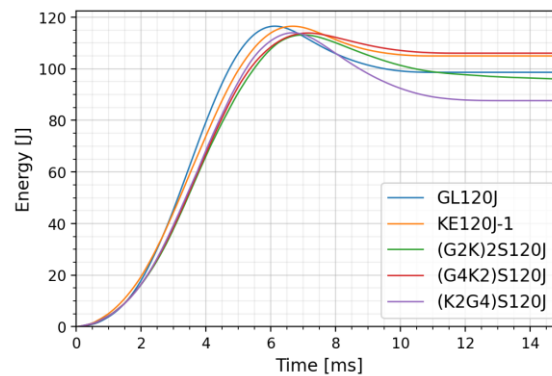
c)

Figure 3-60: Energy-time curves of the impacted specimens at (a) 50J, (b) 90J, and (c) 120J.

a)

b)

c)
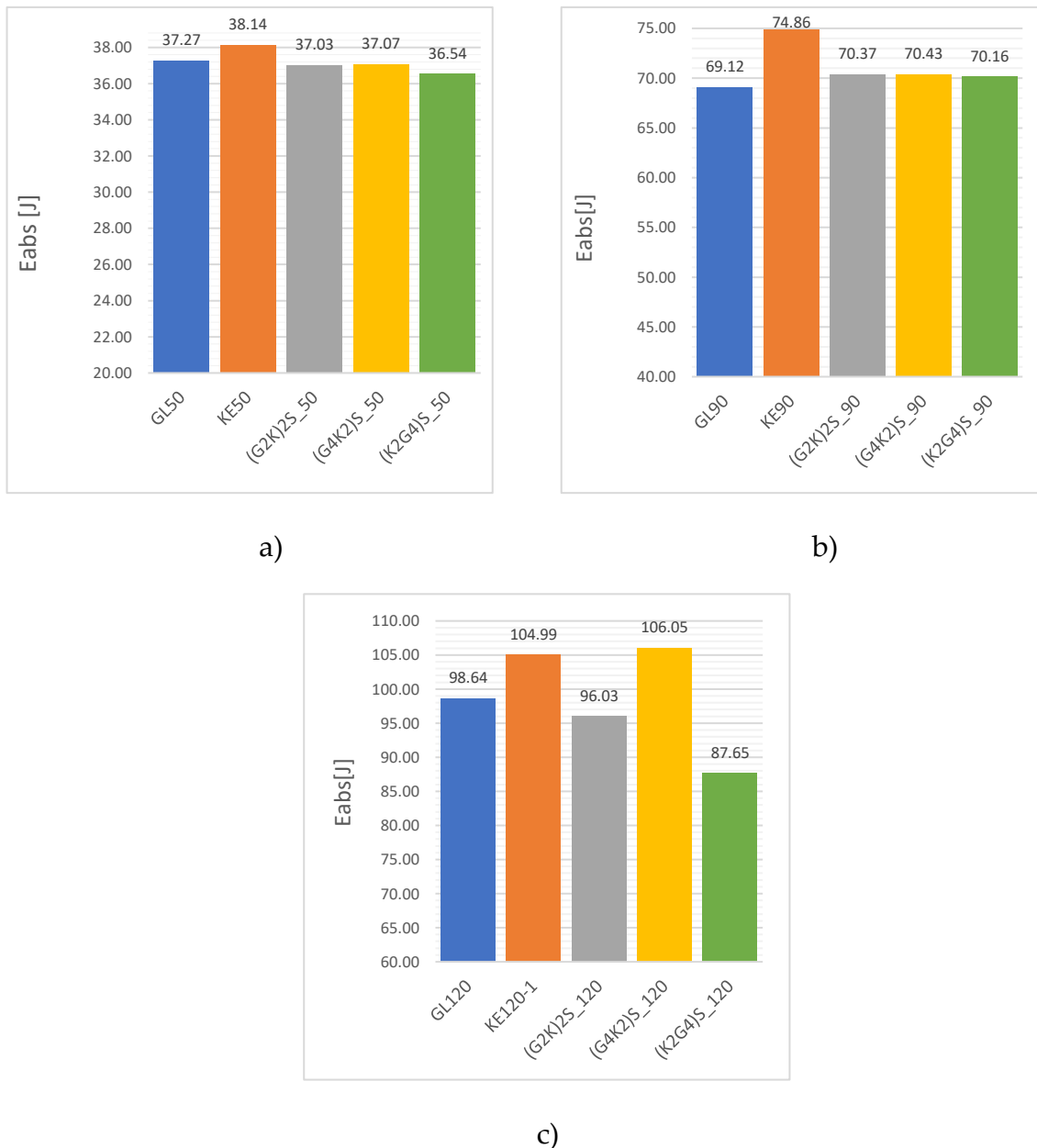
Figure 3-61: Energy absorbed by the impacted specimens at (a) 50J, (b) 90J, and (c) 120J

The E_{abs} value for the (K2G4)S specimen might almost appear to be excessively low respect to the other samples results, considering how close it was in the previous energy cases to the them. As only one sample was tested per energy, no confrontation can be done to assure the precision of this result and if it might have been affected by some experimental variability during the test. Anyway, confronting those two hybrids among them, it is interesting to notice that the contrasting behavior in terms of energy absorption corresponds also to a contrast in their configuration, which is inverted in the two cases. In one case, all glass plies are distributed in the middle of the laminate, with Kevlar layers distributed on the bottom and on the top surfaces of the panel (Figure 3-62). In this configuration (on the left) the lowest energy absorption value was registered. In the opposite case (on the right), with Kevlar plies in-between glass layers,

the highest energy absorption value was reported. According to those results, it might appear then, that having high stiff material layers on the outer composite surface and high energy absorption material in the middle, could increase the energy absorption capabilities of the overall designed structure (keeping for example same number of layers and ratio between the layers). Vice versa, with the other structural configuration, it looks like a much higher amount of elastic energy is generated from the impact event, thus obtaining a stiffer structure. The results for 120J for the remaining hybrid (G2K)2S is in between the other two specimens, which is reasonable considering its more balanced distribution of heterogenous plies (in the middle).

$[K_2G_4]_s$ $[G_2K_1]_{2s}$ $[G_4K_2]_s$
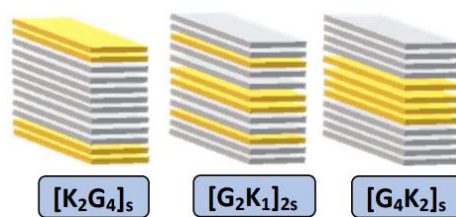
Figure 3-62: hybrid composites stacking sequence illustration.

In Figure 3-63 the absorbed energy is represented as a function of the impact energy, together with the equal energy curve. As commented previously, at higher energies the influence of the different configurations can be better analyzed. For lower energies, samples show closer values between them as can be seen by the almost overlapping points in the graph, while increasing the impact energy, points start to distance progressively. It can be seen with more evidence how till 90J composites shows almost the same absorption value, with exception of K8, while at 120J an evident separation is present, with the highest values given by (G4K2)S hybrid and K8 composites. Anyhow, it can be noticed the closeness of the points to the equal energy line for all specimens and energies, showing evident absorption capabilities from the laminates.
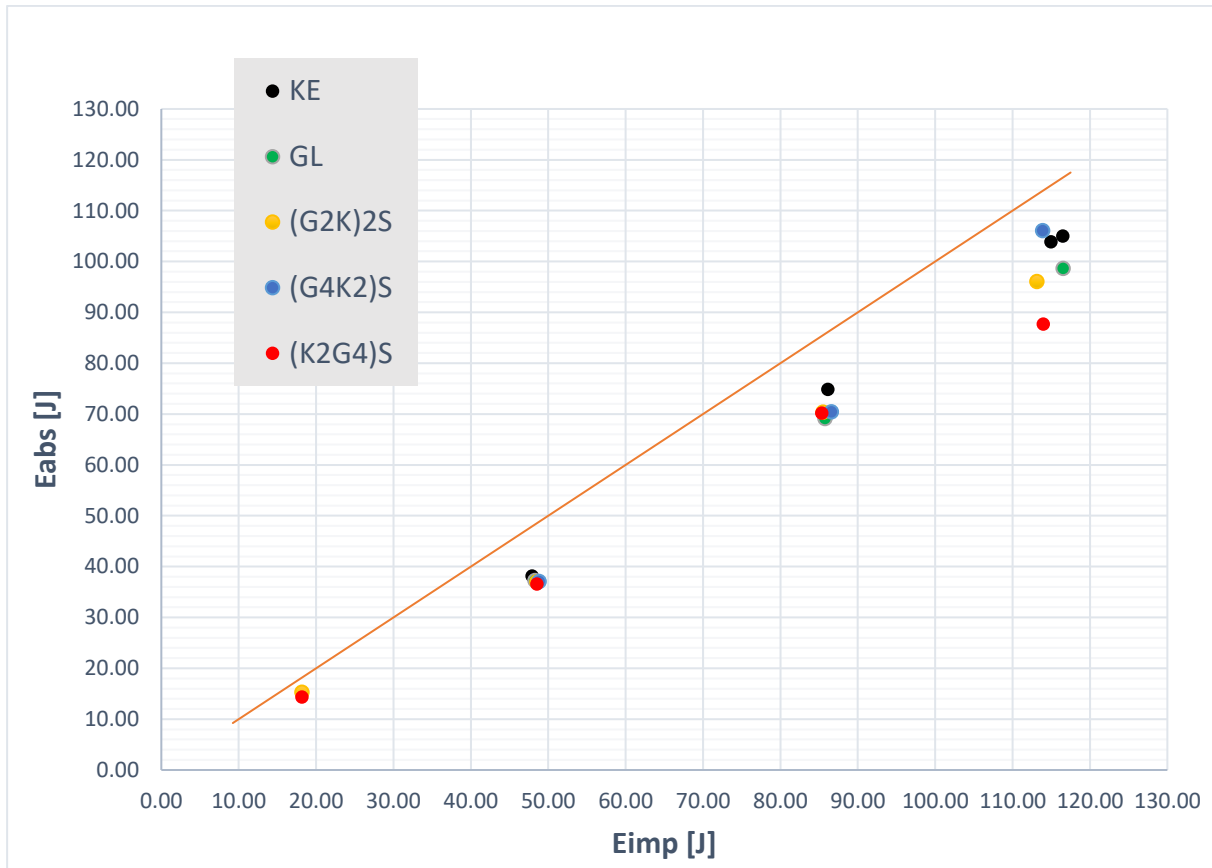
Figure 3-63: E_{abs}-E_{imp} graph with equal energy line representation.

For further considerations concerning this aspect the graph in Figure 3-64 can be analyzed, in which the percentage of E_{abs} with respect to the effective impact energy is shown. In first analysis Kevlar and glass specimens are confronted one to one.

The percentage of energy absorbed during the impact increases with increasing impact energy for both laminates with a certain linearity. Also, as already said, Kevlar values are always higher with respect to the Glass ones, and here it can be noticed even more how the distance in the results increases as well with the increasing energy.

Taking in consideration the percentage of energy absorbed respect to the absolute result shows with greater evidence how high those values actually are, approaching 90% of the total impact energy for Kevlar specimen and 85% for the glass one. This behavior is to be assessed to the novel matrix material which imparts a greater toughness to the structures. This aspect will be even more evident when in the following Section the here investigated composites will be compared with results from the same configuration epoxy matrix composites.
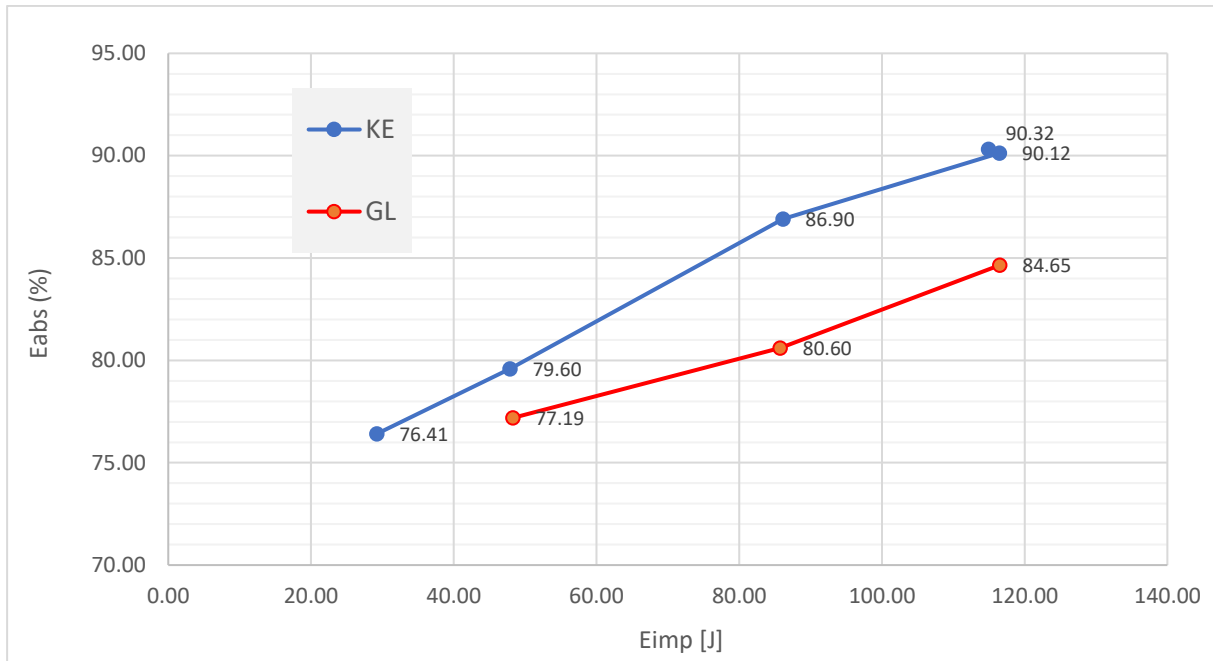
Figure 3-64: percentage value of E_{abs} respect to the E_{imp} for glass and kevlar samples.

When considering the same type of graph including the hybrid PU composites no common trend is observed for those laminates as it was for the pure ones. For example, the percentage of absorbed energy for specimen (K2G4)S from 20J to 50J impact energy first decreases, then increases at 90J, decreasing again for 120J. Also specimen (G2K)2S initially shows a decrease in the percentage of absorbed energy from 20J to 50J but, differently from the previous case, for higher energies the percentage value continues to increase. For the (G4K2)S specimen data recorded at 20J is not available so no confrontation with the last two hybrids can be done at this energy level. However, from 50J to 120J the percentage value of absorbed energy increases rapidly, reaching the highest value among all specimens for 120J. Again, it can be noticed how in those materials the reported percentage values are high. Because of the varying behavior of the specimens it is not straightforward to individualize a trend for increasing energies, characteristic for the hybrid configurations, as it was for the pure ones. However, also in this case, it sounds plausible from the showed results to think of an increasing trend for increasing energies.
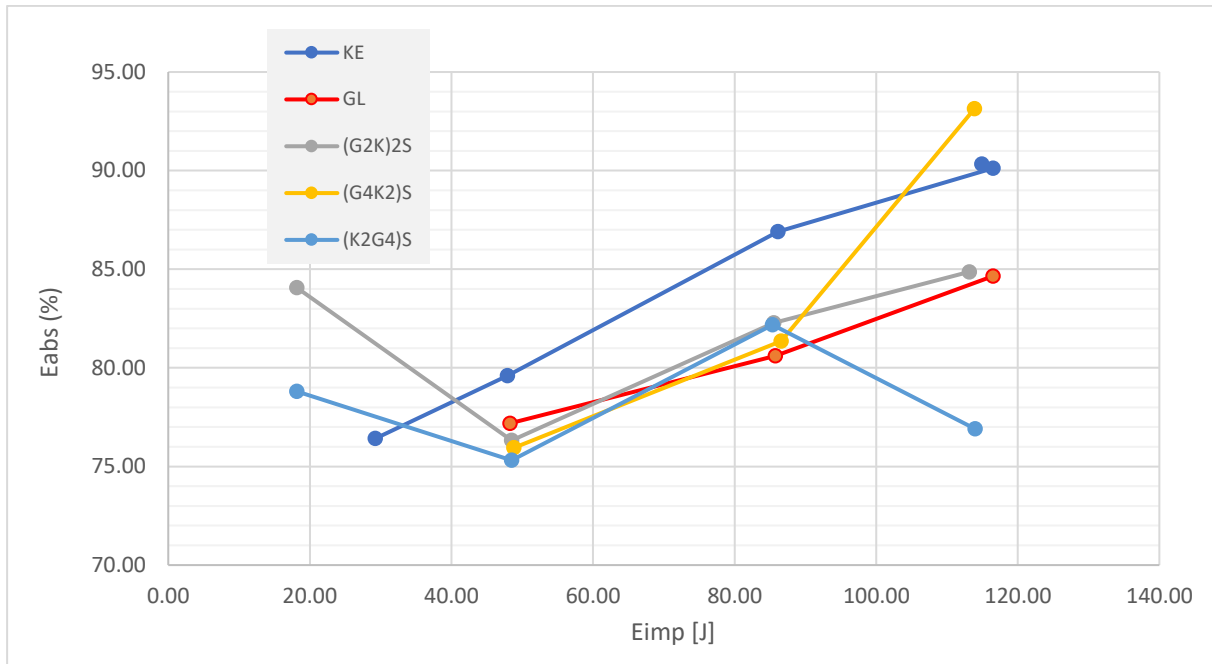
Figure 3-65: percentage value of E_{abs} respect to the E_{imp} for hybrid samples.

Impact force and displacement

Force-displacement curves are represented in Figure 3-66. Comparison between maximum displacement values and maximum impact force are shown respectively through the histograms of Figure 3-67 and Figure 3-68.

As can be seen from all the above-mentioned Figures, pure glass specimen registers the lowest displacement accompanied by the highest maximum impact force for all the testing energies. Particularly, from the force-displacement curves, it is evident how the glass curve deviates from the others. This trending behavior is an indication of the high stiffness of the laminate compared to the other specimens, independently of the energy.

Differences between the remaining specimens' maximum displacement during impact can be considered negligible, and no common trend can be noticed with increasing energy levels (Figure 3-67). Same can be pointed out for what concern the maximum force (Figure 3-68) as, also for this result, there is not repeating behavior arising for the varying impact energies. Nevertheless it can be observed how at 120J the maximum impact force for specimen (K2G4)S increases over the others specimens values, in accordance with the results obtained for the absorbed energy.

a)

b)

c)
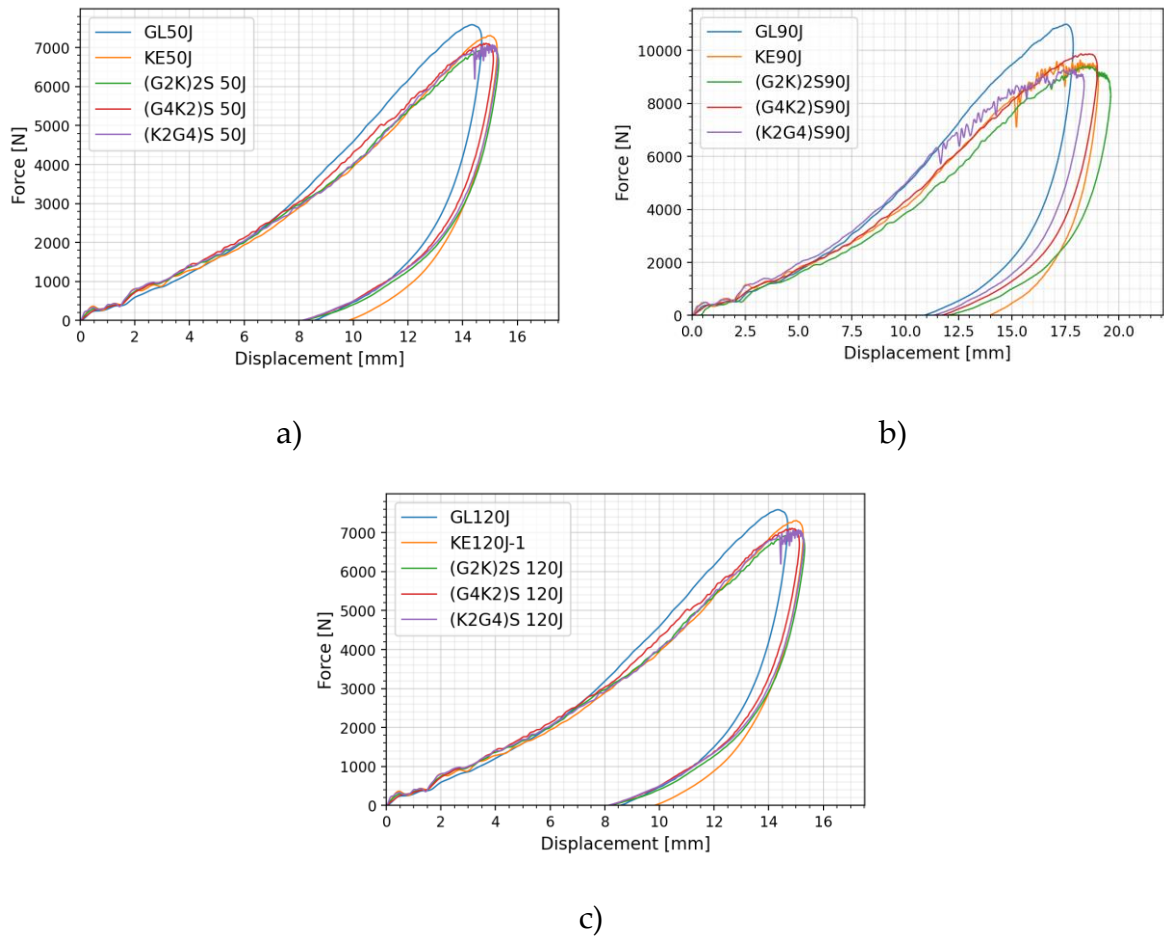
Figure 3-66: Force-displacement curves of the impacted specimens at (a) 50J, (b) 90J, and (c) 120J.

a)

b)
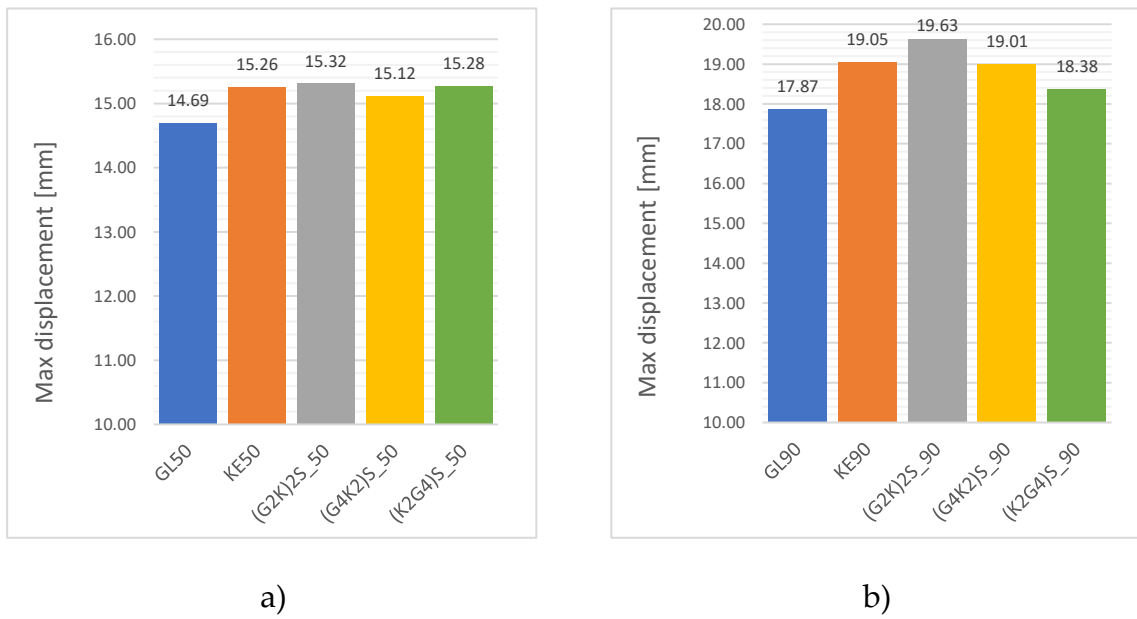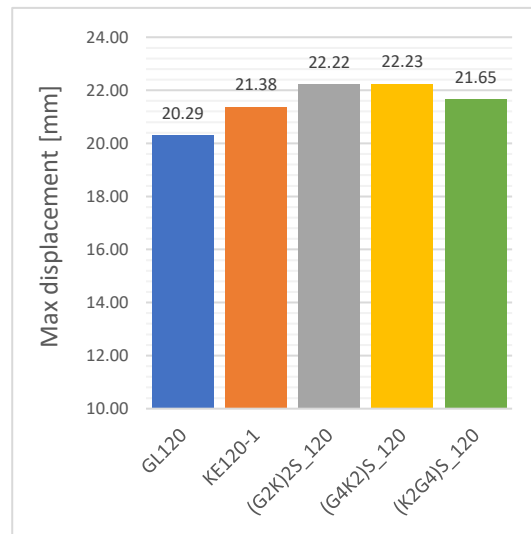
c)

Figure 3-67: Maximum displacement of the impacted specimens at (a) 50J, (b) 90J, and (c) 120J.
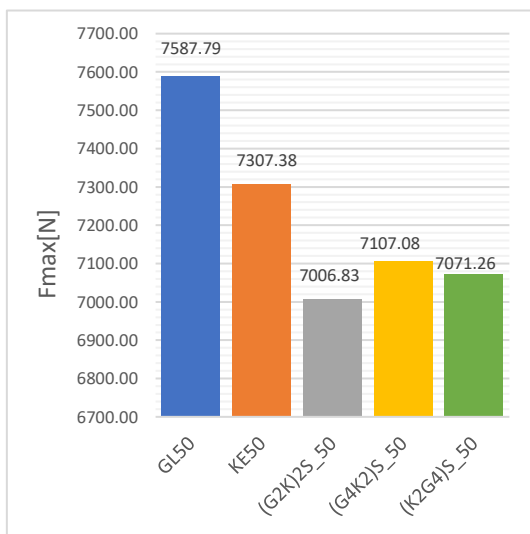
a)
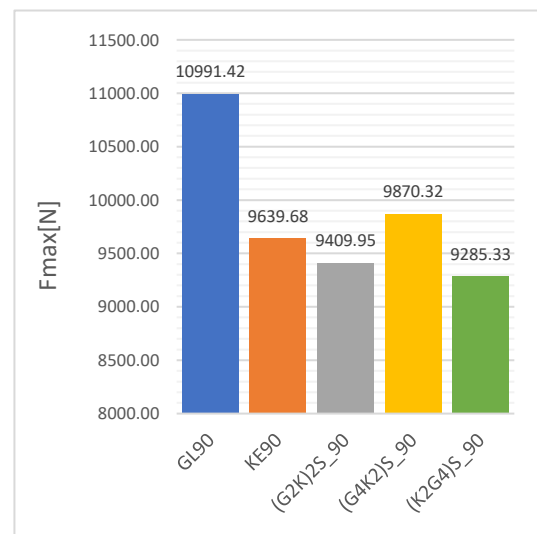
b)
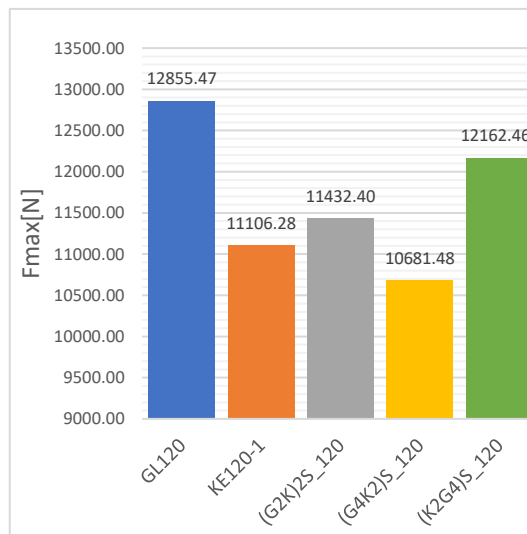
c)

Figure 3-68: Maximum impact force of the impacted specimens at (a) 50J, (b) 90J, and (c) 120J.

3.5.5. Comparison with epoxy resin matrix composite

In this Subsection, results obtained from impact tests on the epoxy resin matrix composites (EP) from previous research projects, will be compared with the results obtained from the current investigated PU matrix material composites. As the boundary conditions for the tests were here changed it was not possible to use the data already collected in the previous experimental works. New tests were performed on the few available remaining EP composites, thus only few energies were selected for the testing.

In the following, results are compared graphically and numerically, starting with glass and Kevlar composites, and then one of the hybrids, as it was the only hybrid left with the epoxy matrix.

Glass composites

Tests were performed at 50J and 90J. In Table 36 the calculated results are reported for both energies and specimens.

In Figure 3-69 tests at 50J are compared one to one. From those results it can be clearly observed that the epoxy composite shows a greater stiffness respect to the PU composite: higher impact force, lower displacement, and a resulting higher elastic energy from the impact.

a)

b)

c)
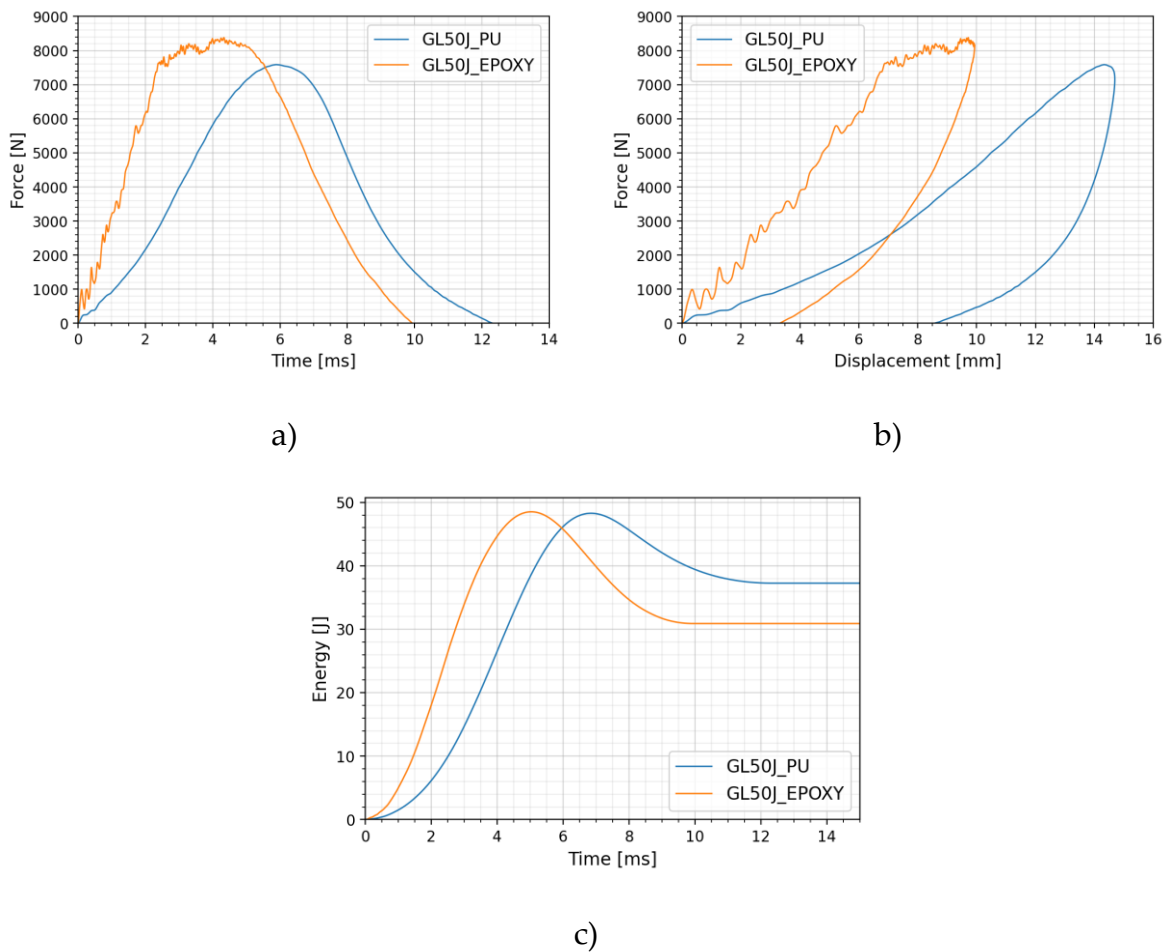
Figure 3-69: (a) Force-time, (b) Force-displacement, (c) Energy-time curves of impacted specimens at 50J.

At 90J, which resulting curves are reported in Figure 3-70, the epoxy specimen was perforated during the impact, as can be seen in Figure 3-71, while for the PU specimen no damage at all is observed on the back side and just some cracks and splits on the impacted surface. Not even at the higher 120J impact energy (Figure 3-51), the extent of damage could be considered as close to the perforation level in the PU laminates.

a)

b)
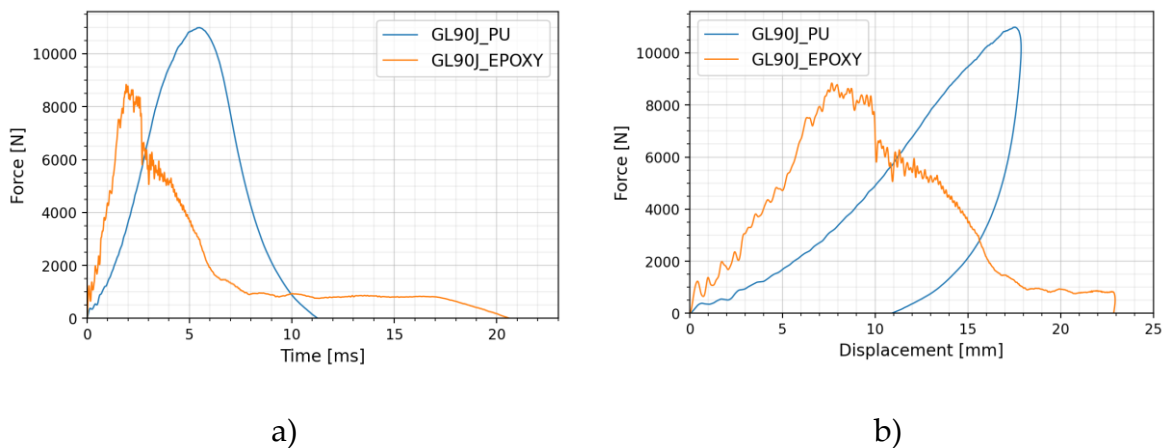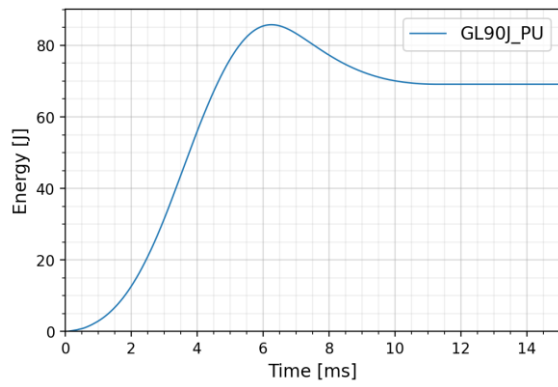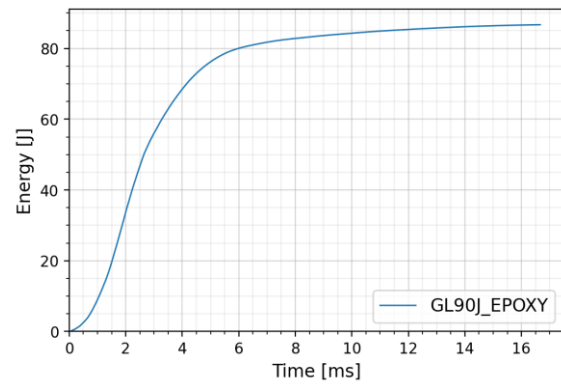
c)   d)

Figure 3-70: (a) Force-time, (b) Force-displacement, (c) Energy-time curves of glass impacted specimens at 90J.

Specimen	E_{eff}[J]	E_{abs} [J]	E_{el} [J]	F_{max} [N]	Max displacement [mm]
GL50J_PU	48.28	37.27	11.01	7587.79	14.69
GL50J_EPOXY	48.52	30.904343	17.612231	8379.29	9.93
GL90J_PU	85.76	69.12	16.64	10991.42	17.87
GL90J_EPOXY	/	/	/	/	/

Table 36: properties derived from glass composites impact tests at different energies.

PU	EPOXY
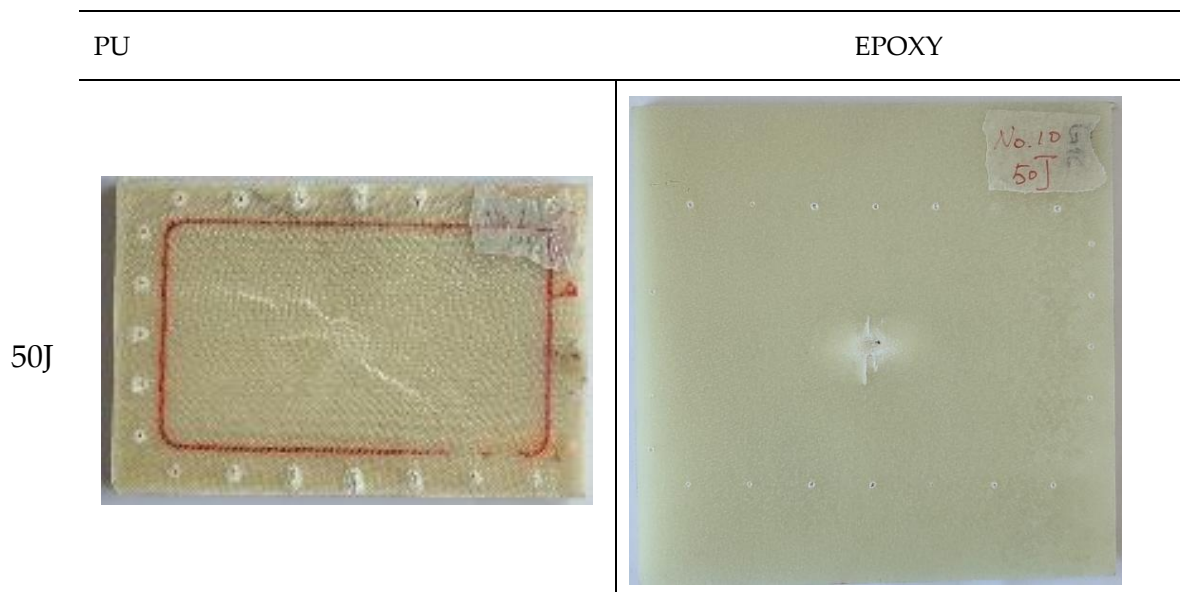
GL50J IMPACT SIDE

50J
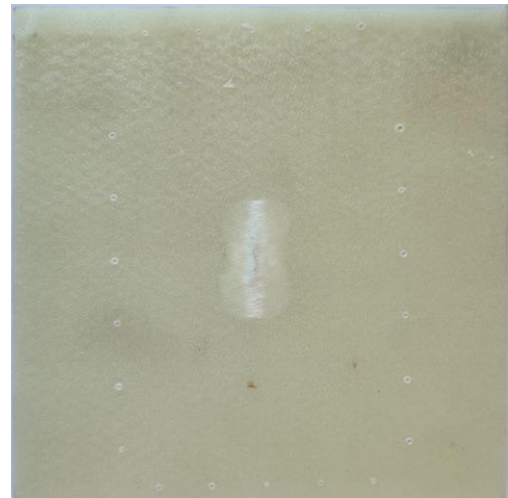
GL50J BACK SIDE

90J
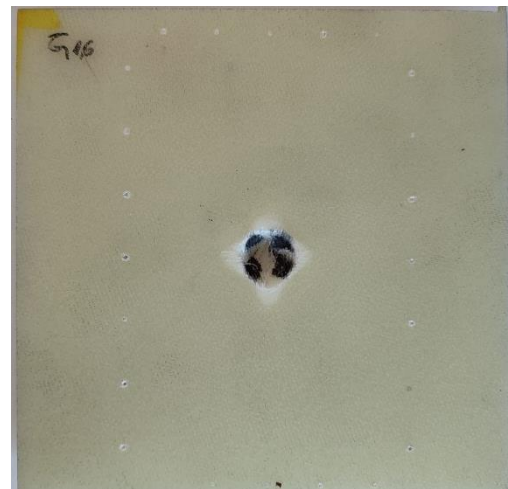
GL90J IMPACT SIDE

90J
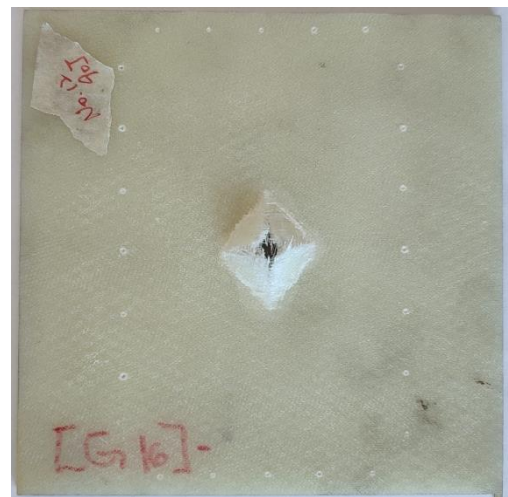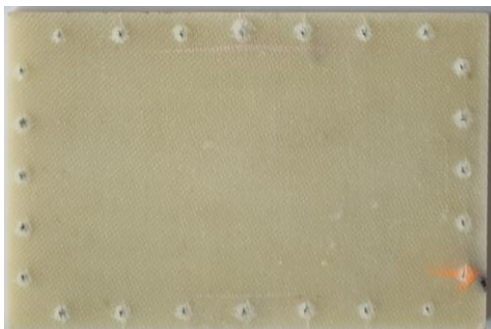
Figure 3-71: visual comparison between impacted PU and EP glass specimens.

Comparison between absorbed energy and displacement at 50J, together with the observed impact response of the specimens at 90J, show the ability of the PU matrix composite to better resist impact events. The PU composite registers a higher deformation respect to the epoxy matrix one, but after the impact it seems visually that actually this deformation is, in a certain amount, recovered.

Kevlar composites

Kevlar samples were tested at 30J, 50J and 90J. All numerical results are reported in Table 37.

Observing Figure 3-72, representing tests at 30J, similar considerations to the glass samples can be done. Epoxy matrix composite shows again greater stiffness respect the PU matrix one, aspect highlighted in the force-displacement curve, where both the higher impact force and lower displacement can be observed simultaneously. Also, the amount of absorbed energy in the EP sample is much lower in comparison.
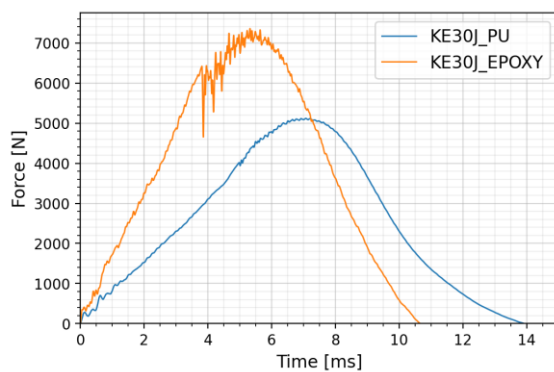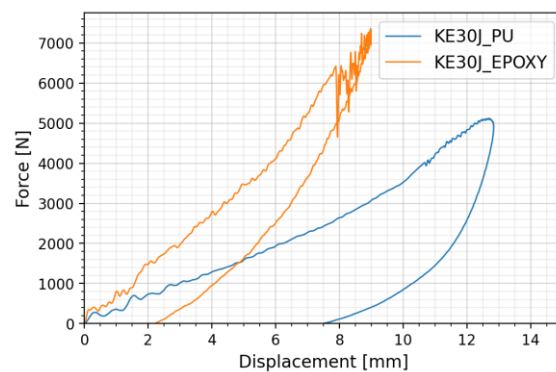
a)   b)
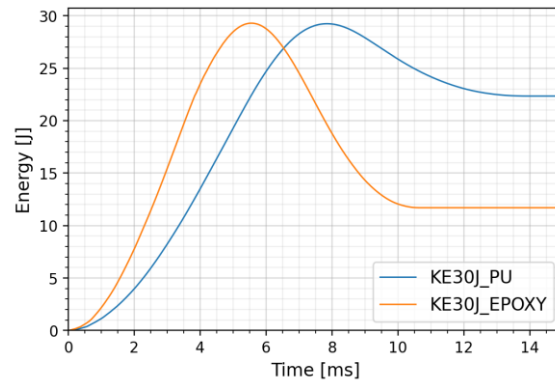
c)

Figure 3-72: (a) Force-time, (b) Force-displacement, (c) Energy-time curves of Kevlar impacted specimens at 30J.

Resulting curves at 50J are shown in Figure 3-73. In the epoxy composite, initial perforation of the specimen is already observed, while again for the PU specimen almost no damage can be visualized externally at the same energy level (Figure 3-75). This behavior is noticed also from the above mentioned history curves.
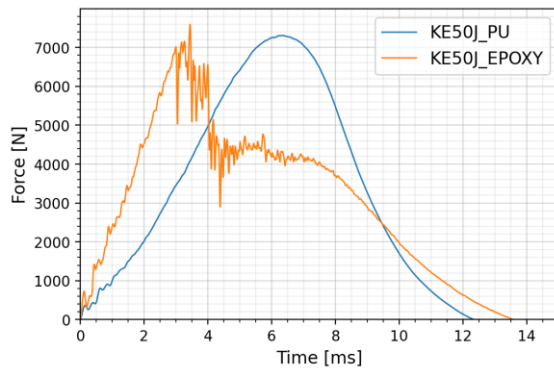
a)
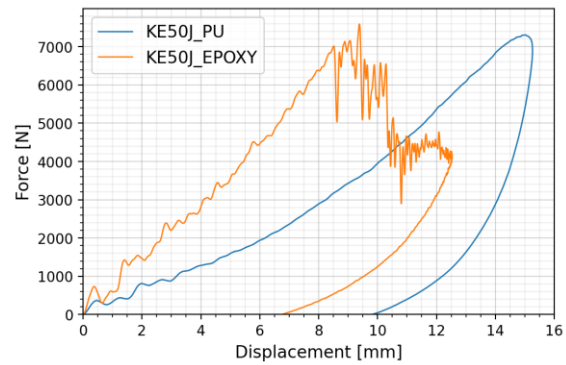
b)
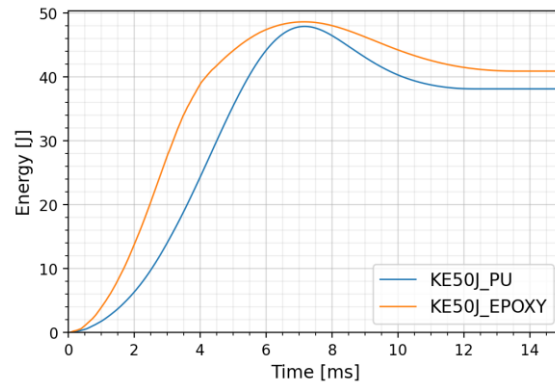
c)

Figure 3-73: (a) Force-time, (b) Force-displacement, (c) Energy-time curves of Kevlar impacted specimens at 50J.

At 90 J, as can be seen also from the graphs in Figure 3-74, complete perforation of the specimen took place. On the PU specimen (Figure 3-75) a more evident deformation in the impact cite is present in relation to what is observed at 50J, also on the back side of the specimen, but yet no perforation has started. Again, as commented for the glass composites, this trending behavior for the specimens, shows the ability of the PU composite to absorb a huge amount of impact energy before reaching a critical (visible) damage.

a)

b)

c)

d)
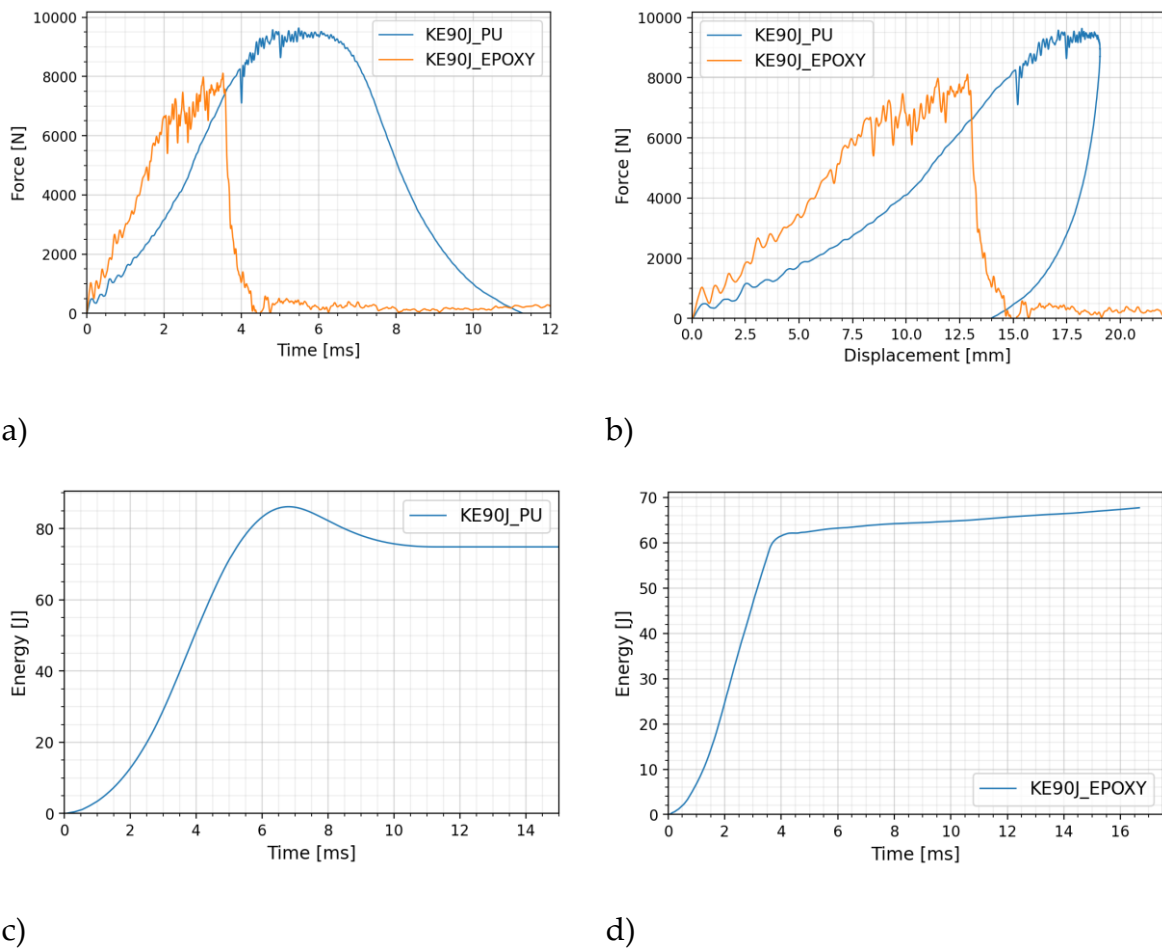
Figure 3-74: (a) Force-time, (b) Force-displacement, (c) Energy-time curves of Kevlar impacted specimens at 90J.

Specimen	E_{eff} [J]	E_{abs} [J]	E_{el} [J]	F_{max} [N]	Max displacement [mm]
KE30J_PU	29.24	22.34	6.90	5118.88	12.84

KE30J_EPOXY	29.29	11.701583	17.584459	758.50	8.99
KE50J_PU	47.91	38.14	9.78	7307.38	15.26
KE50J_EPOXY	/	/	/	/	/
KE90J_PU	85.37	70.16	15.21	9285.33	18.38
KE90J_EPOXY	/	/	/	/	/

Table 37: properties derived from Kevlar composites impact tests at different energies

.

PU	EPOXY

30J

KE30 IMPACT SIDE

30J

128
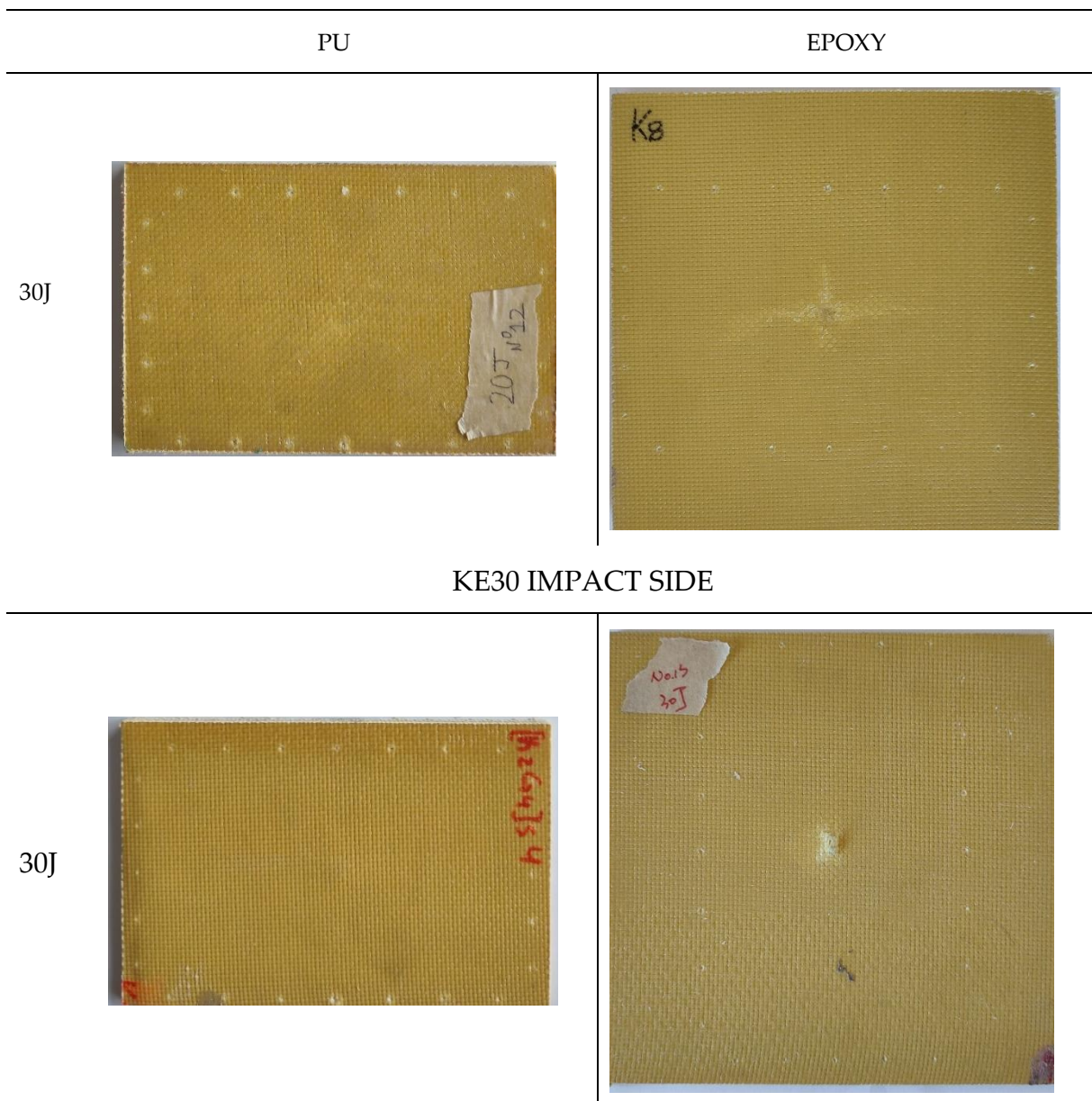
KE30J BACK SIDE

50J		
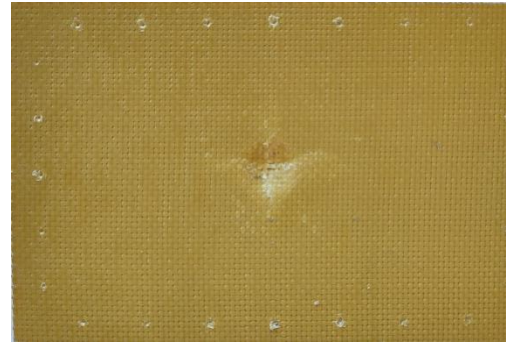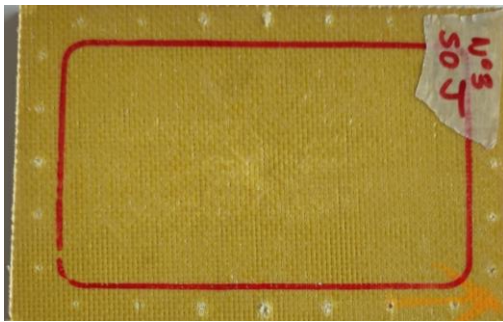
KE50J IMPACT SIDE

50J		

KE50J BACK SIDE

90J		
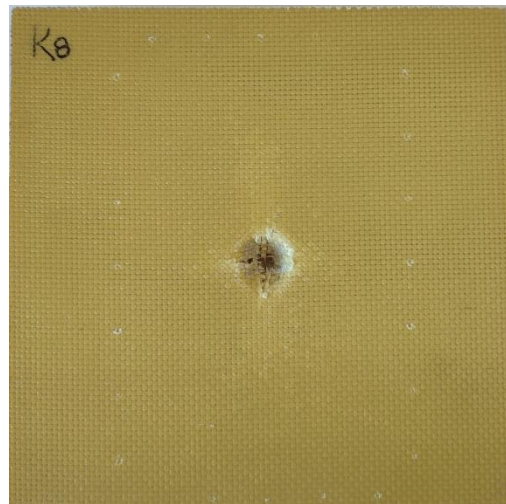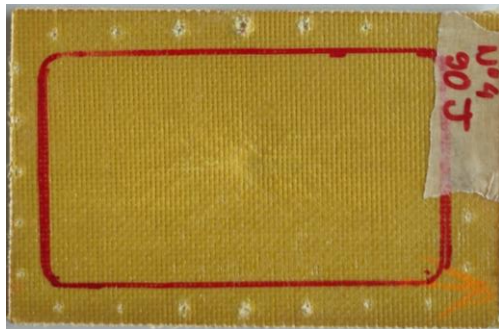
KE90J IMPACT SIDE

90J

KE90J BACK SIDE

Figure 3-75: visual comparison between impacted PU and EP Kevlar specimens.

(K2G4)S hybrid composite

For this hybrid it can be observed the exact same behavior which emerged from the pure glass and Kevlar composites.

In Figure 3-76, regarding the tests at 20J, the divergence in the composites behavior is pretty evident from the graphs. Same for 50J impact tests, which curves are represented in Figure 3-77. It can be seen that, as happened for Kevlar/epoxy sample at 50J, extent of damage begins to be consistent for the EP laminate, with starting signs of perforation, while the corresponding PU specimen at 50J shows almost no external damage on the impact side and a only small deformed area on the back side (Figure 3-78).
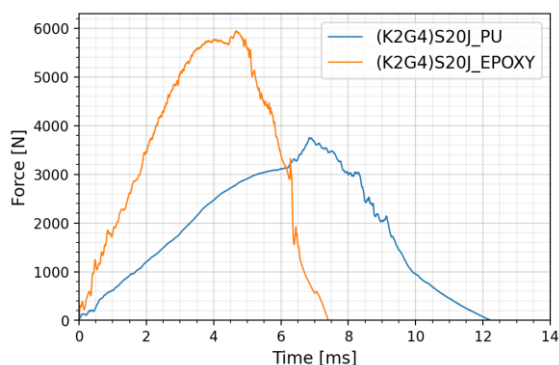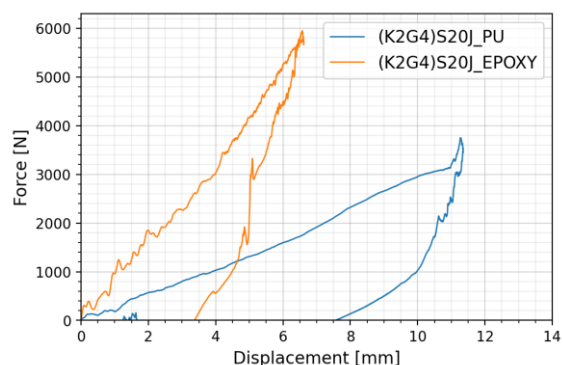
a)   b)
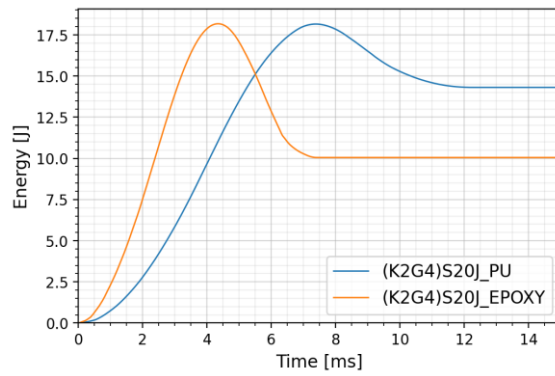
c)

Figure 3-76: (a) Force-time, (b) Force-displacement, (c) Energy-time curves of hybrid impacted specimens at 20J.
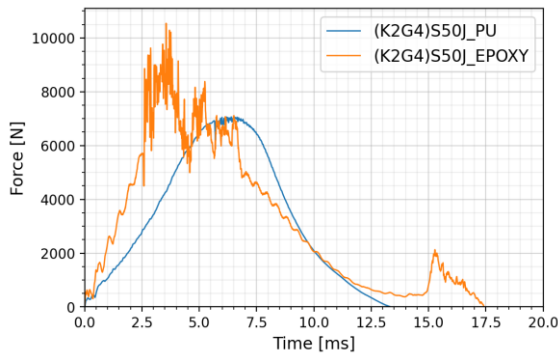
a)
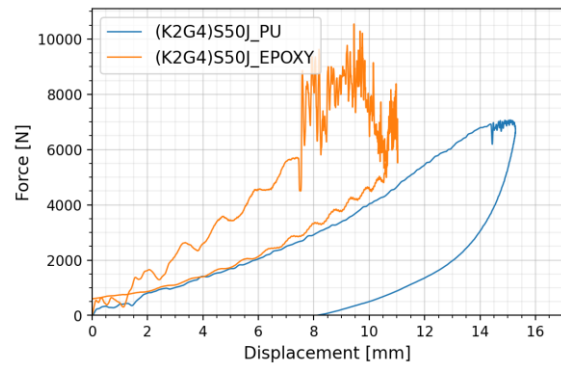
b)
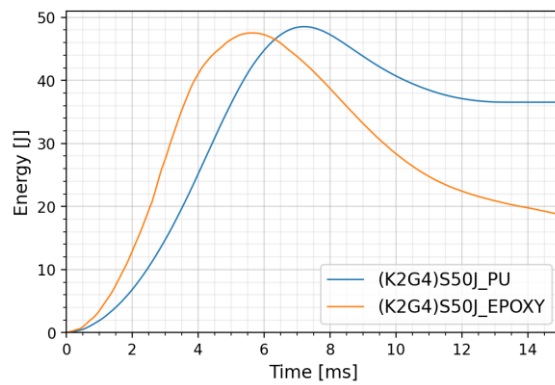
c)

Figure 3-77: (a) Force-time, (b) Force-displacement, (c) Energy-time curves of hybrid impacted specimens at 50J.

Specimen	E_{eff} [J]	E_{abs} [J]	E_{el} [J]	F_{max} [N]	Max displacement [mm]
(K2G4)S20_PU	18.16	14.31	3.85	3749.44	11.35
(K2G4)S20_EPOXY	48.52	36.54	11.98	7071.26	15.28
(K2G4)S50_PU	48.52	36.54	11.98	7071.26	15.28
(K2G4)S50_EPOXY*	47.52	18.65	28.88	10542.99	11.03

Table 38: properties derived from (K2G4)S PU and EPOXY composites impact tests at different energies.

(K2G4)S20 IMPACT SIDE

(K2G4)S20 BACK SIDE

(K2G4)S50 IMPACT SIDE

(K2G4)S50 BACK SIDE
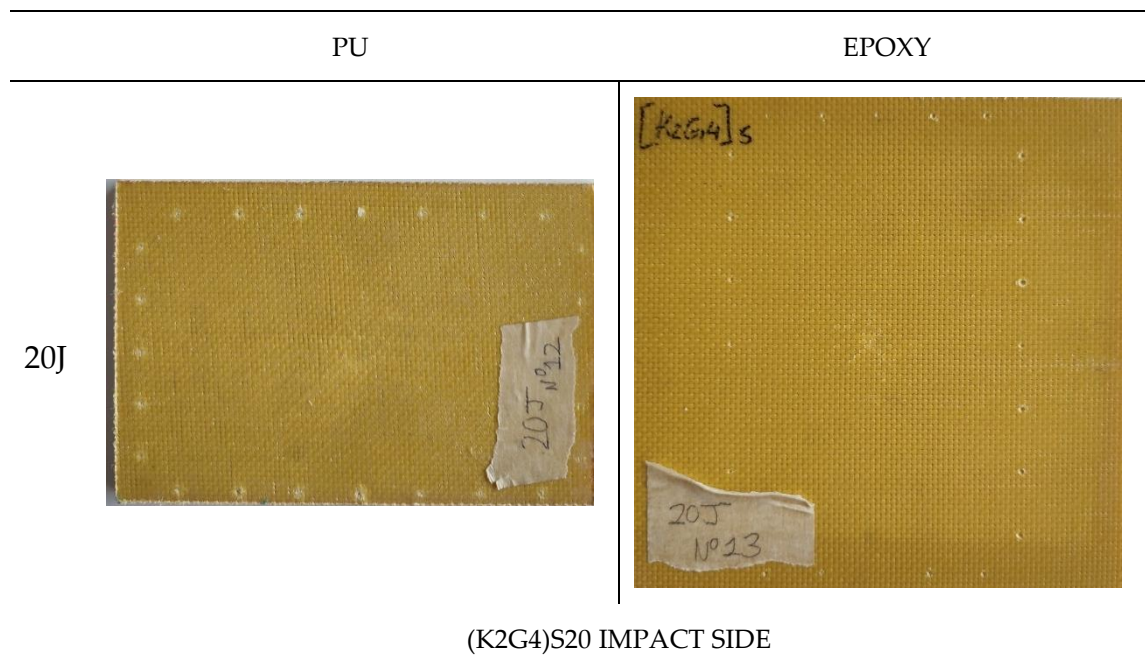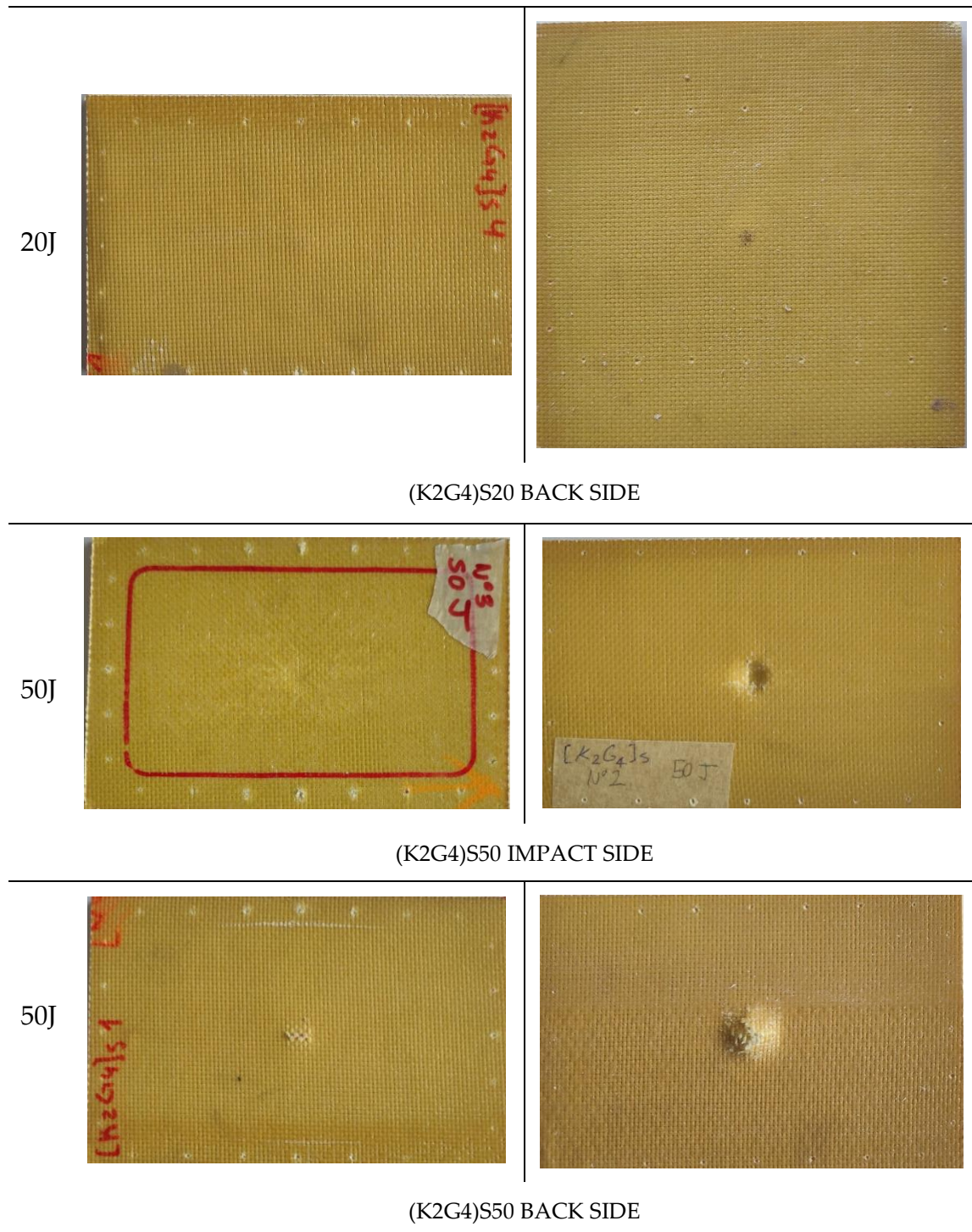
Figure 3-78: visual comparison between impacted PU and EP hybrid specimens.

Conclusive considerations

The histogram depicted in Figure 3-79 further highlight the divergence between the two kinds of composites in terms of absorbed energy. The blue columns represent the epoxy matrix composites while the orange ones the polyurethane matrix ones. Figure 3-79:For the PU matrix specimens, the percentage of absorbed energy is always above

75% for all samples, even for the lowest impact energies, and, as shown in Section 3.5.4, this percentage tends to increase. The EP composites, in comparison, always show a lower value. Moreover, it should be emphasized the fact that none of the novel specimens were perforated during the impacts, which reached 120J impact energy. On the other side, for the EP samples, the resulting impact damage started to be critical already at 50J. It can be asserted that the composites constituted by the elastomeric PU matrix material exhibits the enhanced capability, respect to the EP composites, to absorb a consistent amount of energy though its deformation before reaching a critical extent of damage, thus an increased toughness.
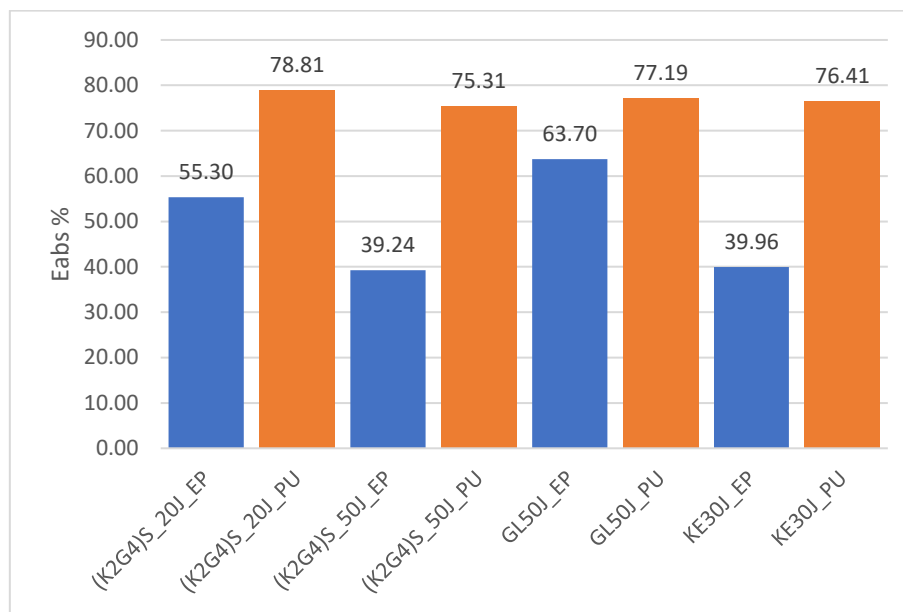
Figure 3-79: comparison between the E_{abs}% of EP and PU matrix composites.

In Table 39 values of absorbed energy and the resulting percentage difference between the two kinds of composites are reported. The recorded values are 90% higher in the PU specimens compared to the epoxy ones.

Sample	(K2G4)S_20J	(K2G4)S_50J	GL50J	KE30J
E_{abs} PU	14.31	36.54	37.27	22.34
E_{abs} EP	10.05	18.65	30.9	11.7
% difference	42.39	95.92	20.61	90.94

Table 39: E_{abs} values of EP and PU matrix specimens and relative %difference.

Additionally, it can be observed in Figure 3-80 how the maximum displacement is always higher in the elastomeric matrix composite with respect to the epoxy matrix one , while it is the opposite for the impact force, which is always lower, as shown in Figure 3-81: comparison between the maximum impact force of EP and PU matrix

composites. Those considerations illustrate the higher stiffness of the EP composites respect to the PU ones, which shows a softer behavior.
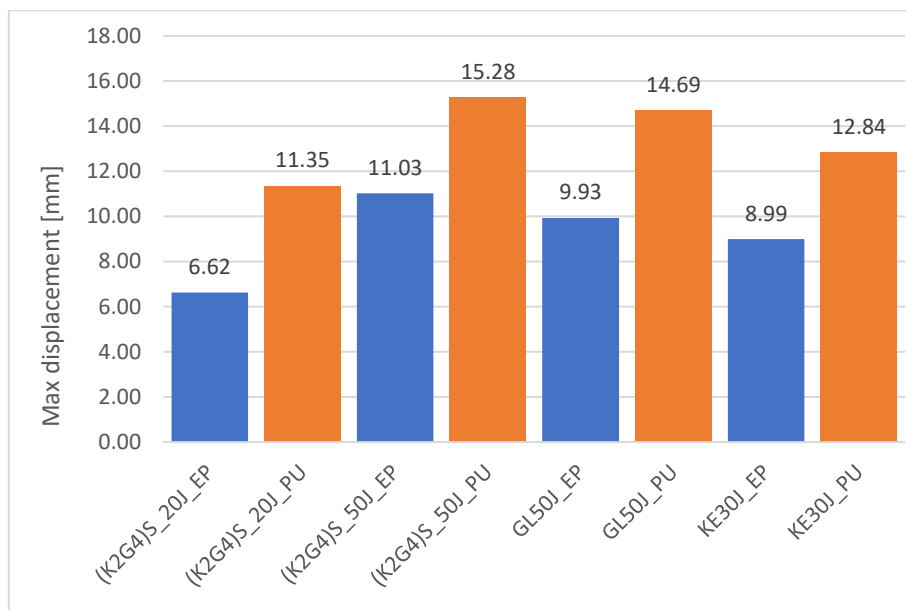
Figure 3-80: comparison between the maximum displacement of EP and PU matrix composites.
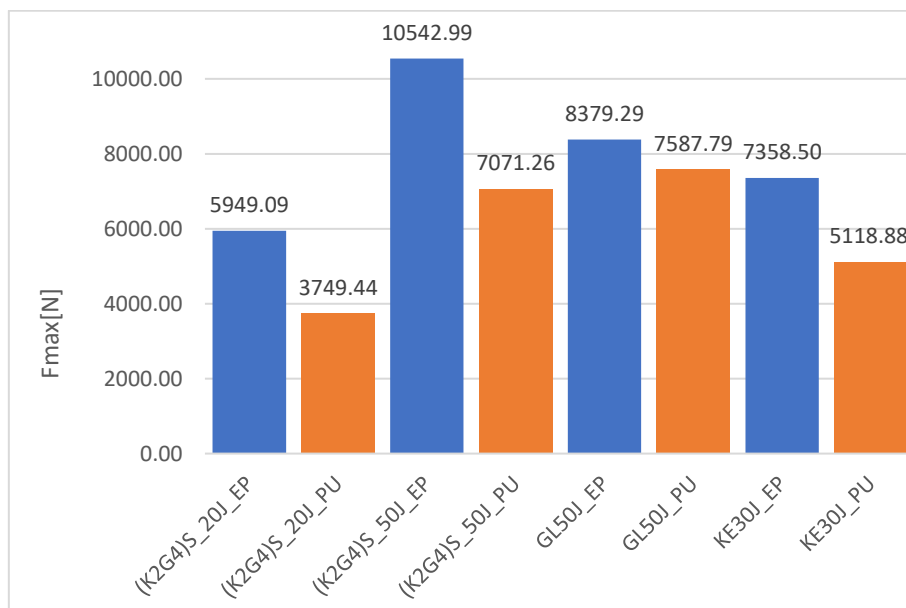
Figure 3-81: comparison between the maximum impact force of EP and PU matrix composites.

3.5.6. Thermographic nondestructive investigation

From this subsection results which are explicit exposed will be again related only the PU matrix composites.

In order to investigate the damage extent on the panels, NDI was performed after tests, in particular, thermographic images were taken from the specimens. The images were taken both from the impacted side and from the back side of the panels.

From the images obtained it was not easy to localize precisely damaged regions on the panels. Comparing with images taken in the previous impact experimental campaign, performed with the same thermographic camera, the damaged area was readily identified in that case. Here, instead, the damage investigation with this method did not gave the same satisfactory results. However, it must be considered that the epoxy resin composites showed also externally more evident damage and often perforation, thus it is not completely surprising that also from the NDI the damage identification resulted more complicated.

As indicated in the D7136/D7136M – 15 standard, an indicative extent area of damage was calculated for the panels, as well as maximum diameter of damage and width.
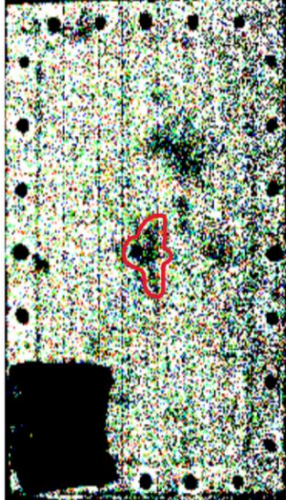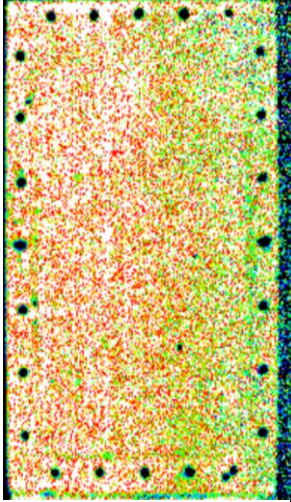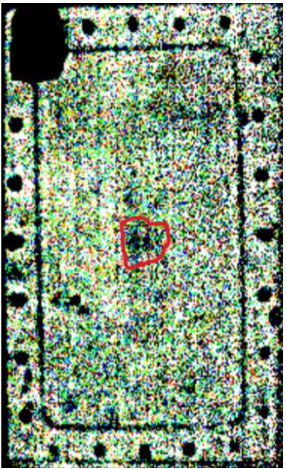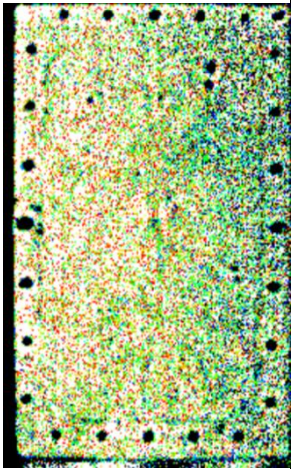
The raw data obtained from the thermographic camera was elaborated using Python. For each panel a different output scale was set for the best possible visualization of the damage. Then, ImageJ software was adopted for the measurement of the damage extent parameters on the impacted panels.

The identification of the damaged area is to be considered as rather arbitrary in this specific case. As it is not evident, it depends on how the subject performing the analysis consider or not an area to be damaged to identify its extent. Also, in some of the images, nothing is observed. It shall be noticed anyway that this result is to be considered normal as thermography is not the best choice for NDI on PMC. More appropriate techniques should be adopted to obtain better results.

3.5.6.1. Glass composites

In the Table below the thermographic images of the impacted glass specimens are shown both from the impact front and from the back front, aside to the pictures of the tested samples. For the panels tested at 50J and 90 J the extent of the damaged area identified for the impacted side is similar for the two energies, while a consistent increase is observed for the panel tested at 120J, as expected. Also for the panel at 90J an increase respect to the 50J measures was expected, but actually the area calculated is slightly smaller. Moreover, for all tested energies, none of the images taken from the back side of the panels, shows indication of damage. These two last considerations might be already an indication of how this kind of NDI could not be the best choice when examining similar materials.

Sample	Impact side damage extent [mm]		Back front damage extent [mm]

GL50J	Area=1.783 Dmax=2.509 W=1.246		/
GL90J	Area=1.764 Dmax=1.882 W=1.764		/
GL120J	Area=5.534 Dmax=3.338 W=1.686		/
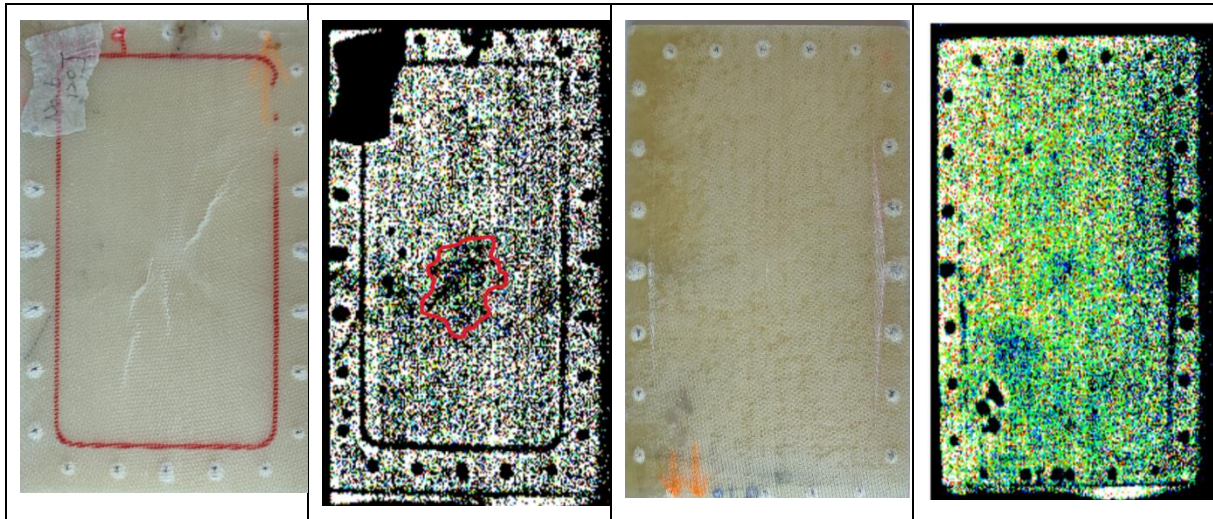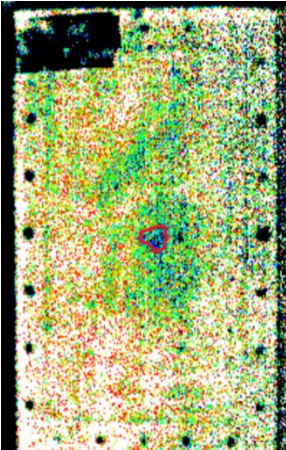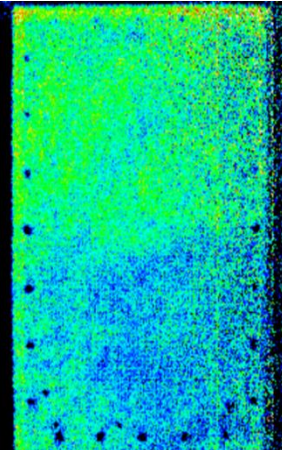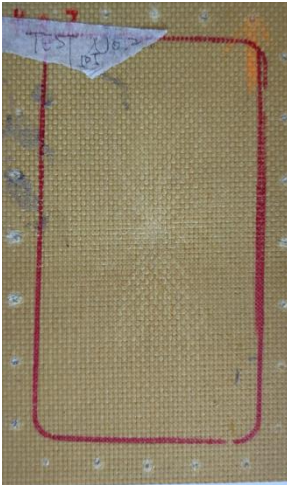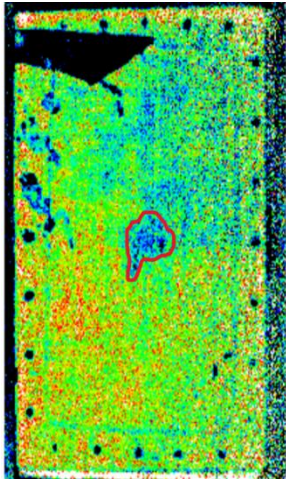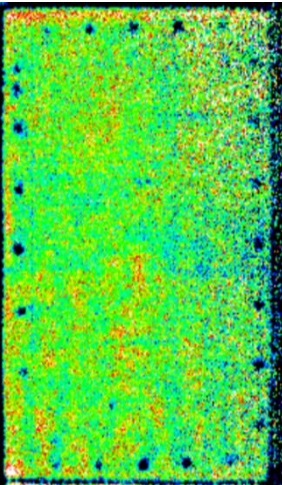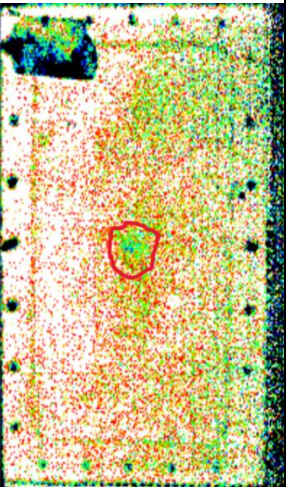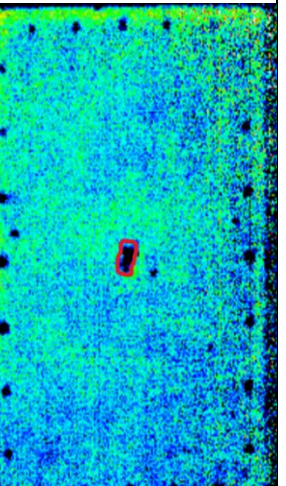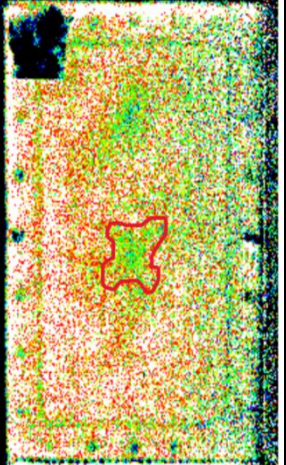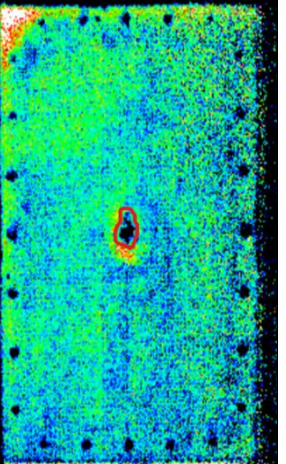
Table 40: thermographic results of impacted glass composites.

3.5.6.2. Kevlar composites

Better visualization was reached when examining the Kevlar panels, as can be seen in the following Table. In that case the extent of the identified damaged area, for the impacted side, increased in a reasonable way with increasing impact energies, reaching its maximum for sample K8_120J-1. For what concern the back side of the panels nothing can be observed for 30J and 50J impact energy, as for the glass back side specimens. For 90 and 120J back side panels instead an associated area of damage can be individualized, very limited for samples K8_90J and K8_120J-1, much more extended for the K8_120J-2 sample.

Sample	Impact side damage extent [mm]		Back side damage extent [mm]
KE30J	Area=0.513 Dmax=0.924 W=0.874		/

KE50J	Area=1.680 Dmax=2.349 W=1.470		/
KE90J	Area=1.908 Dmax=1.670 W=1.314		Area=0.400 Dmax=1.091 W=0.508

KE120J-1	Area=3.226 Dmax=2.878 W=2.591		Area=0.678 Dmax=1.235 W=0.721
KE120J-2	Area=2.338 Dmax=1.969 W=1.281		Area=2.132 Dmax=1.799 W=1.298

140
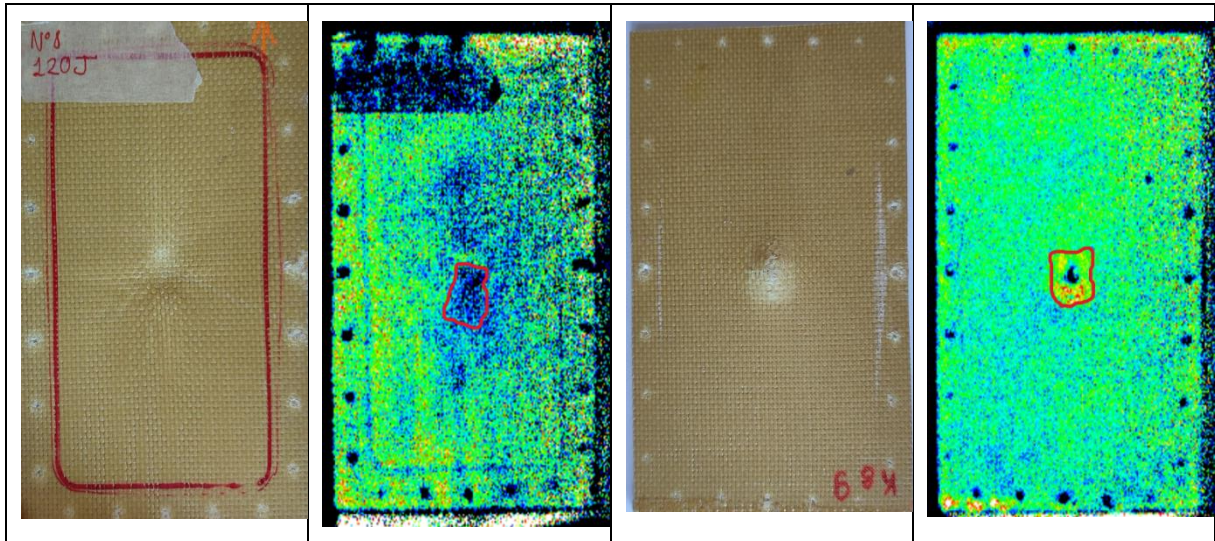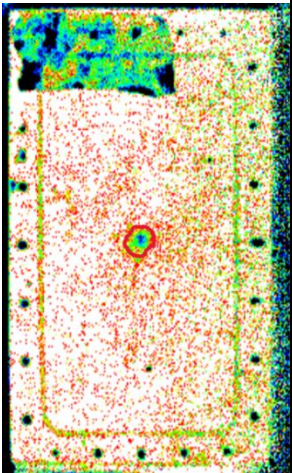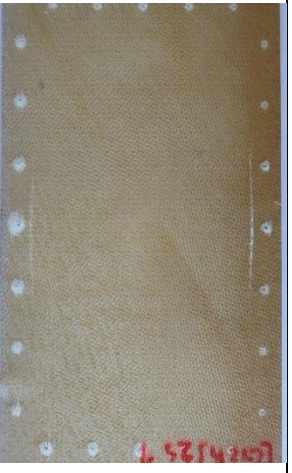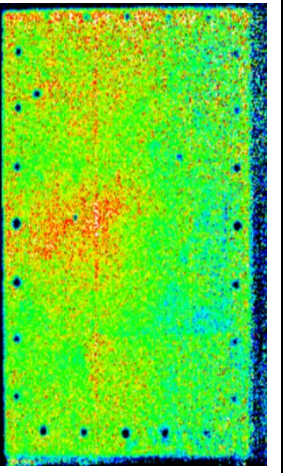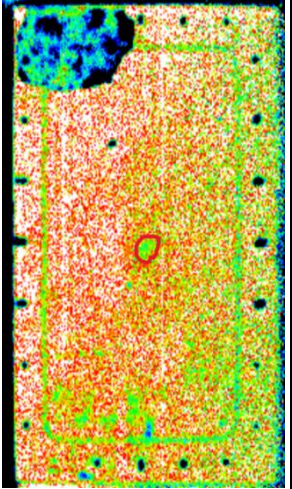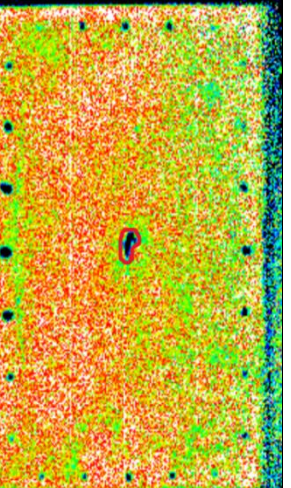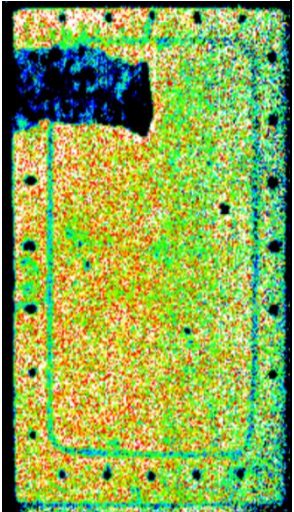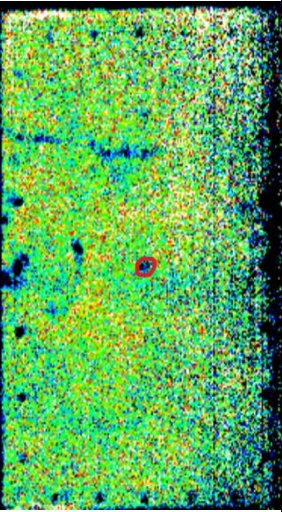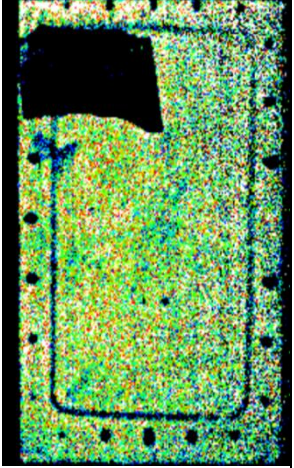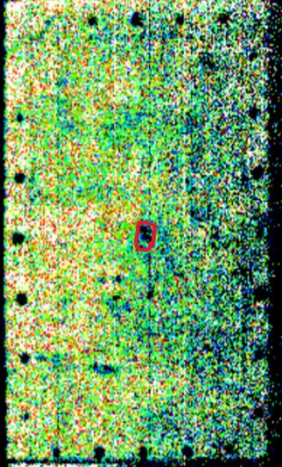
Table 41: thermographic results of impacted Kevlar composites.

3.5.6.3. Hybrid composites

Results are exposed in the below Table. For the hybrids, unexpectedly, and contrary to what is observed for the pure Kevlar and glass samples , in three out of six panels ((G4K2)S_50J, (G2K)2S_90J, K2G4)S_90J)   no damage is visualized from the thermography on the impacted side of the samples, while, even if limited, for the same samples a damaged region is captured from the back side. Overall, the extent of the damaged area for the hybrids is anyway very limited for all the samples here examined.

Sample	Impact side damage extent [mm]		Back side damage extent [mm]
(G2K)2S_50J	Area=0.660 Dmax=0.970 W=0.940		/

(G2K)2S_90J	Area=0.434 Dmax=0.758 W=0.639		Area=0.408 Dmax=1.078 W=0.379
(G4K2)S_50J	/		Area=0.203 Dmax=0.408 W=0.410

(G2K)2S_90J	/		Area=0.452 Dmax=1.001 W=0.519
(K2G4)S_50J	Area=0.336 Dmax=0.714 W=0.543		/
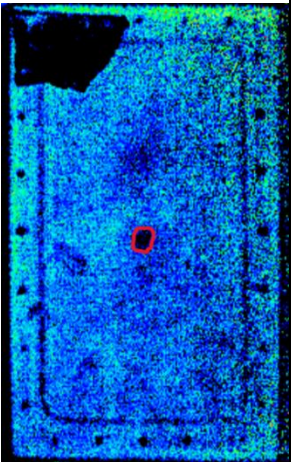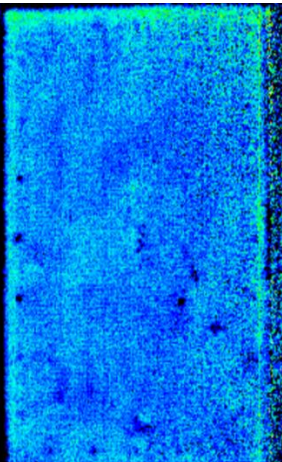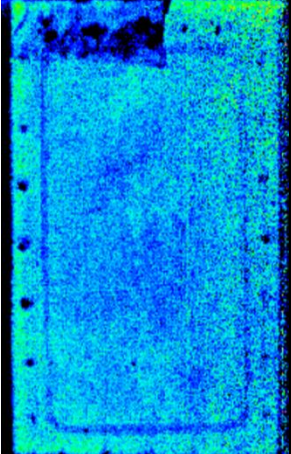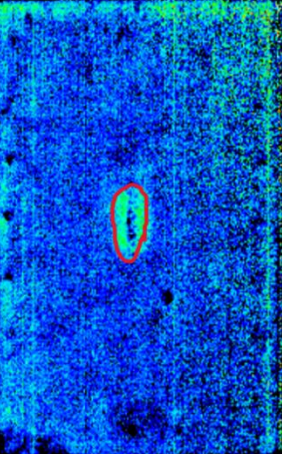
(K2G4)S_90J	/		Area=2.287 Dmax=2.220 W=0.889

Table 42: thermographic results of impacted hybrid composites.

4 Numerical investigation

In this Chapter the model adopted for the impact simulations is first described in detail, with indication of the imposed most relevant settings for this kind of analysis. The comparison between the numerical and the experimental results is then depicted for the tested specimens at 50J and 90J, with the related discussion.

4.1. Material model

The material properties of the composite panels were defined according to the constitutive model for fabric reinforced composites which was described in detail in Section 2.4.

To activate the model the material name must start with the string ABQ_PLY_FABRIC. The number of solution dependent variables (DEPVAR) is 16.

In Table 43 the specific properties calculated from the experimental campgain for the numerical simulations are shown. The only values which were not possible to calculate directly from experimental tests are the fracture energy per unit area in tension and in compression. The values adopted then in the numerical simulations were taken from the literature considering epoxy resin matrix composites. Another approximation regards the values of the Young's modulus and the Poisson ratio in compression, which were taken as equal to the ones obtained from tension tests.

Description	Symbol	Glass	Kevlar
Young's modulus in tension along fiber direction 1	E_{1+}	18299.04	5305.88
Young's modulus in tension along fiber direction 2	E_{2+}	17355.88	8220.51
Poisson ratio in tension	ν_{12+}	0.056	0.36
Shear modulus	G_{12}	523.4	357.11

Young's modulus in compression along fiber direction 1 *	E_{1-}	18299.04	5305.88
Young's modulus in compression along fiber direction 2 *	E_{2-}	17355.88	8220.51
Poisson ratio in compression *	ν_{12-}	0.056	0.36
Tensile strength along fiber direction 1	X_{1+}	367.7	293
Compressive strength along fiber direction 1	X_{1-}	37	8.01
Tensile strength along fiber direction 2	X_{2+}	326.72	329.05
Compressive strength along fiber direction 2	X_{2-}	37	13.15
Shear stress at the onset of shear damage	S	7	5
Energy per unit area for tensile fracture along fiber direction 1 **	G_f^{1+}	34	40
Energy per unit area for compressive fracture along direction 1 **	G_f^{1-}	34	40
Energy per unit area for tensile fracture along fiber direction 2 **	G_f^{2+}	34	40
Energy per unit area for compressive fracture along direction 2 **	G_f^{2-}	34	40
Parameter in the equation of shear damage	α_{12}	0.1208	0.0858
Maximum shear damage	d_{12}^{max}	1	1
Initial effective shear yield stress	$\tilde{\sigma}_{y0}$	6	3
Coefficient in hardening equation	C	483.75	179.61
Power term in hardening equation	p	0.4352	0.4744

*compression values taken from tensile tests
**data from literature

Table 43: material properties obtained from experimental tests (*; **)

4.2. Impact test model building

The numerical simulations about the low velocity impact tests were performed using the Explicit analysis method.

The symmetry of the experimental test configuration allows the modelling of the test considering only one firth of the real case dimensions. The panel and the impactor are cut though their thickness direction in the z-y and z-x planes, and, in the model, the impactor hits the panel on its left-down corner. This aspect is important when running the numerical analysis for computational costs saving.

International system of units was adopted, using mm as a measure of length. All input data must be inserted with consistent units and output data are given accordingly.

Quantity	lenght	force	mass	time	stress	energy	density
SI(mm)	mm	N	tonne	s	MPa	mJ	Tonne/mm3

Table 44: consistent units of measure.

The composite panel is defined as a 3D deformable body to which a homogeneous-shell/continuum-shell section was assigned. Material properties were defined according to the constitutive model for fabric reinforced composites previously described, with the material properties obtained from the experimental tests. Simpson thickness integration rule was adopted, with thickness integration points equal to 5, recommended for homogeneous shell sections. The part was created as a single body which was then partitioned though the thickness in order to generate the composite layers: 16 layers for glass, 8 layers for Kevlar and 12 layers, with varying thicknesses and distribution, for hybrids. No contact properties were specified between the layers. This choice was dictated by the fact that observing the damage on the composite panels after impact tests, delamination did not seem to be the dominating cause of damage. Moreover, from the experiments, considering the emerged toughness from the specimens, the above approximation seemed reasonable in first analysis. A simplified approach was preferred and, if considered necessary for the analysis, contact properties could have been defined in a second moment.
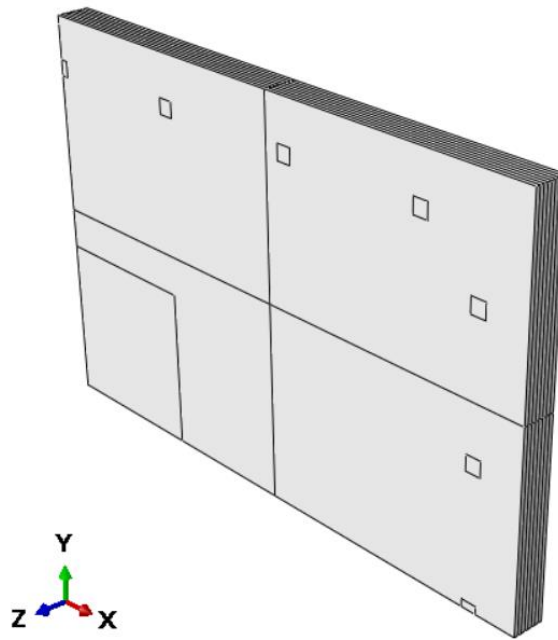
Figure 4-1: Kevlar specimen part.

The impactor is defined as a 3D-discrete rigid body. A rigid body constraint was generated to link the part to its rigid body reference point. All the rigid body properties were then assigned directly to the RP, such as mass, impact velocity, and boundary conditions.
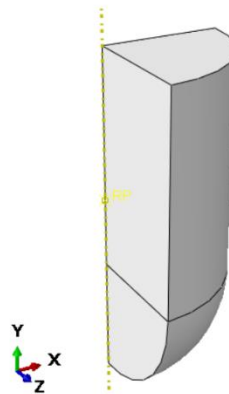
Figure 4-2: impactor part.

Procedure adopted for the impact step analysis is general Dynamic/Explicit. The time period is 0.0015 seconds. Nonlinear effects of large displacements for the impact step is considered. For what concern the incrementation, the automatic type was chosen, with a global stable increment estimator. Remaining parameters for the step definition were left by default.

The interaction between composite panel and impactor is defined in a limited square region, of dimensions 20x20, around the impact area on the panel surface and the hemispherical surface of the impactor. Surface-to-surface (Explicit) type of interaction is set, and the mechanical constraint formulation chosen is the penalty contact method

with finite sliding formulation. Penalty friction formulation is defined for the tangential behavior, with friction coefficient equal to 0.3. For the normal behavior hard-contact option is set, with default constraint enforcement method.
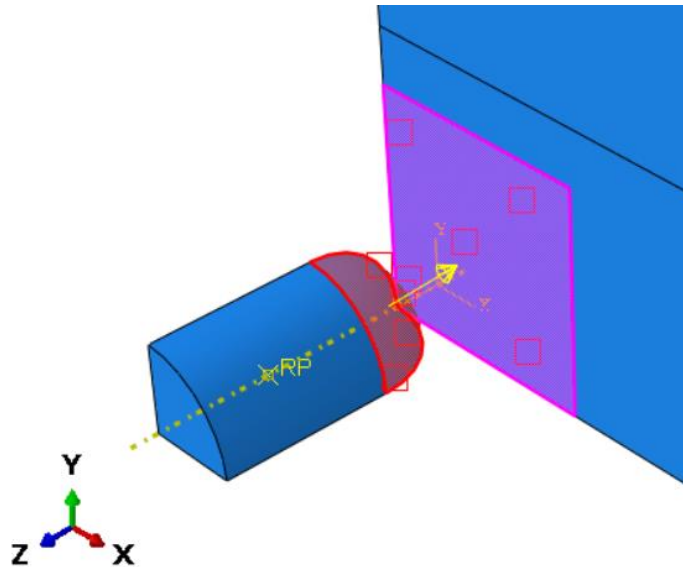
Figure 4-3: highlighted participating surfaces in the defined specimen-impactor interaction.

The element type assigned to the composite panel is a 8-node quadrilateral in-plane general-purpose continuum shell with reduced integration and enhanced hourglass control (SC8R). Second order accuracy is activated for the elements. Mesh size in the impact area is 0.2 while the seed global size is set to 1.5.

In the first simulations attempts, starting with lowest energies, seed size around impact area was coarser (0.5), hourglass control was left by default, and second order accuracy was not active. Hourglass effect completely dominated the deformation of the elements in the impact area and the phenomenon was clearly visible also immediately after the impact. In Figure 4-4 the deformed part at step time 0.003 s is shown and hourglassing phenomenon is evident on the impact location.
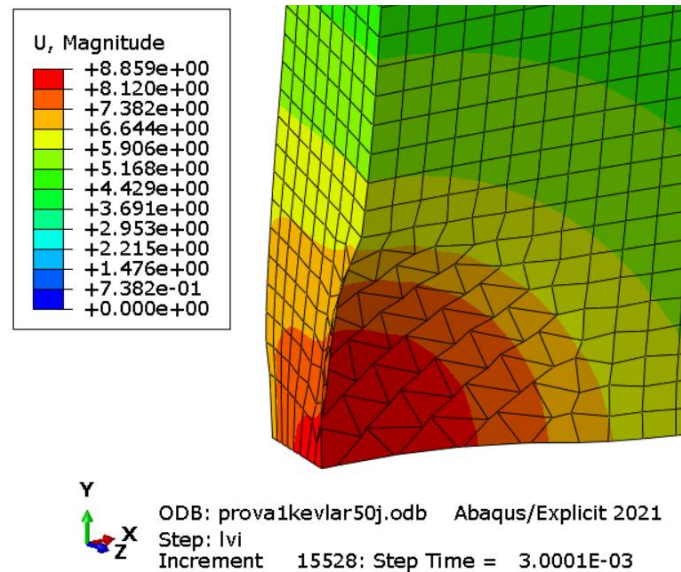
Figure 4-4: impacted area in Kevlar composite model showing elements hourglassing.

As a rule of thumb, for results to be considered reliable, the artificial energy generated due to hourglass modes in a numerical simulation should be lower than 10% of the total internal energy measured in the model. From the first simulations with default hourglass settings this percentage overpassed 20% during the analysis for glass simulations (Figure 4-5: percentage of artificial energy respect to internal energy for glass sensitivity simulations., simu1) and reached 16% for the Kevlar composite simulations (Figure 4-6: percentage of artificial energy respect to internal energy for Kevlar sensitivity simulations., simu1 and simu2).

To act on the hourglass phenomenon (Section 2.3), sensitivity tests were performed on the model keeping all settings unchanged, except for the element type control settings. First, as coarser elements are more affected, the mesh was refined but not excessively (from 0.5 to 0.4), trying to avoid too much the increase of the computational analysis cost and time. Hourglass control was then set to relax stiffness. The scale factor for the hourglass displacement was set first to 3 (Figure 4-5Figure 4-5: percentage of artificial energy respect to internal energy for glass sensitivity simulations., simu2 for glass and Figure 4-6, simu3 for Kevlar) and then to 5 (simu3 for glass and simu4 for Kevlar). The measured hourglass energy remained high and also visually the phenomenon was still evident. As there was no significant improvement for the hourglass effect with first variation in the hourglass scale displacement, the idea to further increase its value from 3 to 5 in this case was to verify if the inefficiency in solving the issue was related to the scale factor or to the hourglass control mode itself. As no improvement was observed neither in that second case a different hourglass control mode had to be chosen. Moreover, in the Abaqus user 's manual, it is recommended not to use excessively high values for the displacement scale factor for the hourglass control, as it might generate too much stiffness in the material.
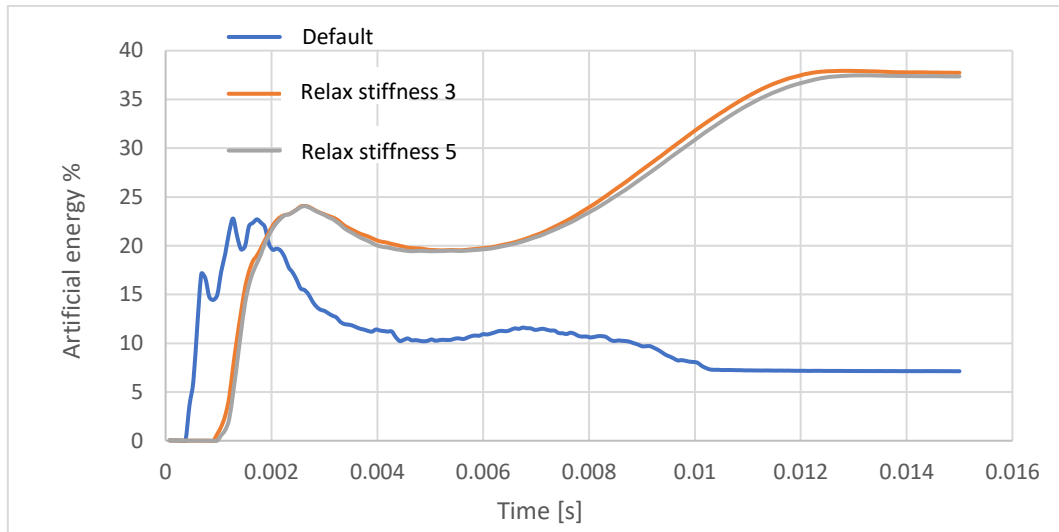
Figure 4-5: percentage of artificial energy respect to internal energy for glass sensitivity simulations.
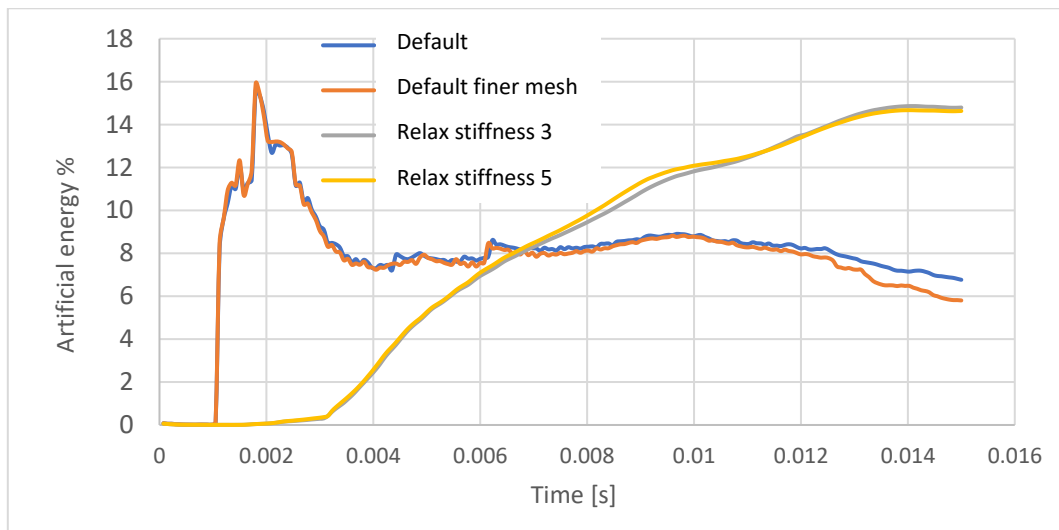
Figure 4-6: percentage of artificial energy respect to internal energy for Kevlar sensitivity simulations.

From a deeper investigation about the performance of continuum shell elements under bending, it was decided in the following sensitivity analysis to activate the enhanced hourglass control, and the mesh was further refined, from 0.4 to 0.2. In practical examples given in ABAQUS reference manual, with similar loading cases, it is shown how significant improvements were obtained about element hourglassing with the variation of these two parameters. From those last simulations results hourglass phenomena was almost completely eliminated as shown in Figure 4-7. Also, in Figure 4-8, it can be observed for the Kevlar material model, how the percentage of artificial energy respect to the internal one in the last described sensitivity test (simu5) is greatly reduced to a value lower than 1.2%.
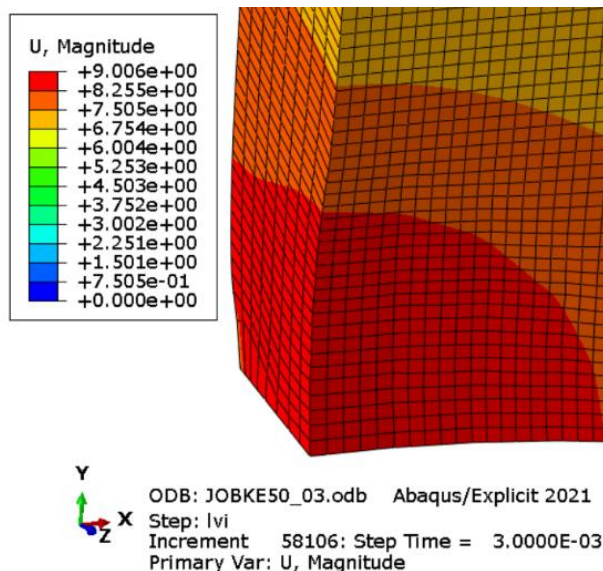
Figure 4-7: impacted area in the adjusted Kevlar composite model.
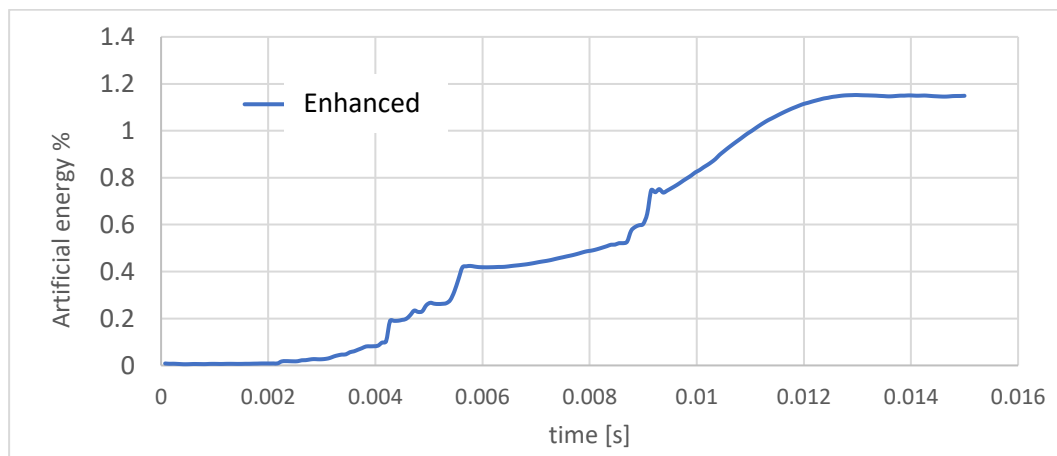
Figure 4-8: percentage of artificial energy respect to internal energy for.

Another sensitivity test was then also performed to verify if the enhanced control mode could be used also with a coarser mesh (0.4) but hourglass phenomena was again present, indication that for our analysis seed size must be kept below a certain limit.

For what concern the impactor, element type is a 4-node 3-D bilinear rigid quadrilateral element. No other control settings are available for rigid elements.

Boundary conditions active on the model are (Figure 4-9):

- Pin BC replicating the screws in the fixture in contact with the surface. In total 6 squares of area 2x2mm were created on both sides of the panel for this purpose.
- X-symmetric (U1=UR2=UR3=0) BC on the surfaces where the model was cut through its thickness by the Z-Y plane;
- Y-symmetric (U2=UR1=UR3=0) BC on the surfaces where the model was cut through its thickness by the Z-X plane.
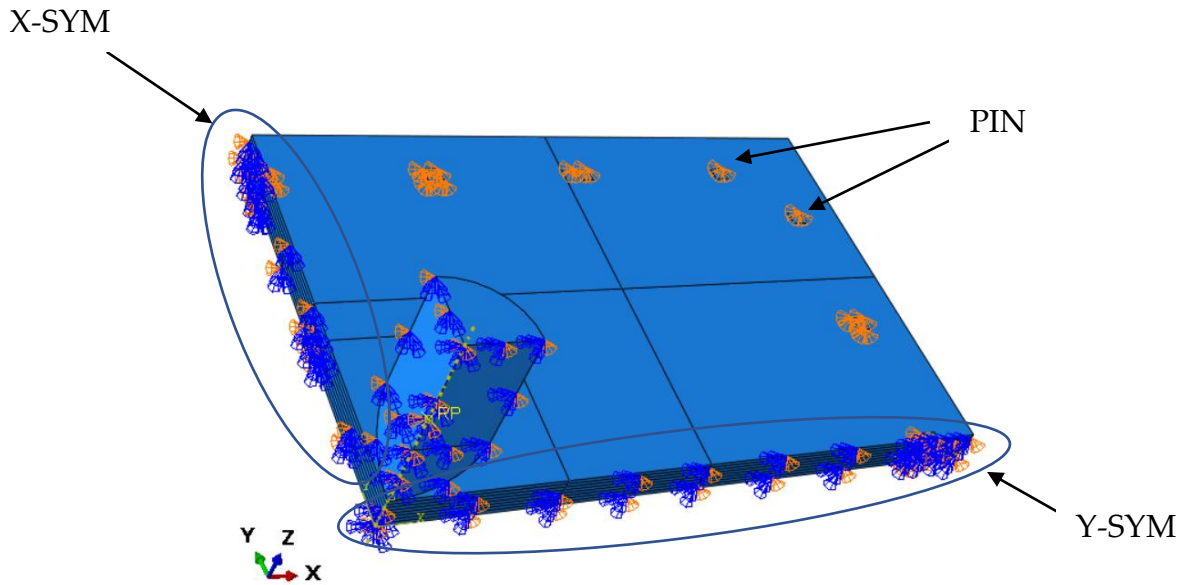
Figure 4-9: impactor-panel assembly with assigned boundary conditions.

4.3. 50J impact energy simulations

Once the hourglass problem arising from the impact simulations was solved for the Kevlar composite material, the analysis was run also for the other models, maintaining the previously defined settings for the analysis. In the following section the results obtained from the numerical simulations of the 50J impact energy are exposed.

Results for glass and Kevlar composites will be exposed together, and subsequently also the hybrids. Experimental results are compared with the numerical analysis results through the usuals force-time, force-displacement, and energy-time curves. Relevant properties from the tests, such as maximum displacement, force, and absorbed energy, will be confronted in terms of absolute value and the percentage difference between experimental and numerical analysis values are reported as well.

4.3.1. Pure composites

Comparing experimental and numerical analysis results in Table 45 for the Kevlar composite it can be observed a good match in terms of maximum impact force and maximum displacement measured. It can be noticed how the percentage difference between those values is quite small, below 1% for the maximum displacement and under 3% for maximum impact force. This match is highlighted by the representing curves in Figure 4-10. It can be seen how the trend of the curves during the impact, especially for the slopes, is very close to each other. In the unloading phase, however, this proximity in behavior starts to diminish. For glass composite instead the simulation results compared to the experimental ones give less comparable results. Maximum impact force and maximum displacement measured from the simulation

shows a high deviation from the experiments, in percentage around 28% and 26%, respect to the 3% and 1% showed by Kevlar. The resulting curves from the simulation show a material with a much greater stiffness with the respect to the effective one. It is interesting to notice how those curves look alike the epoxy matrix composites when they were confronted with the PU laminates in Section 3.5.5.

In both cases, for what concern instead the absorbed energy from the material, the numerical simulation is not able to reproduce the behavior of those kinds of composites. As commented in final sections of Chapter 3, the laminates under investigation show an enhanced toughness due to the elastomeric matrix material, thus also showing a high value of absorbed energy. In the simulations most of the impact energy is instead converted in elastic energy, again showing a characteristic of stiffer materials. For Kevlar, the initial trend of the curves almost overlaps, but after the impact also for this material deviation becomes more evident. Here the value of the effective absorbed energy respect to the simulation test is almost twice. For the glass composite the difference is even higher, reaching a percentage difference value of almost 60%.
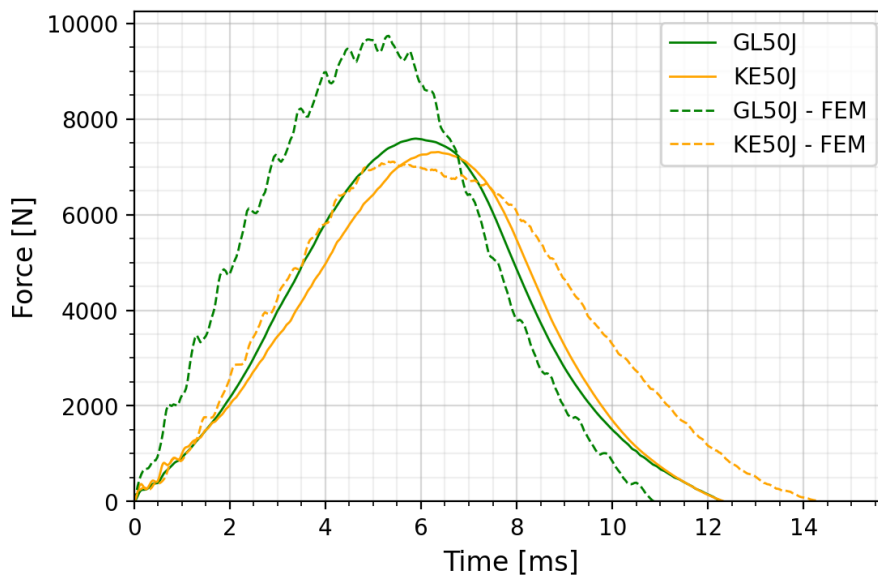
a)
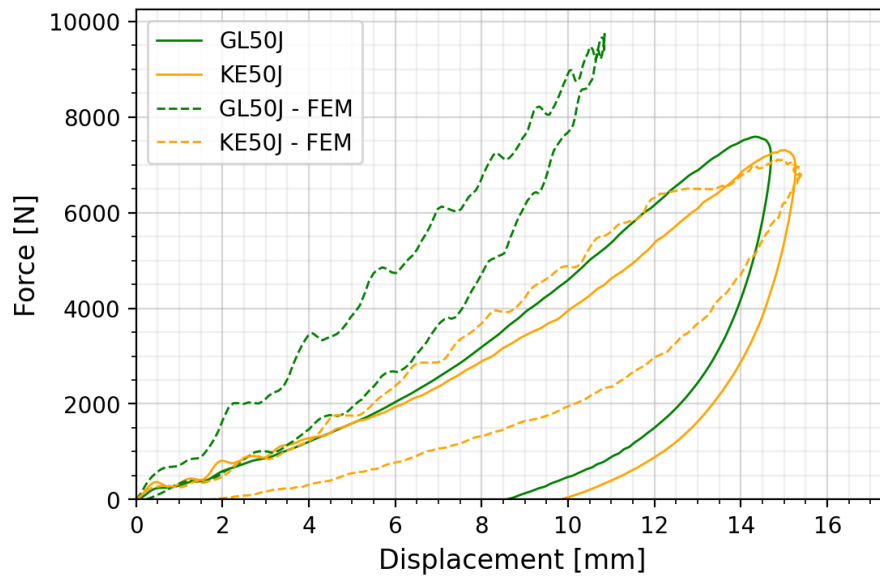
b)
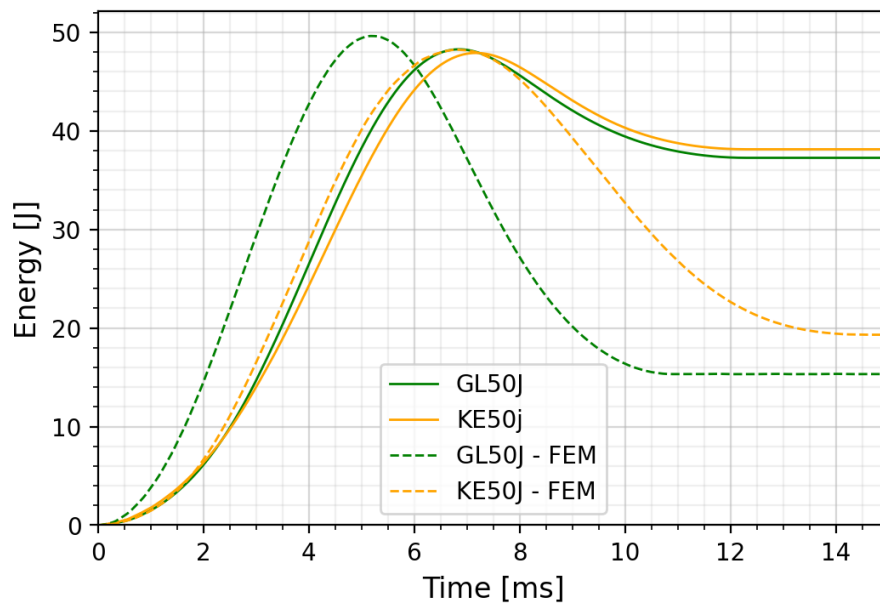
c)

Figure 4-10: glass and Kevlar experimental and numerical (a) Force-time curves , (b)Force-displacement curves, (c) Energy-time curves at 50J.

Property	F_{max}[N]	Maximum displacement [mm]	E_{abs}[J]
GL50J	7307.38	15.26	38.14
GL50J - FEM	7108.811	15.393	19.332
|%difference|	2.71735	0.86041	49.30717
KE50J	7587.79	14.69421	37.26948
KE50J - FEM	9736.982	10.8455	15.328
|%difference|	28.3243	26.192	58.87252

Table 45: comparison between experimental and numerical results for glass and Kevlar composites at 50J.

4.3.2. Hybrid composites

For the hybrid composites it can be noticed how for the configuration in which Kevlar plies are on the outer surface numerical and experimental results show a better match respect to when glass plies are on the outside. From the curves in Figure 4-11 it is also readily noticed how the curves from (G2K)2S and (G4K2)S are almost overlapping. This can be observed also by the results reported in Table 46: comparison between experimental and numerical results for hybrid composites at 50J.Table 46. Those considerations are an indication of how the performed simulations are very much influenced by the material immediately in contact with the impactor, not taking much into account the overall laminate configuration. The percentage differences in results for specimen (K2G4)S are around 17% for what concern the maximum impact force and 6% for the displacement, actually not a bad result when considering impact simulations, while for the remaining hybrids they are respectively around 32% and 17%. What just discussed is in accordance with results obtained from pure composites, where in fact a better match was obtained from the single fiber Kevlar laminate. As before for all configurations the value of absorbed energy is far distant from the effective experimental value.
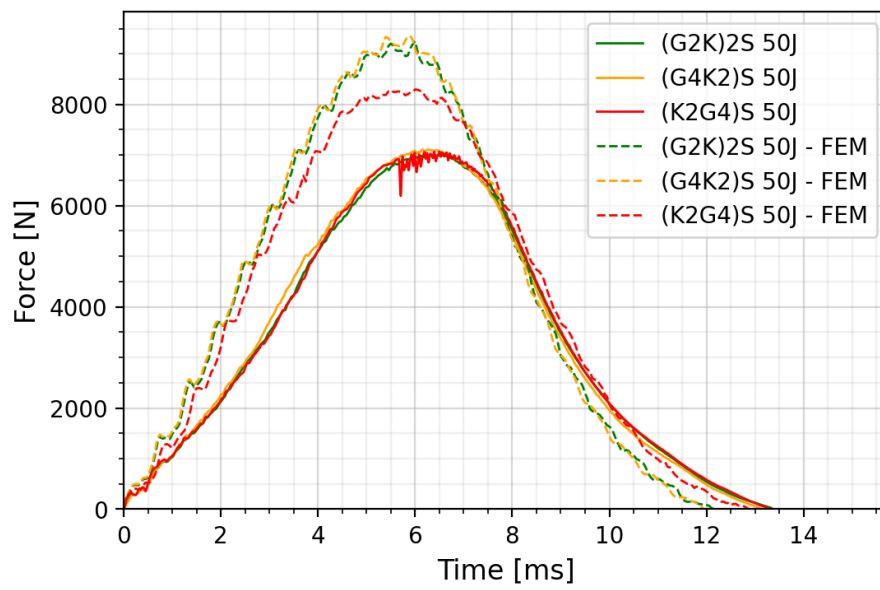
a)
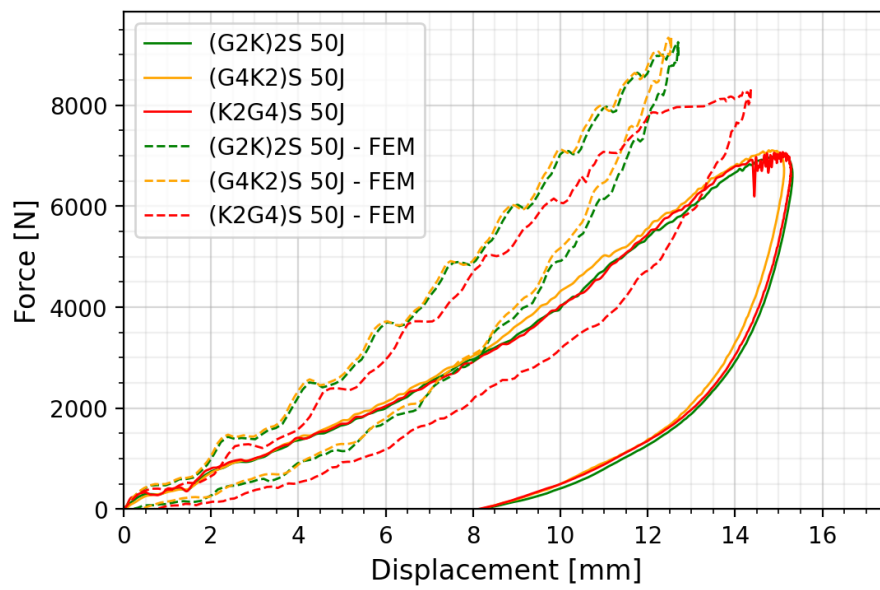
b)
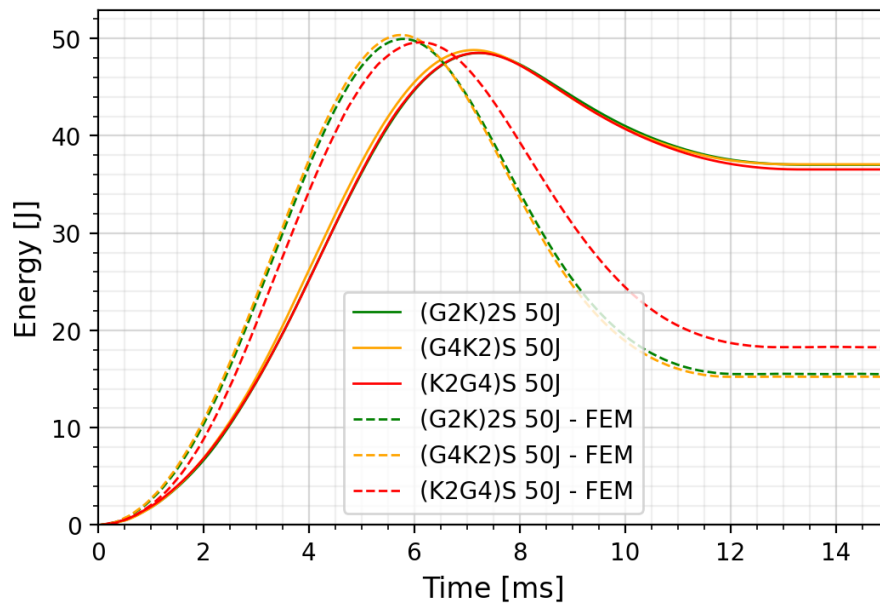
c)

Figure 4-11: hybrids experimental and numerical (a) Force-time curves , (b)Force-displacement curves, (c) Energy-time curves at 50J.

Property	F_{max}[N]	Maximum displacement [mm]	E_{abs}[J]
(G2K)2S 50J	7006.83	15.32	37.03
(G2K)2S 50J - FEM	9249.69	12.703	15.512
|%difference|	32.00966	17.0556	58.1052
(G4K2)S 50J	7107.08	15.12	37.07
(G2K)2S 50J-FEM	9356.126	12.5445	15.232
|%difference|	31.6451	17.04829	58.90902
(K2G4)S 50J	7071.26	15.28	36.54
(K2G4)S 50J - FEM	8296.363	14.3593	18.272
|%difference|	17.3252	6.018942	49.99655

Table 46: comparison between experimental and numerical results for hybrid composites at 50J.

4.4. 90J impact energy simulations

Simulations at 90J showed some complications respect to the ones performed at 50J. Among the performed simulations three out of five were completed. In specimens (G4K2)S and pure Kevlar numerical problems occurred and it was not possible to end the simulations. For instance, excessive rotation and/or distortion of elements took place. A further investigation was performed about possible solutions for those kinds of errors and were applied in the model, but even if some little improvements were observed while running the simulation, at a certain point it would interrupt. The variations concerned mainly the further refinement of the mesh, which also led to a relatively much higher processing time, and modification of the contact properties between impactor and panel. As no real enhancement was observed, for the remaining samples, simulations were run keeping the initial setting parameters already described for mesh size and contact properties.

4.4.1. Glass composite

Respect to the simulation at 50J the results obtained for the glass specimen at this energy level show a better match with the experimental results. Closer measured values of force, displacement and absorbed energy and slope of the curves. The absorbed energy still represents the property with greatest divergence between numerical analysis and experiments, with a percentage difference of 45%. Maximum force and maximum displacement are in good match with percentage differences of about 6% and 14%.
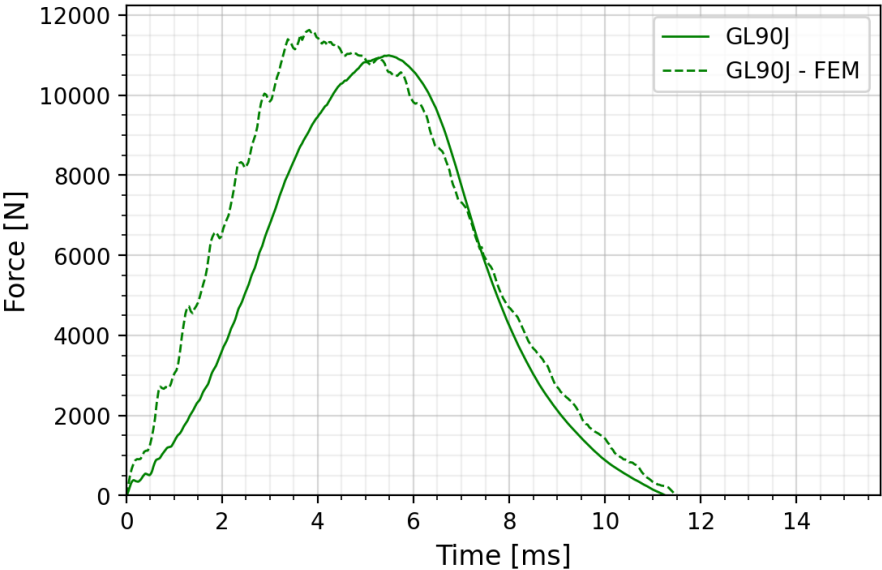
a)
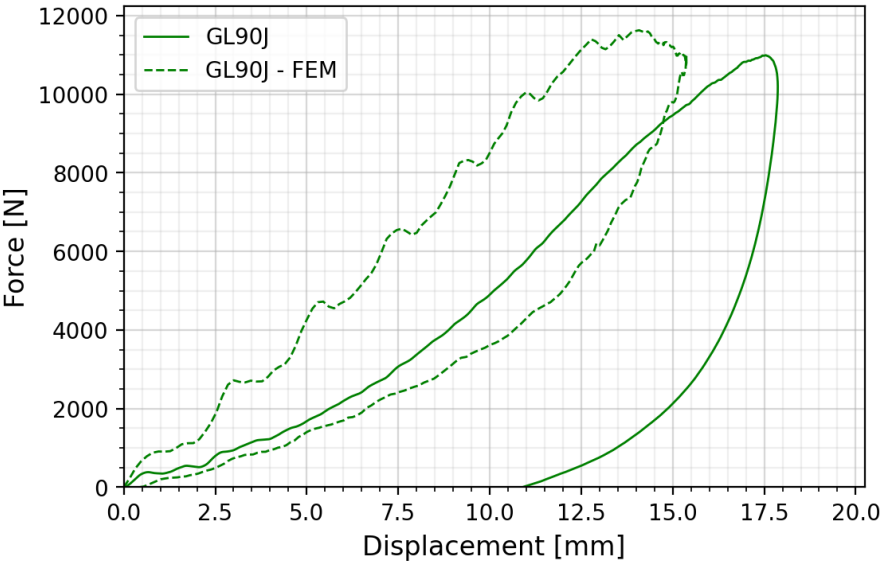
b)
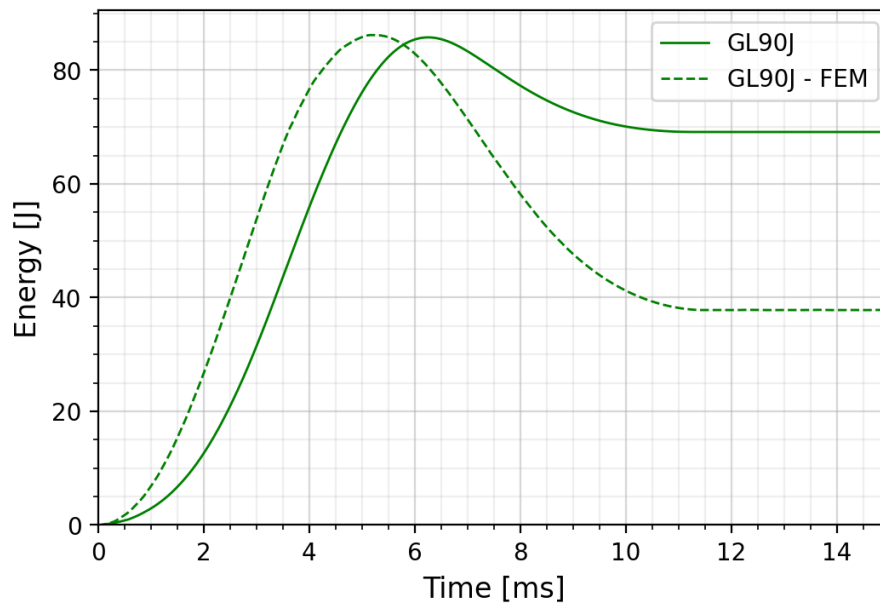
c)

Figure 4-12: glass experimental and numerical (a) Force-time curves , (b)Force- displacement curves, (c) Energy-time curves at 90J.

Property	F_{max}[N]	Maximum displacement [mm]	E_{abs}[J]
GL90J	10991.42	17.87	69.12
GL90J - FEM	11627.44	15.38	37.80
|%difference|	5.79	13.97	45.31

Table 47: comparison between experimental and numerical results for glass composite at 90J.

The reason why the results registered show an improvement in matching terms respect to the previous energy for glass composite is not easy to tell. An hypothesis can be that respect to the previous case, where the simulation showed a much stiffer material, here the more severe damage generated is affecting the materials response in terms of measured properties. For instance, to illustrate this concept, in the below Figures the tensile damage output variables at 50J and 90J are considered, and damage extension qualitatively confronted. SDV1 (Figure 4-13) is the tensile damage along fiber direction 1 (x axis) and SDV3 (Figure 4-14) is the tensile damage along fiber direction 2 (y axis). Maximum damage is registered when the output variable value is equal to one. It can be observed how at 90J the maximum damage of the material is registered from the

impact site through all the panel thickness, both for SDV1 and SDV3. Also, at the impact surface extensive damage is observed. As the measured properties from the simulations depend much on the response of the material constituting the external layers subjected to the impact, reaching the maximum damage in this area affect the material performance in terms of stiffness, leading then to values closer to the experimental ones.

a)   b)
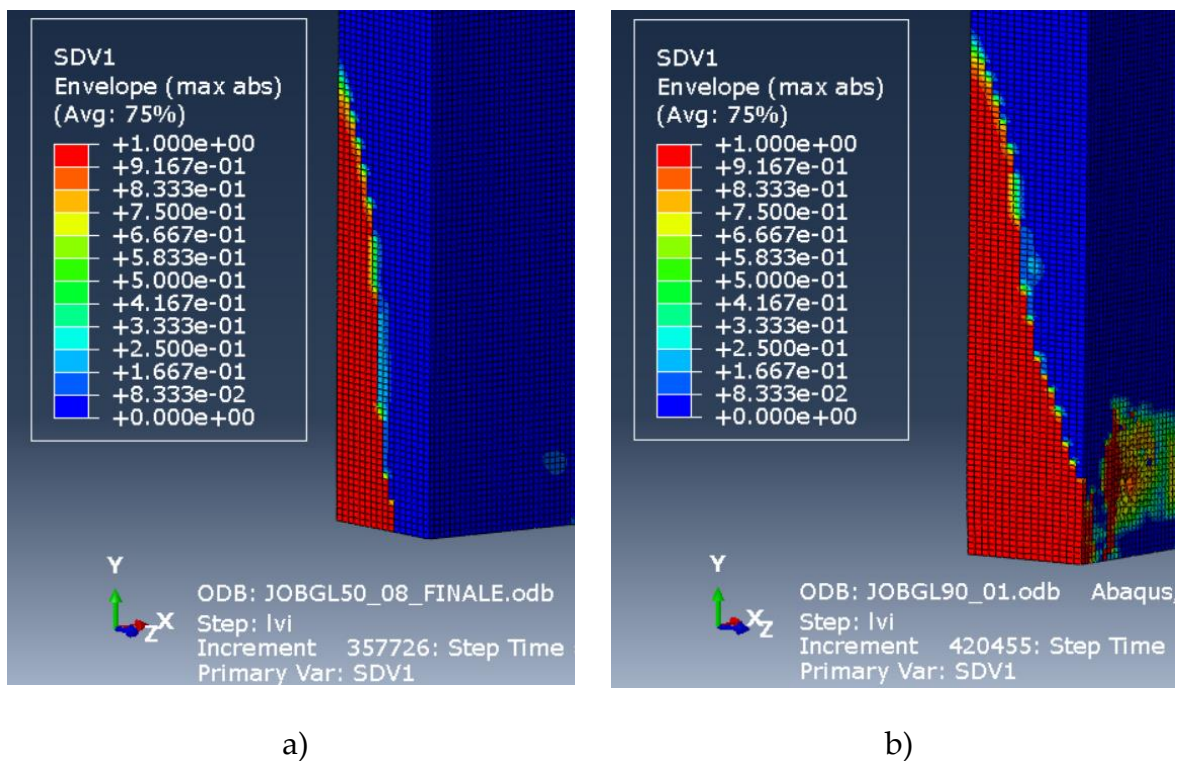
Figure 4-13: comparison between SDV1 of glass specimen at (a) 50J and (b) 90J.
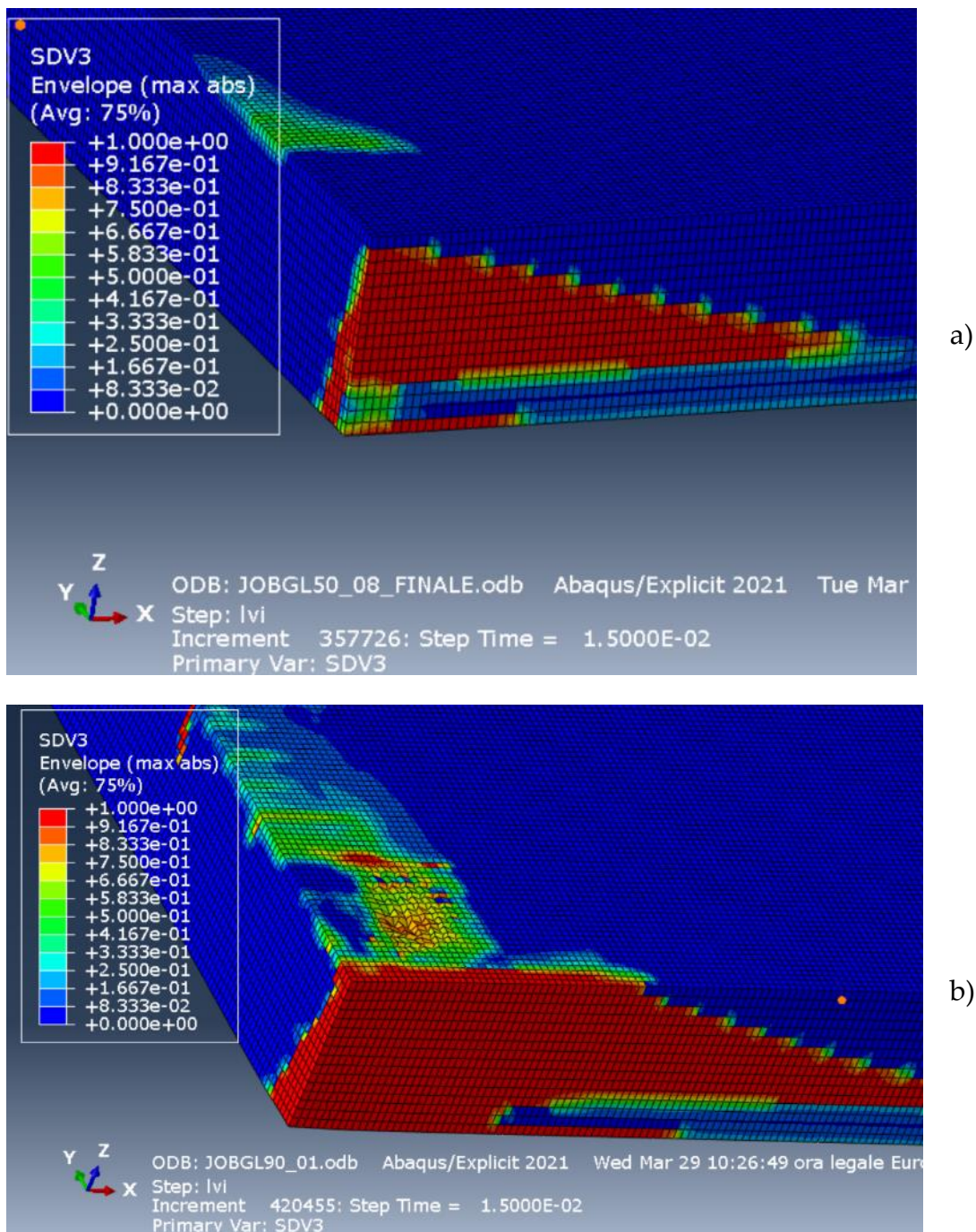
Figure 4-14: comparison between SDV3 of glass specimen at (a) 50J and (b) 90J.

4.4.2. Hybrid composites

It can be observed in Figure 4-15 the similar shape of the simulated curves for (G2K)2S and (K2G4)S configurations. The force-time curves represented are typical of a composite in which critical damage, such as perforation, takes place. This trend is similar to the one observed for the glass composite when going from the 50J impact simulation to 90J. Also for the hybrids at 50J the results from the simulations showed

a behavior typical of a stiffer material respect to the experimental evidence, while at 90J the damage reached in the material becomes critical in a highly extended area, leading to results which indicate the almost complete loss of the materials performance. The simulations at 90J predicted a premature degradation of the specimens. As the simulations show the behavior of a material which in a real impact experiment would be approaching its perforation it makes not complete sense to compare the registered results with the experimental tests as in the previous cases. This is the same concept expressed when the epoxy resin matrix composites which were critically damaged were not taken in consideration to be confronted with the PU composites. For instance, in Figures Figure 4-16Figure 4-17 a visive confrontation between the extent of damage in specimen (G2K)2S is performed.
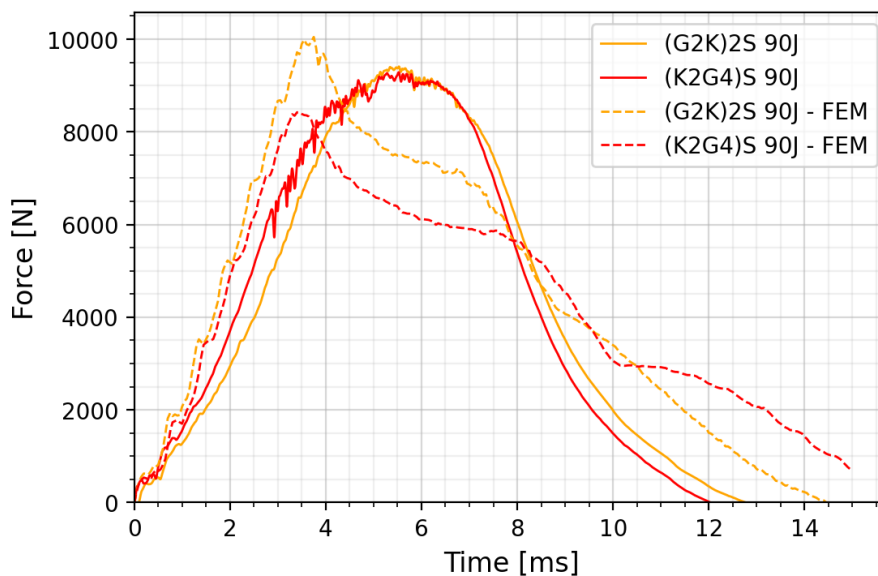
a)
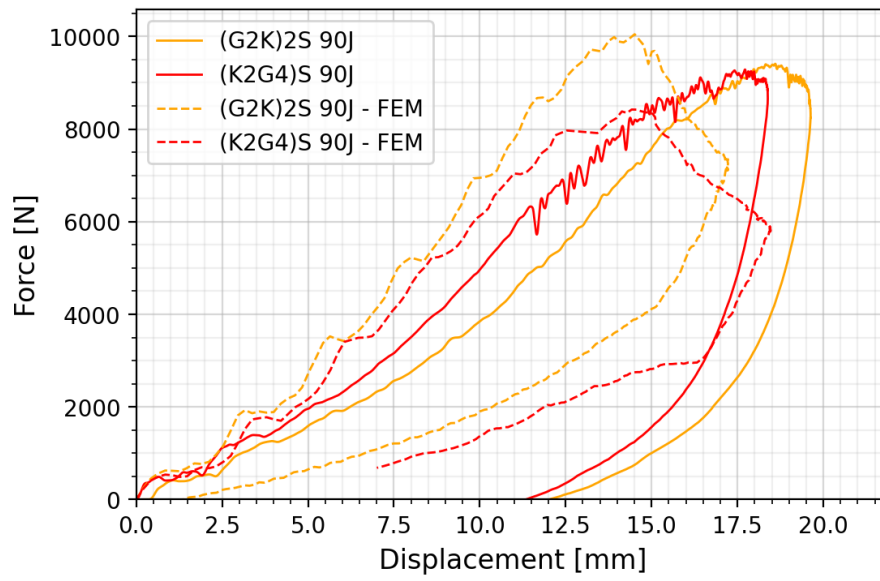
b)
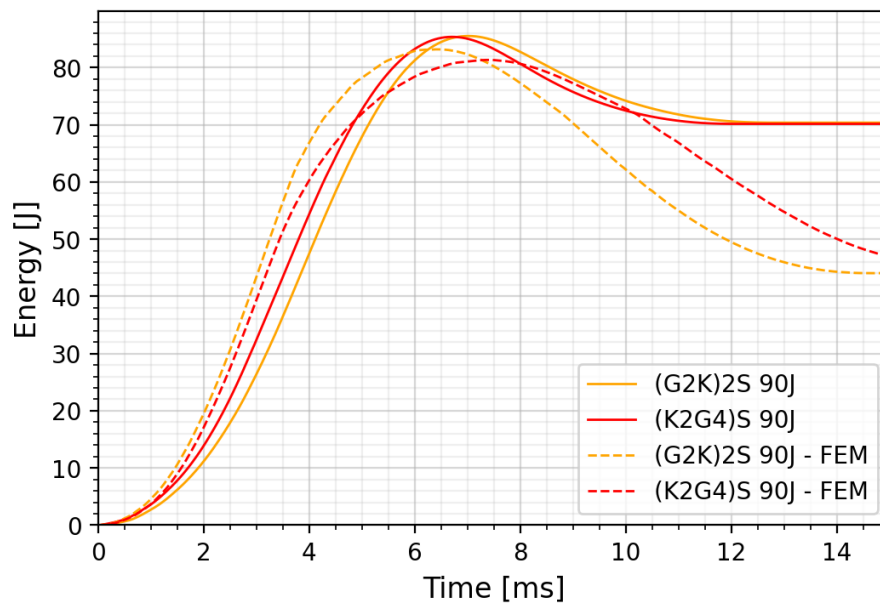
c)

Figure 4-15: hybrids experimental and numerical (a) Force-time curves , (b)Force-displacement curves, (c) Energy-time curves at 90J.
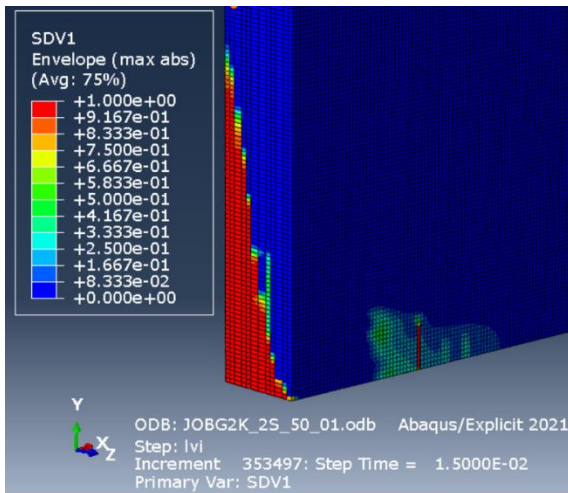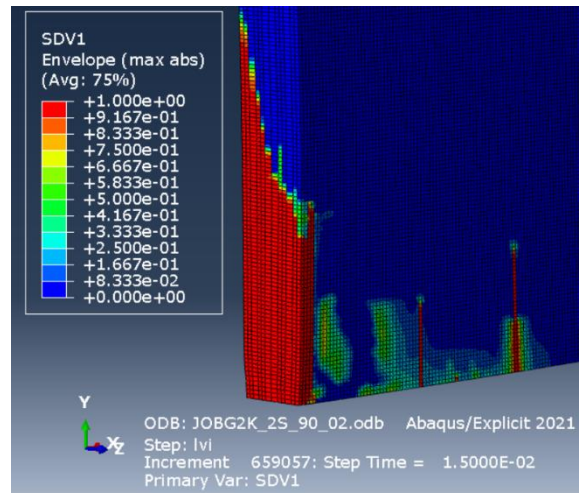
a)   b)

Figure 4-16: comparison between SDV1 of (G2K)2S specimen at (a) 50J and (b) 90J.
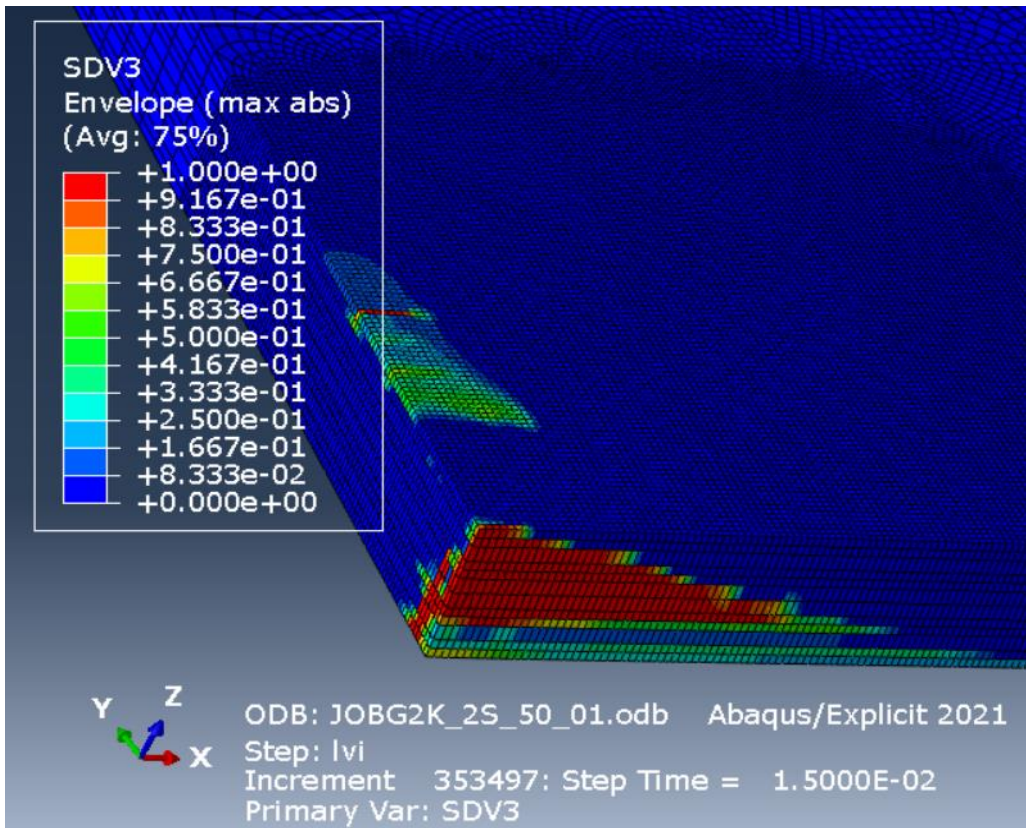
a)
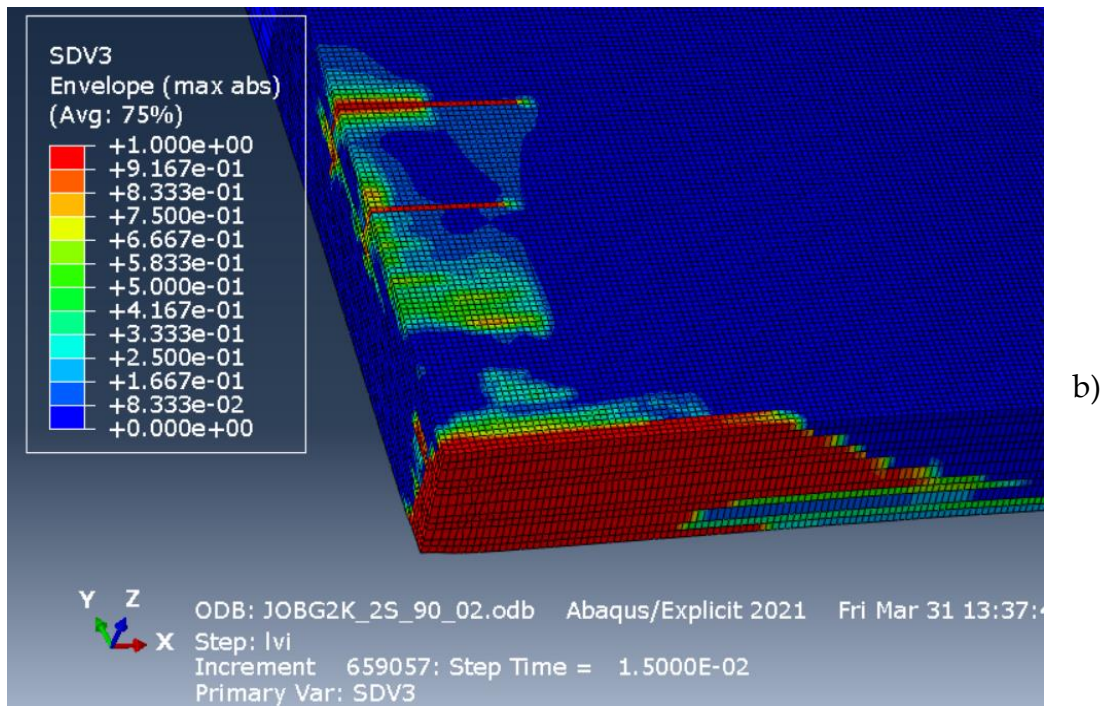
Figure 4-17: comparison between SDV3 of (G2K)2S specimen at (a) 50J and (b) 90J.

5   Conclusion and future developments

This thesis project was aimed at investigating the mechanical behaviour of glass, Kevlar, and inter-ply hybrid composites, in which an elastomeric resin was adopted in their manufacturing. The means of the investigation included an experimental campaign for the calibration of mechanical properties, impact tests for the study of the composites impact resistance, and finite element modelling of the above-mentioned impact tests. Numerical simulations represent a useful instrument to investigate the influence of different parameters on the materials response when subjected to specific solicitations. First objective was to validate the numerical model through the experiments and use it as a tool to design and predict behaviour of composites with varying configurations, with costs and time saving.

The calibration of the mechanical properties of the investigated composites was successively performed by means of tensile, compressive, and shears tests, from which the main engineering properties of the fabrics, i.e., glass and Kevlar composites, were derived.

Also the impact experimental campaign was concluded with satisfactory results as the main objectives from the tests were achieved.
In first place it was possible to observe the influence of the different stacking sequence in the hybrid composites on the impact response. In particular a positive hybridisation effect emerged from the (K2G4)S configuration, in which at increasing energy showed the highest value of absorbed energy over all samples.
Secondly also the influence of the elastomeric matrix material on the composite impact response could be well investigated from the obtained results. Concerning this aspect, the polyurethane resin matrix composites were also compared with same configuration composites manufactured with a standard epoxy resin matrix. This confrontation allowed to further confirm the behavior which emerged from the polyurethane composites when they were first analysed individually: the elastomeric matrix material contributed to the composites enhanced capability in resisting to the impact loads by absorbing a high amount of energy and through an increased deformation.

The absorbed energy in the polyurethane matrix composites reached a value up to 90% higher respect to the one reported in the epoxy ones. In engineering terms, the laminates here investigated showed an enhanced toughness with respect to the counterpart laminates made by the epoxy matrix. Moreover, it must be pointed out how the epoxy matrix laminates failed at a much lower energy level respect to the polyurethane matrix ones, with initial perforation being detected already at 50J while for the polyurethane case critical damage started to be observed at 90J or even 120J. Those results about the matrix influence on the impact resistance of composites can be considering as promising and could represent a starting point for further related research.

In the numerical analysis instead, results were not entirely consistent with the experimental ones. The material model adopted in the analysis consists of a user subroutine (VUMAT) incorporated in Abaqus/Explicit which is specifically designed to define the behavior of woven composites. The properties in the material model are the ones derived from the calibration tests first performed. The results from the simulations show a behavior which is typical of stiffer materials, for instance composites constituted by standard epoxy or similar resin materials. The material model here adopted might not be able to replicate the peculiar behavior of the investigated composites which is much influenced by the matrix material, as it was demonstrated also by the experiments. In fact, it is interesting to notice how the simulated curves and numerical results appear much closer to the obtained results from the tests performed on the epoxy resin composites with the same configurations. Another consideration regards an approximation performed initially about the composite's delamination, which was neglected in the modelling. Even though it might not be the principal cause of the emerged divergences in results it could represent partially a source of error in the analysis.

For a deeper investigation about the influence of an elastomeric matrix on the composite impact resistance more tests should be performed for future developments. Fundamental is the confrontation with same configuration composites and different matrix. For instance, as shown in this research project, the tested epoxy composites failed at energies slightly higher than 50J. Also, impact tests are performed to investigate mainly the internal damage and its effect on the structure residual strength after the impact. On those terms it would be more useful to design an experimental campaign in which the composites to be compared are tested at less severe energies, permitting a better analysis of the impact damage on specimens in which no critical damage is observed yet.

Regarding the numerical analysis in first place a more sophisticated material model should be adopted to describe the peculiar behavior exhibited by the composites. Best choice probably would be to use a specifically designed/writen user subroutine for the material model which uses more suitable equations to account for influence of the matrix material in the structure. The applied simplifications in the model, such as

neglecting delamination, might affect as well in a certain amount the simulations final results, but they cannot be considered as the principal sources of error. For future developments it is fundamental to develop/adopt a good material model which is able to finely describe the here investigate structures, accounting for the peculiar matrix material, and subsequently concentrate on the other modelling aspects, such as considering or not delamination damage for example.

Bibliography

[1]   T. J. Reinhart, "Overview of Composite Materials," in *Handbook of Composites*, Boston, MA, Springer US, 1998.

[2]   M. Rezasefat, A. Beligni, C. Sbarufatti, S. C. Amico and A. Manes, "Experimental and Numerical Study of the Influence of Pre-Existing Impact Damage on the Low-Velocity Impact Response of CFRP Panels," *Materials*, vol. 16, no. 3, 2023.

[3]   R. Scazzosi, S. D. B. d. Souza, S. C. Amico, M. Giglio and A. Manes, "Experimental and numerical evaluation of the perforation resistance of multi-layered alumina/aramid fiber ballistic shield impacted by an armor piercing projectile," *Composites Part B: Engineering*, vol. 230, 2022.

[4]   D. Ma, S. C. Amico, M. Giglio and A. Manes, "Effect of fibre bundle uncertainty on the tensile and shear behaviour of plain-woven composites," *Composite Structures*, vol. 259, 2021.

[5]   S. A. A. Xavier, S. Riccardo, M. Andrea and A. Sandro, "High-Velocity Impact Behavior of Aramid/S2-Glass Interply Hybrid Laminates," *Applied Composite Materials*, vol. 28, 2021.

[6]   A. A. X. d. Silva, Í. J. d. A. Silva, A. C. M. Miranda, A. Manes and S. C. Amico, "Influence of hybridization on the mechanical and dynamic mechanical properties of aramid/S2-glass hybrid laminates," *Materials Today Communications*, vol. 32, 2022.

[7]   M. Rezasefat, A. A. d. Silva, S. C. Amico, M. Giglio and A. Manes, "Repeated impact behaviour of inter-ply hybrid aramid/S2-glass epoxy laminates," *Thin-Walled Structures*, vol. 186, 2023.

[8]   J. A. Cruz, S. C. Amico and O. Bianchi, "Effect of the aramid pulp on the physicochemical, viscoelastic properties and rheokinetics of polyurethanes," *Journal of Polymer Research*, vol. 30, 2022.

[9] J. A. Cruz, E. F. Kerche, O. Bianchi, A. Manes and S. C. Amico, "Castor Oil-Based Polyurethane/S2 Glass/Aramid Hybrid Composites Manufactured by Vacuum Infusion," *Polymers,* vol. 14, 2022.

[10] R. Frassine, Tecnologie e proprietà dei materiali compositi, Milano , 2021.

[11] B. Zuccarello, "Cap1-Introduzione ai materiali compositi," in *Progettazione meccanica con materiali non convenzionali*, 2008.

[12] D. Tommaso, R. Frassine and A. Calabrese, *note del corso "Composite materials for structural applications"*, Politecnico di Milano, 2021-2022.

[13] T.-D. Ngo, "Introduction to composite materials," in *Composite and Nanocomposite Materials-From knowledge to Industrial applications*, DOI: 10.5772/intechopen.91285, July 2020.

[14] P. Pop and B. Gheorghe, "MANUFACTURING PROCESS AND APPLICATIONS OF COMPOSITE MATERIALS," *ANNALS OF THE ORADEA UNIVERSITY. Fascicle of Management and Technological Engineering.,* vol. XIX (IX), 2012.

[15] T. Gajjar, D. B. Shah, S. Joshi and K. Patel., "Analysis of Process Parameters for Composites Manufacturing using Vacuum Infusion Process," *Materials Today: Proceedings,* vol. 21, pp. 1244-1249, 2020.

[16] "BFG International," 2023. [Online]. Available: https://www.bfginternational.com/what-we-do/vacuum-infusion.

[17] B. Zuccarello, "Cap5-Laminati compositi," in *Progettazione meccanica con materiali non convenzionali*, 2008.

[18] M. Daniel and O. Ishai, in *Engineering Mechanics of Composite Materials.*, New York, Oxford University Press, 2006.

[19] G. Vairo, "Laminate Theory: Laminate Plate," University of Rome- "Tor Vergata", Roma.

[20] E. Oterkus, C. Diyaroglu, D. D. Meo and G. Allegri, "4-Fracture modes, damage tolerance and failure mitigation in marine composites," in *Marine Applications of Advanced Fibre-Reinforced Composites*, Woodhead Publishing, 2016, pp. 79-102.

[21]   B. Zucarello, "Cap6-Modalità di rottura e criteri di resistenza," in *Progettazione meccanica con materiali non convenzionali*, 2008.

[22]   T.Tay, "Characterization and analysis of delamination fracture in composites: An overview of developments from 1990 to 2001," *Applied Mechanics Reviws,* 2003.

[23]   J. V. Aguirre, R. Álvarez, J. Noguera, L. Tortosa and A. Zamora, "Finite Element Guidelines for Simulation of Delamination Dominated Failures in Composite Materials Validated by Case Studies," *WSEAS Trans. Comput.,* vol. 5, no. 1, pp. 171-176, 2006.

[24]   A. Eijo, E. Onate and S. Oller, *Finite Element Modeling of Delamination in Advanced Composite Beams and Plates using one-and two-dimensional Finite Elements based on the Refined Zigzag theory,* Barcelona, Spain: Monograph CIMNE , 2014.

[25]   A. Barut, E. Madenci and A. Tessler, "A refined zigzag theory for laminated composite and sandwich playtes incorporating thickness stretch deformation," *53rdAIAA/ASME/ASCE/AHS/ASC structures, structural dynamics, and materials conference,* 2012.

[26]   I. Daniel, *Failure of Composite Materials,* Gdoutos, E.E. (eds) Fracture of Nano and Engineering Materials and Structures. Springer, Dordrecht. https://doi.org/10.1007/1-4020-4972-2_5, 2006.

[27]   F.Brinson and L. C. Brinson, Polymer engineering scince and viscoelasticity: An introduction, Springer US, 2008.

[28]   Z.Hashin, "Failure criteria for unidirectional fiber composites," *Applied Mechanics,* vol. 47, pp. 329-334, 1980.

[29]   M. Nahas, " Failure and Post-Failure Theories of Laminated Fiber-Reinforced Composites," *Journal of Composites Technology and Research,* vol. 8, no. 4, pp. 138-153, 1986.

[30]   S. V.Lomov and I. Verpoest, "Textile Composite Materials: Polymer Matrix Composites," *Encyclopedia of Aerospace Engineering,* 2010.

[31]   P. Ladeveze and E. Le Dantec, "Damage modelling of the elementary ply for laminated composites," *Comp. Sci. Technol.,* vol. 43, pp. 257-267, 1992.

[32] P. Sjoblom, T. Hartness and T. M. Cordell, "On low-Velocity Impact Testing of Composite Materials," *Journal of Composite materials,* vol. 22, no. 30-52, 1988.

[33] R. Olsson, "Analytical prediction of large mass impact damage in composite laminates," *Composites Part A: applied science and manufacturing,* vol. 32, pp. 1207-1215, 2001.

[34] A. Soto, E. González, P. Maimí, F. M. d. l. Escalera, J. S. d. Aja and E. Alvarez, "Low velocity impact and compression after impact simulation of thin ply laminates," *Composites Part A: Applied Science and Manufacturing,* vol. Volume 109, pp. 413-427, 2018.

[35] C. Kassapoglou, "Impact," in *Modelling the Effect of Damage in Composite Structures: Simplified Approaches*, John Wiley & Sons Ltd, 2015.

[36] K. Kaware and M. Kotambkar, "Low velocity impact response and influence of parameters to improve the damage resistance of composite structures/materials: a critical reviw," *International Journal of Crashworthiness,* vol. 27, no. 4, pp. 1232-1256, 2022.

[37] E. V. González, P. Maimí, P. Camanho, A. Turon and J. Mayugo, "Simulation of drop-weight impact and compression after impact tests on composite laminates," *Composite Structures,* vol. 94, no. 11, pp. 3364-3378, 2012.

[38] M. Richardson and M. J. Wisheart, "Review of low-velocity impact properties of composite materials," *Composites Part A: Applied Science and Manufacturing,* vol. 27, pp. 1123-1131, 1996.

[39] A. Yudhanto, H. Wafai, G. Lubineau, S. G. Pattapu, M. Mulle, R. Yaldiz and N. Verghese, "Revealing the effects of matrix behavior on low-velocity impact response of continuous fiber-reinforced thermoplastic laminates," *Composite Strucutures,* vol. 210, 2018.

[40] E. Panettieri, D. Fanteria, C. Montemurro and C. Frostey, "Low velocity impact tests on carbon/epoxy composite laminates: A benchmark study," *Composites Part B: Engineering,* vol. 107, no. 9-21, 2016.

[41] G. Marzio and X. Yigeng, "Threshold Identification and Damage Characterization of Woven GF/CF Composites under Low-Velocity Impact," *Journal of Composites Science,* vol. 6, no. 10, 2022.

[42] *D7136/D7136M – 15 Measuring the Damage Resistance of a Fiber-Reinforced Polymer Matrix Composite to a Drop-Weight Impact Event.*

[43] S. Abrate, Impact on Composite Structures, Cambridge: Cambridge University Press, 1998.

[44] J.-K. Kim and M. L. Sham, "Impact and Delamination Failure of Woven-Fabric Composites," *Composites Science and Technology,* vol. 60, 2000.

[45] Z. Wu, L. Zhang, Z. Ying, J. Ke and X. Hu, "Low-velocity impact performance of hybrid 3D carbon/glass woven orthogonal composite: Experiment and simulation," *Composites Part B: Engineering,* vol. 196, 2020.

[46] M. Bulut and A. E. E. Yeter, "Hybridization effects on quasi-static penetration resistance in fiber reinforced hybrid composite laminates," *Composites Part B: Engineering,* vol. 98, pp. 9-22, 2016.

[47] C. Dong and I. J. Davies, "Flexural and tensile strengths of unidirectional hybrid epoxy composites reinforced by S-2 glass and T700S carbon fibres," *Materials & Design (1980-2015),* vol. 54, pp. 955-966, 2014.

[48] N. Sela and O. Ishai, "Interlaminar fracture toughness and toughening of laminated composites," *Composites,* vol. 20, pp. 423-435, 1989.

[49] "Abaqus-Assitenza utenti SIMULIA," 2022. [Online]. Available: https://help.3ds.com/2022/english/dssimulia_established/SIMULIA_Establish ed_FrontmatterMap/sim-r-DSDocAbaqus.htm?contextscope=all&id=ec01bc8c83d743a6a30123c5a034edca .

[50] D. S. S. Corp., ABAQUS-Theory Manual, 2011.

[51] A.E.H.Love, "On the small free vibrations of elastic shells," *Philosophical trans. of the Royal Society ,* Vols. Vol. serie A, N°17, pp. 491-549, 1888.

[52] R.D.Mindlin, "Influence of rotatory inertia and shear on flexural motions of isotropic, elastic plates," *ASME Journal of Applied Mechanics,* vol. 18, pp. 31-38, 1951.

[53] B. a. J. Budiansky, "On the 'Best First Order Linear Shell Theory," *Progress in Applied Mechanics ,* vol. The Prager Anniversary Volume, pp. 129-140, 1963.

178

[54] "ABAQUS Analysis user's manual," 2011. [Online]. Available: https://classes.engineering.wustl.edu/2009/spring/mase5513/abaqus/docs/v6.6 /books/usb/default.htm?startat=pt06ch23s06alm15.html.

[55] S. S. Corp., *VUMAT for Fabric Reinforced Composites*, Providence, RI, USA, 2008.

[56] J. S. Alastair F.Johnson, "Modeling Fabric Reinforced Composites under Impact Loads," in *Impact and Damage Tolerance of Composite Materials and Structures*, London, Imperial College of Science Technology and Medicine, September 1999.

[57] *ASTM D3039/D3039M-17 Standard Test Method for Tensile Properties of Polymer Matrix Composite Matreials.*

[58] *D3410/D3410M – 16 Standard Test Method for Compressive Properties of Polymer Matrix Composite Materials.*

[59] *D3518/D3518M – 13 In-Plane Shear Response of Polymer Matrix Composite Materials by Tensile Test of a 45 laminate.*

[60] A. Qiu, K. Fu, W. Lin, C. Zhao and Y. Tang, "Modelling low-speed drop-weight impact on composite laminates," *Materials and Design,* vol. 60, 2014.

List of Figures

List of Tables